In Vitro Corrosion Behaviour of Biodegradable Magnesium Implants

In vitro Korrosionsverhalten von biologisch abbaubaren Magnesiumimplantaten

Von der Fakultät für Maschinenwesen der Rheinisch-Westfälischen Technischen Hochschule Aachen zur Erlangung des akademischen Grades einer Doktorin der Ingenieurwissenschaften genehmigte Dissertation

vorgelegt von

Julia Alessandra Nachtsheim

Berichter: Univ.-Prof. Dr.-Ing. Dr. h. c. (PSACEA) Bernd Markert
apl. Prof. Dr.-Ing. Marcus Stoffel

Tag der mündlichen Prüfung: 5. September 2025

Report No. IAM-25
Institute of General Mechanics / Institut für Allgemeine Mechanik (IAM)
RWTH Aachen University, Germany, 2025

Editor:

Univ.-Prof. Dr.-Ing. Dr. h. c. (PSACEA) Bernd Markert

© Julia Nachtsheim
Institute of General Mechanics
RWTH Aachen University
Eilfschornsteinstraße 18
52062 Aachen, Germany

Tel: +49 / (0)241 / 80 94 60 0
Internet: www.iam.rwth-aachen.de

Acknowledgements

I would like to express my sincere gratitude to my supervisors Prof. Bernd Markert and Prof. Marcus Stoffel for offering me the opportunity to join their research group, guiding me throughout the journey of this dissertation and for all the support and encouragement. During my time as a research assistant, I was able to contribute to innovative projects related to engineering and science in the field of mechanics and medicine. I am grateful for the broad knowledge I gained. Teaching young students in mechanics and biomechanics has been an honour.

I would like to express my deepest gratitude to Dr. Songyun Ma, who initiated and supervised the interdisciplinary research project. He always provided valuable guidance, encouragement and continuous support. Furthermore, sincere thanks go to the German Federal Ministry of Research and Education for funding the research project RePlaSys (13GW0352B) and making the research possible. I am deeply thankful to the project partner Medical Magnesium GmbH, who provided necessary resources.

I would like to express my deepest gratitude to doc. dr. Jaka Burja for the fruitful collaboration and for providing valuable guidance from the metallurgical perspective. He was always encouraging and open for discussions. My sincere appreciation goes to Prof. Godec, dr. Barbara Šetina Batič, dr. Borut Žužek, Tina Sever and Miro Pečar for their valuable assistance on experimental analysis.

Furthermore, I would like to extend special thanks to Mario Hackbarth and Uwe Navrath, whose valuable assistance in both the design and laboratory work significantly enriched this project. I would like to thank Access e.V. for generously granting me access to their microscope. A heartfelt thanks goes to Thomas and Dongxu for valuable assistance on experimental work. Special appreciation is extended to my research students Laurent, Devran, Efdal and Jan, who have supported me enormously. It has been a great pleasure and an unforgettable experience working with them. A sincere thanks to all the students I had the privilege of teaching and supervising. A special thanks to Dr. Ban for all the invaluable support in these tasks.

A special thanks to my former colleagues. It has been a pleasure to work together and to share unforgettable moments. And heartfelt gratitude to my friends who dedicated their time to proofread this thesis.

I extend my heartfelt appreciation to my family for their endless love and encouragement during this challenging journey. Their unwavering belief in my abilities has been my source of strength and motivation.

Aachen, September 2025 Julia Nachtsheim

On ne fait jamais attention à ce qui a été fait ; on ne voit que ce qui reste à faire.

Marie Curie (1867-1934)

Posvečeno moji ljubljeni družini.
Dedicated to my beloved family.

List of publications

This thesis is based on the following peer-reviewed articles:

- **Nachtsheim, J.**, Ma, S., Burja, J., Kopp, A., Seitz, J. M. & Markert, B.: In vitro corrosion-fatigue behaviour of rare-earth containing magnesium alloy WE43 in sterile complex cell culture medium. *Int. J. Fatigue* **188** (2024), 108531.
- **Nachtsheim J.**, Ma, S., Burja, J. & Markert, B.: In vitro evaluation of stress corrosion cracking susceptibility of PEO-coated rare-earth magnesium alloy WE43. *Surf. Coat. Technol.* **477** (2022), 130391.
- **Nachtsheim, J.**, Ma, S., Burja, J., Batič, Š. B. & Markert, B.: Tuning the long-term corrosion behaviour of biodegradable WE43 magnesium alloy by PEO coating. *Surf. Coat. Technol.* **474** (2023), 130115.
- **Nachtsheim, J.**, Burja, J., Ma, S. & Markert, B.: Long-term in vitro corrosion of biodegradable WE43 magnesium alloy in DMEM. *Metals* **12.12** (2022), 2062.
- Zhang, D., Ma, S., **Nachtsheim, J.**, Zhang, S. & Markert, B.: A variational phase-field framework for multiphysics modelling of degradation and stress corrosion cracking in biodegradable magnesium alloys. *J Mech Phys Solids* (2024), 105694.
- **Nachtsheim, J.**, Burja, J., Ma, S., & Markert, B.: In vitro degradation behaviour of biodegradable magnesium alloys. *PAMM* **22** (2023), e202200326.

Additionally, parts of the thesis were published in the final project report of RePlaSys.

Moreover, I contributed to the following peer-reviewed articles in the field of tissue-engineering:

- **Nachtsheim J.**, Dursun, G., Markert, B., & Stoffel, M.: Chondrocyte colonisation of a tissue-engineered cartilage substitute under a mechanical stimulus. *Med. Eng. Phys.* **74** (2019), 58-64.
- Stoffel, M., Dursun, G., **Nachtsheim, J.**, Fuhrmann-Nelles, N., & Markert, B.: Bioreactor development for regenerative tissues of the locomotor system. *PAMM* **18** (2018), e201800108.
- **Nachtsheim, J.**, Dursun, G., Markert, B., & Stoffel, M.: Chondrocyte migration in an acellular tissue-engineered cartilage substitute. *PAMM* **18** (2018), e201800425.
- **Nachtsheim, J.**, Markert, B., & Stoffel, M.: Mechanobiological processes of tissue engineered cartilage replacement materials. *PAMM* **17** (2017), 211-212.

Contents

Abstract

Biodegradable magnesium implants can potentially resolve major challenges of conventional implant technologies. They provide mechanical support to the fracture site and gradually degrade within the body. This can eliminate the need for an implant-removal surgery, which is beneficial to the patient and to healthcare systems. Magnesium alloys are especially suitable for bone fracture treatments, as they are highly biocompatible and possess mechanical properties similar to those of native bone. Their similar elastic moduli improves load transfer. Thereby, the recovering bone is continuously subjected to physiological stresses. This reduces the risk of stress-shielding and pathological tissue development. Their broad application, however, is limited by their fast material degradation in physiological conditions, which can cause harmful side effects and can result in catastrophic implant failure. In this context, research and development efforts are required to establish in-depth understanding of the relevant degradation processes and to derive strategies to overcome these limitations.

The aim of this thesis is to systematically study the in vitro corrosion behaviour of a biodegradable magnesium alloy WE43, which is currently under development for load-bearing implant applications. The material is alloyed with rare-earth elements, and a PEO coating is applied for an improved protection against corrosion. For this purpose, experimental in vitro studies were conducted to assess the degradation behaviour of the material under different external load protocols. In service conditions, the implant is exposed to considerable mechanical loadings and aggressive physiological corrosion environments. This combination triggers adverse mechano-chemical interactions, which accelerate material degradation. Hence, understanding the underlying mechanisms is particularly important.

The experimental results reveal a localised corrosion process of WE43, which can be attributed to the fine and evenly dispersed secondary phases. The barrier effect of the coating fully preserves the mechanical integrity for 14 days and delays the degradation process for longer periods. Under constant loadings, a critical stress level is identified, which leads to a high probability of failure in the short term. The protection of the coating against material degradation is limited to its undamaged state. High local stresses trigger coating damage, which adds another source for material failure. Under very slow and continuously increasing straining in slow strain rate testing, the material suffered significant embrittlement. Synergetic mechanisms of corrosion and crack propagation are revealed on fracture surfaces. In corrosion-fatigue experiments, the fatigue performance is considerably reduced and the failure mode changes in comparison to the pristine alloy.

The experimental findings provide valuable information on the environmentally assisted mechanisms. Based on the experimental results, strategies for further improving the material's functionality are derived and some findings can be translated into recommendations for therapeutic strategies.

Zusammenfassung

Die Entwicklung resorbierbarer Implantate aus Magnesium ist für die Versorgung von Knochenfrakturen sehr vielversprechend, da diese einige Vorteile gegenüber konventionellen Therapielösungen bieten. Das Material ist biokompatibel und wird vom Köper biologisch abgebaut. Dadurch kann dem Patienten eine zweite Operation zur Entnahme des Implantats erspart werden, mit positiven Effekten für das Gesundheitssystem. Aufgrund der ähnlichen Elastizität zu Knochengewebe wird die Bruchstelle während des Heilungsprozesses physiologischen Lastbedingungen ausgesetzt, was den Heilungsprozess begünstigt. Limitiert werden Fraktursysteme aus Magnesium jedoch durch die geringe Korrosionsbeständigkeit des Materials unter physiologischen Bedingungen. Dies führt zu einem unkontrollierten und vorzeitigen Verlust der mechanischen Integrität des Implantats. Dies motiviert Forschungs- und Entwicklungsvorhaben, die Überlagerung dieser komplexen mechano-chemischen Mechanismen zu verstehen und darüber hinaus Strategien zu entwickeln, um diese Hürde zu überwinden.

Ziel dieser Arbeit ist die systematische Untersuchung des Degradierungsprozesses einer Speziallegierung mit seltenen Erden für die medizinische Anwendung. Darüber hinaus wird der Einfluss von einer mittels plasmaelektrolytischer Oxidation keramisierten Oberfläche analysiert. In diesem Rahmen wurden mehrere in-vitro-Studien durchgeführt, um den Einfluss verschiedener Belastungen zu untersuchen. Besonders die Kombination aus aggressiver Korrosionsumgebung und mechanischer Belastung beschleunigt den Verlust der mechanischen Integrität. Diese mechanisch-chemischen Prozesse zu verstehen ist für erfolgreiche Entwicklungsvorhaben von zentraler Bedeutung.

In organischer physiologischer Korrosionsumgebung korrodiert die Speziallegierung relativ homogen, ohne Tendenz zu Lochfraßkorrosion. Dies kann auf die Mikrostruktur mit sehr feinen und gleichmäßig verteilten Sekundärphasen zurückgeführt werden. Die PEO-Beschichtung erhält die mechanische Integrität vollumfänglich über einen Zeitraum von 14 Tagen und verlangsamt den Degradationsprozess. Bei Korrosion unter konstanter Last kann ein kritisches Spannungsniveau identifiziert werden. Die Überschreitung dieser Lastgrenze führt zu einer hohen Versagenswahrscheinlichkeit. Die Überlagerung von Korrosionsprozess und Risswachstum ist in den Bruchflächen klar erkennbar. Die Schutzwirkung der Beschichtung ist auf den unbeschädigten Zustand beschränkt. Aufgrund der spröden Beschaffenheit reißt die Beschichtung unter hohen Spannungen, was den Degradationsprozess beschleunigt. Die Deformation mit einer konstanten Dehnungsrate verstärkt den schädlichen Einfluss der Beschichtung. Bei beschichteten und unbeschichteten Proben ist eine deutliche Versprödung erkennbar. In Korrosionsermüdungsversuchen wurde die Lebensdauer des Materials deutlich reduziert und es konnte eine Änderung in der Bruchart festgestellt werden.

Die in-vitro-Studien liefern wertvolle Erkenntnisse zu umgebungsbasierten Versagensprozessen. Basierend auf den experimentellen Ergebnissen lassen sich Strategien zur Verbesserung der Materialfunktionalität ableiten. Darüber hinaus können Empfehlungen für die postoperative Therapie entwickelt werden.

1 Introduction

1.1 Biodegradable orthopaedic magnesium implants

Biodegradable magnesium alloys are a new class of temporary orthopaedic implant materials and considered propitious in replacing permanent implant materials [142]. As the implant self-degrades inside the patient, a second surgery to remove the implant can be avoided. This relieves pressure on overburdened healthcare systems while also sparing the patient from additional painful therapy and morbidity. In this context, biodegradable materials are particularly suitable for implants that do not need to remain permanently inside the patient, as it is the case with fixation of bone fractures. The state of care in the treatment of bone fractures is temporarily fixation with titanium implants. These implants rarely remain inside the patient permanently and in most cases are removed again after convalescence, as they entail a persistent risk of undesired side effects [138]. Permanent implants are foreign objects to the body that can cause inflammations even several years after implantation. A critical factor of titanium implants in the treatment of bone fractures is their mismatching elasticity [150]. Titanium is significantly stiffer than bone, with elastic moduli of about 110GPa and 3-20GPa, respectively [103]. As a result, the mechanical loads are predominantly carried by the implant and the healthy bone tissue is no longer exposed to physiological loading regimes. According to Wolff's law, the bone tissue will undergo pathological changes (decrease in bone density) at these unphysiologically low stress levels, which is described as stress-shielding. The effect can be significantly reduced by using magnesium alloys because the elastic modulus of magnesium is much closer to that of native bone (approximately 45GPa [103]).

In summary, magnesium alloys have considerable advantages over conventional permanent implant materials [151, 157]. Nonetheless, the limiting factors for its broad use are its high corrosion rates and its rapid material degradation [2]. Two aspects must be considered in this context. Firstly, the corrosion process of alloy systems leads to the release of their constituents, which are subsequently metabolised by the human body. Therefore, the corrosion rate must correspond to the patient's metabolic capacity, otherwise toxic side effects may occur [46]. For magnesium, which plays an important role in human metabolism, the daily allowance of about 225-320mg/day for a female adolescent and 330-420mg/day for a male adolescent should not be exceeded [47]. Corresponding limits must also be taken into account for all alloying elements. Adverse effects can also result from the formation of gas pockets from hydrogen which is released during

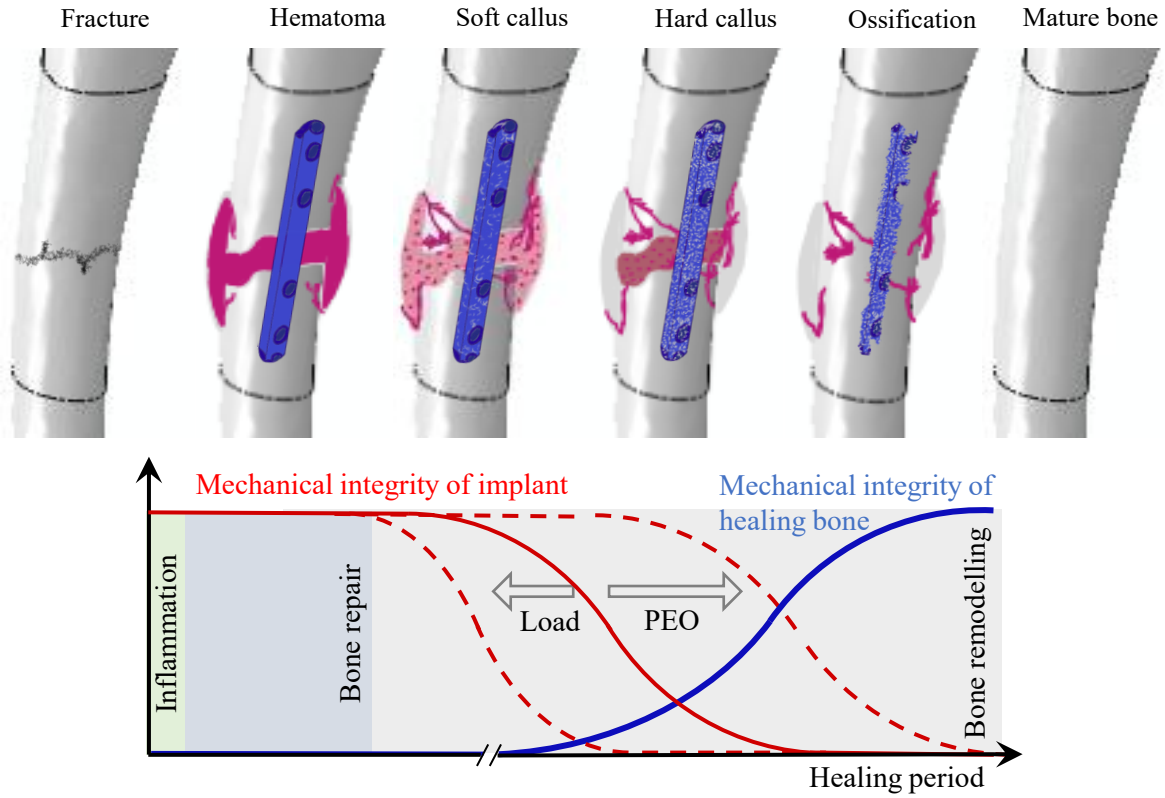

Figure 1.1.: Re-strengthening of bone tissue after fracture and degradation of the implant, adapted from [35, 142].

magnesium corrosion. This can only be prevented by suitable corrosion rates [71, 147]. Secondly, corrosion involves loss of mechanical integrity either through material loss or, more importantly, through the adverse interactions of external loads and the aggressive physiological corrosion environment [72]. This combination may cause premature failure due to stress corrosion cracking or corrosion-fatigue.

For adequate functionality, biodegradable implants must be designed to provide sufficient support throughout the healing process. Reliable support of the fracture site must be ensured during the hardening process of the bone callus from soft fibrous tissue to harder bone tissue, as shown in Figure 1.1. This could theoretically be achieved by oversizing implants. However, this concept is certainly not appropriate: in the long term, the entire implant will degrade in the patient and the entire implanted mass will be metabolised, necessitating an optimised implant of minimised mass. Based on this, controlling the corrosion rate plays a decisive role in implant design. Alloying elements and microstructural features can influence the corrosion rate of magnesium alloys to a limited extent. A more effective and propitious approach to decelerating the corrosion process is applying biocompatible coatings. Surface modification by plasma-electrolytic oxidation (PEO) provides a highly biocompatible coating, which offers corrosion protection along with other beneficial features that favour its medical functionality. PEO coating on magnesium alloys has been found to increase biocompatibility, improve osseous integration and promote bone formation [136, 175]. However, the protective capacity

of the coating is attributed to certain structural parameters [32], which may limit or confine its functionality to the short term [6]. Furthermore, brittle coatings easily crack when exposed to mechanical loads, offering sites for corrosion attack. Improving the functionality of protective coatings is an ongoing and dynamic field of research [43, 44].

Coping with the complex adverse mechano-chemical interactions is the second key challenge in the development of biodegradable implants. In service conditions, the implant is subjected to a combination of mechanical stresses as well as a corrosive environment, which triggers environmentally-assisted failure mechanisms. From the engineering perspective this is a serious concern, as it compromises the integrity and structural reliability of the implant and can lead to premature and unforeseen failure. Depending on the type of loading, stress corrosion cracking (SCC) and corrosion-fatigue (CF) phenomena are distinguished. Magnesium alloys are susceptible to SCC and CF and failure mechanisms are often accompanied by material embrittlement due to hydrogen-assisted phenomena. Hence, a biodegradable implant material must demonstrate the ability to withstand environmentally assisted failure to a certain extent to ensure safe in vitro applications.

Concluding, magnesium alloys offer significant advantages over conventional titanium implants, but certain issues related to the challenging in vitro service conditions remain unresolved. Identifying suitable magnesium alloys has been addressed by interdisciplinary research groups in recent years. Improving their corrosion resistance as well as assessing and understanding the highly complex mechano-chemical interactions is getting more and more attention in interdisciplinary research. Especially, since a comprehensive understanding of the degradation processes is inevitable for designing safe load-bearing biodegradable magnesium alloys.

1.2 Objectives and study design

In 2016, the first two biodegradable magnesium implants received CE marking of conformity; both magnesium alloys are alloyed with rare-earth elements. BIOTRONIK SE & Co. KG (Berlin, Germany) has approved a biodegradable stent for coronary intervention based on a WE43 scaffold. Syntellix AG (Hannover, Germany) has approved biodegradable orthopaedic screws, pins and smaller one-piece implants based on a Mg-Y-RE-Zr alloy. In general, the rare earth-containing alloy WE43 is considered a prime candidate for biodegradable magnesium implants [71].

A fully biodegradable implant system of PEO-coated WE43 magnesium has recently been developed by Medical Magnesium GmbH (Aachen, Germany) for orthopaedic applications. The design and medical approval process for podiatric treatments are ongoing, with a focus on the correction of hammer toes, claw toes or the treatment of hallux valgus. The treatment of hallux valgus is shown in Figure 1.2. The deformity is corrected and fixed with an implant consisting of a plate and screws.

For an optimised implant functionality, the degradation process of the material in physiological service conditions must be systematically studied, which is the objective of this thesis. In this context, several incompletely assessed research issues are addressed.

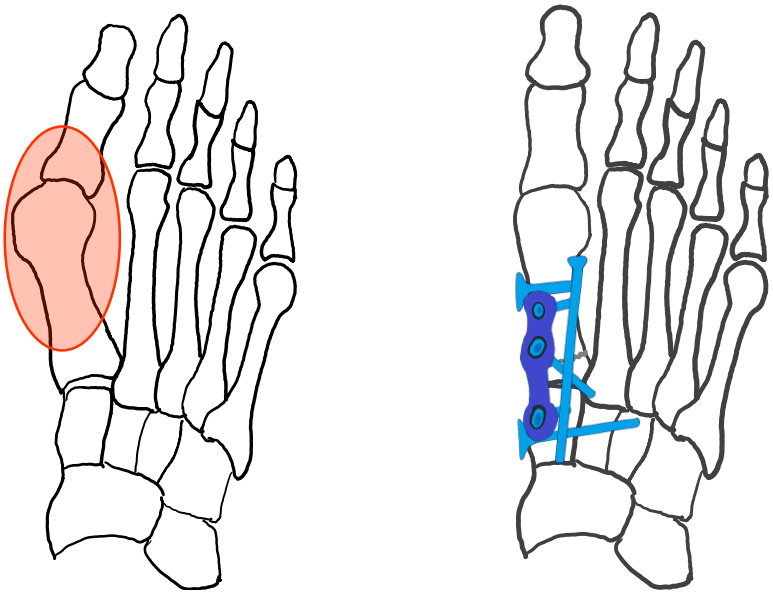

Figure 1.2.: Hallux valgus disorder (left) and after surgical correction by fixating implant composed of plates and screws (right).

In the past, various studies have focused on potentially harmful aluminium-containing alloys, but more systematic studies on aluminium-free alloys are needed. This especially applies for corrosion studies under mechanical loadings. Moreover, inorganic fluids are often applied for experimental simplicity, although organic constituents impact the corrosion mechanisms and have been recommended for studying in vitro corrosion, as they are closer to in vivo conditions. In this context, the corrosion behaviour of the rare earth-containing alloy in an organic fluid is studied and the influence of the PEO coating is examined. Experiments are performed in a long-term manner to take the persistent healing process into account and to consider time-dependent changes in the corrosion process. Additionally, the detrimental effects of the adverse mechano-chemical mechanisms are systematically analysed. In vitro studies are performed with specimens subjected to external stresses in the aggressive corrosion environment. To consider the broad range of loading scenarios during implant service, the influence of different load protocols is studied.

1.2.1 Research objectives

Concluding, this thesis addresses the following research questions:

1. How does the rare earth-containing alloy WE43 degrade in the long-term in an organic physiological corrosion environment? How susceptible is the alloy to pitting corrosion and to which extent does the corrosion impair mechanical integrity?
2. How does the PEO coating influence the long-term corrosion behaviour, the susceptibility to pitting and to which extent can it retain the material strength?
3. How susceptible is the WE43 alloy to stress corrosion cracking? How do the

adverse mechano-chemical interactions accelerate degradation? Does the PEO coating offer protection? What are the underlying failure mechanisms?

4. To which extent does corrosion detriment the fatigue performance of the alloy? How do the adverse mechano-chemical interactions deteriorate the material integrity?
5. Which conclusions can be drawn for the implant design and therapeutic approach?

1.2.2 Study design

To address the above-listed research questions, several in vitro studies are conducted, in which various physiological loading scenarios are applied to study the adverse mechano-chemical interactions. For modelling the in vitro environment, a cell culture fluid is used that contains organic compounds and is therefore vulnerable to contamination. To ensure the required experimental sterility, adequate processes are implemented and an experimental setup is developed for corrosion experiment under loading. The experimental setup is presented in section 3.6 and published in [122].

The following in vitro corrosion studies are performed:

- **In vitro corrosion experiments** are conducted with round tensile test specimens of PEO-coated and uncoated WE43 magnesium alloy, to address research questions No. 1 and 2. The corrosion rate is measured continuously using the hydrogen evolution method. After predefined periods of up to 4 or 10 weeks, the mechanical degradation is quantified by tensile tests. The susceptibility to localised corrosion is analysed using scanning electron microscopy of specimens' cross-sections. Additionally, the formation of corrosion products is chemically analysed by elemental mapping and XRD measurements in order to identify corrosion mechanisms and coating-related changes. The experimental results are presented in chapter 5. The results of the microstructural analysis of the WE43 alloy and of the PEO coating are summarised in chapter 4. Experimental results were published in the following research articles [118–120].
- **Constant load tests** are carried out under in vitro conditions at three different stress levels over periods of 1 or 3 days to address research question No. 3. After constant load tests, the changes in the mechanical integrity are quantified by tensile tests, and fracture surfaces of specimens that failed in the constant load tests are fractographically analysed. The results were published in [122] and are summarised in chapter 6.
- **Slow strain rate tests** are performed at three different strain rates to address research question No. 3. After the destructive testing procedure, the fracture surfaces are fractographically analysed. The experimental results were published in [122] and are summarised in chapter 6.
- **Corrosion-fatigue tests** are carried out to assess the influence of cyclic loading on the material degradation. Specimens are dynamically loaded in the fluid or after pre-corrosion in air. After fatigue failure, the fracture surfaces are fractographically analysed. The results are used to address research question No. 4. Experimental results are presented in chapter 7 and published in [121].

A research collaboration with the Slovene research institute "Institute of Metals and Technology" (IMT) in Ljubljana was initiated as part of this research project. Some experimental analysis was conducted at IMT, in particular scanning microscopic analysis, elemental mapping, microstructural analysis, transmission electron microscopy, X-ray diffraction and strain-controlled fatigue experiments.

2

Fundamentals of biodegradable magnesium alloys

2.1 Structure property relationship

Magnesium has the lowest density of all commonly used structural metals and possesses excellent elasticity for use in implants for bone fixation. Various alloys are designed to optimise certain mechanical properties such as strength, ductility or fatigue resistance. For orthopaedic applications corrosion resistance, susceptibility to stress corrosion cracking and corrosion fatigue are key properties. However, due to self-degradation and the subsequent metabolism, the most critical parameter might be the biosafety of the individual alloying elements [56]. In this respect, standardised laboratory tests may not be sufficient, as harmful side effects that are not limited to the implant site may occur with years of delay. Therefore, elements that are currently considered harmless may be categorised as harmful in the future.

Alloying elements can be present in solid solution or as secondary precipitates depending on the solubility of the secondary phases and the production process. If the alloy element is in solid solution, the crystal lattice is distorted, which enhances the material strength and is referred to as solution hardening. The mechanical properties can also be influenced by metal strengthening processes like cold working, grain refinement or precipitation hardening.

With regard to corrosion resistance, the distribution and nobility of alloying elements are important factors. Elements with a large potential difference compared to magnesium would promote microgalvanic corrosion (see section 2.3.5) and reduce the corrosion resistance of the material. Therefore, nickel (Ni), copper (Cu), calcium (Ca), beryllium (Be) and iron (Fe) should not exceed a certain limit and are often considered as impurities [103, 170]. Despite its negative effects on corrosion resistance, calcium has a very positive effect on the healing process. As a major component of bone tissue, calcium improves the cellular activity of bone cells, promotes tissue formation, implant integration and inhibits bacterial infections [103].

The vast majority of magnesium alloys that have been assessed for use in biomedical implants were originally developed for industrial purposes [76, 171]. For this reason, aluminium-containing alloys of the AZ-alloy family have been extensively studied in the past as they are readily available [3, 153, 173, 180, 182]. Their main alloying element is

aluminium, which increases the strength and ductility of the material [171]. AZ91 alloys have shown good results in laboratory cytotoxicity tests and no additional negative effects have been reported in in vivo studies, which can cause severe inflammation reactions [132, 170]. However, as aluminium is considered potentially neurotoxic and carcinogenic [17, 34, 37], aluminium-containing alloys have become controversial for implantation and some researchers are calling for more systematic research on aluminium-free magnesium alloys [30, 73, 171].

Alloying elements of similar electrochemical potentials should be favoured to improve corrosion resistance, which is the case in rare earth-containing alloys of the WE-alloy family. Yttrium improves mechanical properties [137] while neodymium enhances corrosion resistance [194], with both elements acting as grain refinement agents [24]. The rare-earth elements reduce the galvanic sites [156] and improve the creep and stress corrosion cracking resistance of the alloy [57, 83, 116]. Compared to the aluminium-containing AZ91, WE43 has a higher corrosion resistance in saline solution [6], a higher tensile strength and ductility [57]. In addition, rare-earth elements have been found to improve resistance to stress corrosion cracking and corrosion fatigue [57, 83]. Rare earth-containing alloys have shown good results in terms of in vitro biocompatibility [136]. Positive results are also reported in in vivo studies [102, 126]. It has been revealed that Zr, Nd and Y are easily absorbed [103]. However, rare-earth elements have shown negative effects on lungs, liver and brain, but their exact health repercussions are still an ongoing topic of research [63, 127]. Nevertheless, WE43 alloys are considered some of the most promising magnesium alloys for temporary biodegradable implants, which is also attributable to their medical approval for stents and orthopaedic screws.

Outstanding performance in terms of biosafety is attributed to magnesium alloys containing zirconium and zinc (ZK-alloy family), but their application is restricted by their poor corrosion performance [103]. Both alloying elements increase the material strength. Negative side effects of zinc are only reported after exceeding certain limits. Furthermore, zirconium is reported to be of carcinogenic character [147].

Along with the choice of alloying elements, processing steps such as the solidification route and heat treatments change the microstructural characteristics that influence the mechanical and corrosion behaviour. A continuous network of secondary phases can act as a barrier and slows down the corrosion process. A discontinuous arrangement of secondary phases, on the other hand, can galvanically accelerate the corrosion process. Within the grain, the distribution and segregation of alloying elements is predominantly inhomogeneous, with lower concentrations often present in the centre of grains. As a result, areas near grain boundaries become cathodic, which influences the corrosion behaviour. In pure magnesium, the grain boundaries are preferentially attacked during corrosion as they are areas of high distortion, imperfection and energy [171]. This would imply that coarse grains should be favoured to improve corrosion resistance. In contrast, segregations occur to a smaller extent in small-grained magnesium, which are found to corrode more homogeneously [9]. For this reason, treatments are used to adjust microstructural features, such as grain size, in the near-surface area to improve corrosion and stress corrosion resistance [77, 77, 130, 191, 193].

2.1.1 WE43 magnesium alloy

Alloy WE43 is an aluminium-free alloy that is alloyed with rare-earth elements and was originally developed for aerospace components. Its composition is defined as follows: Yttrium 3.7-4.3 %, rare-earth 2.4-4.4 %, zirconium 0.4 %. The alloy is characterised by a very low density, high strength, high creep resistance, good corrosion resistance, good castability and can be used at high temperatures.

2.2 PEO coating on magnesium alloys

2.2.1 Coating process

The process of plasma-electrolytic oxidation produces an oxide layer on the surface of a metallic substrate. As it is based on anodic processes, the metal has to tend towards passivity. On biodegradable magnesium, the coating provides corrosion protection and reduces the corrosion rate. In industrial applications, it is also used to improve wear resistance or thermal or electrical insulation.

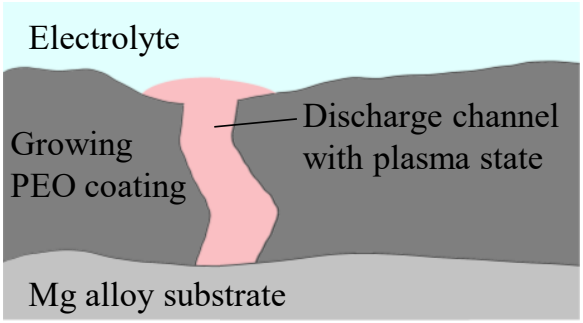

Figure 2.1.: Highly simplified schematics of plasma discharge channels after bi-electric breakdown during the PEO coating process.

During the plasma-electrolytic oxidation process, the metallic specimen is immersed in an electrolytic bath and an electrical field is applied, with the specimen as the anode. The electric field causes dielectric breakdowns of the generated oxide layer, which leads to the growth of the oxide layer. The exact mechanisms of coating growth and mass transfer are yet to be fully understood. However, it has been established that a plasma state develops within the discharging channel, which connects the metallic substrate with the electrolyte and enables mass transfer through the discharging channel [68, 123]. The oxidised metal and constituents from the electrolyte then both contribute to the oxide layer growth. As the layer thickness increases, the resistance of the oxide layer increases and higher electric fields are required for dielectric breakdown. At a certain limit, the electric field can irreversibly damage the coating. This limits the final coating thickness [65]. Since coating growth is associated with discharges caused by a strong electric field, the applied current protocol is a key factor for the generated coating morphology [33]. Significant differences in coating thickness, compactness and porosity

are reported between unipolar or bipolar modes [66]. Pulsed modes are introduced to better control the duration of the discharge [86, 146]. The type of applied current is a very important parameter for achieving the desired coating result. The electrolyte and the metallic alloy also influence the coating result. Two- or three-layer coating structures are proposed [4, 67]. An innermost, dense layer ensures good adhesion of the coating to the metal substrate and offers the most corrosion protection. The outer is porous. In the three-layered structure, this outer layer is divided into a dense inner and a porous outer part [4, 32, 154].

A newer field of research for medical application of PEO coatings is the improvement of their functionality by the incorporation of specific agents that are added to the electrolytic bath. For example, the incorporation of Ag- and Cu-based additives leads to a positive inhibitory effect against bacteria [42].

2.2.2 Coating characterisation

The PEO coating result is usually analysed using scanning electron microscopy (SEM, see section 3.12.1). The SEM image of the surface shows the surface topology as well as the distribution and size of the pores. SEM images of cross-sections provide depth-dependent information such as the dimensions of inner or outer layer, total coating thickness and pore distribution. Cross-sections can also be used to analyse elements within the coating by EDS analysis or elemental mappings (see section 3.12.1). The crystalline structures within the coating can be assessed by XRD measurements (see section 3.13) on the surface. However, due to the thin coating, these measurements are often influenced by the underlying crystalline metallic substrate.

2.3 Corrosion behaviour of magnesium alloys

This section describes the basic corrosion mechanisms of magnesium alloys in aqueous solution and summarises important factors that influence the corrosion rate and material degradation in a physiological environment.

2.3.1 Magnesium corrosion in aqueous solution

Degradation of magnesium implants is based on the oxidation of the metal into cations during corrosion. The following overall corrosion reaction of magnesium takes place in aqueous solution:

$$Mg + 2H_2O \longrightarrow Mg^{2+} + 2(OH)^- + H_2 \ , \tag{2.1}$$

including the anodic oxidation reaction:

$$Mg \longrightarrow Mg^{2+} + 2e^- \ , \tag{2.2}$$

and the cathodic reaction:

$$2H_2O + 2e^- \longrightarrow H_2 + 2OH^- \ . \tag{2.3}$$

2.3.2 Passivation film

Following the anodic and cathodic reactions, magnesium cations react with hydroxides and form a protective layer:

$$Mg^{2+} + 2OH^- \longrightarrow Mg(OH)_2 \ . \tag{2.4}$$

This layer separates the substrate from the corrosive environment and thus provides corrosion protection. Its protective character is influenced by structural features that depend on the substrate material as well as on the corrosion environment (see section 2.3.7). In general, a thicker layer provides improved corrosion protection as the diffusion of magnesium cations through the layer is impeded. On the other hand, the susceptibility of the layer to cracking increases, which in turn limits the protective character. More importantly, the stability of the magnesium oxide layer depends on the pH value (see section 2.3.3) and on the chloride concentration of the corrosion environment (see section 2.3.4) and the protective layer can be disrupted by stress due to external loads, as shown in Figure 2.4.

2.3.3 Influence of pH value

The stability of the protective magnesium hydroxide film depends on the pH value. The correlation between stability and fluid pH is described in the Pourbaix diagram [133]. At pH values exceeding 10.5, magnesium hydroxide and magnesium oxide are insoluble and form a stable protective layer on the substrate surface. At pH values between 8.5 and 10.5, the film is semi-stable and less protective. At pH values below 8.5, the film is unstable and exists in a steady state between formation and dissolution.

The release of hydroxide ions according to equation 2.3 can increase the pH locally if the chemical reaction takes place faster than the diffusion of these ions away from the corrosion front. Hence, the pH at the substrate surface can be higher than the pH of the bulk solution, resulting in stable conditions for the protective film and decelerating the corrosion. To prevent such pH changes, buffer systems are employed in in vitro corrosion experiments to maintain physiological pH values. However, recent studies have identified significant differences between commonly used buffering systems. In particular, synthetic buffers provide poor and inadequate buffering capacity at the substrate-fluid interface where the corrosion reaction takes place. This is discussed in more detail in section 2.3.7.

2.3.4 Influence of chloride concentration

Chloride concentrations exceeding 30mmol/l have a detrimental effect on the protective oxide layer. The chloride can react with the magnesium hydroxide and decompose it into highly water-soluble magnesium chloride according to the following reaction:

$$Mg(OH)_2 + 2Cl^- \longrightarrow Mg(Cl)_2 + 2OH^- \ . \tag{2.5}$$

The dissolution weakens the protective layer and can cause a local passive film breakdown, which can initiate pitting corrosion (see section 2.3.6).

2.3.5 Microgalvanic corrosion

Galvanic corrosion occurs when two dissimilar metals come into contact in the presence of an electrolyte. The metal with more negative electrochemical potential is oxidised. Galvanic corrosion is not only related to the presence of two different substances. Electrochemical potential differences within an alloy can cause microgalvanic corrosion. Local differences in electrochemical potential can be present between the bulk material and intermetallic compounds, secondary phases, impurities or due to inhomogeneous distribution of alloying elements within the grains. As magnesium is a highly reactive material, the addition of noble alloying elements can increase the susceptibility of the alloy to microgalvanic corrosion. However, impurities of more noble materials like iron or aluminium are difficult to avoid completely during the manufacturing process.

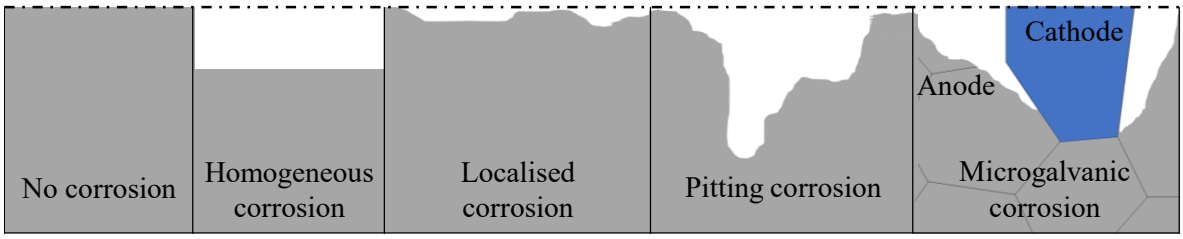

Figure 2.2.: Types of corrosion.

2.3.6 Pitting and localised corrosion

The geometric appearance of the corrosion front determines whether pitting or localised corrosion is present. Inhomogeneous corrosion is usually attributed either to passive film breakdown or to inhomogeneities in the alloy that cause preferential material dissolution. Pits that grow deep into the material are considered extremely dangerous as they deteriorate the mechanical integrity while remaining unnoticed on the surface.

If the anodic and cathodic sites are evenly dispersed in the substrate, uniform and slight inhomogeneous corrosion along the surface is expected. Localised corrosion is the result of passive film breakdown, exposing the bare substrate to the surrounding fluid, which is then further oxidised. If the pit is not passivated by the protective layer,

it can grow continuously. The magnesium cations produced by the corrosion attract chloride ions. These ions can diffuse into the pit and negatively affect the stability of the protective magnesium hydroxide layer. At the same time, hydroxide ions, which are formed during the cathodic reaction close to the pit, increase the pH value locally and thus stabilise the corrosion layer. For this reason, a thick layer of corrosion products is often observed in the vicinity of corrosion pits. After initiation, the pit can either grow laterally, close to the bulk surface, or radially into the material. The latter one can lead to severe material damage. This is why lateral pit growth is often referred to as localised corrosion, as it is less dangerous.

2.3.7 Influence of electrolyte compositions of physiological fluids

In vivo, the implant is exposed to a highly complex fluid containing inorganic compounds, organic compounds and cells. To approach these conditions, several electrolyte systems of varying complexity have been developed, which are summarised in Figure 2.3. The comparison of ionic concentrations with those of human blood plasma is generally accepted, but it remains an open research question which further constituents are of critical importance. The composition of the corrosion fluid can significantly influence the corrosion layer formation and the corrosion behaviour of an alloy system and should be carefully selected.

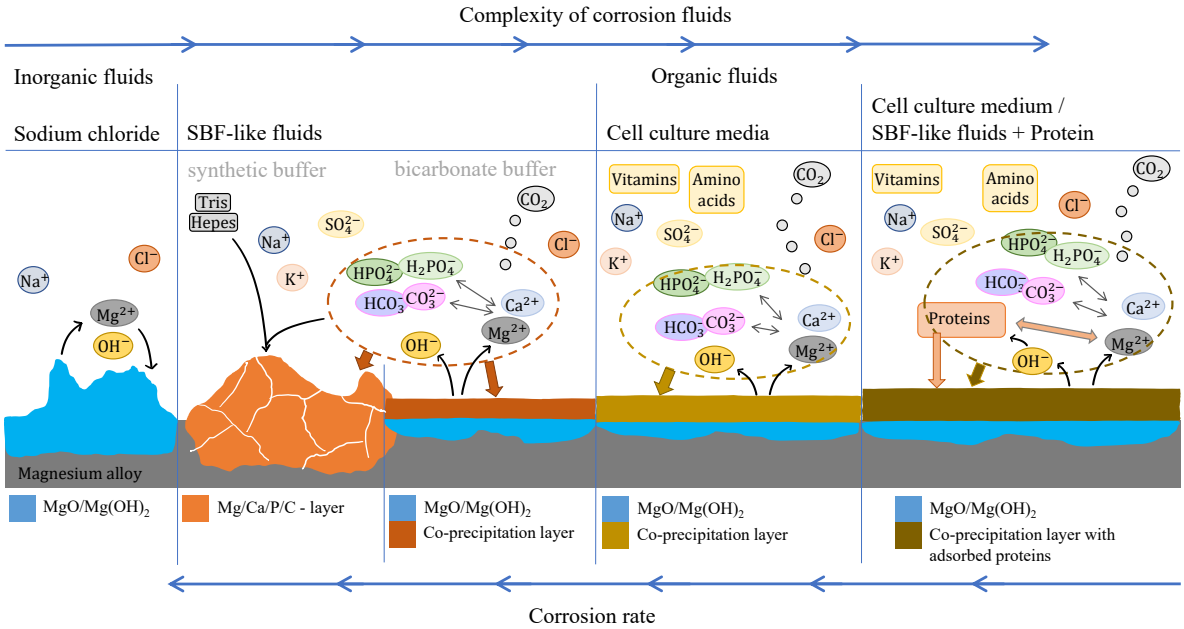

Figure 2.3.: Layer formation and corrosion rate depending on the fluid complexity, cf. [111]

The simplest fluids for studying in vitro corrosion are "simulated body fluids" (SBF), which are inorganic in nature and widely applied in in vitro experiments [21, 83, 87, 92]. The corrosion of magnesium alloys in such fluids is dominated by the synergistic effects of Ca^{2+}, Mg^{2+}, HCO^{3-} and $HPO_4{}^{2-}$, which form a protective layer over the magnesium oxide

or magnesium hydroxide layer that grows over time and slows down the corrosion [109]. Interestingly, this effect leads to similar corrosion rates of different magnesium alloys in SBF, which have varying corrosion rates in NaCl. Buffer systems, which simulate the humoral regulation of the pH value, must be added to the corrosion fluids. The use of synthetic buffers such as HEPES and Tris accelerates the corrosion rate as it impedes the formation of a protective layer [31, 38, 82, 89, 90, 110, 158, 177, 178]. Additionally, these buffers show very poor buffering of the fluid at the corrosion front, where it is actually important [111]. Hence, some researchers recommend to avoid synthetic buffers [111, 177]. Instead, bicarbonate buffers should be preferred, as they act similarly to the humoral buffering of human blood plasma and have a smaller influence on the corrosion in comparison to synthetic buffer systems [111, 179].

The addition of organic compounds increases the complexity of the corrosion environment. In this case, cell culture fluids are often used as they incorporate organic compounds and nutrients in low concentrations. Similar corrosion products to those found for simulated body fluids are reported in corrosion in cell culture media using synthetic buffers [155]. Unfortunately, little information is available on changes in the corrosion rate between inorganic and cell culture fluids, which might be related to a more dominant role of synthetic buffering systems [178]. The electrochemical measurement results of a study comparing magnesium corrosion in SBF and DMEM (both contain bicarbonate buffers of different concentrations) showed lower corrosion rates in DMEM and changes in the morphology of the corrosion layer [160]. It must be noted that certain differences might also be related to the atmospheric environment of the experiment, which did not provide ideal buffering conditions for bicarbonate buffer systems. However, after corrosion in DMEM, inhomogeneous corrosion along the surface is consistently reported [160]. In general, the lower sensitivity to pitting corrosion may also be related to the bicarbonate buffering system accelerating passivation [179]. Further supplements of cell culture fluids such as glucose and the colour indicator phenol red have shown no influence on the corrosion [90, 109]. The same applies for low concentrations of antibiotics e.g. penicillin concentrations below 100 units per ml and streptomycin concentrations below 100μg per ml.

In recent years, the influence of individual constituents of the corrosion fluid on the corrosion of magnesium has been intensively examined [79, 89, 107, 109, 110, 181, 189, 196]. It has been found that the corrosion rate decreases with increasing complexity of the solution [111]. Yamamoto et al. [187] have observed that proteins and insoluble salts slow down the corrosion process, while amino acids accelerate magnesium degradation. The addition of most proteins like albumin, bovine serum albumin (BSA) and fetal bovine serum (FBS) has shown an inhibiting effect and decreases the corrosion rate. However, this effect is partly reported to be of time-limited nature. Comparison between studies is difficult due to many variations in boundary conditions, which are based on a lack of standardisation. Larger amounts of proteins are only added to evaluate the influence of individual constituents or the interaction of different proteins. The addition of organic compounds significantly increases the complexity of the interactions between constituents, especially when protein mixtures are added. They also increase the experimental challenges due to the risk of contamination, which in turn limits the

experimental corrosion periods.

After a systematic evaluation of the available fluid systems for in vitro experiments and the influence of inorganic and organic constituents, Hou et al. [64] has concluded that cell culture media with protein mixtures would be the most suitable medium for in vitro corrosion studies, as they are closest to human blood plasma in composition and concentration. However, due to their vulnerability to microbial development, their application is limited to short-term experiments that are performed in a closed setup [111].

2.4 Corrosion behaviour under external loading

The joint action of external loads in an aggressive corrosion environment can be detrimental to the material. Dangerous and unforeseen failure can occur due to a severe loss of mechanical integrity, often accompanied by significant embrittlement. Two phenomena are distinguished: stress corrosion cracking (SCC) and corrosion fatigue (CF). SCC describes the synergy of static or quasi-static loads, while CF addresses cyclic load scenarios. In both cases, the material suffers significant embrittlement in the corrosive environment and failure often occurs at stress levels that are considered safe in air.

2.4.1 Stress corrosion cracking

Stress corrosion cracking is related to a slow and sub-critical crack growth that proceeds unnoticed until the material suddenly fails. A ductile material that considerably elongates in air before failure will fail in a brittle manner without necking. It is well accepted that hydrogen embrittlement (HE) plays an important role in SCC of magnesium alloys. The most common method for analysing a material's susceptibility to SCC is slow strain rate testing, where specimens are slowly strained to failure inside the corrosive environment. Another standardised method is the constant load test, in which the samples are exposed to a constant stress level in the corrosion fluid.

Corrosion pits have been consistently reported as the main precursor for SCC in magnesium alloys. The formation of pits depends on the electrochemical system and can be promoted by external stresses. Stresses can cause stress-induced cracks in the passive layer as shown in Figure 2.4, exposing some of the material unprotected to the fluid. The unprotected material is in a stressed condition, which facilitates corrosion attack and hydrogen-assisted mechanism (see section 2.4.3). At the corrosion pit, the stress concentration is locally increased, which facilitates crack initiation, as shown in Figure 2.4. Hence, passive film breakdown is a possible trigger for SCC. The passive film can be ruptured by external stresses or weakened by chemical dissolution in the presence of high chloride concentrations. As a result, magnesium alloys that are more susceptible to pitting corrosion have been identified to be more susceptible to stress corrosion cracking [30, 130].

Stress corrosion cracking can occur either transgranularly (TGSCC) or intergranularly

(IGSCC) as shown in Figure 2.4. The prevalent mode depends mainly on the alloy's microstructure and the corrosive environment [52].

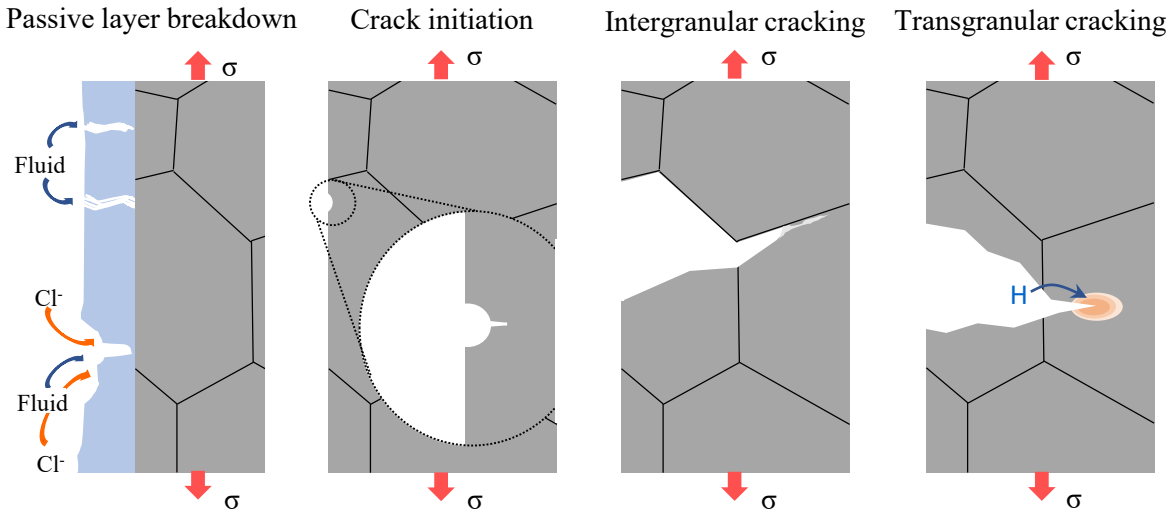

Figure 2.4.: Stress corrosion cracking.

Intergranular cracking is associated with a continuous crack propagation caused by preferential dissolution of the α-Mg matrix. This is related to microgalvanic corrosion between the α-Mg matrix and secondary phases or to microgalvanic corrosion along the grain boundaries, which are of cathodic character. As the mechanism is related to chemical dissolution, it depends on the alloy's microstructure and electrochemical properties of the alloying elements. To prevent IGSCC, a continuous segregation of second phases along grain boundaries needs to be controlled and prevented during the manufacturing process.

Crack propagation in SCC is also linked to the balance between the re-formation of the passive protective layer and the stress concentration at the crack tip. If the stress concentration is low enough, a passive layer can form at the crack tip, providing protection against additional corrosion attack and delaying the process of crack propagation. If the layer cannot be formed, material dissolution enlarges the crack, increasing the stress concentration and facilitating crack propagation. Film rupture can also create a small galvanic cell. The area with protective layer is slightly cathodic compared to the non-protected anodic area, which favours the anodic dissolution of the α-Mg matrix [105].

Transgranular cracking is linked to discontinuous crack propagation, also known as cleavage fracture. Due to a lack of slip systems in magnesium alloys, the material is prone to cleavage. TGSCC in magnesium alloys has been strongly attributed to hydrogen embrittlement (see section 2.4.3). A model on the TGSCC mechanism suggests a repetitive process of embrittlement of an area around the crack tip. The crack propagates throughout the embrittled region and stops temporarily at the transition to non-embrittled parent material. If the parent material in front of the crack tip has suffered embrittlement, the crack will continue to propagate [69]. Embrittlement in TGSCC is strongly related to hydrogen-assisted mechanisms, which are described in

section 2.4.3.

2.4.2 Corrosion fatigue

Corrosion fatigue describes the combined effect of repeated or cyclic loadings and corrosion. As with SCC, the material suffers embrittlement and failure occurs at stress levels and at fatigue limits well below those in air.

Under cyclic loading, fatigue cracks initiate at sites of increased stress concentration. In air, the fatigue crack likely nucleates at microstructural imperfections. In corrosion fatigue, the fatigue crack nucleates predominantly at a corrosion pit, as it is also the case in SCC. Pit nucleation is influenced by the electrochemical conditions and is fostered by the stress state of the alloy. The crack develops through an interplay of electrochemical dissolution at the crack tip, hydrogen ingress and passive layer breakdown, as it has been described in SCC. The intensity of each of the three mechanisms depends on the applied stress level and the electrochemical conditions. Anodic dissolution of the α-Mg matrix accelerates the crack propagation. Since magnesium alloys tend to form deformation twins, fatigue cracks can additionally be initiated at twin boundaries or at slip planes. After crack initiation, the crack grows with every loading cycle. This leaves a pattern of striation on the fracture surface. Each striation corresponds to the crack front of one loading cycle. The distance between striations corresponds to the crack propagation between loading cycles.

2.4.3 Hydrogen embrittlement in magnesium alloys

Hydrogen is a very small atom that can easily be adsorbed and diffuses inside the metallic matrix. After absorption from the environment, the hydrogen concentration increases in surface-near regions of few atomic distances to the surface. Within the metallic matrix, atomic hydrogen accumulates in areas of high hydrostatic stress and weakens the atomic bonds. This typically occurs at grain boundaries, at interfaces between matrix and particles or at locations of slight dilatation in the metal lattice. This phenomenon is called hydrogen-enhanced decohesion (HEDE). Hydrostatic stresses are also increased at crack sites, leading to an accumulation of hydrogen in these areas. The hydrogen can be absorbed from the corrosive fluid or after formation in the cathodic reaction (according to equation 2.3). It has also been observed that the increased hydrogen concentrations at the crack tip increase the mobility of dislocations and thus facilitate crack propagation. This phenomenon is referred to as hydrogen-enhanced localised plasticity (HELP) [13]. In conclusion, hydrogen-assisted mechanisms play an important role in the failure mechanism of magnesium alloys subjected to stress and corrosion. For a more comprehensive overview on hydrogen-assisted mechanisms in magnesium alloys, the reader is referred to [52].

2.5 Experimental methods for assessing biodegradable metals

2.5.1 In vitro studies

In vitro experiments are a powerful and cost-efficient tool for systematic evaluation of corrosion and material degradation of potential implant materials. They enable initial material approval, also from the point of cytotoxicity and biocompatibility, and prevent unnecessary and unethical animal studies. Nevertheless, it should be noted that positive results on biosafety do not completely rule out harmful side effects that occur after implantation due to material metabolism. Unfortunately, there is still no standard solution for in vitro experiments and discussions on the required complexity and key constituents of physiological fluids are still ongoing. However, none of the fluids used for in vitro experiments will ever be able to fully mimic the complex conditions inside animals or the human body. This might be one of the reasons why studies comparing in vitro and in vivo corrosion predominantly show divergent results [139]. This discrepancy may be related not only to the corrosion fluid, but also to differences in physical or mechanical boundary conditions. As previously discussed, some alloying elements decrease corrosion resistance but have a positive influence on the healing process. In extreme cases, an alloying element could promote bone formation to a larger extent than its detrimental effect on the corrosion resistance. If inflammation is caused by certain alloying elements, the inflammation response can considerably increase the corrosion rate [171]. To summarise, the complex interactions cannot be entirely covered nor foreseen. Despite these limitations, the fundamental need for systematic in vitro studies is undeniable.

2.5.2 Mass loss experiments

In this context, mass loss experiments are the simplest method for in vitro corrosion studies and allow the use of a wide range of corrosion fluids as the environment can be kept enclosed and aseptic conditions can be easily maintained. In mass loss experiments, corrosion products are removed after a defined immersion period and mass loss is quantified by weighing the remaining material. This method is limited by the fact that only a single data point is generated. The single data point on mass loss or corrosion rate is an averaged value over the entire experimental duration. No insights into time-dependent mechanisms are possible. Furthermore, the corrosion layer cannot be analysed as it is removed with hazardous chromium trioxide.

2.5.3 Hydrogen evolution measurements

Time-dependent mass losses and corrosion rates can be recorded using hydrogen evolution measurements, in which the escaped hydrogen gas is collected in a measuring tube (burette). Based on the corrosion reaction (1mol dissolved magnesium corresponds to the release of 1mol hydrogen), the corrosion rate can be calculated. The corrosion environment can be easily controlled so that even complex fluids can be used. The method is often applied to compare different alloys. However, as sufficiently large volumes of hydrogen are required for reliable measurements, the method is less suitable for highly corrosion-resistant alloys.

2.5.4 Electrochemical measurements

Insight into underlying electrochemical corrosion mechanisms can be obtained by electrochemical measurements. Open circuit potential measurements (OCP) provide information on the kinetics of anodic and cathodic reactions and can be used to identify the influence of single components, such as metallic phases, microstructural features or single fluid constituents. However, the application of OCP is limited due to its destructive character as between measurements the surface needs to be re-polished. On this account, the method is not suitable for analysing time-dependent or long-term corrosion. Electrochemical impedance measurements (EIS) are time continuous and non-destructive electrochemical measurements. In this method, the complex electrochemical system is described by an equivalent electrical circuit. The modelling and parameter fitting allow for a quantification of the passive layer formation and its contribution to the corrosion protection, and allow evaluation of the protective character of coatings. However, due to an increasing thickness of corrosion products on the surface, the method has shown unsatisfactory results in long-term experiments [143].

2.5.5 Additional analytical methods

Often several methods are combined in in vitro studies and supplemented by additional analysis. The corrosion rates measured in in vitro experiments are averaged values in relation to the exposed corrosion surface and do not provide information on pitting or localised corrosion. For the development of medical implants geometric information on the corrosion front is of essential importance. For this reason, micro-CT scans or profilometric measurements are often performed after removal of corrosion product. Alternatively, cross-sections are analysed using scanning electron microscopy (see section 3.12.1). Recently, a new approach has been developed for geometric evaluation using micro-CT measurements without product removal [50].

The composition and structure of the corrosion layer provides valuable information for the analysis of the corrosion mechanisms. Therefore, EDS (see section 3.12) measurements are performed either on the surface or on cross-sections to identify the chemical elements inside the layer. X-ray diffraction (see section 3.13) measurements on the surface provide information about the crystalline structures inside the protective corrosion product

layer. X-ray photoelectron spectroscopy measurements provide information about the chemical composition.

2.5.6 Corrosion experiments under external loading

Corrosion experiments with joint action require an adaptation of the experimental setup. The experimental complexity depends on the mode of external load and the used corrosion fluid. In a very simple test arrangement, the specimen is clamped in a tool that applies a static load on the specimen. The assembly is then immersed in the corrosion fluid [25, 53]. For a wider range of loading scenarios, the specimen needs to be integrated into a test bench. In this context, one experimental setup has been widely used: The specimen is clamped vertically at both ends in a testing device, and a liquid bath is positioned around the specimen. The bottom of the bath seals the lower grip area of the specimen. A fluid circuit is established between the liquid bath and an external reservoir, which is heated and supplies the physiological temperature. The open nature of the fluid bath allows the integration of electrochemical EIS measurements while limiting the choice of corrosion fluid.

Standard tests to evaluate changes in mechanical integrity during the combined action of external loads and corrosive environment are usually constant load tests (CLT), slow strain rate tests (SSRT), and corrosion fatigue tests (CF). The first two experiments are performed to assess susceptibility to stress corrosion cracking (SCC). In CLT tests, specimens are subjected to a constant stress level either for a limited period or until failure. In SSRT testing, specimens are subjected to at constantly increasing elongation and changes in material parameters are evaluated by introducing sensitivity factors. The very slow strain rates are an important feature in SSRT. The strain rate needs to be sufficiently low to be able to evaluate the resistance of the material to environmentally assisted cracking phenomena or hydrogen embrittlement [39]. Changes in the fatigue life are analysed using CF experiments. Despite the standardised uniaxial CLT, SSRT and CF experiments, multiaxial loading scenarios would better approach in vivo conditions, but they increase the complexity of the experimental setup. After failure, the fracture surfaces are usually analysed using SEM analysis, which provides valuable insight into failing mechanisms.

3
Materials & Methods

3.1 WE43 magnesium alloy

Specimens are manufactured from extruded 6.5mm rods by meotec GmbH (Aachen, Germany) and provided by Medical Magnesium GmbH (Aachen, Germany). The chemical composition of the alloy WE43MEO is given in Table 3.1.

Y	Nd	Al, Fe, Cu, Ni, Mn, Zn, Zr	Mg
1.4-4.2	2.5-3.5	<1	Bal.

Table 3.1.: Composition of WE43 in wt.%.

3.2 Specimen design

The test specimens are designed according to DIN 50125. An overview of utilised specimen geometries is given in Figure 3.1. Technical drawings with detailed dimensions are included in appendix A.

Tensile test specimens are depicted in Figure 3.1 a (uncoated) and b (coated). Uncoated and coated specimens share an identical geometry: a gauge diameter of 4mm, a parallel length of 24mm, a total length of 76mm and a grip section diameter of 6mm. Tensile test specimens are used in immersion tests (section 5), in slow strain rate tests (section 6) and in constant load tests (section 6).

For stress-controlled fatigue experiments (section 7), fatigue specimens with a diameter of 2.5mm are used, as shown in Figure 3.1e. For strain-controlled fatigue tests in air, specimens shown in Figure 3.1f are used.

In addition, non-standardised pin specimens are used in the immersion tests, as shown in Figure 3.1e. In contrast to the tensile test specimen, they include a flat surface.

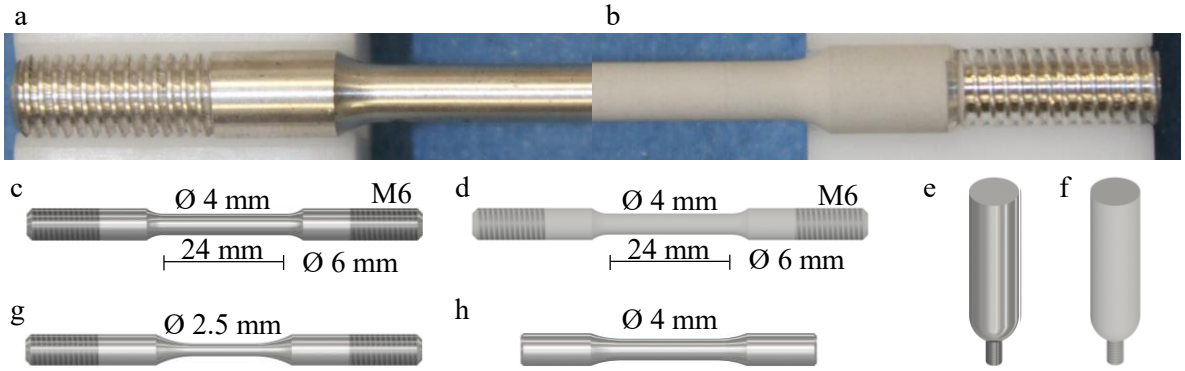

Figure 3.1.: Specimens used for corrosion tests: (a) picture of an uncoated WE43 specimen, (b) picture of a PEO-coated specimen, (c) tensile test specimen, (d) coated tensile test specimen, (e) uncoated pin specimen, (f) coated pin specimen, (g) fatigue specimen, (h) fatigue specimen for strain-controlled experiments.

3.3 PEO coating on WE43 magnesium alloy

For surface modification, tensile test specimens are plasma-electrolytically oxidised. The process is conducted by meotec GmbH (Aachen, Germany), and coated specimens are provided by Medical Magnesium GmbH. During the oxidation process, the sample functions as the anode. For circuit integration, a small connection piece is manufactured at the sample thread, which can then be easily detached. This ensures that an intact coating is created across the entire surface of the sample. During the process, specimens are immersed in a phosphate-based electrolytic bath (Kermasorb), which is continually agitated at a controlled temperature between 20 and 34°C. A pulsed rectifier set (M-PEO A1, meotec GmbH, Germany) is utilised to apply high current densities. The workpiece undergoes continuous rotation (100-200rpm) to achieve a homogeneous coating thickness. Process time and parameters are adjusted galvano-statically, starting at $10 A/m^2$ to attain the specified coating result.

3.4 Corrosion fluid

To approach physiological conditions, the organic cell culture medium Dulbecco's Modified Eagle's medium (DMEM, L0101-500, Biowest, Nuaillé, France) was used in the corrosion experiments. The ionic concentrations of DMEM are similar to those of human blood plasma, as indicated in the comparison in Table 3.2. The composition of the DMEM is provided in appendix B. A volume of 500ml of DMEM is used for the immersion tests, while 650ml are used in the experiments with superimposed loads. The selection of fluid volume is based on the recommendations regarding the ratio between fluid volume and sample surface area [87].

DMEM contains organic compounds and high a level of sugars, making it very susceptible to contamination. Therefore, sterile conditions are required in experiments. DMEM also contains a sodium bicarbonate buffer system, which is recommended for in vitro experiments (see section 2.3.7). Changes in the pH value can be detected by observing

changes in the colour of the pH indicator phenol red in the fluid. A pH shift towards acidic values causes a yellowish colour change, indicative of bacterial contamination. Fungal infections, on the other hand, result in an alkaline pH value, leading to a colour change to dark red or purple. To prevent contamination, 5ml of penicillin-streptomycin (ThermoFisher Scientific Inc., Waltham, MA, USA) is added to the fluid, supplemented with either 20mg of sodium azide (VWR International LLC, Radnor, PA, USA) in experiments with gas measurement or 5ml amphotericin B (ThermoFisher Scientific Inc., Waltham, MA, USA) in all other experiments.

Ion	Na^+	K^+	Mg^{2+}	Ca^{2+}	Cl^-	HCO_3^-	HPO_4^{2-}	SO_4^{2-}
Blood Plasma	142	5	1.5	2.5	103	27	1	0.5
DMEM	154	5.4	0.8	1.8	119	44	1	0.8

Table 3.2.: Comparison of ionic concentrations of human blood plasma and DMEM in mmol/l.

3.5 Experimental setup for immersion experiments

The experimental setup for the immersion experiments including gas measurement is presented in Figure 3.2a and is adapted from [88]. Specimens are placed horizontally underneath an inverted funnel, which collects the released hydrogen gas and guides it into a burette. This way, the collected gas can be measured continuously. As sterile experimental conditions are important, all parts are sterilised before use and the experiment is set up in a clean bench class 100 with a HEPA filter. An overview of the sterilisation protocol for each component is given in the appendix C. After assembly, the setup is placed in a CO_2 incubator with a CO_2 concentration between 5 and 7%, as shown in Figure 3.2b. To limit the exposed area to the central part of the specimen, the specimen's ends are sealed. A magnetic stirrer in one corner of the bottle creates a gentle fluid agitation. After completing the immersion period, specimens are removed from the corrosion fluid, rinsed with distilled water to remove the soluble corrosion products [155], dehydrated with ethanol and air-dried. A more detailed description of the experimental procedure is given in the appendix C. Figure 3.2c shows the experimental setup for corrosion experiments without gas measurement. Specimens with sealed ends are positioned vertically in the corrosion fluid using nylon threads. Specimens can either be immersed in the DMEM bottle or in a wide-neck bottle. Both bottles must be sealed with a custom-made 3D-printed lid that allows gas exchange with the environment via a filtering cap. Sterility is ensured in the same way as in the gas measurement experiments, and the setup is placed inside the CO_2 incubator for the duration of the corrosion. The same applies to the pin specimens. One end of the pin specimen is sealed, leaving an area corresponding to the exposed surface of the tensile test specimens to ensure a steady surface-to-fluid ratio.

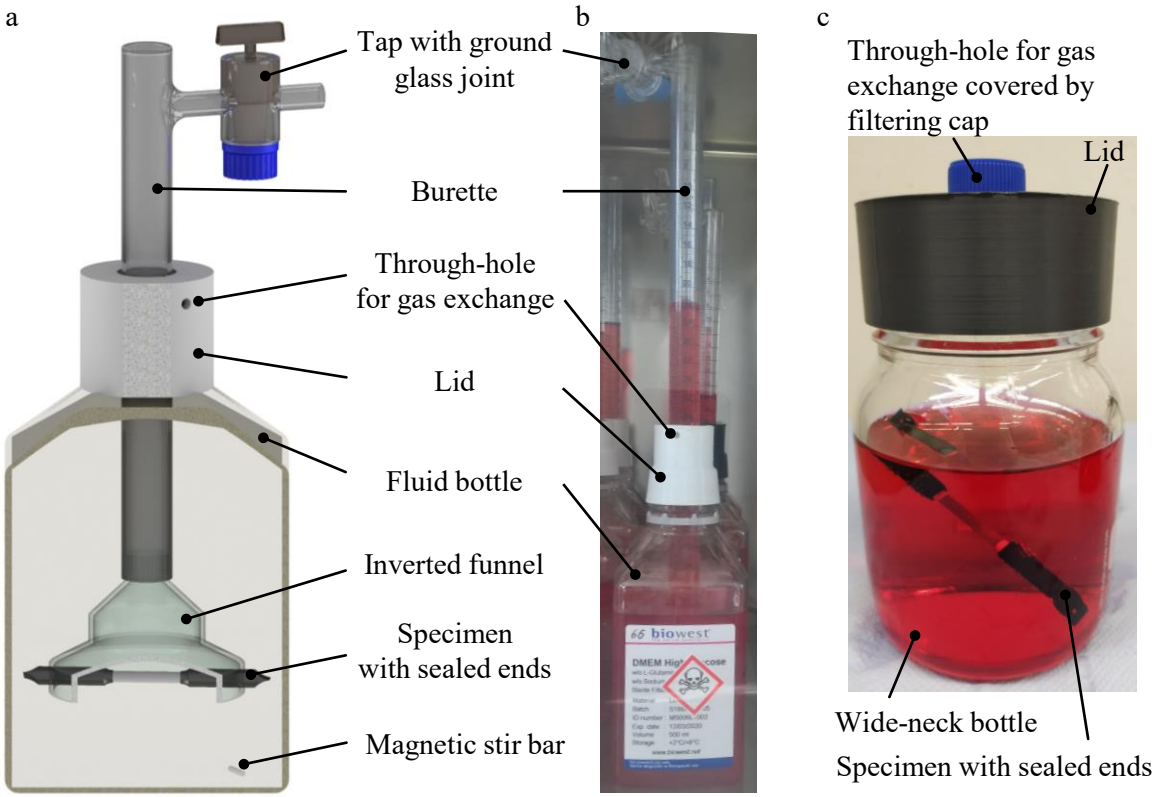

Figure 3.2.: Experimental setup of static immersion tests, adapted from [120, 121].

3.6 Experimental setup for corrosion experiments under loading

To analyse the influence of mechanical stresses on the corrosion behaviour of biodegradable implants, an experimental setup is developed that allows the subjection to external mechanical loadings during corrosion under sterile conditions. For this purpose, a closed corrosion chamber is developed in which sterile conditions can be maintained outside of sterility-controlling industrial laboratory devices. This unique feature overcomes certain limitations when using organic fluids, which are highly susceptible to contamination.

The corrosion chamber is the central part of the newly developed setup. It encloses the corrosion fluid with the specimen and separates the corrosion environment from the surrounding atmosphere. In this way, sterile conditions can be maintained inside the corrosion chamber. The entire setup is modular and up to three specimens can be tested in series. As each specimen is enclosed in its own chamber, contamination cannot spread between chambers. The horizontal loading direction enables the simultaneous application of the hydrogen evolution method. For a steady physiological test temperature, the corrosion chambers were placed inside a temperature control unit and the specimen ends connected to the test machine for force transmission.

This section presents the experimental setup and its components. A detailed description of the test preparation and assembly procedure is presented in Figure C.3 in appendix C. Parts of the experimental setup were published in [122].

3.6.1 Corrosion chamber

The corrosion chamber is presented in Figure 3.3. It is composed of three main parts: a central cube, a wide-neck bottle and a lid. All parts of the corrosion chamber are made of sterilisable materials. In addition, the functionality of the colour indicator of the corrosion fluid DMEM must be taken into account in the design (see section 3.4). This is why translucent materials were chosen for the chamber.

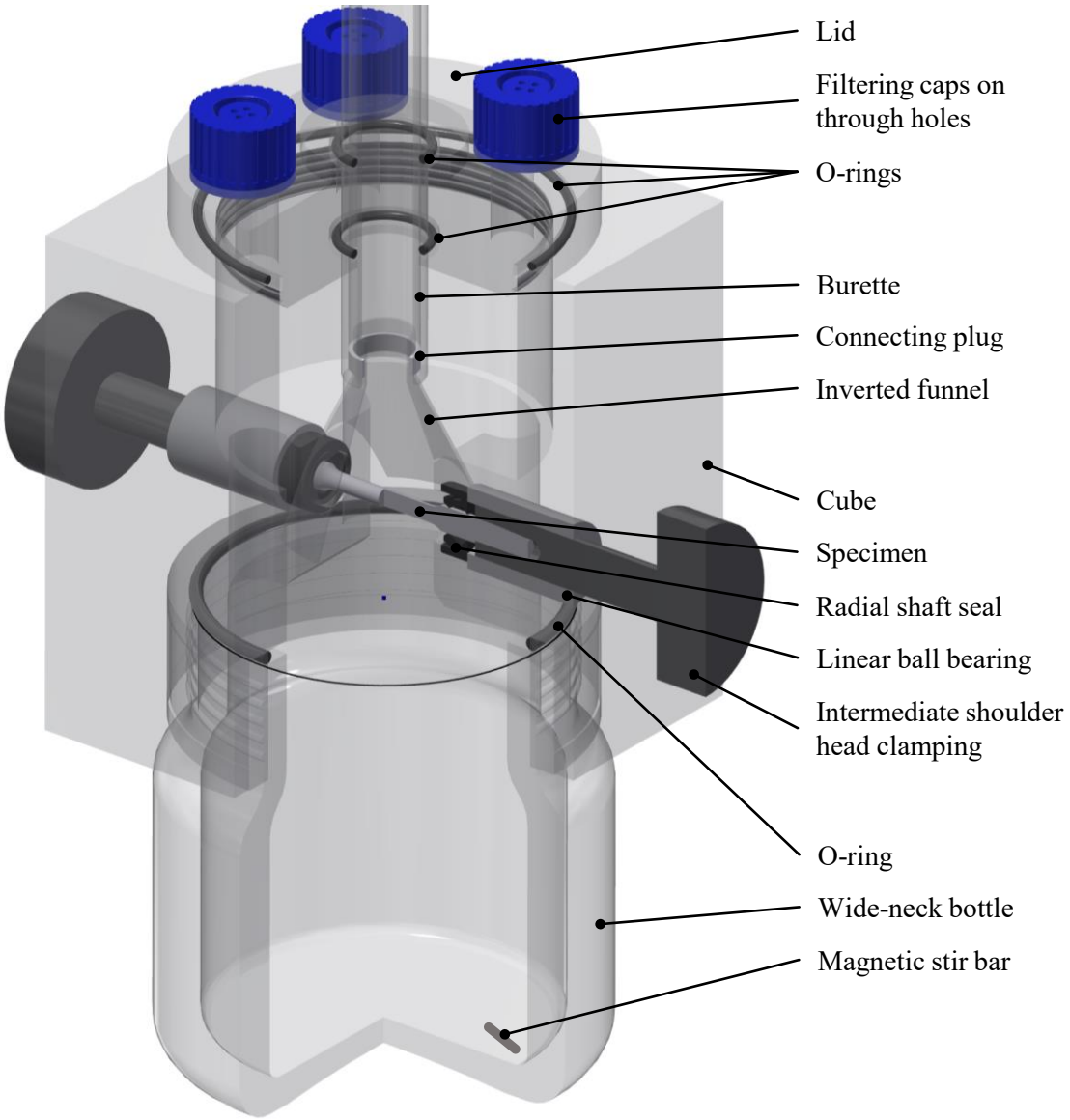

Figure 3.3.: Experimental setup of corrosion tests with superimposed loading.

The cube is manufactured in the in-house workshop from colourless acrylic glass and connected to a wide-mouth bottle (DURAN® GLS 80® Laboratory Bottle, wide mouth, clear, 250ml, DWK Life Sciences GmbH, Wertheim, Germany). For a sufficiently large fluid volume of corrosive liquid, it is necessary to select an appropriate bottle capacity.

Due to the very small thread pitch of the bottle (GLS 80®), the counter-thread was manufactured separately and glued to the cube. The seal between the cube and bottle is improved by polishing the bottle opening to a flat surface and using an O-ring between tangent surfaces. The specimen is inserted horizontally into the cube and radial sealing shafts (6-16-7 BAVI of Viton material) are used to limit the corrosion chamber. The radial shafts are designed to fit around the shoulders of the specimens. This is why the dimensions of the cube (distance between radial shaft seals) and the specimen (distance between specimen's shoulders and length of specimen's shoulder) must match. The contact surfaces between cube and cover are again sealed with an O-ring. It is not necessary to use a translucent material for the lid. The lid has two feed-throughs that are covered with disposable filtering caps for cell culture flasks (screw caps with filter for EasyFlask 25cm², Thermo Fisher scientific GmbH, Dreieich, Germany), which filter the gas exchanged between the atmosphere and the corrosion chamber. The setup presented in Figure 3.3 includes a hydrogen gas measurement, which is optional and described in more detail in section 3.6.3. Without hydrogen collection, a different lid without the central guide hole for the burette and neither burette nor funnel are integrated in the setup.

3.6.2 Corrosion chamber integration into testing machine

The horizontally aligned test bench is controlled by FlexTest 60 (MTS Systems Corp., Minneapolis, USA) and equipped with a force transducer (Model 661.20F-03, MTS Systems Corp., Minneapolis, USA). A shoulder head grip system is used to facilitate the installation in the test bench. An intermediate clamp is screwed onto the thread of the specimen, which can be inserted freely into the grips of the test bench from the front, as shown in Figure 3.4a. In serial testing, a different intermediate clamping is used to connect two specimens. Figure 3.4b shows the connection between two specimens using pin connectors. To prevent specimen bending in the horizontal arrangement, linear ball bearings (linear bearings KB-1 ISO 10285 Series 1, MÄDLER GmbH, Stapelfeld, Germany) have to be integrated between the cube and the connecting part, as shown in the setup of the corrosion chamber in Figure 3.3.

3.6.3 Gas measurement

Due to its horizontal orientation, the experimental setup enables measurements of hydrogen evolution. The setup with the integrated gas measurement is shown in Figure 3.3. In this case, a lid with a central guide tube for the burette is used, and the contact points between the burette and lid are sealed with O-rings. The burette is customised by Klüver & Schulz GmbH (Seevetal, Germany). An inverted funnel is attached to the opening of the burette, which interlocks with a 3D-printed elastic plug of TPU 95A. The inverted funnel is cut with a diamond saw from a funnel of borosilicate glass to fit into the corrosion chamber. Borosilicate glass is used because it is easy to process and stable in an autoclave. During first tests, gas accumulation was observed at the transition between the funnel opening and the funnel stem, which falsified the

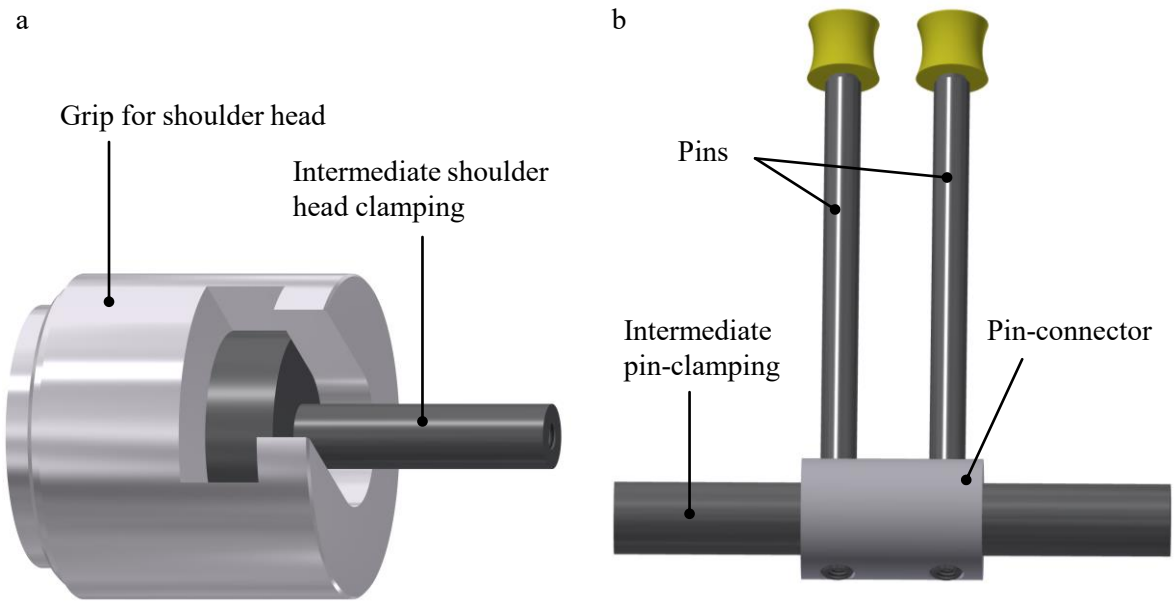

Figure 3.4.: Clamping systems for specimens into the test bench: (a) shoulder head clamping, (b) pin-connectors.

measurement of liquid level in the burette. This issue is eliminated by using funnels with a wider stem (inner stem diameter of 8.9mm).

3.6.4 Temperature control unit

A steady temperature of $37°C \pm 1°C$ is required for physiological test conditions. The temperature control unit is composed of a rectangular frame with solid base and top and the frame is covered with 3mm thick neoprene, which has excellent insulating properties. The neoprene textile and the frame are joined together using Velcro. The through-axis of the test bench is enclosed in neoprene from the front and rear. This design allows lateral movement of the actuator side while maintaining thermal isolation. Physiological conditions inside the temperature control unit are achieved by a heat exchanger system. The system is composed of coils that can be placed around the glass bottle of the corrosion chamber and are connected to the heat exchanger (S/N 104344044 by Thermo Electron, Newington, USA).

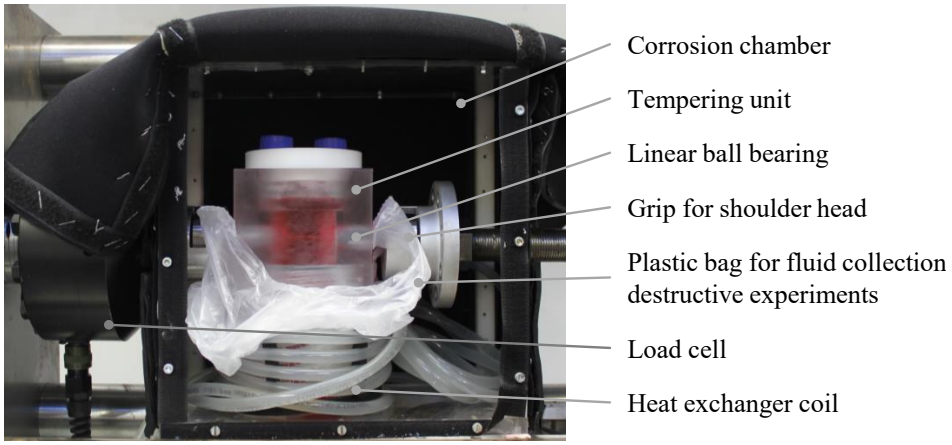

Figure 3.5.: Experimental setup in use.

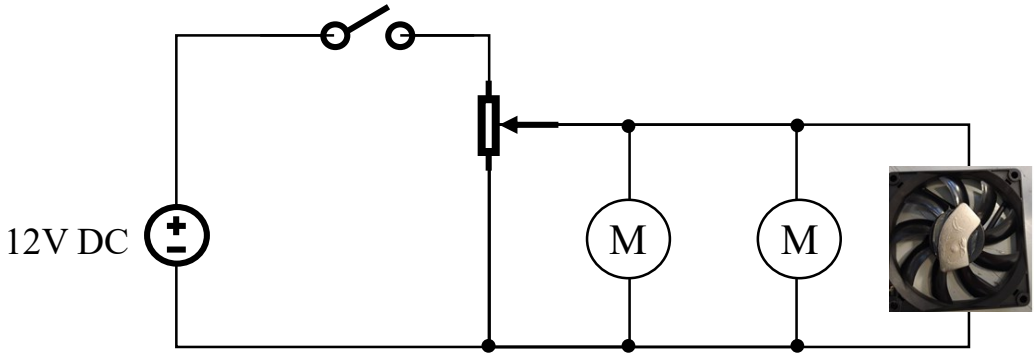

Figure 3.6.: Electric circuit of the magnetic stirrer.

3.6.5 Magnetic stirrer

Magnetic stirrers are produced in an unconventional way due to budget restrictions. Computer fans are equipped with neodymium magnets. These physically rotating magnets generate an oscillating magnetic field. The angular velocity of the rotational movement is manually adjustable via a potentiometer. An overview of the circuit is presented in the Figure 3.6. The fans are suspended below the base of the corrosion chamber in the T-slot guide rails.

3.7 Tensile tests

Tensile tests are carried out at a velocity of 1mm/min on an MTS Minibionix test machine. The resulting strain is measured with an optical extensometer system (GOM Aramis SRX Adjustable, Carl Zeiss GOM Metrology GmbH, Germany). An analogue signal is used for data transfer to the MTS testing system. Data is then processed using MATLAB and material parameters evaluated in accordance with ISO 6892-1:2016.

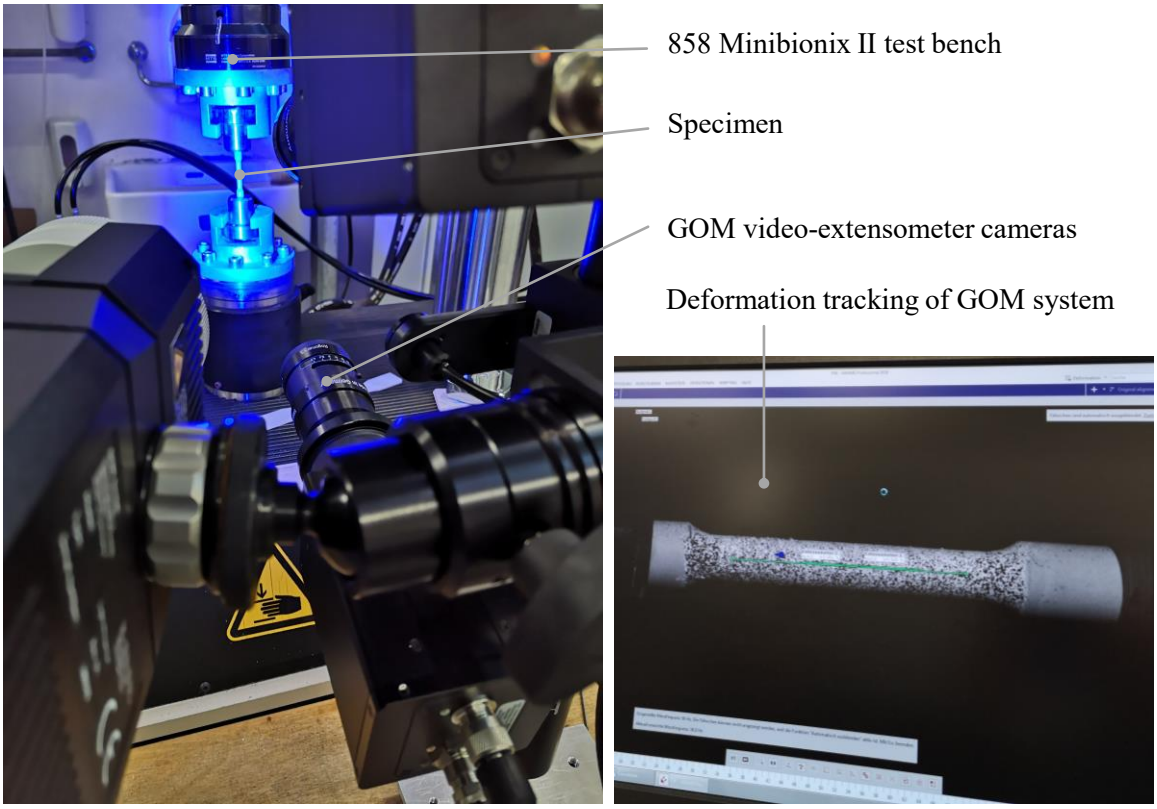

Figure 3.7.: Tensile testing setup.

3.8 Constant load tests

In constant load tests, the newly developed corrosion setup is used and experiments are set up according to the procedure described in Figure C.3 in appendix C.

After the installation of the enclosed corrosion chamber into the test bench, load is applied at a rate of 40N/s until the target load is reached. The fluid level is immediately topped up. At the end of the test period or after failure of the specimen, samples are washed in distilled water and 90% ethanol and laied out to dry.

3.9 Slow strain rate tests

The newly developed setup is used for slow strain rate tests in fluid, and experiments are set up according to the procedure described in Figure C.3 in appendix C.

After the integration of the enclosed corrosion chamber into the test bench, a preload of 20N is applied, the fluid level topped up and the test started. After failure, specimens are washed in distilled water and 90% ethanol and air-dried.

Reference measurements in air are performed on an MTS Minibionix test machine. The resulting strain is measured with an optical extensometer system (GOM Aramis SRX Adjustable, Carl Zeiss GOM Metrology GmbH, Germany). An analogue signal is

used for data transmission with the MTS testing system. Experimental data is then processed using MATLAB.

3.10 Fatigue experiments in air

Stress-controlled fatigue tests in air are performed on an MTS Minibionix testing machine. The resulting strain is measured with an optical extensometer system (GOM Aramis SRX Adjustable, Carl Zeiss GOM Metrology GmbH, Germany). An analogue signal is used for data transmission with the MTS testing system. The fatigue tests are carried out at room temperature with an axial sinusoidal tensile load and a stress ratio of $R = 0$. Tests are performed until failure or stopped at $2\text{x}10^6$ cycles. Experimental data is processed using MATLAB.

Strain-controlled fatigue tests in air are performed at room temperature on an ISTRON 8820 test machine, equipped with 250kN load cell. The strain is measured using a contact extensometer. Fatigue tests are performed fully-reversed with a stress ratio of $R = -1$. Experimental data is processed using MATLAB.

3.11 Fatigue experiments in fluid

The newly developed setup is used in the corrosion-fatigue experiments. Experiments are prepared according to the procedure described in Figure C.3 in the appendix C. Specimens are loaded in the corrosive environment with an axial tensile sinusoidal loading and a stress ratio of $R = 0$. Experimental data is processed using MATLAB.

3.12 Electron microscopy

3.12.1 SEM, SEM BSE, EDS analysis

SEM, SEM BSE and EDS analysis are performed on a Zeiss CrossBeam 550 with an Octane Elite EDAX ED micro-analyser (Carl Zeiss AG, Oberkochen, Germany).

For cross-sectional analysis, specimens are cut perpendicularly to the extrusion direction, mounted in epoxy resin and then prepared by grinding and polishing. To analyse the average grain size, one cross-section is additionally etched with 2% nital and sputtered with carbon.

Basic principles of scanning electron microscopy are described in the appendix D in section D.1.

3.12.2 TEM analysis

TEM analysis is performed on a JEM-2100 Electron Microscope (JEOL Ltd., Akishima, Japan). Samples are prepared using argon ion-slicing with a JEOL EM-09100IS Ion Slicer (JEOL Ltd., Akishima, Japan).

An introduction on transmission electron microscopy is given in the appendix D in section D.1.

3.13 XRD analysis

X-ray diffraction analysis (XRD) is performed on a Bruker AXS D4 Endavor diffractometer with Bragg-Brentano geometry, applying Cu Kα radiation at $\lambda = 0.15406$nm. 2θ ranged from 15° to 90° with a step size of 0.04°. Acquisition time per channel is 6 seconds.

Basic principles of X-ray diffraction analysis are summarised in appendix D in section D.2.

4

Microstructural analysis

This chapter summarises the results of the material characterisation of the WE43 alloy and the PEO coating. The chapter presents data published in [118, 120, 122].

4.1 Microstructural analysis of WE43 alloy

Figure 4.1 shows the α-Mg matrix of the WE43 alloy with intermetallic precipitates of less than 0.1μm in diameter, which are found at grain boundaries as well as inside grains. The EDS analysis reveals precipitates composed of Mg-Y-Nd. Neodymium is predominantly present inside the intermetallic precipitates, with concentrations of up to 27wt.%. Yttrium is present inside the precipitates as well as inside the α-magnesium matrix. Higher Yttrium concentrations are identified inside the intermetallic precipitates ($\leq$13wt.%.). The EDS analysis is presented in Figure E.1 in appendix E. These secondary Mg-Y-Nd precipitates are typically β ($Mg_{14}YNd_2$) and $\beta 1$ (Mg_3(Y,Nd)) [114].

The etched TEM image in Figure 4.1 reveals very fine grains with some visible twins. An average grain size of 2.7μm is determined using the intercept method [122]. The grain size distribution is shown in Figure 4.2.

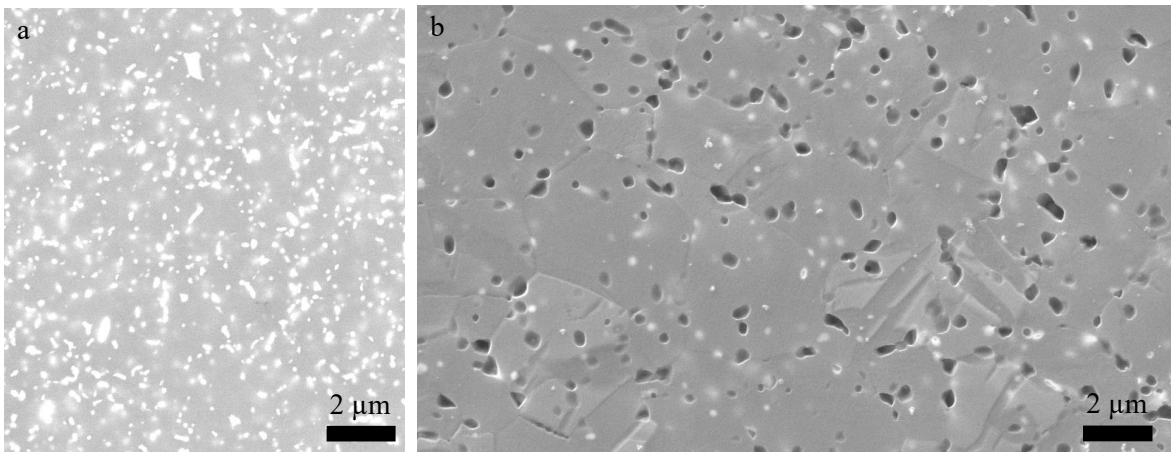

Figure 4.1.: Microstructure of WE43: (a) SEM BSE image, (b) SEM image of etched specimen, adapted from [122].

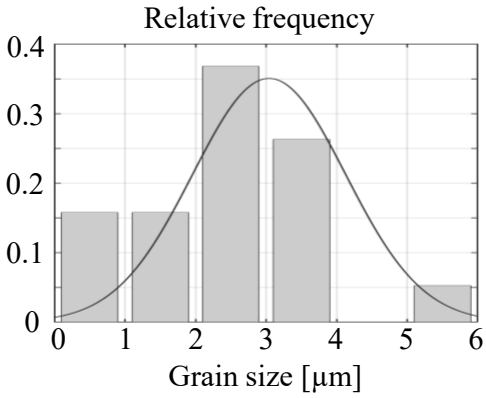

Figure 4.2.: Grain size distribution of WE43, adapted from [122].

4.2 Microstructural analysis of PEO coating on the WE43 alloy

Figure 4.4 shows the cross-section of the coating and the interface between coating and WE43 alloy substrate. The coating has a smooth surface with a thickness of 19±5μm and is composed two layers: a very thin and dense inner barrier layer and an outer porous layer. The outer porous layer has both interconnected and isolated pores. Elemental mapping shows a homogeneous distribution of oxygen, phosphors and magnesium in the outer layer. The inner layer is rich in magnesium and contains less phosphorus. The constituents of the coatings are quantified by EDS analysis on the surface: 18.4wt.% magnesium, 68.0wt.% oxygen and 13.6wt.% phosphorus. The surface morphology of the coating is shown in Figure 4.3b. Irregularly and regularly shaped pores can be recognised, which cover about 7% of the surface area. The pore diameters range from 0.3μm to 7μm.

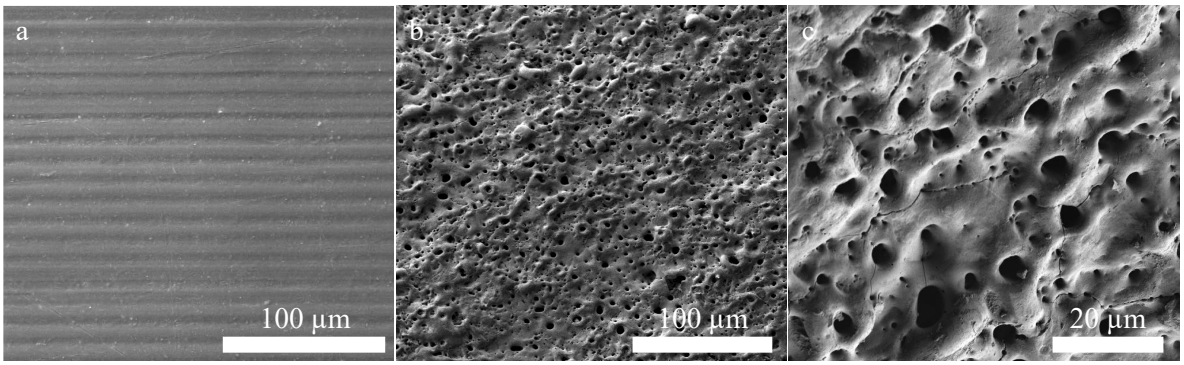

Figure 4.3.: SEM images of surfaces: (a) machine threads of uncoated WE43 specimens, (b) SEM image of PEO coating, (c) SEM image of PEO coating at higher resolution, adapted from [120].

Compared to the results presented in literature for biodegradable PEO coating, the coating has smaller pores in the area close to the barrier layer and a lower proportion of pores on the surface [5, 6].

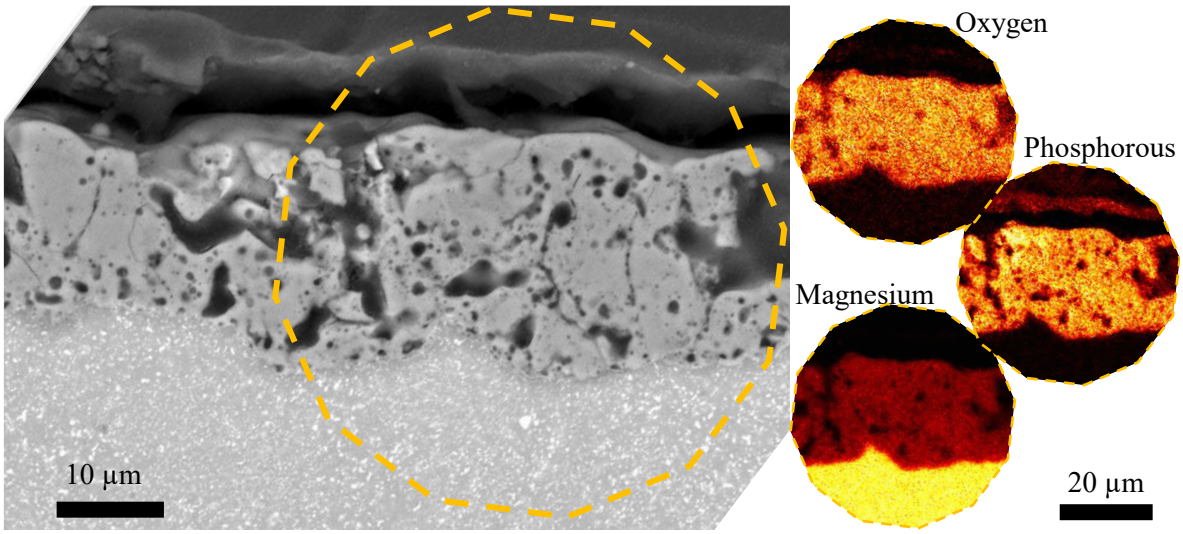

Figure 4.4.: SEM BSE image of substrate-coating interface with elemental mapping. High concentrations are shown in yellow, low concentrations in red and no detection is indicated by black colour, adapted from [120].

5

Long-term corrosion behaviour of WE43 alloy in physiological conditions and the influence of PEO coating

In this chapter, the corrosion behaviour of the rare earth-containing WE43 alloy of medical-grade is systematically examined and the influence of the PEO coating is assessed. The comprehensive understanding of the corrosion mechanisms and their impact on mechanical integrity is of paramount importance for successful implant development. On this account, an in vitro study is conducted to acquire foundational insight into the long-term degradation in organic and physiological fluid and to link the material degradation processes to the deterioration in mechanical integrity.

To study the corrosion in a time-dependent manner, uncoated and PEO-coated specimens are exposed to the corrosion environment for different time periods. The in vitro corrosion is studied in a physiological fluid with organic compounds in the long-term. The corrosion rate is recorded time-continuously using the hydrogen evolution method. Corrosion mechanisms are studied with scanning electron microscopy (SEM). Microgalvanic corrosion is analysed as are the geometric features of the corrosion front to evaluate susceptibility to pitting corrosion. Furthermore, corrosion product layer formation is assessed with energy dispersive spectroscopy (EDS) and X-ray diffraction (XRD). Additionally, changes in the mechanical integrity are evaluated with tensile tests.

The results of the presented in vitro study are based on the following published research articles: [118–120, 190].

5.1 Progress on corrosion resistance of biodegradable magnesium alloys

In the corrosion reaction of magnesium in aqueous solution, hydroxide is formed. The hydroxide accumulates on the alloy surface and forms a protective layer [171]. The stability of the hydroxide layer depends strongly on the local pH value and the chloride concentration of the fluid [133]. At chloride concentrations exceeding 30mmol/l, the hydroxide layer will react with chloride ions and transforms into a readily water-soluble

magnesium chloride (see section 2.3.2-2.3.4). As a result, pitting corrosion increases [171]. Since human blood plasma contains chlorides in high concentrations, it is important to perform in vitro corrosion experiments in an aqueous solution with comparable ionic concentrations. Various fluid systems were introduced to study in vitro corrosion. As discussed in section 2.3.7, the constituents of the fluid can strongly influence the corrosion and the complexity of the experiments and should be carefully selected. As a consequence, results obtained in different studies often cannot be straightforwardly compared. Hou et al. [64] concluded that cell culture media containing protein mixtures are the most suitable medium for in vitro studies as they are closest in composition and concentration to human blood plasma. On that basis, the cell culture fluid DMEM is used in the in vitro experiments.

Alloying elements and microstructural parameters can significantly affect the corrosion resistance of magnesium alloys, as it is described in section 2.1. To this end, various magnesium alloy systems have been developed for use in biodegradable implants with biosafe alloying elements that steadily increase the material's corrosion resistance. The aluminium-containing magnesium alloy AZ91 showed good biocompatibility in in vitro studies and promoted the formation of bone tissue due to Ca-P phases [173]. Comparing the in vitro and in vivo degradation behaviours, AZ91 showed higher corrosion rates under in vitro conditions. This has been explained by its microstructure with a coarse second phase, which leads to more microgalvanic corrosion in in vitro conditions [1]. In vivo studies in animals using AZ31 implants to fix bone fractures have demonstrated an improved fracture healing process. This was attributed to the effect of magnesium in promoting osteogenic differentiation [176].

In recent years, the need for a more comprehensive analysis of aluminium-free alloys has been claimed, as aluminium-containing alloys are not recommended for in vivo applications. This is attributed to the potentially harmful effect of aluminium. A promising aluminium-free magnesium alloy is WE43 [55, 108], as it safely degrades in vivo [102]. The alloy contains rare-earth elements and zirconium and has excellent mechanical properties, corrosion resistance and biocompatibility, as described in more detail in section 2.1. In comparison with the aluminium-containing alloy AZ91D, WE43 showed better corrosion resistance in 3.5wt.% NaCl [6]. Similar results were obtained when comparing AZ31B and WE43, with the latter showing better corrosion resistance in 3.5wt.% NaCl [145]. Severe galvanic corrosion was observed in the AZ31B alloy due to Al-Mn secondary phases, which cause corrosion pits. In WE43, in contrast, no corrosion pits developed after 24 hours.

When WE43 is exposed to m-SBF, a protective layer composed of $Mg(OH)_2$ and amorphous carbonated apatite is formed on the metallic surface [7]. Its thickness grows over time, which restricts fluid access to the metal. Over time, the layer dehydrates at the substrate surface, leading to the formation of an innermost MgO-layer. The protective nature of this layer decelerates the corrosion process and leads to an equilibrium between formation and dissolution of the protective layer. In SBF, this equilibrium is reached after approximately 48 hours [7]. It has also been observed that the $Mg_{24}Y_5$ phases corrode to Y_2O_3 and stabilises the protective layer [145].

The short-term corrosion behaviour ($\leq$24 hour) in physiological solutions has been

studied intensively, but there is little data available on the long-term corrosion with periods exceeding 5 or 14 days [1, 8, 20, 78, 194], although time-dependent changes were reported. For the application of the alloy in orthopaedic implants, it is necessary to consider the long-term corrosion behaviour. Öecal et al. [201] observed a sudden increase in the corrosion rate of WE43 in SBF after about one week. This resulted in severe pitting and corrosion damage, although no severe corrosion damage was observed during the initial 5 days. An increase in the corrosion rate was also observed after 11 days in 3.5wt.% NaCl [143]. Volumetric analysis revealed significant corrosion damage in an Mg–Zn–Zr–RE alloy after 30 days in Hank's Balanced Salt Solution [103]. These time-dependent changes emphasise the need for more comprehensive long-term studies, which additionally link changes in mechanical strength to the corrosion behaviour.

To increase the corrosion resistance of magnesium alloys for medical application, protective coatings are regarded as an effective method. Different methods of surface modification have been developed to control the degradation rate and to improve the corrosion resistance of the alloy [6, 58, 71, 92, 188, 197]. Jin et al. [78] significantly improved the corrosion resistance of WE43 by enriching the surface layer with neodymium. Li et al. [92] decreased the corrosion of WE43 by introducing a thin amorphous SiC film on the alloy surface, which also improved the material's suitability for medical applications. The surface modification by plasma-electrolytic oxidation (PEO) can improve corrosion resistance and biocompatibility [22, 43].

It has been shown that the PEO coating significantly reduces the corrosion rate of an AZ91 alloy in SBF over a period of at least 14 days [18]. First animal studies on PEO-coated WE43 implants have demonstrated a significant reduction of the degradation rate in vivo and an enhanced osseous implant integration due to the coating [136]. In that study, neither the uncoated WE43 alloy nor the PEO-coated WE43 alloy was found to have cytotoxic potential in in vitro tests. This is of significant importance for its medical application. Furthermore, the PEO coating has shown a positive effect on cell proliferation in cytocompatibility tests [175]. PEO coatings on magnesium alloys are generally composed of two or three layers: an outer layer, which is sometimes split into a more porous and a less porous part, and a thin compact layer, which connects the coating to the magnesium substrate [33]. The protective effect of the PEO coating mainly depends on the corrosion resistance of this inner barrier layer [32]. By comparing PEO coatings on two different magnesium alloys, Arrabal et al. [6] identified the overall compactness of the PEO coating as a critical factor for its corrosion protection. They observed that a less compact PEO coating on a WE43 alloy provides corrosion protection in NaCl solution only at the initial phase of the experiment. Similar results were reported by Li et al. [95]. They concluded that the density of the ceramic surface coating of a micro-arc oxidation-treated AZ31 alloy is a critical factor for its corrosion resistance. In the last few years, significant progress has been made in further improving the functionality of PEO coatings for its medical application [19, 40]. Two-layered polymer-based coatings were introduced in which the PEO coating defects are sealed. In this way, the corrosion resistance has been improved as liquid is prevented from penetrating into the porous coating [42]. Another promising approach is the addition of specific agents to the electrolyte to enhance biocompatibility, wear resistance, and

antibacterial activity of the coating [43, 44, 117, 192].

In the assessment of biodegradable magnesium corrosion, the impact of corrosion on mechanical properties is often overlooked. The majority of in vitro studies focus solely on corrosion processes without considering their correlation with mechanical parameters [21, 45, 81, 171, 186]. However, in the design of implants for load-bearing applications, the relationship between corrosion front geometry and mechanical performance is crucial. Boland et al. [16] demonstrated that taking corrosion pits into account is essential for accurately describing the non-linear correlation between mass loss and material strength reduction. Simplifying the process by assuming uniform corrosion fails to capture this correlation adequately. Wang et al. [165] analysed the correlation between pitting corrosion and the mechanical integrity of a modified AZ91 alloy in 3.5wt.% NaCl. They concluded that residual strength depends more on the dimensions of the deepest pit than on the overall amount of pits. Consequently, they observed an exponential decline in strength over an experimental period of up to 8.5 days. Van Gaalen et al. [49] investigated the effect of localised corrosion on the mechanical integrity of the WE43 alloy in an inorganic fluid. They found that the smallest remaining cross-sectional area correlated most strongly with remaining material strength. Zhao et al. [195] observed a detrimental effect of long-term corrosion. While they noted minor changes in material integrity of a ZEK100 magnesium alloy after 4 days in phosphate-buffered saline, larger decreases of about 12 to 13% in ultimate tensile strength and yield strength were observed after 28 days. Van Gaalen et al. [50] examined the protective capacity of PEO coating on mechanical strength. In an inorganic SBF solution, they observed a reduction in pitting depth and a lesser decrease in tensile strength in PEO-coated specimens. A positive influence of PEO coating on the material strength retention was confirmed in animal studies. The protection has been attributed a time-dependent characteristic [71].

5.2 Materials and methods

To study the time-dependent material degradation, corrosion experiments are performed with tensile test specimens over varying immersion times of 7, 14, 21, 28 and 70 days, and specimens are tensile-tested afterwards. To identify the influence of the PEO coating, uncoated WE43 specimens and PEO-coated WE43 specimens are examined. The specimen design is presented in section 3.1. The experimental setup is described in section 3.5 and includes the hydrogen evolution measurement. During the immersion tests, the exposed sample area is limited to the parallel length and both ends are sealed according to the procedure described in appendix C. At least four specimens are analysed in each configuration. After corrosion, one sample is processed for analysing corrosion mechanisms and the remainder are used in mechanical testing.

The complex physiological cell culture medium DMEM (see section 3.4), which incorporates organic compounds and high levels of sugars, is utilised in the in vitro corrosion experiment. Its critical vulnerability to contamination is considered in the experimental design and processes are developed to ensure sterility (detailed description is included in appendix C). Contaminated tests are not included in the evaluation.

The gas level in the burette is recorded following predefined intervals and related to the exposed surface area. To ascertain the exposed area, the uncovered length is measured at three points. The resulting mean gas volume per area is then averaged across all measurements. This means that with increasing test duration, fewer and fewer samples are included as samples were taken every 7 days.

The resulting mass loss relative to the exposed surface area $\Delta m_{A,Mg}$ can be calculated on the basis of the ideal gas equation and the overall corrosion reaction, which relates the dissolution of 1mol magnesium to the generation of 1mol hydrogen [143]:

$$\Delta m_{A,Mg} = pM_{Mg}V_H/(RTA) \ , \tag{5.1}$$

with the pressure p, molar mass of magnesium M_{Mg}, the gas volume V_H in ml, molar gas constant R, temperature T and the exposed surface area A in cm^2. The experimental temperature of 37°C, the standard atmosphere of 1atm and the molar mass of magnesium of 24.31g/mol are considered in the calculation.

The corrosion rate CR in mm/year can be subsequently determined based on the mass loss [80]:

$$CR = 87.6\Delta m_{Mg}/(\rho_{Mg}A\Delta t) \ . \tag{5.2}$$

with the mass loss Δm_{Mg} in mg, the density of magnesium ρ_{Mg} in g/cm^3, the specimen's exposed surface area A in cm^2 and the immersion time Δt in hours.

To examine the degradation of mechanical properties, three specimens of each group are tensile tested according to section 3.7. Pristine specimens are additionally tested for reference. Moreover, one sample of each group is used for analysis on corrosion mechanisms. Corroded surfaces and metallographically prepared cross-sections are analysed with scanning electron microscopy (see section 3.12.1). Furthermore, XRD measurements are performed on the circumferential surface, according to section 3.13.

Cross-sectional images of uncorroded specimens are processed using GeoGebra (GeoGebra Classic 5.0.720.0-d, Linz, Austria) to determine the parameters describing the geometrical appearance of the corrosion front for evaluating susceptibility to corrosion pitting. The minimum radius is measured at the deepest pit and the maximum radius at the least corroded site. An average sample radius is calculated from a minimum of 19 measuring points along the circumference. The reduction in the cross-sectional area of the corroded specimens is assessed using fiji software [140].

In addition, coated and uncoated pin specimens are immersed in DMEM for up to 28 days according to the experimental protocol described in section 3.5. Specimens' ends are sealed and the unprotected surface area is equal to the unsealed surface of the tensile test specimens. Hydrogen evolution is not measured. A single pin specimen is corroded for 7, 14, 21, and 28 days, and optical microscopic images (Hirox Co Ltd., Tokyo, Japan) are taken of the smooth corroded surfaces.

5.3 Results and discussions

5.3.1 Optical microscopy

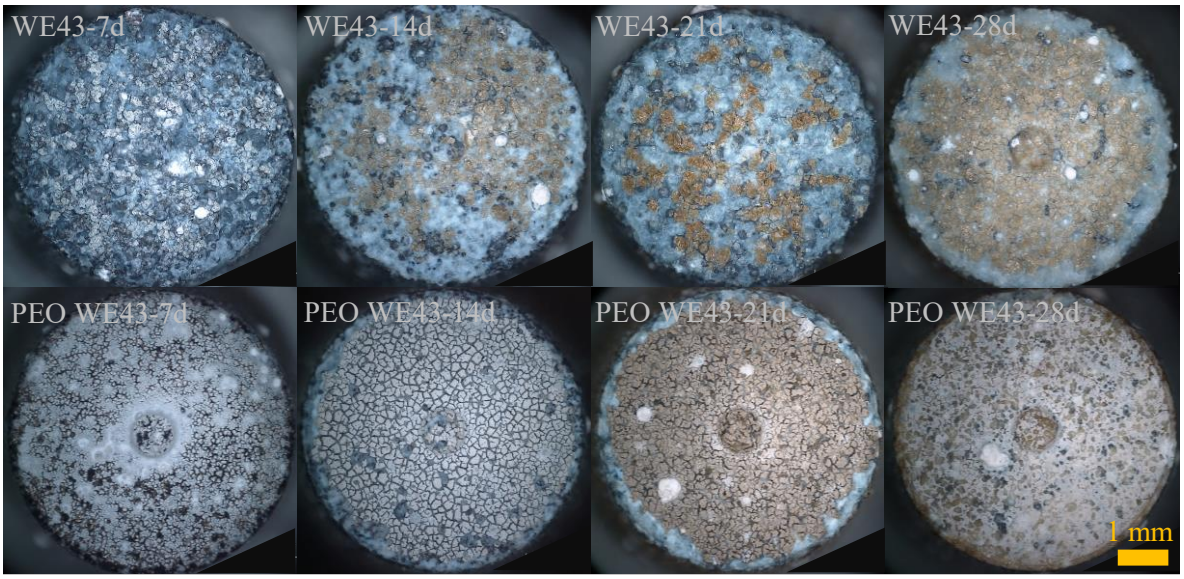

Figure 5.1.: Optical microscope images of the flat surfaces of corroded pin specimens after varying immersion periods.

Figure 5.1 shows the surface morphology of the flat and corroded surfaces of the pin-specimens. Exposure to the corrosion environment results in the deposition of corrosion products on the specimens' surfaces, with an evident formation of the corrosion products. Time-dependent macrostructural changes and differences between uncoated and coated samples can also be observed. The corrosion products appear greyish/whitish after 7 days and become more brownish with increasing exposure time. The whitish precipitates are considered $Mg(OH)_2$ [187]. Some accumulations of the white precipitates are visible in all uncoated specimens. These mound-like accumulations have been associated with structures indicating localised galvanic corrosion between the precipitates and the α-matrix [7]. After 5 days in m-SBF, some non-corroded areas were found at these structures [7]. Laser microscopical images of areas around these mounds reveal grooves-like patterns that might indicate machine threats, suggesting the presence of less corroded areas (see section F.1). These mound-like accumulations only appear on the coated specimens after 21 days. In general, the coating changes the visual appearance of the corroded surfaces. The surface is more brownish and many microcracks are visible inside the corrosion layer.

5.3.2 Surface analysis

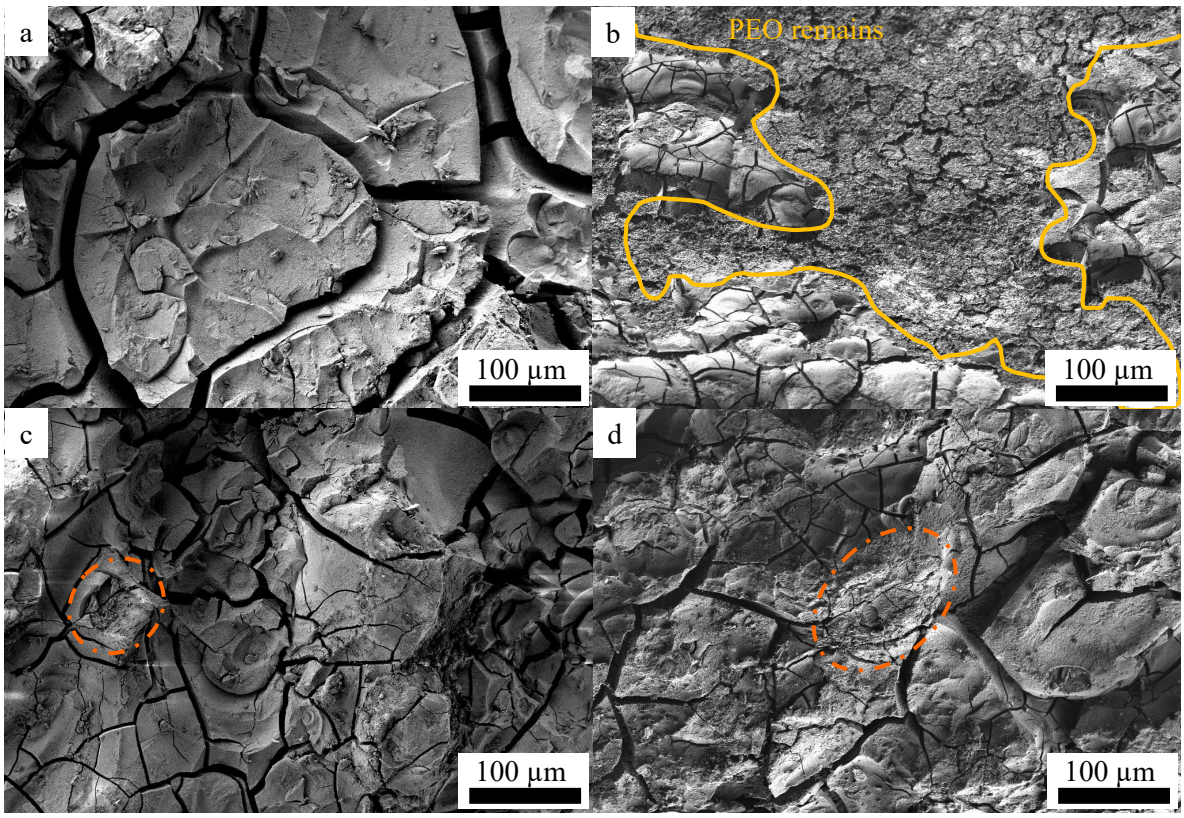

Figure 5.2.: SEM images of specimen's surfaces: (a) of an uncoated specimen after 7 days, (b) of a coated specimen after 7 days, (c) of an uncoated specimen after 14 days, (d) of a coated specimen after 14 days, adapted from [120].

The SEM images of corroded surfaces of tensile test specimens reveal differences between uncoated and coated specimens in terms of the morphology of the corrosion products. The corroded sample surfaces show a cracked-mud morphology, as shown in Figure 5.2. After 7 days, the uncoated sample has a coarser appearance. The coated sample shows a much finer network of cracks and partial remains of the original PEO coating can be identified. After longer immersion times, however, the appearance of the coated samples becomes more similar to the morphology of the uncoated samples and the PEO residuals can no longer be seen on the surface. With increasing corrosion time, the surface morphology of the uncoated samples becomes finer and exhibits a higher crack density. Ascencio et al. [7] suggested that the cracked surface morphology may indicate preferential dissolution of the α-Mg matrix due to microgalvanic corrosion between the magnesium matrix and the intermetallic precipitates, which will be discussed in section 5.3.4. They also suggested that the round or oval defects in the cracked morphology, marked in orange colour in Figure 5.2c and d, are indicative of a localised corrosion process.

The X-ray diffraction (XRD) patterns of WE43 and PEO-coated WE43 before and after immersion in DMEM are shown in Figure 5.3. The result of the uncoated WE43 control

specimen show diffraction peaks corresponding to hexagonal close-packed Mg, with the strongest peak at $2\theta = 36.5°$. The intensity of the peaks in the spectra confirms crystallinity of the WE43 surface. In the PEO-coated specimens, Mg and MgO are the main crystalline phases with the two peaks partly overlapping. After 28 days of immersion in DMEM, additional $Mg(OH)_2$ is detected at $2\theta = 18.7°$ for both specimen groups. The peak intensity of the magnesium matrix decreases after immersion due to the corrosion process.

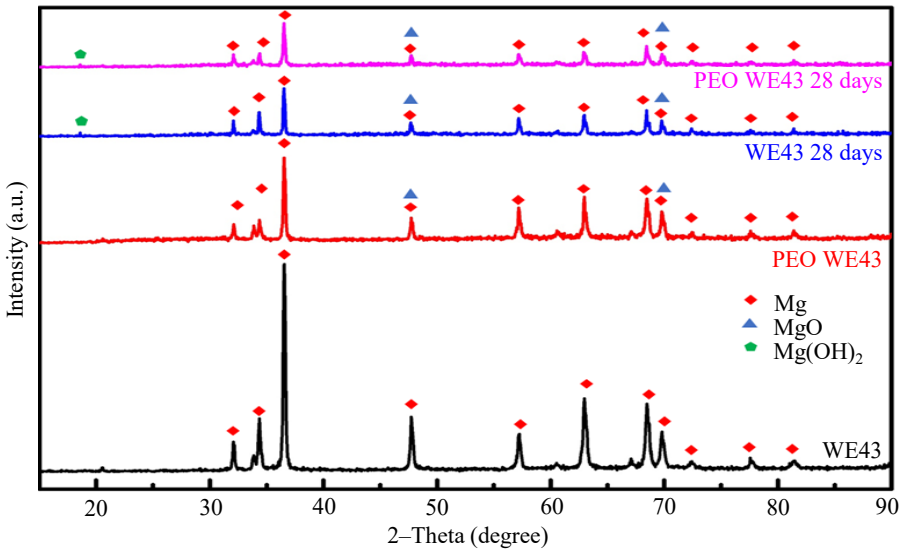

Figure 5.3.: XRD patterns of uncorroded WE43 specimens (black), uncorroded PEO-coated WE43 specimens (red), uncoated WE43 specimens after 28 days in DMEM (blue) and PEO-coated WE43 specimens after 28 days (pink) [120].

5.3.3 Cross-sectional analysis

Figure 5.4 and 5.5 provide an overview of the SEM BSE images of the cross-sections of the coated and uncoated tensile test specimens after different immersion times. At the beginning, the specimens have a smooth and round shape. After corrosion, this shape has changed due to inhomogeneous corrosion along the circumference. The entire surface is covered by corrosion products of varying thickness.

After 7 days, regions of localised corrosion are visible along the circumference of the uncoated specimen. The regions do not grow deep and form some non-corroded ridges. As the immersion time increases, the sites of uncorroded ridges become smaller as the corrosion progresses. The alloy's susceptibility to pitting corrosion in a physiological environment plays an important role from the mechanical point of view, as homogeneous dissolution of the matrix is highly desired for preserving fracture resistance of implants. The cross-sectional images allow the direct analysis of the localised corrosion. The images of corroded cross-section indicate that the WE43 alloy suffers limited pitting corrosion in DMEM and that the corrosion progresses rather inhomogeneously at the corrosion interface. A rather uniform degradation behaviour of WE43 alloy was also

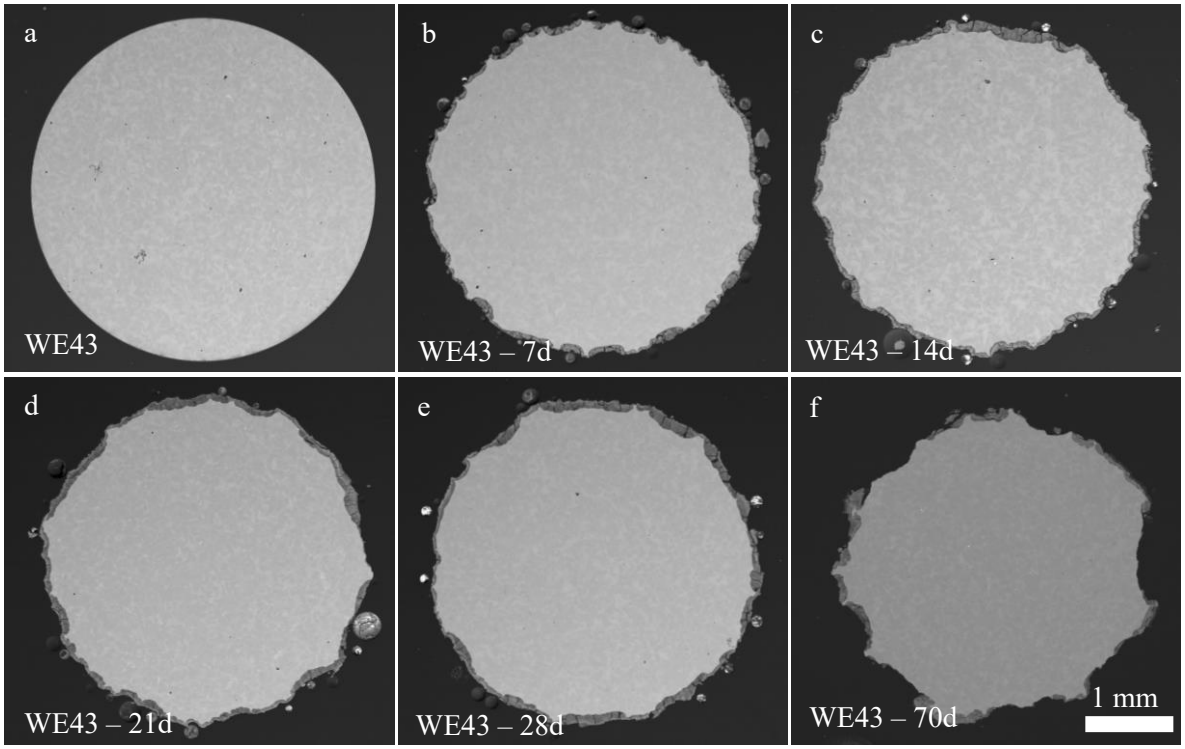

Figure 5.4.: SEM BSE images of cross-sections of non-coated specimens in uncorroded state as well as after varying immersion times, adapted from [120].

reported by Imwinkelried et al. [71] in long-term in vitro experiments in inorganic SBF. Considerably more severe pitting was observed in Hank's Balanced Salt Solution for a rare earth-containing magnesium alloy [103].

The morphological changes of the specimen's circumference are most obvious after the initial 7 days. Between 7 and 28 days, an ongoing corrosion process is indicated by small changes in the geometrical appearance of the corrosion front. This is also confirmed by the image analysis presented in Table 5.1. The radius at the most corroded site has reduced to 1749μm, which corresponds to a decrease of 11%. The radius at the least corroded spot remains in the range of the initial radius, confirming the presence of nearly uncorroded ridges. The average radius has decreased by 6%. After 28 days, no change is observed in the radius at the most corroded spot, but the ridges shrank. In this stage of corrosion, a noticeable reduction in the number of less corroded ridges is observed, which also become smaller. This indicates a more homogeneous corrosion along the surface. However, the cross-sectional image shows considerable corrosion damage after 70 days, which indicates an ongoing dissolution of the magnesium matrix. The diameter has decreased by 21% at the most corroded spot, on average by 15%, and at the largest ridge by 5%. Uncorroded ridges are not obviously affected compared to shorter corrosion times, as the intermetallic precipitates in the ridges resist corrosion. Consistent results on the formation of corrosion pits in WE43 were reported by [50]. In a more aggressive and inorganic corrosion environment, the pits were found to not grow significantly after 2 weeks. This led to a more homogeneous dissolution along the

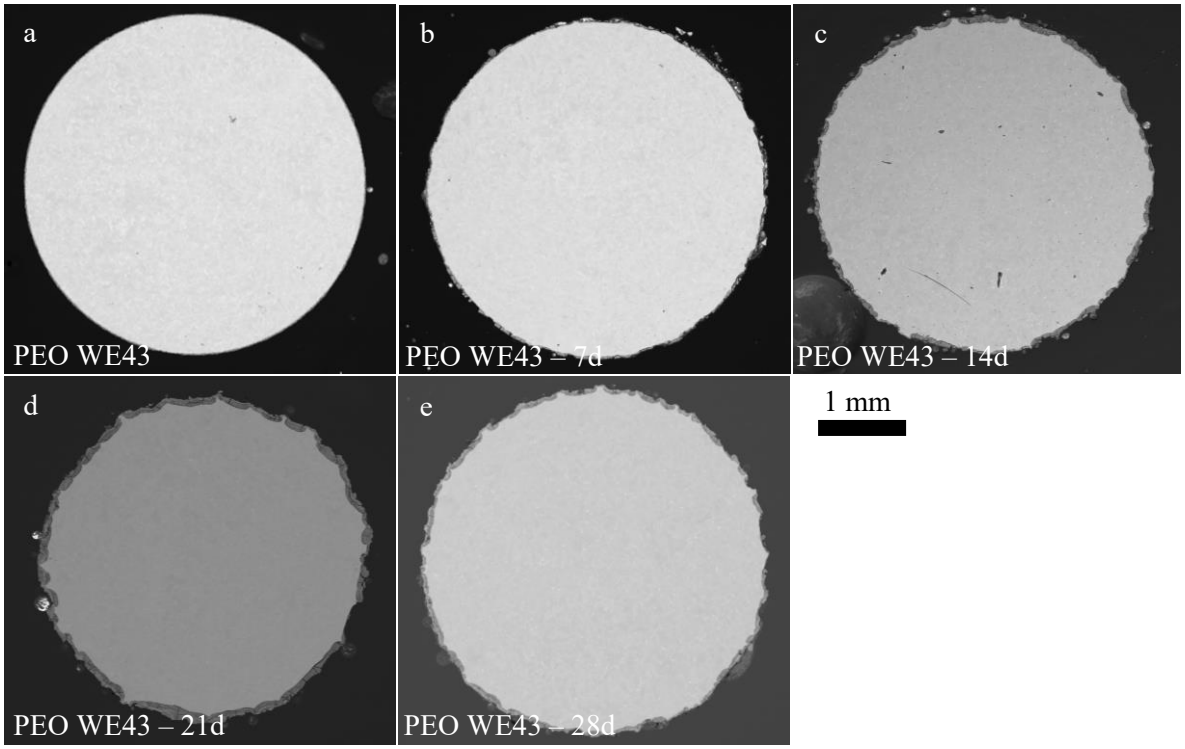

Figure 5.5.: SEM BSE images of cross-sections of PEO-coated specimens in uncorroded state as well as after varying immersion times, adapted from [120].

	0d	7d	14d	21d	28d	70d
R_{min} [μm]	1979	1749	1795	1678	1753	1881
R_{max} [μm]	1979	1968	1981	1898	1946	1571
R_{avg} [μm]	1979	1861	1874	1783	1840	1677

Table 5.1.: Results of image analysis: minimal radius at most corroded spot R_{min}, maximal remaining radius at least corroded spot R_{max}, average radius R_{avg}.

circumference for longer immersion periods.

A rather general analysis of the cross-sectional images reveals that the non-corroded cross-sectional area of the non-coated specimen have decreased by 10.5%, 12.2%, 16.6%, 16% after 7 days, 14 days, 21 days, and 28 days, respectively. The SEM BSE images show that the round shape of the PEO-coated specimen changes less. The SEM BSE images show that the 7-day PEO-coated specimen is covered by corrosion products and has suffered significantly less corrosion, with fewer and smaller uncorroded ridges in comparison to the uncoated specimen. In the image analysis, a reduction of the cross-sectional area by only 2% after 7 days, and by 3% after 28 days is measured in the PEO-coated group. After 28 days, the corrosion attack on the PEO-coated specimen appears comparable or even slightly less than the uncoated 7-day specimen. In other words, the PEO coating significantly delays the corrosion of the underlying alloy also for longer immersion periods.

5.3.4 Microgalvanic corrosion

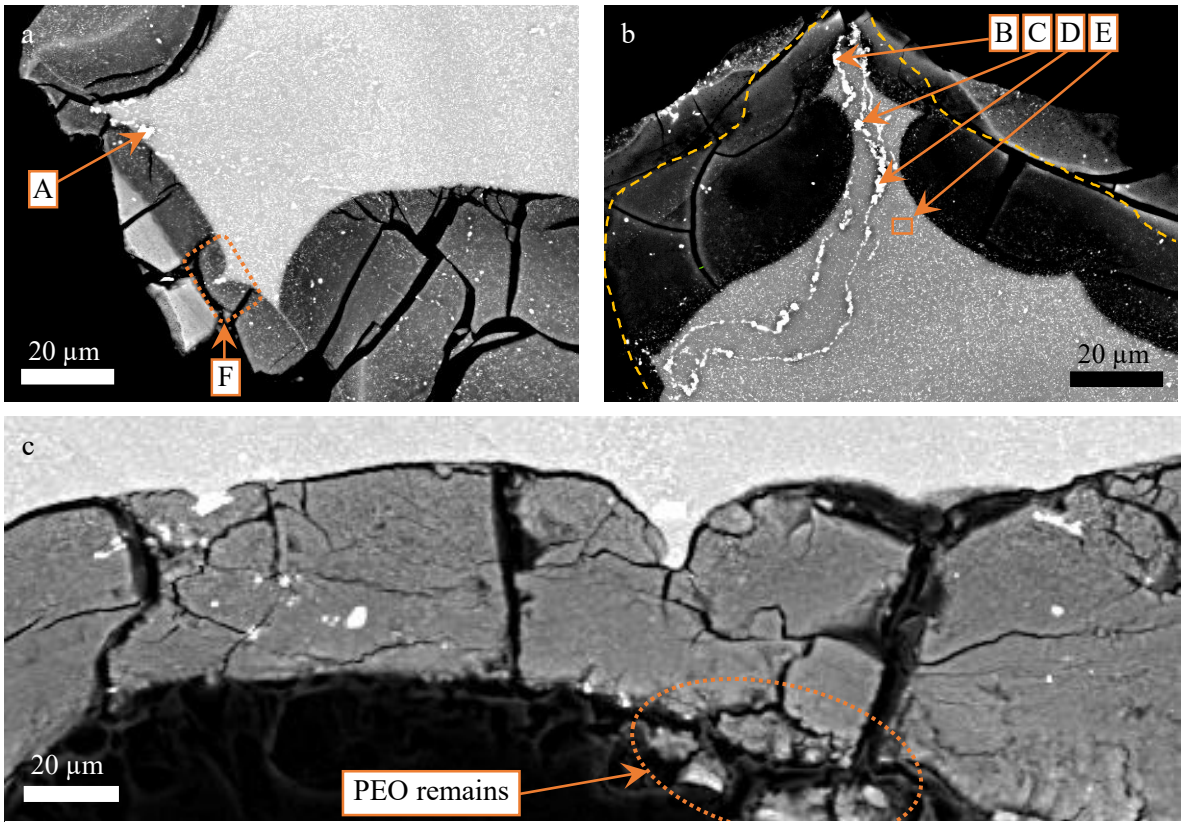

Figure 5.6.: SEM BSE image of microgalvanic corrosion at the alloy surface: (a) of an uncoated specimen after 7 days [118, 120], (b) of an uncoated specimen after 21 days [118] and (c) of a coated specimen after 14 days (c).

Spot	Mg	Y	Nd	Fe
A	8.9	89.9	1.2	-
B	18.9	28.6	-	52.5
C	22.8	28.8	-	48.4
D	7.8	52.4	-	39.8
E	99.1	2	2.1	-

Table 5.2.: EDS measuring results in wt.% of spots marked in Figure 5.6.

Microgalvanic corrosion occurs due to differences in the electrochemical potential between the α-Mg matrix and the intermetallic phases, which can be seen in Figure 5.6. SEM BSE images reveal phase differences through different shades of grey. The SEM BSE images show that the α-Mg is preferentially dissolved and areas rich in precipitates remain uncorroded. This is seen in the SEM BSE images showing precipitate-rich ridges (bright appearance). The images reveal that not all intermetallic phases remain uncorroded, as the oxidised product of rare-earth elements is identified inside the corrosion layer. This confirms that different corrosion mechanisms contribute to the

corrosion process, which is related to the combination of the corrosion media and the distribution of intermetallic phases [6].

Figure 5.6a shows the BSE image of a ridge in an uncoated specimen after 7 days of immersion. The EDS analysis of spot A (see Table 5.2) reveals a high concentration of yttrium inside the precipitate. A thicker corrosion layer can be identified around areas of microgalvanic corrosion. The marked area F in Figure 5.6a shows the dissolution of the α-Mg around a precipitate that appears to remain unaffected. Figure 5.6b shows the formation of a corrosion pit in the uncoated specimen after 21 days. A high concentration of precipitates can be identified within the ridge, which is the product of chemical segregations, and the corrosion front appears to grow much deeper next to the ridge. EDS analysis (see Table 5.2) shows that the precipitates contain high concentrations of iron. In terms of the corrosion resistance of WE43 magnesium alloy, iron is considered an impurity as it is much more noble than magnesium and most other alloying elements. The presence of iron increases the electrode potential difference between the α-magnesium matrix and the Fe-rich precipitate, leading to a more pronounced magnesium dissolution. Severe microgalvanic corrosion at Fe-rich areas has already been reported by other researcher groups in WE43 corrosion. The microgalvanic corrosion was pronounced at zirconium-rich regions and was related to the bonding of zirconium to Fe, Ni, or Si, which are considered as impurities in the alloying process [81]. The geometrical appearance of the uncorroded Fe-rich ridge demonstrates its strong cathodic character. According to the anodic reaction (see equation 2.2), hydroxide ions are generated at cathodic sites, which increase the pH locally and favour the conditions for passive layer formation. For this reason, a thickened corrosion layer is often found adjacent to cathodic sites. Furthermore, the inner part of the corrosion layer (marked in Figure 5.6b in yellow colour), which surrounds the cathodic site, is enriched with magnesium and oxide. It offers a superior corrosion protection to the underlying alloy. The corresponding elemental mapping is presented in Figure F.5 in the appendix F. It has been reported that volcano-like structures form on the cathodic sites at very short immersion times [7, 81]. These structures form due to the release of hydrogen gas at the cathodic centres. The hydrogen escapes though the growing oxide layer and forms a passageway. The remains of these structures are difficult to detect after slightly longer immersion times [7, 81]. As much longer immersion times were considered in the experiment, volcano-like structures could not be properly identified, but the cross-sectional ridge can be associated with them. In the frame of analysing fracture surfaces of the small strain rate tests presented in chapter 6, an image of a volcano-like structure was captured, which is included in the appendix F in Figure F.4.

The corrosion resistance of the WE43 alloy in the physiological environment is much higher than that of pure magnesium [129]. The rare-earth elements in the WE43 alloy both enhance the corrosion resistance and slow down the corrosion process by stabilising the passive layer, especially when present in solid solution. However, the galvanic coupling between the α-matrix, which acts as the anode, and the intermetallic particles, that act as the cathode, can cause pitting corrosion [91]. Depending on the alloy's microstructure and the corrosion environment, more pronounced pitting has been reported [7, 45, 81]. It must be emphasised that the intermetallic precipitates of the

evaluated WE43 alloy are very fine and homogeneously distributed. This microstructural feature is likely to contribute to the less pronounced microgalvanic corrosion, even at infrequent locations of Fe-impurities, and explains the overall good corrosion resistance of the WE43 alloy.

A thicker layer of corrosion products is consistently observed at more corroded sites, while less corroded ridges are covered by a thinner layer of corrosion products. This agrees with the previous description on thicker products next to cathodic sites. The image analysis reveals that the average thickness of the protective layer is 44μm after 7 days, then increases linearly to approximately 66μm after 21 days, and remains constant for longer immersion times. The difference between 7 and 14 days can be attributed to the reduction of the less corroded ridges. The stable thickness of the protective layer at longer immersion times indicates that the corrosion product degrades over time. The SEM BSE images of the side view (see Figure 5.6) show many microcracks in the corrosion layer leading to the detachment of the corrosion product, which is consistent with results reported by Wagener and Virtanen [160]. Since detachment can also occur during the cleaning or preparation process, the above-mentioned values on layer thicknesses likely include uncertainties. However, cracks are linked from the surface of the corrosion products to the alloy interface. They are an important factor for the corrosion process as they facilitate fluid access to the alloy interface. The microcracks can be caused either by the chemical reactions between the DMEM fluid and the corrosion product, which increase the volume and causes stresses, or by the generation of hydrogen gas during magnesium hydroxide formation [81].

After plasma-electrolytic oxidation, the corrosion front appears quite homogeneous in the SEM BSE images (see Figure 5.5), which indicates less localised corrosion. This is particularly the case after 7 days, as the corrosion front shows very few and small less corroded ridges. This can be explained by the barrier effect of the ceramic coating, which separates the alloy from the corrosive environment. After 14 days, some microgalvanic corrosion can be identified, which appear similar to the area F marked in Figure 5.6a (additional SEM images showing the corrosion front are provided in the appendix F). The dissolution of the α-Mg matrix progresses around the precipitate. Hence, the alloy with its microgalvanic cells is not directly in contact with the fluid and is continuously protected by the coating or the passive layer. This leads to a slower dissolution process and less pronounced corrosion at the microgalvanic cells and thus to a more homogeneous corrosion. Figure 5.6c reveals morphological changes in the protective layer. The layer of corrosion products appears denser with fewer cracks, which are aligned more perpendicularly to the alloy interface. The SEM images of the cross-sections in Figure 5.5 indicate that the corrosion front of the coated specimens becomes more similar to the uncoated specimens with longer immersion times. This is also confirmed by SEM BSE images with a higher resolution, which are shown in the appendix F in Figures F.7 and F.8. They reveal fewer corroded ridges developing after 21 days. These results are consistent with results of a study on the long-term pitting susceptibility of PEO-coated WE43 in inorganic fluid [50]. It was shown that maximal pitting depth does not change significantly between 1 and 3 weeks, but increases continuously for longer immersion times.

5.3.5 Chemical composition of corrosion products

To evaluate the differences in corrosion mechanisms between coated and uncoated WE43, the microchemical composition of the corrosion products are analysed by elemental mappings. The different grey shades of the corrosion products in the SEM BSE images indicate differences in chemical composition. This heterogeneity is confirmed by the elemental mappings of Mg, O, P, Ca, and C. The limitations of the EDS analysis must be taken into account, as light elements such as H cannot be detected.

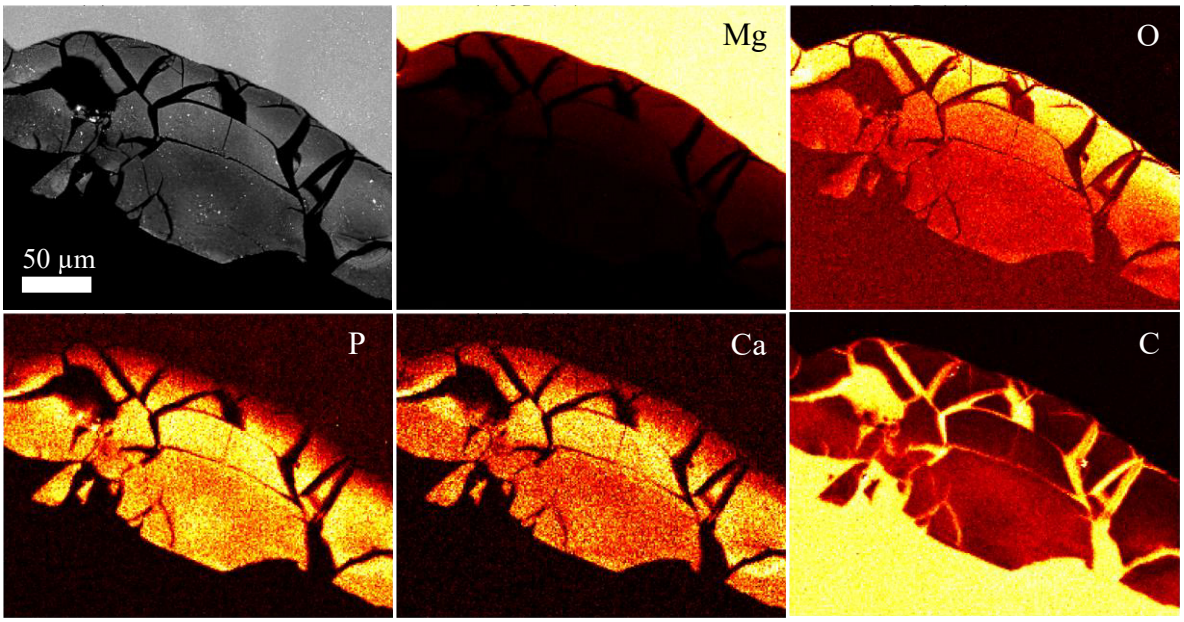

Figure 5.7.: Elemental mapping of the corrosion product and the alloy interface with analysis of the elements magnesium (Mg), oxygen (O), phosphorus (P), calcium (Ca) and carbon (C). The corresponding SEM BSE image is shown top left. High concentrations are shown in yellow, low concentrations in red and no detection is indicated by black colour [118].

Figure 5.7 shows that the corrosion product on the uncoated sample consists of three layers. As the metallic matrix is rich in very reactive magnesium, the inner layer appears to consist mainly of Mg-O. The intermediate layer is enriched with Ca and P, and the outer layer is additionally enriched with C. These three layers are observed in all uncoated specimens, regardless of the immersion periods. The three layers indicate that at the initial stage of the corrosion process, magnesium hydroxide and magnesium oxide is formed. This is followed by the penetration and chemical reaction of components of the corrosion fluid with the oxidised layer. The reactions of the corrosion product with the fluid in turn results in Ca- and P-enrichment. As the thickness of corrosion products increases, the inner layer of magnesium hydroxides dehydrates and magnesium oxide is formed. Finally, after sufficient exposure time, the outer layer is enriched with carbon. The carbon can be either in the form of carbonates or organic compounds. Organic compounds such as glucose are constituents in DMEM high-glucose fluid. The corrosion progress appears to be controlled to a certain extent by the cracking of the corrosion products. The cracks inside the corrosion products of the uncorroded specimens form a

network throughout the entire thickness. This means that the supply of DMEM fluid is controlled by capillary forces. These conditions limit the supply of oxygen and other components to the alloy surface, resulting in a relatively slow corrosion progress. Ca is in the Ca^{2+} form, P is in the PO_4^{3+} form, while C is in the HCO_3^- form. Calcium ions have no influence on the corrosion of magnesium. However, calcium phosphates can form on the magnesium surface in DMEM and thus inhibiting corrosion [57]. This finding is also interesting for biocompatibility, since calcium phosphate improves osseointegration [141]. The complexity of DMEM is clearly responsible for inhibition of the corrosion process compared to simpler inorganic solutions such as NaCl or SBF. Organic compounds have been found to contribute to an inorganic-organic hybrid corrosion product that provides superior corrosion protection to the underlying metallic substrate in comparison with purely inorganic corrosion product [26]. The phenol red in the DMEM is a sensitive colour indicator in the physiological pH range. It is added to enable optical control of the pH value during corrosion to ensure physiological conditions. The experiments are controlled at pH values between 7.3 and 7.7. In the case of magnesium hydroxide dissolution, the pH value would rise. This would be an indicator of severe corrosion of the alloy. If the pH value drops, bacterial growth will be observed and contaminated samples have been excluded from validation. The stable pH values during the tests are consistent with the mild corrosion observed. The Pourbaix diagrams for magnesium state that at pH values above about 8.5 and up to 11.5, a protective oxide or hydroxide layer forms, which slows down the dissolution of magnesium in aqueous solutions [133]. This means that there is a local pH increase taking place at the first Mg-O layer, allowing the formation of $Mg(OH)_2$, as observed by Kalb [81]. In addition, PO_4^{3+} and Ca_{2+} ions nucleate on the alloy surface at high pH levels and grow with time. Phosphates with Mg/Ca accumulate on the corrosion layer. The precipitation of the insoluble phosphates can be described as [193]:

$$H_nPO_4^{(3-n)+} + Mg^{2+} + Ca^{2+} + OH^- \longrightarrow Mg_xCa_y(PO_4^{3+})_z \tag{5.3}$$

The complicated Mg/Ca phosphates and MgO are referred to as the Mg-O-Ca-P layer. Compared to the three-layered time-independent corrosion product of the uncoated specimens, the corrosion product of the coated samples is more time sensitive. After 7 days, a change in the morphology of the PEO coating and a change in the chemical composition can be observed. These changes become more pronounced as the corrosion continues. Initially, the PEO is rich in phosphorus and oxygen with a fair amount of magnesium. After 7 days, a distinct Mg-O-rich layer of about 2.6μm thickness can be identified underneath the calcium and phosphorus-rich outer layer. The outer layer is heterogeneous as it consists of a thick, non-porous Mg-O-Ca-P corrosion product and a Ca-enriched porous layer of the PEO coating. The outer layer also shows cracks, while the small pores typical of the PEO coating are missing. The degradation and chemical conversion of the coating was approximated by a three-step process by [192]. In the first step, the fluid penetrates the porous PEO coating and the chloride ions in aqueous solution destroy the different layers of the coating. After longer corrosion times, the inner Mg-O-rich layer significantly thickens (approx. 32μm after 28 days), as marked in the elemental mapping in Figure 5.8. This indicates that the conditions for Mg

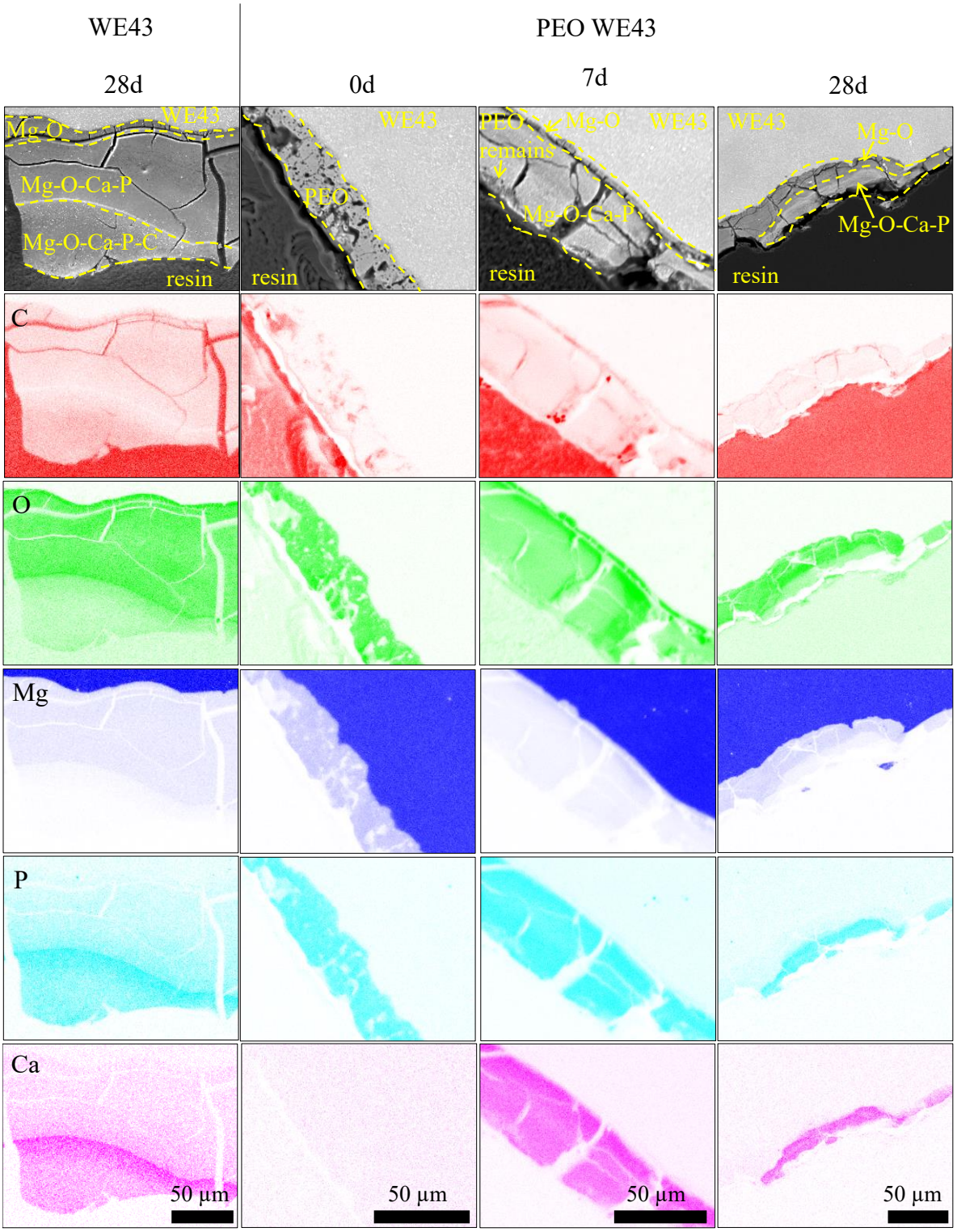

Figure 5.8.: Elemental mappings of corrosion products and the alloy interface, analysing the elements carbon (C), oxygen (O), magnesium (Mg), phosphorus (P) and calcium (Ca) on an uncoated WE43 alloy after 28 days immersion, on coated specimens after 7 and 28 days immersion and of the uncorroded PEO coating/alloy interface [120].

dissolution are different, as the local pH values are significantly higher and thus stabilise the magnesium hydroxide passive layer [133]. This experimental finding correlates with the second step of the proposed PEO degradation mechanism, which states that a Mg-O-rich layer forms with increasing corrosion and alkalinity. The Mg-O-rich layer provides efficient corrosion protection for the alloy, which can reasonably explain the continuous slow corrosion process. However, it should be noted that these local pH changes are difficult to measure with the colour indicator in the corrosion medium. The physiological regime requires a relatively stable pH value in the range of 7.2 to 7.6. For the corrosion media with Tris and HEPES buffering systems, the local pH at the electrolyte/substrate interface can rise into the alkaline range [90, 111], whereas the bicarbonate buffer of the DMEM has a better functionality at the interface [111]. The third step of the PEO degradation describes the attack of the chloride ions, which convert the $Mg(OH)_2$ into soluble $MgCl_2$. In contrast to the uncoated samples, the corrosion layer of the PEO-coated specimens does not contain a carbon-rich layer. This interesting phenomenon is attributed to fact that the PEO coating prevents carbon-rich molecules from reacting with the Mg-O-Ca-P corrosion layer. In conjunction with the XRD results shown in Figure 5.3, it is shown that most of the corrosion products covering the surface have amorphous structures. This has also been confirmed by other researchers [7].

5.3.6 Gas measurement and corrosion rate

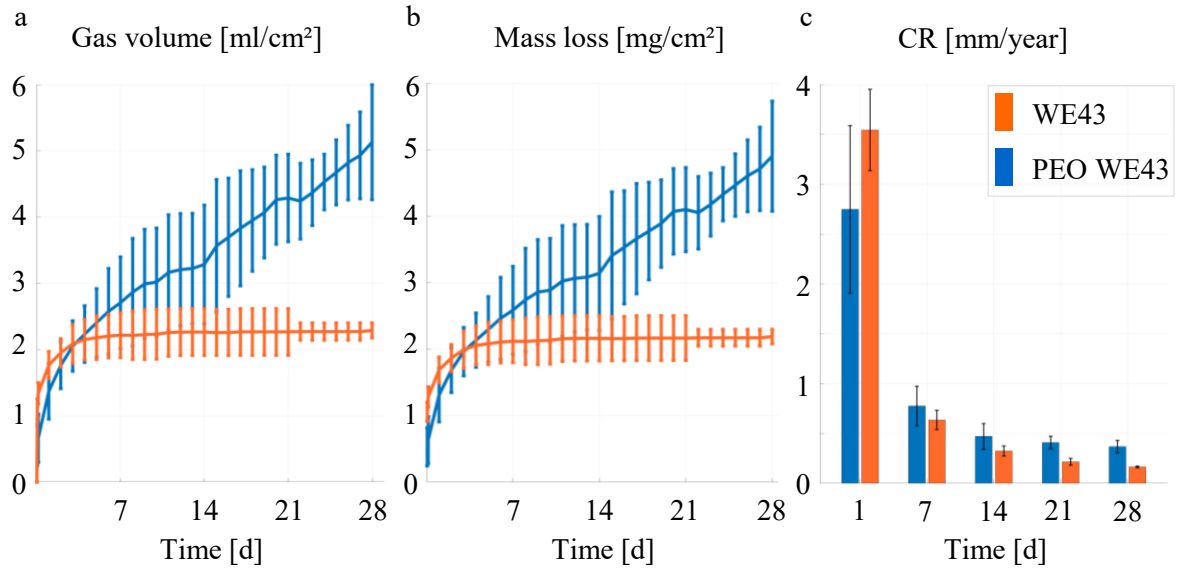

Figure 5.9.: Gas measurement results: (a) hydrogen gas volume per surface area, (b) mass loss per surface area and (c) corrosion rate. Results of non-coated specimens in blue and of coated specimens in red [120].

The hydrogen gas measurements show different corrosion behaviour of the uncoated and coated WE43 alloy, as shown in Figure 5.9. The uncoated sample group shows a rapid and continuous increase in gas evolution in the initial experimental stage. After about four days, the gas measurements show a linear evolution process, indicating a

continuous dissolution of the magnesium matrix. The time-dependent characteristic of the corrosion rate of the uncoated WE43 is consistent with corrosion results on different WE43 alloys in inorganic SBF, which all show an initial high corrosion rate followed by a constant corrosion rate reached after about 5 to 7 days [21, 161]. Nonetheless, the quantitative results on the corrosion rate of WE43 in DMEM or SBF vary with values of 3.5mm/year and 15.12mm/year, respectively, as they also depend on processing and microstructural parameters of the alloy [21, 161]. It should be noted that the resulting corrosion rates might be underestimated as the corrosion fluid is not pre-saturated with hydrogen. In contrast, the PEO-coated specimens show a continuous increase in gas evolution only in the initial experimental stage. This might be caused by measuring errors that only relate to the initial phase. After four days, the measured gas volume does not significantly change any more. As a consequence, the corrosion rate decreases with increasing immersion time, which implies a very slow dissolution of the magnesium matrix. After four weeks, the total hydrogen evolution has decreased by 55% due to PEO coating. A significant reduction of the hydrogen evolution was also observed by Daavari et al. [32], who found that the PEO coating reduced the hydrogen generation of an AZ31 alloy in SBF by 74% after 15 days, resulting in a matching total hydrogen release of about 2ml/cm^2. The SEM BSE images of the PEO-coated cross-sections in Figure 5.5 confirm that the corrosion progresses significantly slower compared to the uncoated specimens. However, the image of the 7-day corroded coated specimen shows only slight corrosion along the circumference. This is not consistent with the stronger hydrogen evolution measured in the first few days. The PEO-coated WE43 specimen proved to be highly resistant to corrosion and showed very little hydrogen evolution in the immersion experiments. Therefore, this method may not be suitable for quantifying the corrosion rate of the coated WE43 specimen. Yet, it is a suitable qualitative measure for comparing the corrosion of the coated and non-coated alloy [87].

5.3.7 Degradation of tensile strength

Figure 5.10a shows the stress-strain characteristics of tensile tested specimens. The alloy possesses a comparatively high tensile strength with excellent ductility. The tensile strength of the uncorroded WE43 alloy is 305.6MPa and that of the PEO-coated WE43 alloy 293.8MPa. The differences of 3.8% can be attributed to statistical characteristics of the material property and the surface changes during the coating process. The changes in tensile strength as a function of the immersion time are presented in Figure 5.10b. The tensile strength is evaluated according to the standard procedure described in section 3.7, and the tensile stress is calculated in relation to the initial sample diameter before corrosion. In the non-coated specimen group, the tensile strength decreases with increasing immersion time and the results are in line with previous findings on mass loss and cross-sectional analysis. The loss in tensile strength is the largest in the first 7 days of corrosion. This corresponds to the largest mass loss, which has also been observed during the first 7 days. Additionally, the 10.6% decrease in the tensile strength corresponds to the 10.5% decrease in the sample's cross-sectional area. The mechanical strength has decreased to a significantly smaller extent than reported in

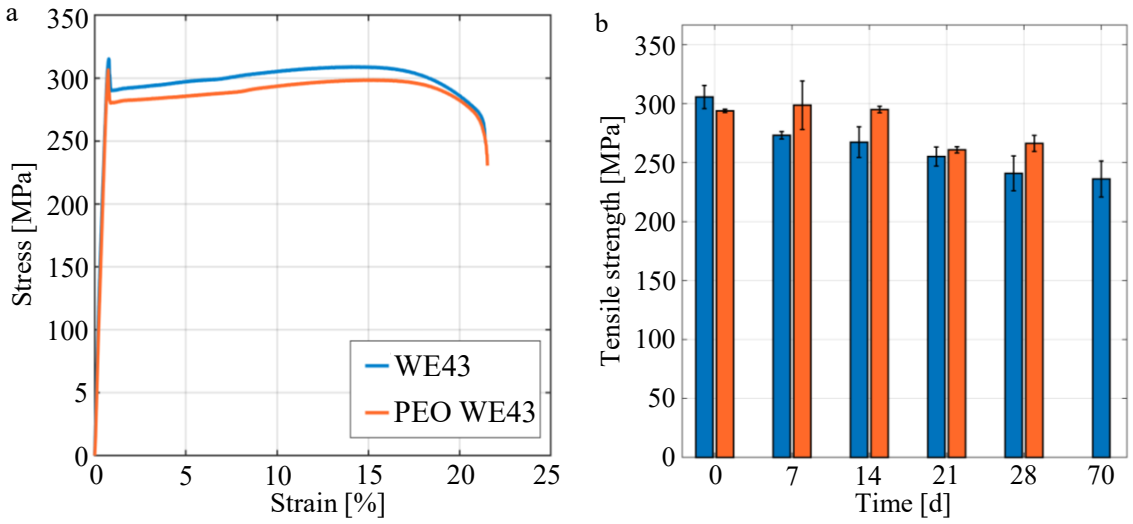

Figure 5.10.: Tensile test results: (a) Stress-strain characteristic of non-coated and PEO-coated WE43 specimens, (b) tensile strength after various corrosion periods. Results of non-coated specimens in blue and of coated specimens in red, adapted from [120].

in vitro experiments on WE43 in SBF, where a decrease in tensile strength of cuboids with a cross-sectional area to perimeter ratio of 1:2.6 was observed by 46 and 80%, respectively [21]. The ratio of cross-section to volume is 1:1 for specimens used in experiments. When comparing quantified changes in material strength, the variations between the sample geometries must always be considered. Specimen with a smaller surface area to volume ratio retain their mechanical properties better as they expose less surface area to corrosion. Between 7 and 28 days, a linear decrease in the tensile strength and in the mass loss is observed. The degradation of mechanical strength coincides with the changes in the cross-section: the tensile strength has decreased by 12.5% after 14 days, by 16.5% after 21 days, and by 21.2% after 28 days. The degradation after 28 days is comparable to experimental results on the degradation of WE43 in SBF, where a reduction in the yield strength by 15% was quantified in three-point bending tests with a specimen with surface area to cross-section ratio of 1:1.7 [71]. The tensile strength in the PEO-coated specimen group does not significantly change during the first 14 days. The mechanical strength of the alloy is preserved by the coating. After immersion periods exceeding 14 days, a decrease in the mechanical strength of about 10% can be quantified. The results show that the PEO coating delays the degradation of the mechanical strength for the initial period of 14 days and also significantly decelerates material degradation for longer immersion periods. Furthermore, the loss of mechanical strength is found to be similar in the coated test group after 21 and 28 days. These results indicate that the PEO coating has an ongoing protective effect to the underlying alloy and provides some protection even for extended immersion times. A significantly smaller decrease was assessed for the coated WE43 alloy in SBF after 4 weeks with a minor reduction of 2.5% in the yield strength [71]. The yield strength of the specimens has decreased similarly. Changes in the yield strength and elongation-to-failure are included in appendix D, as well as SEM images of the fracture surfaces.

5.3.8 Degradation of PEO coating

PEO coating plays an important role in decelerating the corrosion process. Therefore, understanding the degradation behaviour of coated magnesium alloys is crucial for orthopaedic implant design. Arrabal et al. [6] stated that the PEO coating on WE43 failed after only a short immersion time. They assumed that all benefits were lost once a new corrosion layer had formed underneath the coating. In this study, it is found that an additional corrosion layer underneath the calcium-enriched PEO coating provides a persistent corrosion protection of coated specimens, as it is shown in the SEM BSE image of the 28-day PEO-coated specimen. To understand the corrosion mechanism of micro-arc oxidation treated AZ31 in SBF, Li et al. [95] suggest that the Mg(OH) layer dissolves with increasing immersion time through the attack of Cl^- ions and $MgCl_2$ is formed as a less stable and more soluble compound. On the other hand, the corrosion resistance is increased by the formation of a thin layer rich in calcium and phosphorus, which prevents the dissolution of magnesium chlorides. In the elemental mappings, a thicker calcium and phosphorus rich layer is detected in the coated specimen group after 28 days of corrosion. Additionally, a thickening of the Mg-O-layer is observed with increasing time, see Figure 5.8. Both experimental observations confirm the continuous corrosion resistance of the PEO-coated specimen group compared to the non-coated WE43 alloy. With regard to the surface morphology of the PEO coating, it can be observed that cracks or through-pores in the ceramic coating facilitate fluid access to the substrate and localised corrosion attack is expected [22]. Moreover, the results indicate that the amorphous layer of the corrosion products contain significant phosphate related composition, as the XRD does not show any significant peaks for the phosphate related crystalline structure.

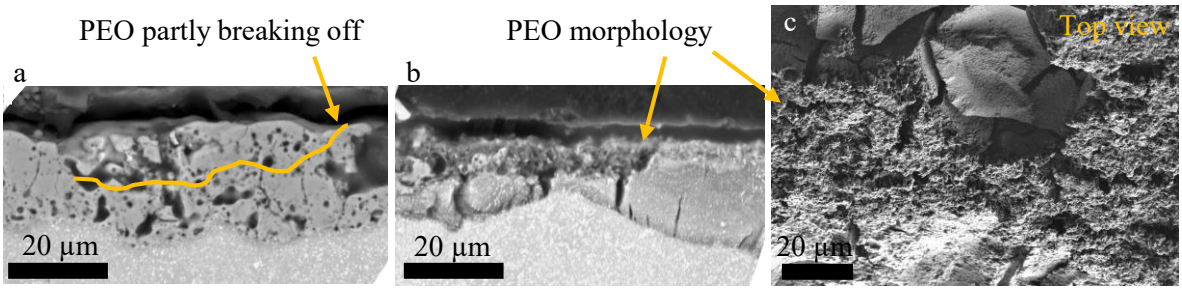

Figure 5.11.: Morphological changes of PEO coating: (a) SEM BSE images of the uncorroded coating-alloy interface, (c) SEM BSE image of the coating-alloy interface after 7 days in DMEM, (c) surface of the coated specimen after 7 days in DMEM [120].

The different corrosion mechanism of coated WE43, as described previously, significantly reduces the degradation of the WE43 alloy components. Moreover, the PEO coating reacts with the corrosion medium DMEM by incorporating calcium, which results in chemical and morphological changes of the corrosion layer towards a non-porous nature. The SEM images show that only a top layer of the PEO coating partially breaks off from the surface. A similar observation was made by Lin et al. [96], with parts of the coating breaking off from the underlying substrate during the PEO degradation

process. Based on the observation in the microscopic analysis, this can be attributed to the interconnection of pores in the PEO layer, as shown in Figure 4.4 in chapter 4. When the pores fill with fluid that reacts chemically with the coating, pressure is built up that can lead to cracks within the coating, facilitating the partial detachment of the coating. The surface analysis (see top view) shows regions of a PEO morphology and regions covered by the new outer corrosion layer. Furthermore, the residual PEO coating cannot be chemically differentiated from the new corrosion layer, but only by microstructural analysis, as shown in Figure 5.8 in the 7-day PEO-coated mapping.

5.4 Results beyond the scope - PEO degradation

Immersion tests are also carried out with PEO-coated specimens over the longest period of 10 weeks. They are not included in the evaluation as manufacturing parameters are not consistent. The SEM BSE image of the specimen's cross-section is presented in Figure 5.12 and shows an almost ideal round shape with insignificant corrosion attack. An excellent retention of mechanical strength is measured in the tensile tests, with an average tensile strength of 284.5MPa, which corresponds to a reduction of 3.2% compared to the uncorroded initial state. The low standard deviation of the test group of 3.2MPa additionally implies that all four specimens of the sample group behave similarly.

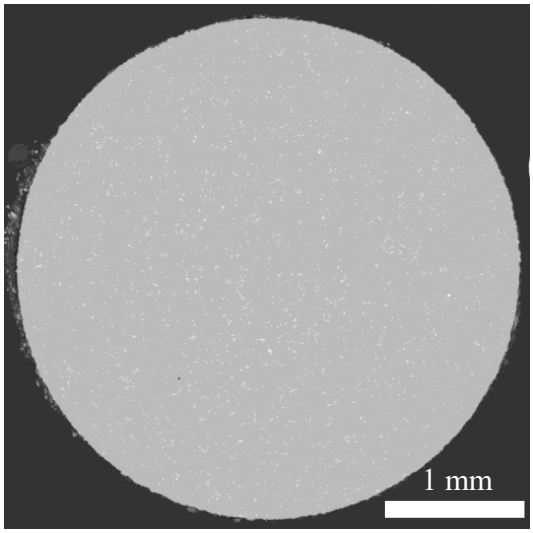

Figure 5.12.: SEM BSE images of the cross-section of a PEO-coated specimen after 70 days in DMEM.

Differences in the surface finish of the bare WE43 specimens prior to the coating process could cause this disparity between the sample groups. The average roughness Ra measures 257.9nm for the 10-week PEO-coated specimen group, which is lower than 439.4nm in other samples. The same applies for the mean peak-to-valley roughness Rz of 1.4804μm compared to 2.1189μm in the other specimen groups. The correlation between substrate surface finish and PEO coating result was first investigated in 2017 on a titanium alloy [199]. It was found that the coating showed better corrosion resistance

on an initially smoother substrate. These results emphasise the need for more systematic studies on the influence of the surface properties of magnesium alloys on the corrosion protection of PEO coatings.

5.5 Conclusions

Long-term corrosion experiments are performed on tensile test specimens in a physiological corrosion environment to study the influence of a PEO coating on the degradation behaviour of WE43 magnesium alloy. The corrosion rates are determined by using the hydrogen evolution method. To characterise the corrosion behaviour and to clarify the underlying corrosion mechanisms, SEM images of cross-sections are used to analyse the alloy's susceptibility to pitting or localised corrosion, and EDS and XRD are utilised to identify the composition of the corrosion product layers. In addition, the degradation of mechanical properties is evaluated in tensile tests. Finally, the long-term protective effect of PEO coating on the mechanical integrity is linked to the degradation process of the coating. The findings show that the holistic approach of applying analytical and mechanical methods is indispensable for studying the degradation behaviour of materials for load-bearing applications, as is the case in orthopaedic implants. The long-term behaviour cannot be predicted or extrapolated from short-term corrosion studies. The results provide valuable information for a better understanding of the in vitro degradation process in PEO-coated magnesium alloys.

Based on the experimental investigations and analysis, the following conclusions can be drawn:

1. The WE43 alloy in DMEM corrodes in an inhomogeneous manner with no severe susceptibility to pitting corrosion. This can be explained by the very fine and homogeneously distributed intermetallic precipitates of Mg-Y-Nd.
2. Mild microgalvanic corrosion occurs between the α-Mg matrix and the Mg-Y-Nd intermetallic precipitates, with the magnesium matrix being preferentially dissolved. More pronounced localised corrosion is only present at Fe-rich impurities that form cathodic sites.
3. The corrosion of the WE43 alloy progresses fastest within the first 7 days. Localised corrosion with some less corroded ridges is observed. Between 7 and 28 days, the corrosion progresses steadily, which is also confirmed by a linear hydrogen evolution. In this stage, the less corroded ridges are preferentially attacked and the smallest uncorroded diameter is not significantly reduced.
4. A three-layered, time-independent corrosion layer is identified in the uncoated specimens: an inner layer of Mg-O, an intermediate layer of Mg-O-Ca-P, and an outer layer of Mg-O-Ca-P-C. Microcracks in the corrosion layer enable liquid medium to penetrate to the alloy.
5. The coating significantly affects the corrosion mechanism.
6. A significantly slower corrosion rate is observed for the PEO-coated specimens by the gas measurements. A steady gas level indicates efficient corrosion protection of the PEO coating under in vitro conditions.

7. SEM and EDS analysis reveal significant differences in the morphology and chemical composition of the corrosion products between non-coated and PEO-coated alloy. In the PEO-coated specimens, a thicker Mg-O-rich layer grows from 2.6μm after 7 days to 32μm after 28 days, leading to the persistent corrosion resistance of the coated specimens.
8. Moreover, the protective effect of the PEO coating is also attributed to the relatively thick outer layer, which is rich in calcium and phosphorus, and is found after 28 days in the coated specimen group. In contrast to the corrosion layer of the non-coated specimen, carbon-enriched areas are not present. It is indicated that the PEO coating prevents the incorporation of carbon.
9. Tensile tests show that the tensile strength of the coated specimens does not decrease significantly during the first 14 days and is also preserved for longer periods, as it decreases by 10% after 28 days. On the contrary, the material strength of the uncoated specimen group decreases the most within the first 7 days (by 11%) and continuously decreases by 21% after 28 days.
10. It is indicated that the corrosion resistance of the PEO coating can be improved by optimising the surface roughness of the magnesium substrate.

6

Stress corrosion cracking

The simultaneous exposure of magnesium alloys to mechanical stresses and an aggressive corrosion environment leads to complex mechano-chemical interactions, which accelerate material degradation and trigger environmentally-induced cracking. The expedited deterioration of mechanical integrity can lead to premature failure, which is a catastrophic scenario during therapy. Consequently, implant materials must demonstrate a certain degree of resistance to stress corrosion cracking (SCC) for their safe use within the human body. The systematic investigation of stress corrosion cracking has increasingly gained attention in biodegradable magnesium research, yet the underlying mechanisms remain incompletely understood and there is a strong need for comprehensive studies focusing on medical-grade magnesium alloys in appropriate in vitro conditions. The susceptibility of magnesium alloys towards SCC is characterised by its alloying elements, its microstructure and the applied fluid system. Consequently, it is inevitable to systematically assess the SCC susceptibility of a prospective implant material, which will be addressed in this chapter.

This chapter is based on an in vitro study, which was published in [122]. Within the scope of the study, the stress corrosion susceptibility of the WE alloy is systematically investigated using an organic physiological corrosion environment. Additionally, the influence of the biocompatible PEO coating to the SCC resistance is assessed and underlying failure mechanisms are examined fractographically. For this purpose, the biodegradable material is subjected to static and quasi-static loading in the fluid. Constant load tests (CLT) are conducted at three different stress levels and slow strain rate tests (SSRT) at three different rates. After CLT tests, specimens are tensile tested to quantify material degradation. To reveal the SCC mechanism under different loading configurations, fracture surfaces are analysed by scanning electron microscopy.

6.1 Progress on stress corrosion cracking of biodegradable magnesium alloys

Exposure to mechanical loading inside an aggressive corrosion environment can lead to drastic loss of mechanical integrity due to stress corrosion cracking (SCC) as described in section 2.4.1. Failure is attributed to slow and sub-critical crack growth, which is accompanied by a significant loss of ductility and often remains unnoticed [135, 169]. In general, the susceptibility of magnesium alloys to SCC is related to the general

corrosion resistance, the susceptibility to pitting corrosion, hydrogen embrittlement or anodic dissolution. Furthermore, SCC susceptibility strongly depends on the corrosion environment. High chloride concentrations can dissolve the passive film. This can lead to a more pronounced pitting corrosion and facilitates hydrogen absorption by the metal, leading to hydrogen embrittlement [72]. Moreover, corrosion pits are identified as the main precursor of SCC initiation as they cause local stress concentrations [60, 75]. Therefore, the alloy's pit corrosion resistance plays an important role in the susceptibility to SCC [30].

Recently, considerable research efforts have been devoted to linking the microstructure of magnesium alloys to the SCC behaviour. It is reported that aligned secondary phases serve as preferential crack propagation paths and thereby increase the SCC susceptibility of an Mg–Mn alloy [134]. Alloys with very or ultrafine grain ($\sim$1–2μm) exhibit excellent mechanical properties and corrosion resistance [11, 62, 72]. Grain refinement ($\sim$3–8μm) has been shown to increase the SCC resistance of ME21 and AZ31B alloy [77, 193]. The improvement is attributed to the higher proportion of grain boundaries after refinement, which results in improved protection of the oxide film and high-density crystal defects that promote the passivation process. Furthermore, it has been reported that a wider nanocrystalline layer in a compressive stress state in the near-surface region achieved by cryogenic cooling can significantly improve the SCC resistance of an AZ31 alloy in SBF [131].

In addition to microstructural modification and optimisation, surface coatings are another powerful approach to tailor the corrosion behaviour of magnesium alloys. Nonetheless, the efficiency of the surface coatings to improve SCC resistance under mechano-chemical loadings is still an unresolved issue, as the brittle nature of such coatings can also negatively affect the mechanical integrity of the alloy-coating system. Due to its low fracture toughness, cracks easily initiate in coatings and propagate into the substrate, inducing local stress concentrations and facilitating the initiation of SCC in alloy substrates. In-situ SSRT experiments in air have revealed that cracks initiate at thickened coating sites of the coating-substrate interface and subsequently propagate into the metallic substrate [200]. It was shown that thicker coatings facilitate crack initiation. Cracking of the PEO coating instead of corrosion pits was observed as the driving factor for SCC in slow strain rate tests (SSRT) of magnesium alloy AM50 in an unphysiological fluid [148]. The latest progress has been made in developing self-healing coatings to mend defects that occur due to the brittle nature of the coating. An LSP/MAO composite coating was found to significantly improve the SCC performance of AZ80 alloy in SBF, which was attributed to the coating's self-healing mechanism to form a dense passive film at emerging damaged spots between LSP and MAO layers during SSRT [184]. It is generally accepted that the innermost dense barrier layer determines the coating's efficiency to corrosion resistance. However, the correlation between these critical coating features and the SCC resistance has not been assessed quantitatively.

To characterise the SCC behaviour of magnesium alloy-coating system, the choice of an adequate corrosion fluid plays a critical role in in vitro experiments as described in section 2.3.7. However, using complex solutions involves certain limitations due to the fluid's

vulnerability to microbial development and the high requirements of sterile experimental conditions. As a result, numerous studies of SCC experiments were performed in inorganic chloride solutions without accounting for the effects of organic compounds [134]. The risk of contamination by using organic fluids was emphasised by Chen et al. [26]. They assessed the influence of organic fluid compounds on the SCC susceptibility of an Mg–1Zn alloy in non-sterile conditions. It was confirmed that the inorganic-organic hybrid corrosion product film defers the crack initiation and increases the SCC resistance. Moreover, the protein bovine serum albumin (BSA) was found to temporarily protect the aluminium-containing magnesium alloy AZ91D in a physiological solution, since initial surface adsorption of the protein leads to the chelation of the protein with the corrosion product [60]. Therefore, it is crucial to investigate the SCC behaviour of magnesium alloy-coating systems in physiological organic solutions for a reliable design of biodegradable magnesium implants. Addressing the related critical issues in the application of complex organic fluids, the newly developed experimental setup is utilised for applying external loading while ensuring a sterile corrosion environment.

6.2 Materials and methods

Slow strain rate and constant load tests are performed with uncoated WE43 specimens and PEO-coated WE43 specimens.

Constant load tests (CLT) are performed as described in section 3.9 at three different stress levels that are held constant for periods of either 1 or 3 days. The test period of 1 day is chosen as a result of the long-term corrosion experiments, which are presented in chapter 5. Those experiments have revealed the highest corrosion rate of the WE43 alloy to occur within the initial 24 hours. The longer 3-day period is chosen for comparison with experimental studies of biodegradable magnesium in [27, 161]. Stress levels of 40, 60, and 80% of the material's initial tensile strength are applied. The target force is determined based on the initial specimen diameter, meaning that the engineering stress is used as a reference. Specimens that have not failed during CLT are tensile tested according to section 3.7 to evaluate changes in mechanical integrity. Fracture surfaces of failed specimens are fractographically analysed using SEM and SEM BSE images as described in section 3.12.1. Tests are performed with triplicates to account for statistical differences.

Slow strain rate corrosion tests are performed as described in section 3.9 with three different strain rates. The highest actuator speed of 5.2μm/min corresponds to a strain rate of $1.1\times10^{-6}s^{-1}$ in the elastic regime and is referred to as v1. Additional tests are performed with slower speeds, in particular one-third and one-fifth of v1: 1.733μm/min (referred to as v2) and 1.04μm/min (referred to as v3), respectively. Specimens are continuously strained to failure with the total tensile force on the specimens measured. As no extensometer is attached to the specimen's gauge length in corrosion conditions, the strain in SSRT tests are calculated from the calibrated relation between the measured tensile strain and displacement in air. After failure, specimens are washed according to section 3.9 and finally, fracture surfaces are analysed as described in 3.12.1. Tests are performed with triplicates to account for statistical differences. After testing, specimens

are rinsed with distilled water and ethanol. For evaluating the SCC resistance of the alloy systems in SSRT tests, the SCC susceptibility indices I_{UTS} and I_ε are calculated for the tensile strength UTS and the elongation-to-failure ε_f with respect to the WE43 specimens in pristine conditions:

$$I_{UTS} = (UTS_{air} - UTS_{fluid})/UTS_{air} \times 100\% \ , \tag{6.1}$$

$$I_\varepsilon = (\varepsilon_{f-air} - \varepsilon_{f-fluid})/\varepsilon_{f-air} \times 100\% \ , \tag{6.2}$$

with the ultimate tensile strength measured in air UTS_{air} or in fluid UTS_{fluid}, and the elongation-to-failure measured in air ε_{f-air} or in fluid $\varepsilon_{f-fluid}$.

6.3 Results and discussions

6.3.1 Constant load testing

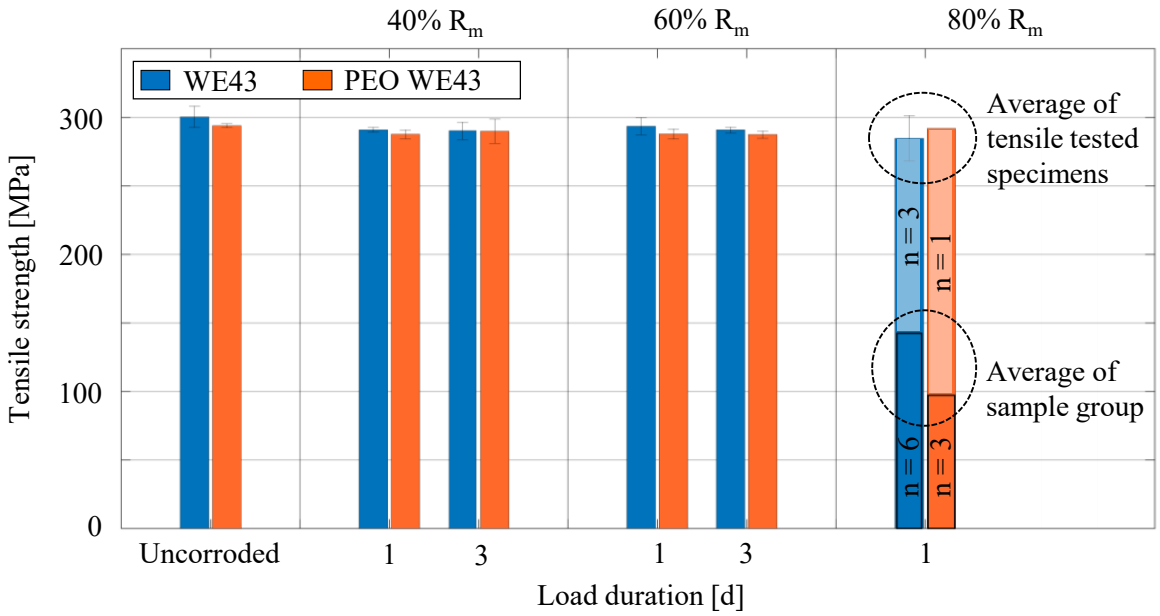

Figure 6.1.: Residual tensile strength of specimens after constant loading tests with varying stress levels for 1 and 3 days. Results of non-coated specimens in blue and of coated specimens in red, adapted from [122].

Figure 6.1 shows the residual tensile strength determined by tensile tests after corrosion in DMEM for one or three days with three different stress levels: 40%, 60% and 80% of the material's initial tensile strength R_m. The material shows an excellent combination of high tensile strength and ductility in the extruded WE43 alloy with fine grain sizes. The alloy's tensile strength of about 300MPa is quite high in comparison with other comparable WE43 alloys tested in [30, 161]. The initial tensile strength of the PEO-coated alloy is marginally lower (approx. 2%), which can be attributed to either the

small reduction in the diameter of substrate material due to the coating process or the brittle coating facilitating the formation of crack initiation sites. The SCC experiment results under constant loadings reveal a critical stress level of 0.8Rm, leading to a high probability of specimen failure during the first 24h in both uncoated and coated specimen groups. In both specimen groups, two out of three specimens failed. In experiments with stress levels below the critical value of 0.8Rm, the residual tensile strength only decreases slightly independent of the stress level and loading duration. The reduction measured for the uncoated specimens is between 2.1 and 3.4%, whereas the reduction of the coated specimen groups is slightly smaller, accounting for values between 1.4 and 2.2%. Interestingly, the residual tensile strength of the specimens that did not fail in the CLT tests with the critical stress level of 0.8Rm is comparable to the residual strength of the specimens after CLT tests with lower stress levels. A comparable minor decrease in the ultimate strength of about 3% after 3 days in CLT conditions in SBF was also observed by Wang et al. [161]. In their experiments, specimens were exposed to significantly smaller stress levels of up to 38% of the initial material strength, and a minor decrease in material strength was reported independently of the stress level. A magnesium alloy ZK40–0.4Sr tested in m-SBF with a stress level of 0.08Rm for 3 days showed a decrease in strength of about 5%, while the tensile strength of the PEO-coated magnesium alloy did not change [27].

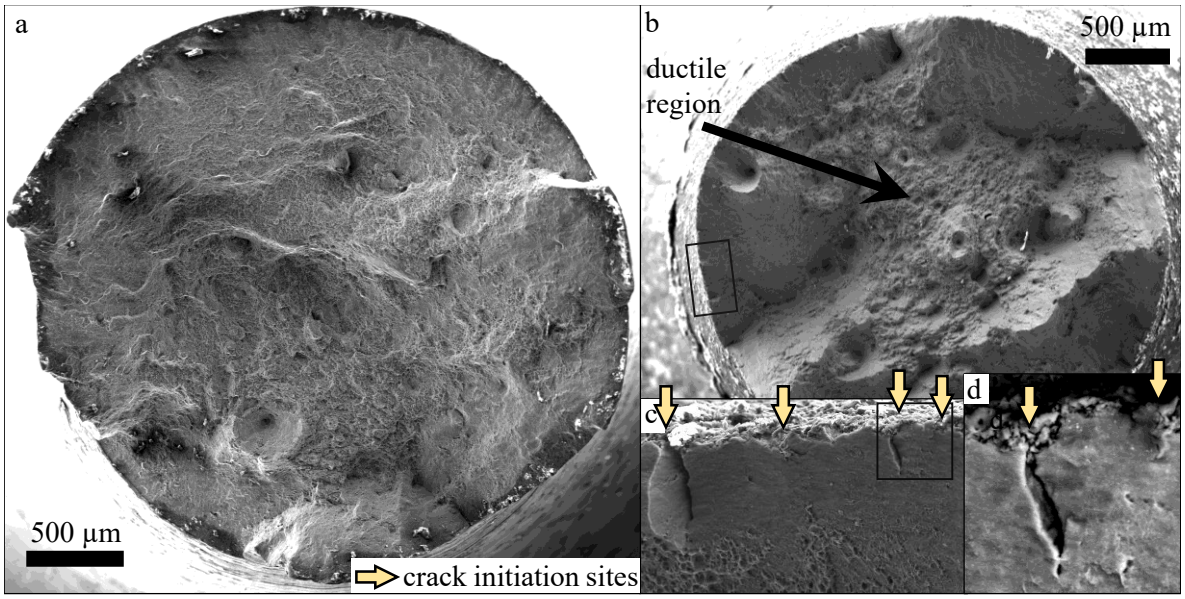

Figure 6.2.: SEM images of the fracture surfaces of specimens tested in air: (a) ductile fracture features of uncoated specimen, (b) a combination of ductile and brittle fracture features of a coated specimen, (c) crack initiation inside the coating in region c, (d) Higher magnification of a crack initiation side propagating from the coating into the substrate material, adapted from [122].

The fracture of the uncoated alloy is of ductile nature, as shown in Figure 6.2a. In contrast, Figure 6.2b shows the coated fracture surface with smooth and brittle fracture regions close to the circumference and ductile regions in the centre. The SEM fracture surface of the coated specimen indicates crack initiation sites inside the brittle coating. Figure 6.2c and Figure 6.2d reveal a large number of secondary cracks that propagate

into the substrate material. This observation confirms the feature of crack initiation of PEO-coated alloys in air reported in [200]. The initiation site has been linked to the irregular interface between coating and alloy substrate and preferentially occurs at thicker coating spots [93]. The brittle nature of the coating changes the overall fracture morphology.

The fracture surface of an uncoated specimen that has failed after 7h loaded with the largest stress level of 0.8Rm is shown in Figure 6.3. Crack growth mechanisms of stress-assisted cracking are clearly identified in the fracture surface. After crack initiation, the crack slowly progresses and allows fluid to access the crack surfaces, which in turn leads to additional material degradation caused by corrosion and hydrogen-assisted mechanisms [73]. It can be seen that the synergy between corrosion and crack propagation leads to a distinct circumferential region of stress corrosion cracking in the fracture surfaces (marked area A), which has been well reported for aluminium-free magnesium alloys [26, 28, 73]. For uncoated magnesium alloys, the size of this area has been related to the alloy's SCC resistance. A thicker area indicates better SCC resistance as the material has been longer exposed to the external load inside the corrosion environment [62, 73]. The fracture surface of a coated specimen failing after 9.7h in the test with a stress level of 0.8Rm is shown in Figure 6.4. Compared with the uncoated specimen, the area of stress corrosion cracking (area A) is smaller, implying that the coated specimen is more susceptible to SCC. Nevertheless, the residual yield strength after CLT tests (see Figure 6.1) shows no differences in SCC susceptibility between coated and non-coated specimens. It is indicated that the coating not only changes the SCC failure mechanism of the alloys, but also changes the crack growth rate in different SCC stages. Furthermore, both fracture surfaces show brittle fracture patterns adjacent to the region of stress corrosion cracking and the SEM images reveal oxidation inside this region as shown in Figure 6.3b and Figure 6.4b.

As illustrated in Figure 6.5, the precursor event of SCC is the development of corrosion pits that locally increase the stress concentration at an early experimental stage. In contrast, the PEO coating protects the underlying substrate from corrosion attack at this stage. Van Gaalen et al. [50] reported that the PEO coating on WE43 alloy not only significantly delays the corrosion at the initial stage of immersion tests, but also leads to a much more homogeneous corrosion front with significantly less deep pits. Therefore, instead of corrosion pits, the crack initiation inside the brittle coating is the precursor event of PEO-coated WE43, which is only initiated at a critical stress level and delayed in comparison with the uncoated alloy. In the second stage, the crack will propagate into the substrate material as well as towards the outside [200]. Consequently, the crack will enable the permeation of the surrounding fluid to the substrate material at an increased stress level, which leads to a faster crack growth compared to that in uncoated WE43. Concluding, the PEO coating provides protection against SCC in its undamaged state, while the degradation of mechanical integrity of the brittle coating triggers deteriorative effects on the substrate magnesium alloy and accelerates crack growth.

In this context, the experimental results of the residual strength after CLT tests reveal that the critical stress level of 0.8 Rm dramatically accelerates the coupled corrosion

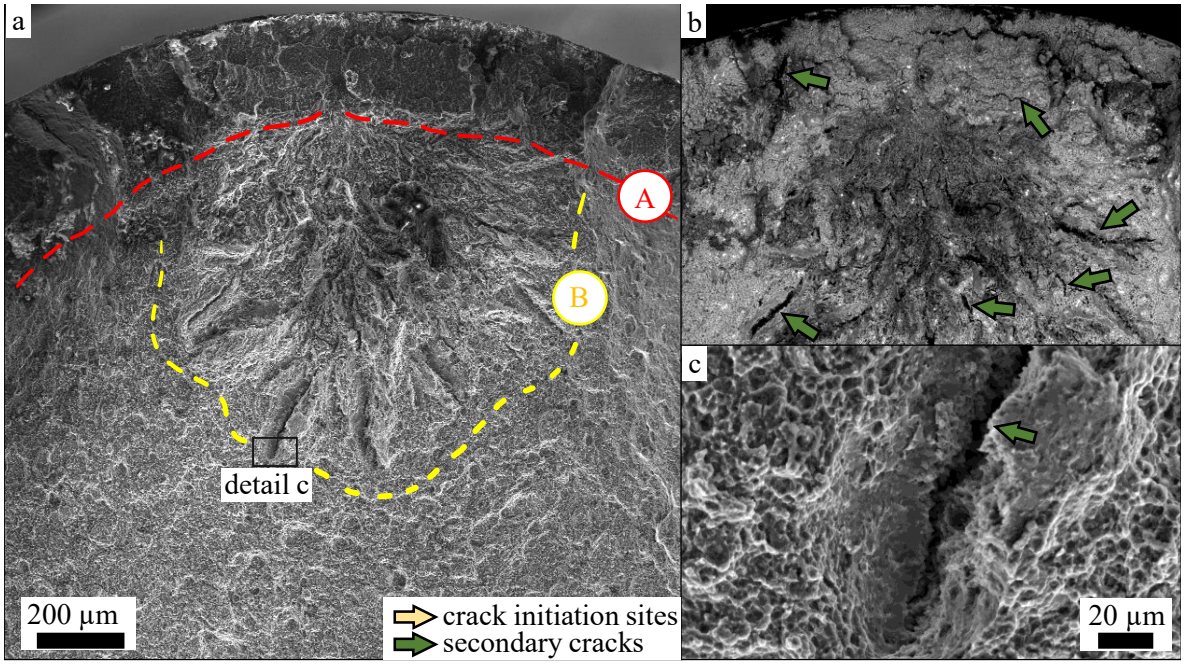

Figure 6.3.: SEM image of the fractured uncoated WE43 alloy in the 0.8Rm CLT test: (a) stress corrosion cracking in area A and brittle fracture features in area B with steep ridges, (b) SEM BSE image revealing oxidations and secondary cracks in areas A and B, (c) detail of secondary cracks in the brittle fracture zone, adapted from [122].

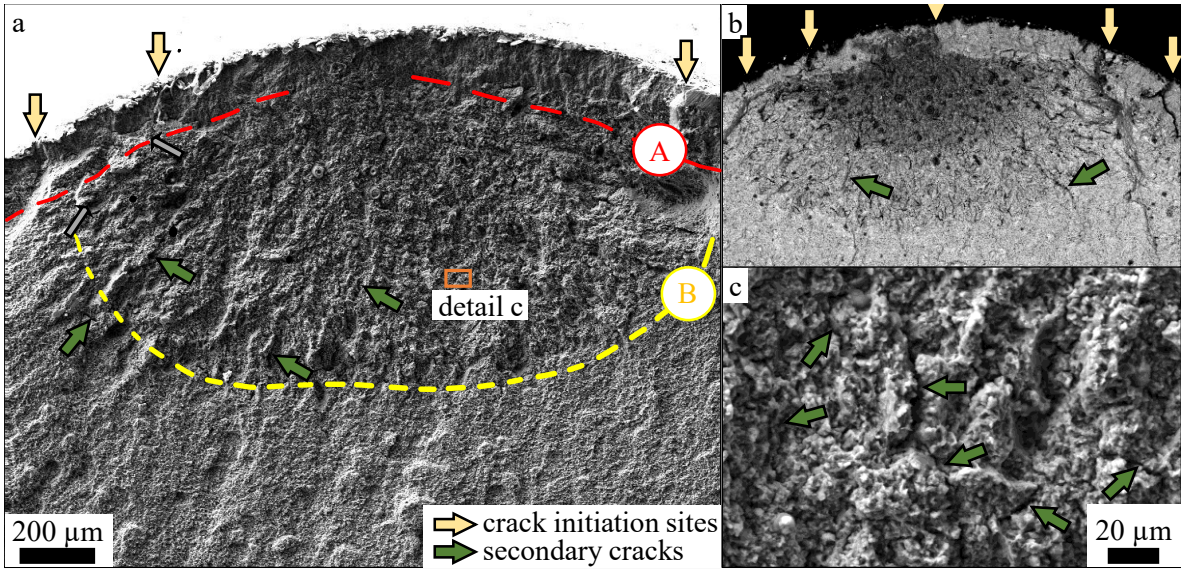

Figure 6.4.: SEM image of the fractured coated WE43 specimen in the 0.8Rm CLT test: (a) stress corrosion cracking inside a smaller area A and brittle fracture features in area B with a smooth appearance, (b) SEM BSE image revealing oxidations and secondary cracks, (c) detail showing a larger number of smaller secondary cracks, adapted from [122].

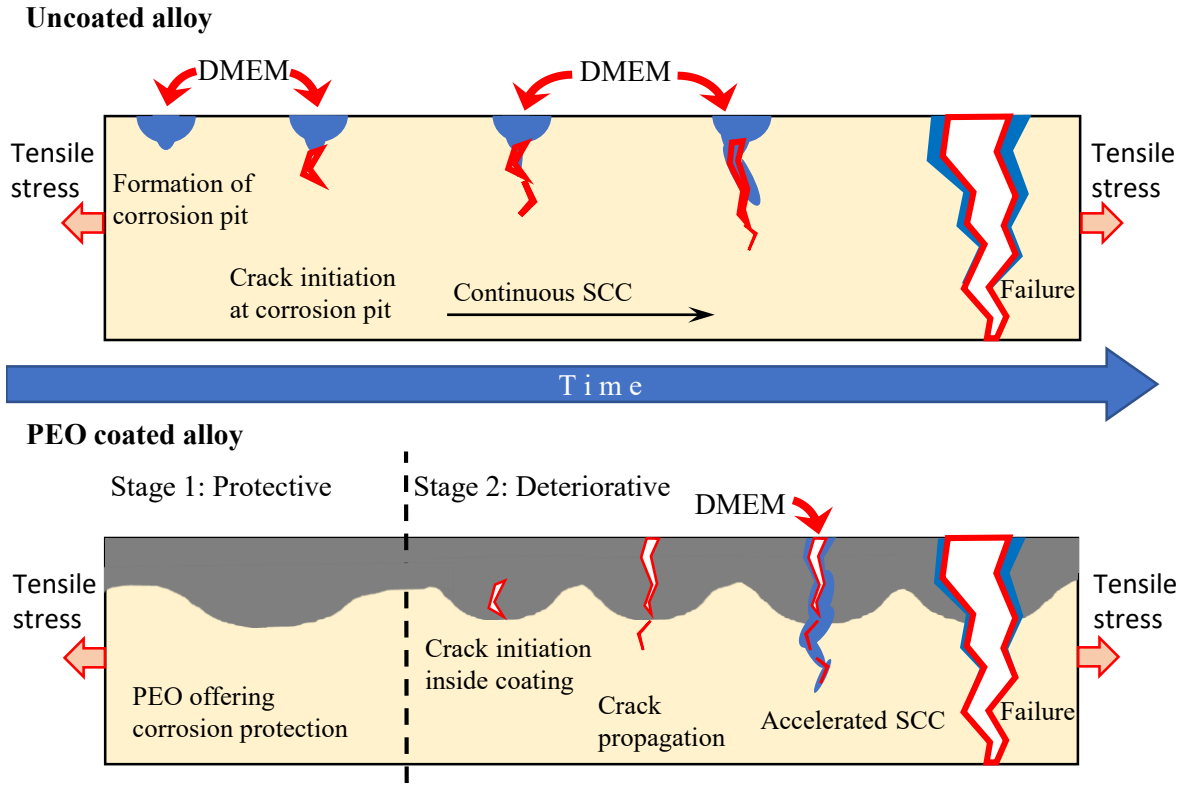

Figure 6.5.: Schematic of different SCC mechanisms between uncoated and PEO-coated magnesium alloys. Corrosion pits lead to SCC initiation in uncoated specimens at an early experimental stage, while crack formation inside brittle coating is the precursor event for SCC in PEO-coated WE43. In the second stage, the crack will enable the permeation of the surrounding fluid to the substrate material under high stresses, which results in a faster crack growth compared to that in uncoated WE43, adapted from [122].

and fracture process in both specimen groups. Moreover, the protective effects of the coating at the early stage of SCC are eliminated by the degradation of the mechanical integrity of the brittle coating under the applied CLT conditions.

Adjacent to area A, which encircles the specimens' circumferences, an oxidised region can be identified by its darker appearance in the SEM BSE images (Figure 6.3b and Figure 6.4b). In both specimens, a significant number of secondary cracks are visible inside areas A and B. Moreover, area B shows V-shaped ridges or chevron markings, which is typical for brittle fractures and implies that the fracture mechanism changes between areas A and B. Following stress corrosion cracking in the circumferential region, a brittle fracture is initiated. In magnesium alloys, the appearance of such brittle fracture morphology in a stress corrosion environment is often associated with hydrogen embrittlement. One underlying mechanism is hydrogen ingress in the region around the crack tip, leading to increased hydrogen concentration in this area, which in turn results in embrittlement and facilitates crack propagation throughout this embrittled area. Furthermore, the source of hydrogen is of importance for hydrogen-assisted failures. In this context, the coating process increases the atomic hydrogen concentration of the underlying substrate material. Therefore, hydrogen-assisted mechanisms are favoured as

critical hydrogen concentrations for crack propagation are reached after shorter times. The initially higher hydrogen concentration of the PEO-coated specimens explains the smoother appearance of fan-shaped ridges as the crack follows an easy path.

The side view of the failed specimens is shown in Figure 6.6. In the uncoated specimen, a large number of secondary cracks is present that are perpendicular to the loading direction, which is a common feature of SCC. In the coated specimen, coating damage is shown by way of aligned microcracks and corrosion products formed on the surface of the coating.

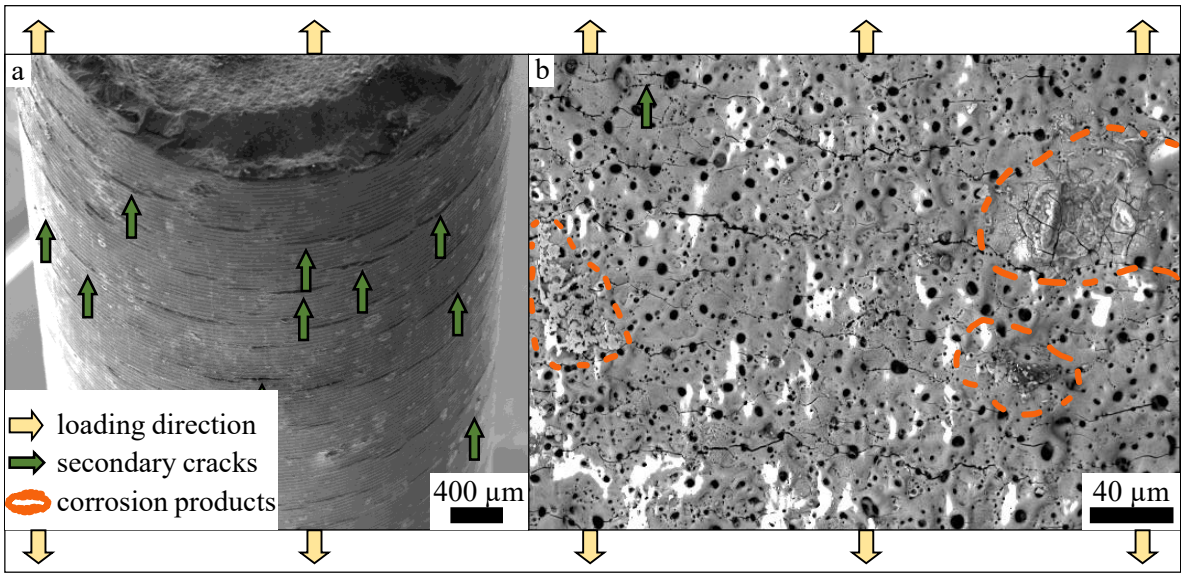

Figure 6.6.: SEM images of a side-view of failed specimens in the 0.8 Rm CLT loading case: (a) overview of uncoated specimen failing after 7h showing aligned secondary cracks, (b) the coating surface with aligned secondary microcracks and corrosion products of the coated specimen failed after 9.7h, adapted from [122].

In general, the fracture surfaces of both specimen groups support the phenomenological description of CLT fractures suggested by Raja et al. [134], i.e., a precursor event occurs, the crack initiates and then grows. The crack growth is driven by a hydrogen-assisted mechanism and proceeds slowly in the initial stage. With increasing crack size, the local stress concentrations become sufficiently high, leading to faster crack propagation until ultimately resulting in overloading.

6.3.2 Slow strain rate testing

Figure 6.7a presents typical stress-strain curves of non-coated and PEO-coated WE43 alloy in the SSRT experiments in DMEM medium with three different strain rates (v1, v2, v3). The curves show that the failures occurred in the plastic deformation stage. The elongation-to-failure significantly decreases in DMEM which indicates that the non-coated and coated WE43 alloy suffered significant embrittlement in DMEM. For quantifying the SCC susceptibility of the two tested groups, the resulting sensitivity values of the tensile strength I_{UTS} and the elongation-to-failure I_{ε} are presented in Figure 6.7. The SCC susceptibility index expresses the percentage loss of the property

in reference to the non-coated alloy tested in air, with higher values indicating higher SCC susceptibility.

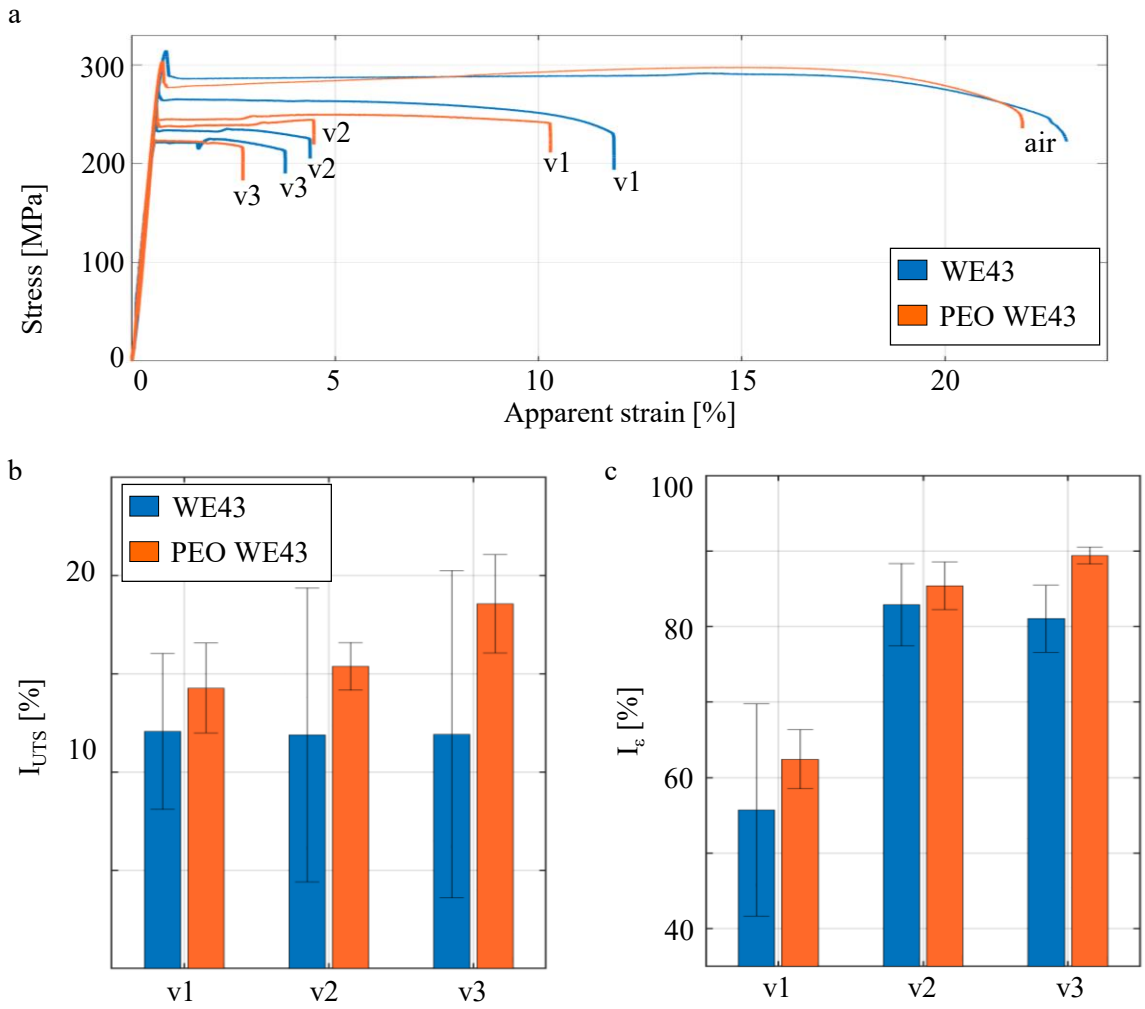

Figure 6.7.: Typical stress-strain curves of non-coated (blue) and PEO-coated (red) WE43 alloy in the SSRT in DMEM medium with three different strain rates (a), and summary of SSRT susceptibility indices of tensile strength I_{UTS} (b) and elongation-to-failure I_ε (c), adapted from [122].

The uncoated WE43 alloy reveals an almost strain-rate independent decrease of 12% in the ultimate tensile strength. In comparison with the results of other magnesium alloys in aggressive environments in Table 6.1, this I_{UTS} value indicates high SCC resistance of the WE43 alloy. In contrast, the elongation-to-failure is significantly decreased by the corrosive environment. I_ϵ is 56% in the case of the strain rate v1 and takes the value of about 82% for v2 and v3, indicating the effect of the decrease in strain rate on more pronounced material embrittlement. The coated specimen group shows similar results, but slightly higher values. However, only the coated specimens show a strain-rate dependent decrease in the material strength, especially in the case of the smallest strain rate v3. The slower strain rate allows more corrosion time for a higher degree of material embrittlement and therefore leads to a smaller elongation-to-failure.

Alloy	Fluid	Strain Rate	I_{UTS}	I_ϵ	Grain size [μm]	Ref.
WE43	DMEM	1.1×10^{-6}	12	56	2.7	
WE43	DMEM	3.6×10^{-7}	12	83	2.7	
WE43	DMEM	2.2×10^{-7}	12	81	2.7	
WE43 + PEO	DMEM	1.1×10^{-6}	14	62	2.7	
WE43 + PEO	DMEM	3.6×10^{-7}	15	85	2.7	
WE43 + PEO	DMEM	2.2×10^{-7}	19	89	2.7	
AZ61	ASTM D1348	1×10^{-6}	33	81	40	[149]
AZ61 + PEO	ASTM D1348	1×10^{-6}	23.4	76	40	[149]
WE43	DMEM	1×10^{-6}	20	32	13	[161]
Mg-Zn-Zr	3.5wt.% NaCl	1×10^{-6}	-	98	5	[162]
ZX50	m-SBF	3.1×10^{-7}	27	82	4	[30]
WZ21	m-SBF	3.1×10^{-7}	31	73	7	[30]
WE43	m-SBF	3.1×10^{-7}	20	53	15	[30]
AZ91D	m-SBF	5×10^{-7}	25	37	-	[29]
Mg3Zn1Ca	m-SBF	5×10^{-7}	42	45	-	[29]
AZ31	Hank's solution	1×10^{-7}	33	82	-	[102]
AZ31 + LSP$*$	Hank's solution	1×10^{-7}	32	80	-	[102]
AZ31 + PC$**$	Hank's solution	1×10^{-7}	33	81	-	[102]
AZ31 + LSP$*$/PC$**$	Hank's solution	1×10^{-7}	29	76	-	[102]
AZ31	SBF	3.5×10^{-6}	9	75	24.1	[130]
AZ31 + CC$***$	SBF	3.5×10^{-6}	7	68	-	[130]
AZ31B	HBSS	1×10^{-4}	53	63	-	[159]
AZ31B + 6h aged	HBSS	1×10^{-4}	53	61	-	[159]

Table 6.1.: Comparison of SCC susceptibility factors for different magnesium alloys in different corrosive fluid [122]. $*$ LSP = laser shock peening, $**$ PC = phosphate conversion, $***$ CC = cryogenic cooling.

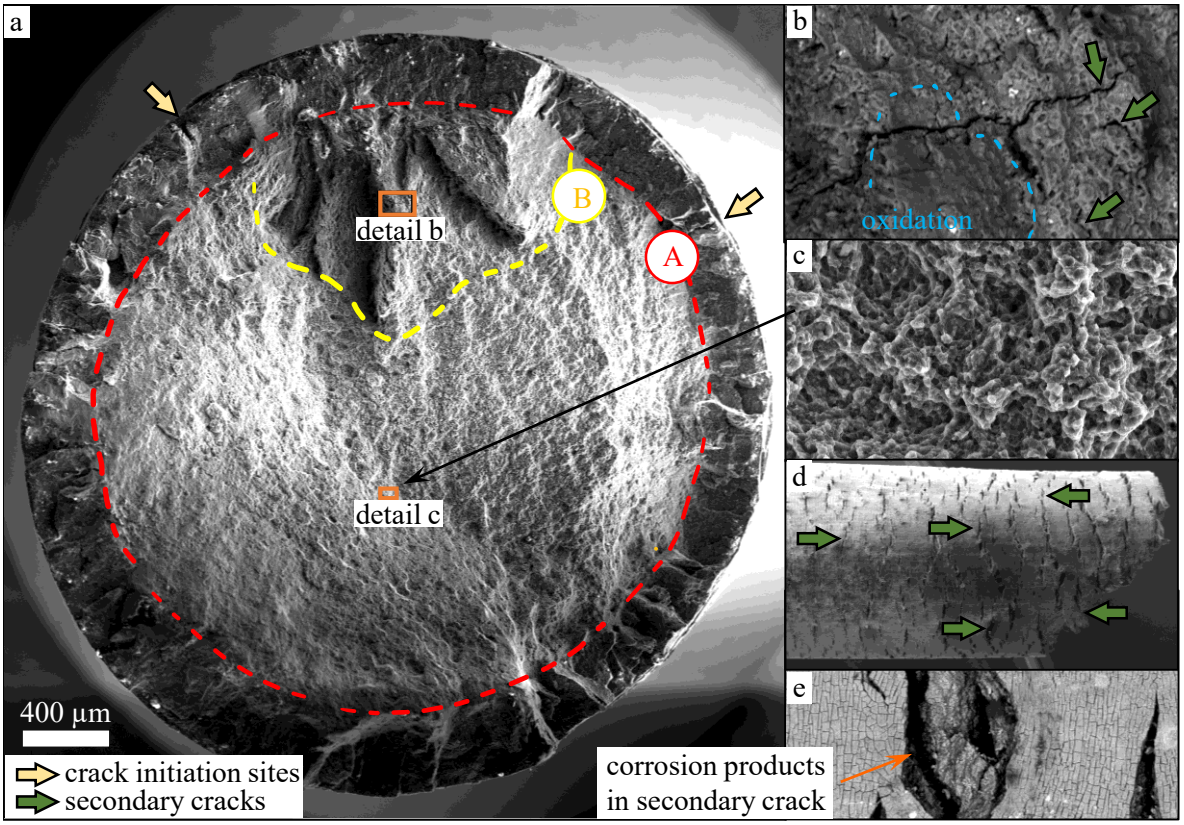

Figure 6.8.: SEM images of the uncoated specimen in SSRT with the strain rate v1: (a) the fracture surface reveals a thick and distinct area A of stress corrosion cracking and area B with steep ridges, (b) higher magnification of detail b inside the brittle region B shows secondary cracks and oxidised areas, (c) higher magnified detail c of overload failure region, (d) side view of fractured specimen shows a large number of aligned secondary cracks, (e) high magnification image reveals corrosion products inside the secondary crack, adapted from [122].

Uncoated (Figure 6.8) and coated (Figure 6.9) specimens tested at the fastest rate v1 show similar fracture characteristics observed in the failing specimens in CLT tests. The fracture surface of the uncoated specimen in Figure 6.8a reveals a distinct area of stress corrosion cracking along its circumference with a larger number of crack initiation sites that are again marked as region A. A side view of the specimen is presented in Figure 6.9d, showing that the surface is covered by corrosion products and contains a large number of cracks perpendicular to the loading axis. Figure 6.9e shows a typical crack in more detail, revealing corrosion products inside the crack, which clearly indicates stress corrosion cracking. Region A is adjacent to a region of steep radial fan-shaped ridges that are typical features for brittle fracture. A more detailed view of area B in Figure 6.9b shows the corrosion-assisted cracking accompanied by a network of secondary cracks and oxidation along primary cracks. A mixed mode of transgranular and intergranular cracking can be identified, which is consistent with the reported embrittlement behaviour of rare-earth alloys with similar grain sizes [30, 83, 162]. The intergranular cracking can also be attributed to the electrochemical dissolution of the precipitates at the grain boundaries, which has also been observed in other studies as

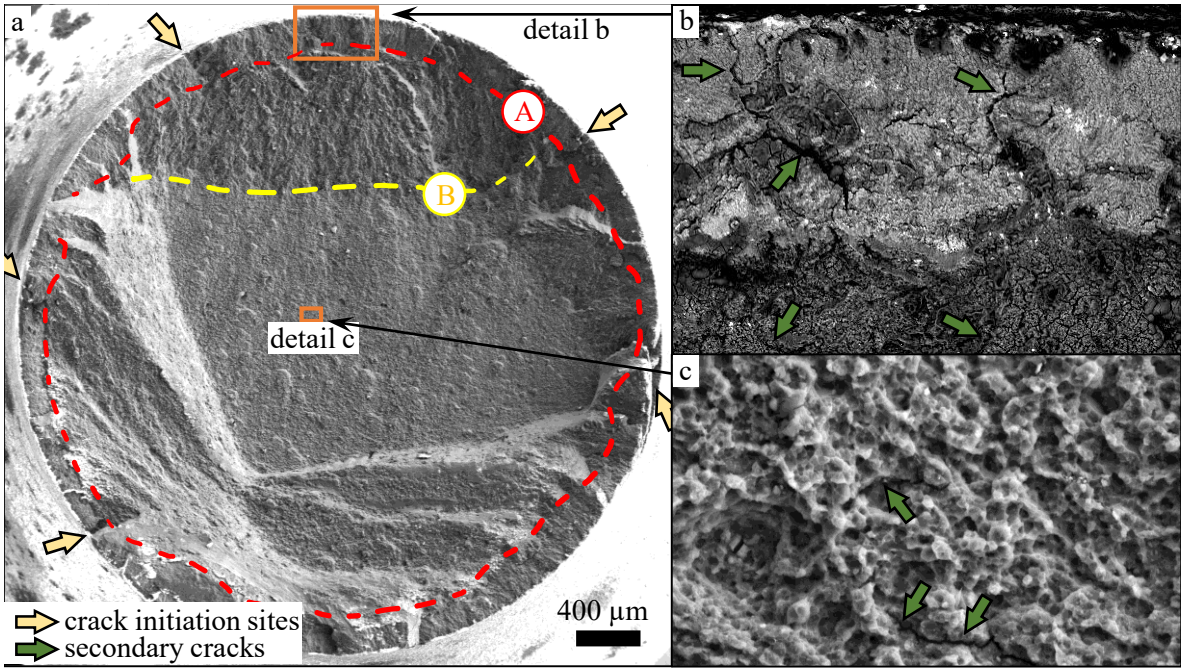

Figure 6.9.: SEM images of fracture surface of coated specimen in SSRT with the strain rate v1: (a) overall fracture surface reveals a thinner distinct area A of stress corrosion cracking and the brittle fracture area B with crack coalescence, (b) SEM BSE image at higher magnification of detail b showing secondary cracks and oxidised areas, (c) higher magnification of detail c of the overload failure region, adapted from [122].

hydrogen-assisted embrittlement [6, 30, 83]. Final failure results from overload, as shown in more detail in Figure 6.8c. Similar characteristics are also observed in the fracture surfaces of specimens tested at slower rates, that are shown in the appendix G in Figure G.1. During SSRT experiments, the exposure to high stress levels favours hydrogen-assisted mechanisms and thereby leads to brittle failure patterns. Furthermore, it is emphasised that the elongation-to-failure exceeds 10%, which is very high in comparison to other reported results [27, 41, 60, 77, 102, 130, 159, 162], although the sensitivity index of the elongation to failure reveals a detrimental effect of the fluid.

As shown in Figure 6.9a, the area of stress corrosion cracking appears smaller in the coated specimen, as already been observed in CLT fracture surfaces. Such differences related to the SSC resistance have already been reported for an AZ80 alloy SSRT tested in SBF of various pH values. A thicker region of stress corrosion cracking was attributed to a better SCC resistance as the specimen had a longer time for crack propagation [62]. Therefore, the thicker area A of the uncoated alloy implies that the uncoated alloy has a better SCC resistance, which is also confirmed by the susceptibility values. Similar to the CLT results, protective/deteriorative effects of the brittle coating on the SCC behaviour of the substrate alloys were observed under SSRT conditions. However, the sensitivity values imply that the protective effect of the coating is lost at a much earlier experimental stage and that its deteriorative impact is more dominant under SSRT conditions. This observation is also confirmed by the side view of the specimen in Figure 6.10a and b. It is seen that a large number of aligned secondary cracks penetrate deep into the substrate material. Compared to the coating damage observed in CLT tests

(Figure 6.6), the coating damage is much more severe in SSRT tests as deep secondary cracks and partial exfoliation can be identified on the coating surface. This extensive coating damage facilitates fluid permeation towards the underlying magnesium alloy and the initiation of SCC. Exfoliation of the coating is not observed in the specimens tested with the lowest strain rate, as shown in Figure 6.10c. It might be attributed to the smallest overall elongation-to-failure, which is not sufficiently large for exfoliation of the coating. Fractographical images of the fracture surfaces of coated specimens are presented in the appendix G in Figure G.3.

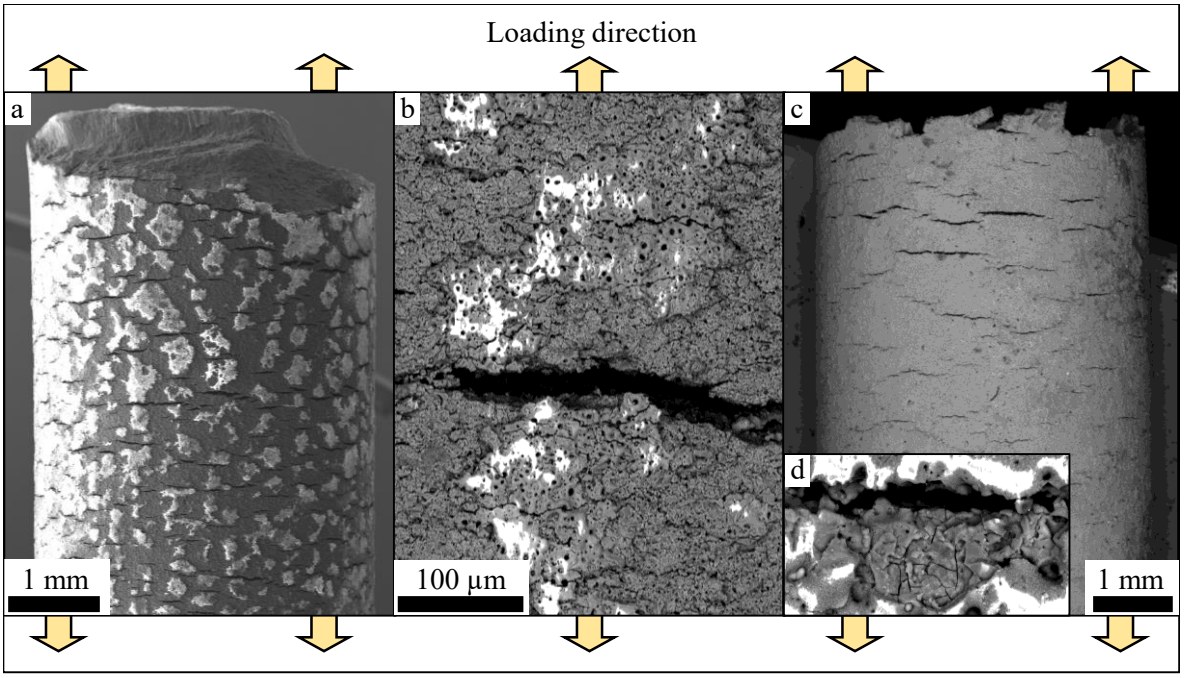

Figure 6.10.: SEM image of the side view of coated specimen in SSRT with the strain rate v1: (a) damaged coating shows large aligned secondary cracks that penetrate into the substrate material covered by coating residuals, (b) higher magnification of large secondary cracks in the coating, (c) side view of the coated specimen tested with v3 with large and deep aligned secondary cracks, (d) high magnification of secondary cracks shows corrosion products inside it, adapted from [122].

6.4 Conclusions

The present in vitro study investigates the effect of PEO coating on the stress corrosion cracking behaviour of an as-extruded rare-earth magnesium alloy WE43 under different loading conditions. To ensure the required sterile test conditions for applying physiological fluids with organic compounds, the new developed experimental setup is used. To quantify the influence of loading conditions on the SCC behaviour, constant loading tests and slow strain rate tests are performed under in vitro conditions. Moreover, the fracture surfaces of specimens are systematically analysed using scanning electron microscopy to clarify the SCC mechanisms. Based on the experimental results and discussions, the following conclusions can be drawn:

1. CLT tests reveal a critical stress level of 0.8Rm, leading to a significant probability of specimen failure in uncoated and coated specimens.
2. The residual mechanical strength of WE43 after CLT tests with stress levels below the critical value is insensitive to the applied stress level and loading duration ($\leq$3 days). The reduction of the tensile strength after 3 days loaded with 0.6 Rm is 3.1% and 2.2% for uncoated and PEO-coated WE43, respectively.
3. Fracture surfaces of uncoated and coated specimens that have failed in CLT tests reveal distinct patterns of stress corrosion cracking: (1) a circumferential area of stress corrosion cracking; (2) a brittle fracture area with an oxidised region; (3) and a region of final overload failure.
4. Fractographical analysis suggests that the coating protects the substrate material only at the initial stage of corrosion under low stresses. The transition from a protective to a detrimental stage is triggered by crack formation inside the brittle coating, which enables the permeation of the surrounding fluid to the substrate material and leads to faster crack growth than in uncoated WE43.
5. Compared to other magnesium alloys in aggressive environments, the uncoated and PEO-coated WE43 alloys show high SCC resistance in SSRT conditions. The resulting sensitivity factor I_{UTS} of the uncoated specimen is 12%, increasing to 19% in the coated specimens with decreasing strain rate.
6. Both specimen groups suffer strain-rate dependent embrittlement in DMEM in SSRT. The elongation-to-failure is reduced in the uncoated specimen group by 56% at $1.1 \times 10^{-6} s^{-1}$ and by 81% at $2.2 \times 10^{-7} s^{-1}$, and in the coated specimen group by 62% at $1.1 \times 10^{-6} s^{-1}$ and by 89% at $2.2 \times 10^{-7} s^{-1}$, respectively. In SSRT conditions, the deteriorative impact of the coating increases with decreasing strain rate, which results in a strain-rate dependent SCC susceptibility of the coated specimens.

7 Corrosion fatigue

This chapter addresses the detrimental impact of cyclical loadings in the physiological corrosion environment on the mechanical integrity of the medical-grade WE43 magnesium alloy. Understanding the adverse interaction of the mechano-chemical processes under dynamic loading conditions is indispensable for the successful development of biodegradable load-bearing implants that can demonstrate high performance. Although the complex mechano-chemical degradation during cyclical loadings is of great importance, the corrosion-fatigue (CF) behaviour of medical-grade magnesium alloys in physiological environments has not been deeply studied and understood so far. This particularly applies to organic corrosion environments and to rare-earth containing alloys. As this alloy group is considered highly promising for implant development, more systematic studies on magnesium alloys with rare-earth elements are required for facilitating magnesium implant development [30, 168, 172]. To this end, an in vitro study is conducted to systematically assess the CF behaviour of the rare earth-containing WE43 alloy in an organic corrosion environment.

In the experimental study, different boundary conditions are implemented for assessing the harmful effects of the corrosion environment. Specimens are loaded in the fluid, in air after pre-corrosion of either 1 or 3 days and under pristine conditions in air. Fracture surfaces are fractographically examined to understand the underlying failure mechanisms. In addition to the stress-controlled CF experiments, strain-controlled fatigue tests are carried out to assess the material properties of the WE43 alloy.

The experimental results presented in this chapter are published in [121] and provide a mechanistic understanding and supportive baseline data for implant development.

7.1 Progress on corrosion fatigue of biodegradable magnesium alloys

Recent studies indicate that the interaction between corrosion and fatigue in a physiological environment can significantly accelerate the damage evolution of magnesium alloys [125]. Chen et al. [23] reported that the elongation-to-failure and the fatigue life of the magnesium alloy AZ31B in SBF were significantly reduced in comparison with the results in air. It was concluded that the detrimental effect is attributed to the interaction between corrosion and ratcheting strain as well as the rupture of corrosion product layer in SBF with physiological pH values. Gu et al. [57] demonstrated that

both magnesium alloys WE43 and AZ91D have a much lower fatigue strength in SBF and exhibit higher corrosion rates under dynamic loading conditions. Furthermore, the CF behaviour of magnesium alloys is strongly affected by microstructural features. Wang et al. [163] characterised the influence of microstructural changes after solution treatments on CF of an Mg-Zn-Y-Zr alloy. It was shown that coarse and homogeneous grains in the solution treated alloy were prone to trigger twinning and localised corrosion at the twin boundaries, leading to an acceleration of CF failure. Moreover, the loading conditions play an important role in the CF interaction. In particular, low loading frequencies result in severe corrosion damage and a significant decrease in the fatigue strength [167]. Linderov et al. [100] concluded that low frequencies should be used in CF test to better understand the interactions of corrosion mechanism, stress corrosion mechanisms and CF mechanism.

In experimental studies on the corrosion performance of biodegradable magnesium alloys for medical applications, the impact of fluid constituents has been extensively investigated [79, 82, 109, 110, 158, 177, 178, 181, 189, 196]. Meng et al. [113] analysed the influence of the solution pH value on the CF performance of an AM60 alloy. It was shown that an instable protective layer in phosphate buffered saline solution with an acidic pH significantly increased the corrosion rate during CF experiments and reduced the fatigue life. Organic compounds, being important constituents of the human body, significantly affect the corrosion behaviour of magnesium alloys [61, 64, 70, 187]. The addition of proteins and amino acids leads to the formation of hybrid inorganic–organic corrosion products, which provide superior corrosion protection compared to purely inorganic corrosion products [111]. Therefore, it is suggested that they are added to the fluids for in vitro SCC or CF studies. However, few studies applied organic fluids in corrosion experiments with external loading, as they considerably increase experimental complexity. Chen et al. [26] identified the formation of a hybrid inorganic-organic corrosion product layer in in vitro corrosion experiments on magnesium alloys, which provides better protection against SCC compared to the purely inorganic corrosion layer in inorganic solutions. Harandi et al. [60] found that in CF experiments on magnesium alloys, the protein bovine serum albumin initially adsorb to the protective layer in CF experiments of magnesium alloys, thereby stabilising the protective layer and delaying the corrosion attack. These findings encourage the use of organic fluids in CF experiments for a better approximation of in vivo conditions. However, the high contamination risks and the commonly non-sterile experimental setups limit the broader use of organic fluids in SCC or CF experiments [26].

Recent studies assessing the effect of pre-corrosion have stated that the duration of pre-corrosion strongly affects the fatigue life [10]. Talesh et al. [152] identified a considerable reduction in the fatigue life of AM60 magnesium alloy after 28 days in SBF. They stated that the fatigue failure initiated at corrosion pits because of the locally increased stress concentration at pits. Zhao et al. [195] related the influence of pre-corrosion duration on the fatigue performance to the time-dependent growth of corrosion pits. Fu et al. [48] confirmed this observation. They furthermore observed higher initial ratcheting strains and higher steady ratcheting strain rates after pre-corrosion. Both values increased with increasing pre-exposure time.

7.2 Materials and methods

Fatigue experiments in air are performed on fatigue tests specimens (see section 3.10). To evaluate the effect of pre-corrosion damage on the fatigue behviour of the alloy, specimens are tested in pristine state and after pre-corrosion of varying periods of either 1 or 7 days. In addition, the interaction between the corrosion and fatigue processes is investigated by dynamically loaded specimen in the fluid. Therefore, the newly developed test setup is used (see section 2.5.6). Specimens are loaded stress-controlled with a stress ratio between maximum and minimum stress of $R = 0$ and with a frequency of 1Hz, which corresponds to the walking frequency of an adult. The stress amplitudes for the fatigue tests in air is selected to cover the fatigue data from the low cycle fatigue to high cycle fatigue regimes. 650ml DMEM are used in corrosion fatigue experiments supplemented with antibiotics as described in section 3.4. For pre-corrosion, specimens are immersed in 500ml DMEM supplemented with antibiotics for the corresponding period, as described in section 3.4. The stress amplitudes in the corrosion-fatigue tests for assessing the influence of the corrosion environment on the fatigue behaviour are selected to compare with the fatigeu performance in air under similar stress levels. After fatigue failure, fracture surfaces are fractographically analysed with scanning electron microscopy in accordance with section D.1.1.

The relationship between the applied stress amplitude σ_A and the fatigue life above the fatigue limit is correlated using the Basquin equation [12]:

$$\sigma_A = AN_f^b \ , \tag{7.1}$$

with the coefficient A, the cycles to failure N_f and the exponential factor b.

The detrimental effect of the corrosion environment on the fatigue strength can be evaluated by the reduction ratio of fatigue strength RRFS, which offers a measure for the reduction in fatigue strength at same lifetimes. In order to compare tests of varying frequencies, the reduction is calculated with respect to 2 hours cyclical loading in the corrosion environment [14]:

$$RRFS = \Big(\sigma_{air} - \sigma_{fluid}\Big)/\sigma_{air} \ , \tag{7.2}$$

with the stress amplitude σ_{air} in air and the stress amplitude in fluid σ_{fluid} after 2 hours dynamic loading.

Strain-controlled fatigue tests are performed in air on fatigue test specimens (see section 3.2) as described in section 3.10. Load was applied fully-reversed, which corresponds to a stress ratio of -1.

The total strain amplitude ε_a can be decomposed into an elastic ε_a^e and a plastic ε_a^p part. The plastic part can then be described as a function of the stress σ, the strengthening coefficient K' and the cyclic hardening coefficient n', leading to the Ramberg-Osgood equation, which describes the correlation between stress and strain in cyclic loading conditions [112]:

$$\varepsilon_a = \varepsilon_a^e + \varepsilon_a^p = \frac{\sigma}{E} + \left(\frac{\sigma}{K'}\right)^{1/n'} , \tag{7.3}$$

with the elastic modulus E.

For predicting the fatigue life as a function of the strain amplitude ε_a, the Manson-Coffin equation can be correlated to the ε-N curve [106]:

$$\varepsilon_a = \varepsilon_a^e + \varepsilon_a^p = \frac{\sigma_f^{'}}{E}\left(2N_f\right)^b + \varepsilon_f^{'}\left(2N_f\right)^c , \tag{7.4}$$

with the fatigue strength coefficient $\sigma_f^{'}$, the elastic modulus E, the cycles to failure N_f, the fatigue strength exponent b, the fatigue ductility coefficient $\varepsilon_f^{'}$ and the fatigue ductility exponent c.

7.3 Results and discussions

7.3.1 Strain-controlled fatigue experiments

Figure 7.1a shows stabilised stress-strain hysteresis of strain-controlled fatigue tests at different strain amplitudes between 0.6% and 1.4%. The cyclic stress–strain curve is fitted by the Ramberg-Osgood equation (see section 7.2). The comparison between cyclic and monotonic stress-strain curves indicates a cyclic softening behaviour of the material.

The ε-N curve in Figure 7.1b demonstrates a comparable fatigue performance to that of a rolled WE43 alloy in the low cycle fatigue regime described by Ghorbanpour et al. [54]. Both WE43 alloys exhibit moderate cyclic softening under cyclic loading. The ε-N curve was additionally supplemented with the data of an extruded WE43 alloy in the high cycle fatigue regime from [57], and the entire data set correlated using the Manson-Coffin equation for predicting the fatigue life (see section 7.2). The resulting fit is included in the ε-N curve. An overview of the material parameter in dynamic test conditions is given in Table 7.1.

Ramberg-Osgood		Manson-Coffin	
Cyclic strengthening coefficient K′	252.15MP	Fatigue strength coefficient $\sigma_f^{'}$	42.92MPa
		Fatigue strength exponent b	0.0574
Cyclic hardening exponent n′	0.0253	Fatigue ductility coefficient $\varepsilon_f^{'}$	9.094×10^{-2}
		Fatigue strength ductility c	-0.352

Table 7.1.: Overview of dynamic material parameters of WE43 alloy [121].

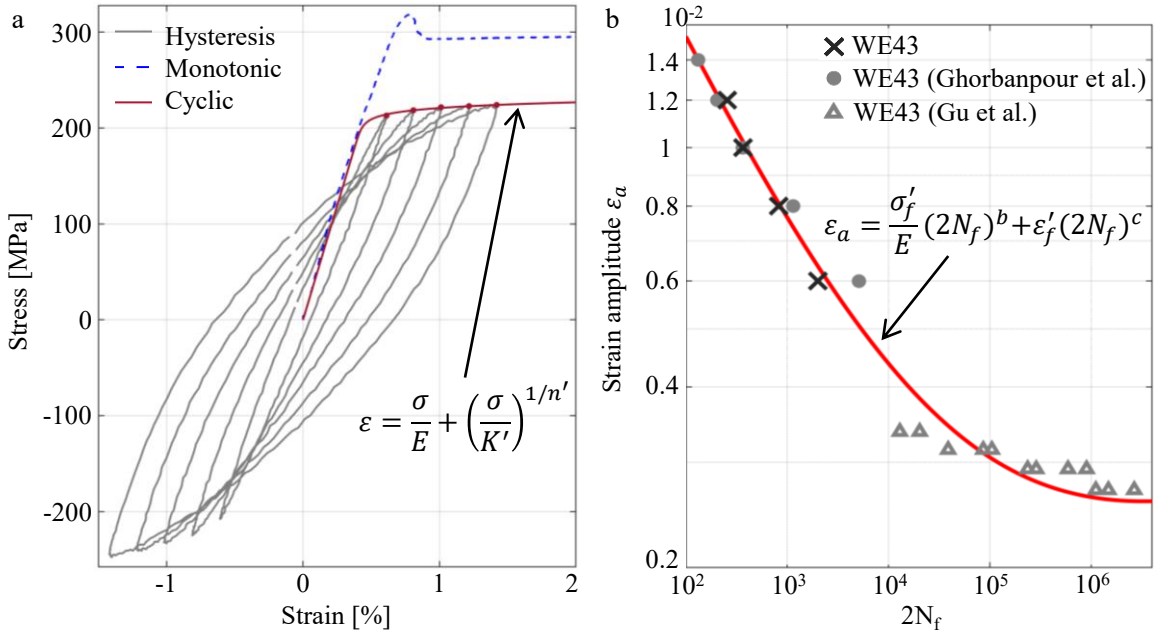

Figure 7.1.: Experimental results of strain-controlled fatigue testes, adapted from [121]: (a) cyclic stress-strain curve obtained from stabilised hysteresis loops of fully reversed ($R = -1$) cyclic loading with different strain amplitudes and stress-strain curve of monotonic tensile test, (b) total strain amplitude versus reversals to failure $2N_f$, supplemented with data from Ghorbanpour et al. [54] and Gu et al. [57].

	Air	1-day pre-corroded	7-day pre-corroded	DMEM
A	147.24597MPa	138.8379MPa	134.06349MPa	334.08618MPa
b	-0.02842	-0.02608	-0.03821	-0.1462

Table 7.2.: Material parameters in the Basquin equation for different test conditions [121].

7.3.2 Stress-controlled corrosion fatigue experiments

The stress-fatigue life (S-N) curves of the WE43 alloy tested in air, after 1–day and 7–day pre-corrosion periods and in the corrosive environment are shown in in Figure 7.2a. The relationship between the applied stress amplitude and the fatigue life above the fatigue limit is correlated using the Basquin equation (see section 7.2). The resulting material parameters for the different test conditions are presented in Table 7.2.

The fatigue endurance of WE43 alloy in air at 2×10^6 cycles is 99MPa. Compared to the fatigue behaviour of AZ31B tested in air with a stress ratio of $R = 0$, WE43 exhibits a better fatigue performance, as shown in Figure 7.2b. At 10^4 cycles, WE43 has a fatigue strength of approximately 113MPa and the AZ31B alloy of 84MPa [174]. This can be attributed to changes in the microstructure due to alloying with rare-earth elements. Rare-earth elements act as grain refiner and form precipitates in the matrix. Both effects hinder deformation twinning and pin dislocation movement [115]. It is indicated that the magnesium alloy WE43 with rare-earth elements is more suitable for highly loaded orthopaedic implant systems. Cracks in fatigue experiments are initiated by internal defects that locally increase the stress concentration. After pre-corrosion, locally

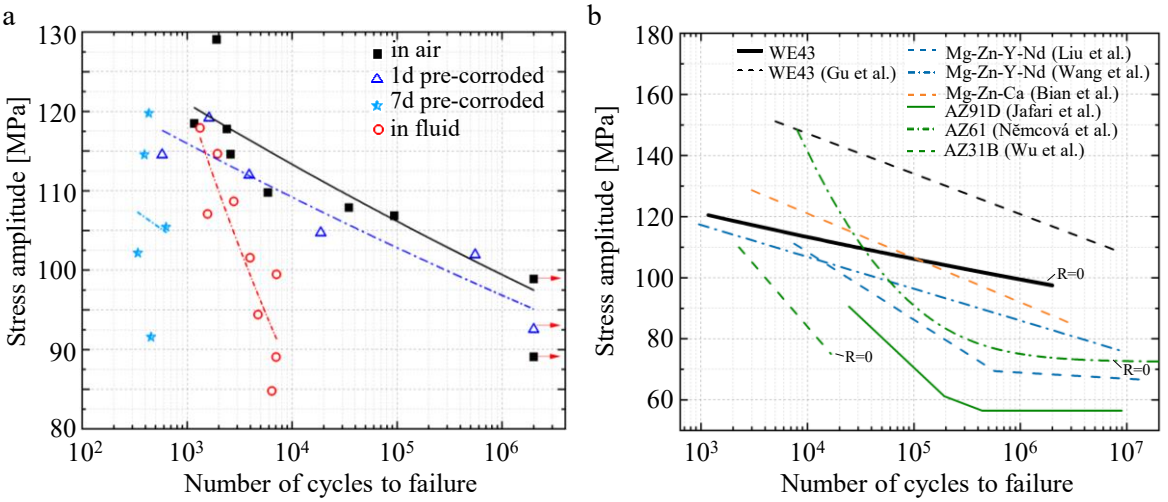

Figure 7.2.: S-N curves, adapted from [121]: (a) of WE43 tested in air in pristine condition, tested in air after 1 or 3 days pre-corrosion and tested in fluid, (b) comparison of the fatigue performance of different biodegradable magnesium alloys tested in air, applying a stress ratio of -1 unless stated differently, Gu et al. [57], Liu et al. [104], Wang et al. [164], Bian et al. [15], Jafari et al. [75], Němcová et al. [124], Wu et al. [174])

increased stresses at corrosion pits facilitate crack initiation. Hence, the pre-corroded specimens are expected to crack at preformed pits. However, the long-term corrosion experiments revealed, which are presented in chapter 5, that the WE43 alloy corroded rather non-homogeneouly and is insensitive to pitting corrosion. This insensitivity explains the rather small difference in fatigue performance between non-corroded and 1-day pre-corroded alloy. The similar S-N curves show that the inhomogeneous corrosion front after 1-day pre-corrosion has no detrimental effect on the fatigue strength. The fatigue limit of 1-day pre-corroded alloy, which is defined at $2{\times}10^6$ cycles, is almost identical to the uncorroded alloy. On the contrary, the progressing corrosion after 7 days in DMEM significantly deteriorates the fatigue performance. The advancing corrosion front leads to significant material dissolution, and fatigue failure occurs in less than 10^4 cycles. Immersion tests with round specimens of 4 mm diameter have revealed inhomogeneous corrosion attack along the circumference. Almost uncorroded ridges and pits with the maximum depth of 440μm were observed on the specimen's surface [74, 101]. This inhomogeneous circumference, which includes a considerable number of corrosion pits with varying depth of up to 35% of the specimen radius, leads to stress concentrations and local plastic deformations, which dramatically deteriorate the fatigue performance. The large scatter of the fatigue life after 7-day pre-corrosion may be attributed to the irregular corrosion front and randomly distributed corrosion pits. As a consequence, the Basquin model does not correlate the fatigue life of the heavily corroded specimens in an adequate manner.

In the CF tests in DMEM, mechanical loading and chemical attack strongly interact each other, leading to a significant change in the S-N curve of the WE43 specimens. The experimental results show that the number of cycles to failure at high stress amplitudes is similar to that of the uncorroded alloy. This confirms previous observations that the

CF behaviour at high stress levels is predominantly influenced by the mechanical loading and the effect of the corrosion environment is relatively limited [61]. At lower stress levels, the fatigue life of the WE43 is significantly reduced, which can be explained by a longer immersion time in the corrosive medium and superimposed corrosion damage due to electrochemical processes [75]. Hence, the degradation of the fatigue performance depends on the material's corrosion properties [104]. It has been observed that the prolonged exposure to the corrosive environment is detrimental to the fatigue [100, 167]. On this account, a comparison of the CF resistance between different alloy systems as potential biodegradable implant material is not straightforward due to large variations in experimental conditions.

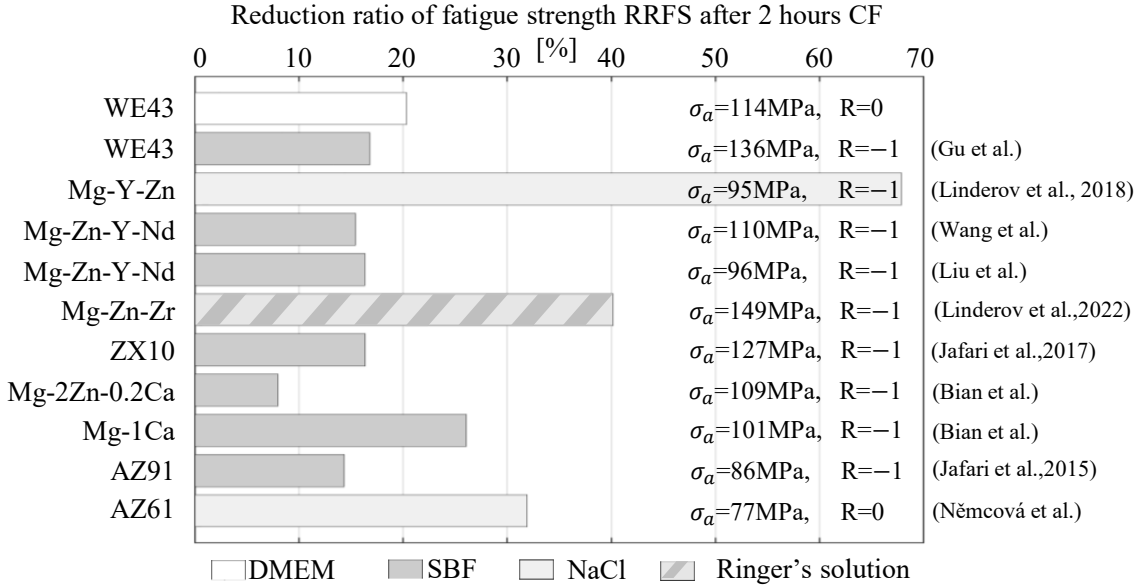

Figure 7.3.: Comparison of relative reductions in the fatigue strength after 2 hours of cyclic loading in different corrosive environments for different magnesium alloy systems with corresponding stress amplitudes σ_a (Gu et al. [57], Linderov et al. (2018) [101], Wang et al. [164], Liu et al. [104], Linderov et al. (2022) [100], Jafari et al. (2017) [74], Bian et al. [15], Jafari et al. (2015) [75], Němcová et al. [124]), adapted from [121].

The detrimental effect of the corrosion environment on the fatigue behaviour can be evaluated by the reduction ratio of fatigue strength (RRFS), which quantifies the relative decrease in the fatigue strength in corrosion environments (see section 7.2). Figure 7.3 compares the relative reduction in fatigue strength RRSF of different magnesium alloys at the fatigue life that corresponds to a cyclic loading of 2 hours in saline solution. To the best knowledge of the author, this has been the first CF experiment using complex DMEM fluid, which is a highly suitable fluid for in vitro corrosion studies as it is close to human blood plasma in compositions and concentrations [64]. After 2 hours of cyclical loading in DMEM, the fatigue strength of the WE43 alloy is reduced by about 20%. This value is higher than the results for Y- and Nd-containing magnesium alloys tested in SBF (WE43 and Mg-Zn-Y-Nd) [57, 104, 164]. However, it is noted that the larger maximum stresses and plastic deformations in the stress ratio case of this in vitro experiment may lead to higher sensitivity of the fatigue performance to corrosive environments.

Mg-Y-Zn and Mg-Zn-Zr show substantial reductions in the fatigue strength [100, 101]. As both alloys contain either Y or Nd, this may indicate that to achieve favourable strength retention, alloying with both Y and Nd is required. Nd and Y are both present in WE43 and Mg-Zn-Y-Nd, with higher concentrations in WE43. The comparison between these two alloys reveals similar relative reductions in the fatigue strength, but the WE43 alloy is subjected to a higher stress amplitude [57, 104, 164]. It is suggested that the larger Y and Nd concentrations in WE43 contribute favourably to the fatigue strength. The comparison also shows that the magnesium alloys containing aluminium or iron (AZ91D, AZ61, ZX10) do not outperform rare-earth alloy systems [74, 75, 124].

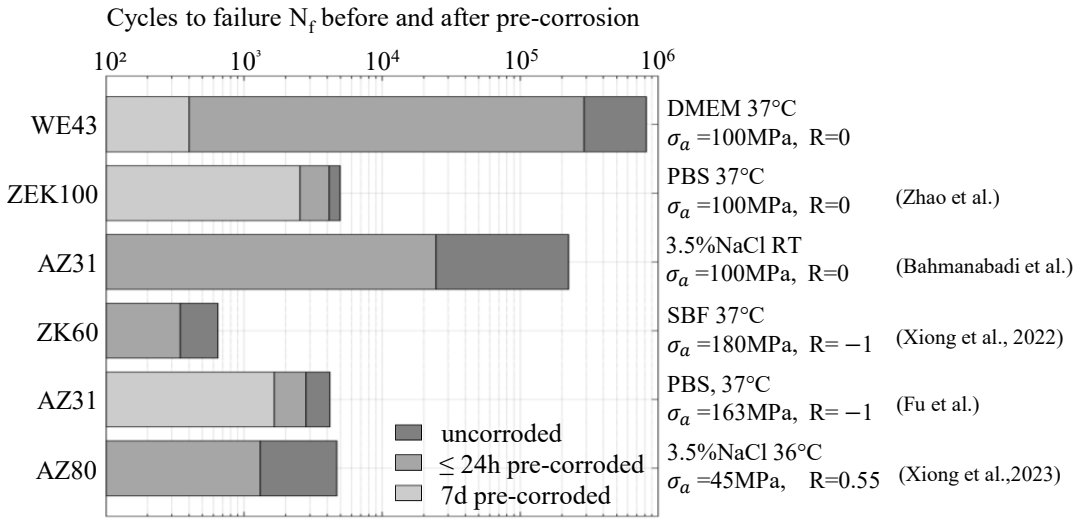

Figure 7.4.: Comparison of the number of cycles to failure in air and after different pre-corrosion periods for different alloy systems (Zhao [195], Bahmanabadi et al. [10], Xiong et al. (2022) [185], Fu et al. [48], Xiong et al (2023) [183]). Short pre-corrosion periods are 24h for WE43 in DMEM and AZ31 in PBS, 12h for ZEK100, ZK60 and AZ80 and 3h for AZ31 in NaCl, adapted from [121].

The effect of pre-corrosion on the fatigue performance of different magnesium alloys is compared in Figure 7.4. It is shown that the WE43 has the highest fatigue life, even after 1-day pre-corrosion. The aluminium-containing alloys exhibit a significantly lower fatigue performance. For longer pre-corrosion periods, the fatigue life of the rare earth-containing alloy ZEK100 decreases the least. The comparison shows that the magnesium alloy system can be tailored by the addition of rare-earth elements for achieving a suitable CF behaviour for medical applications.

Figure 7.5a shows the stress-strain hysteresis of selected cycles of the fatigue test in air with the stress amplitude of 115MPa and the fatigue life of 2,592 cycles. It is observed that the high stress amplitude in the low cycle fatigue regime results in an unstable stress-strain hysteresis with plastic ratcheting strain accumulating in each loading cycle. This ratcheting phenomenon has been reported for magnesium alloys and is related to twinning and dislocation slips [166]. The mean strain versus the normalised number of cycles is plotted in Figure 7.5b. At the initial stage, the mean strain increases rapidly. This rapid ratcheting rate then converts into a steady stage. The steady-ratcheting strain has been attributed to a balance between softening due to micro-crack development

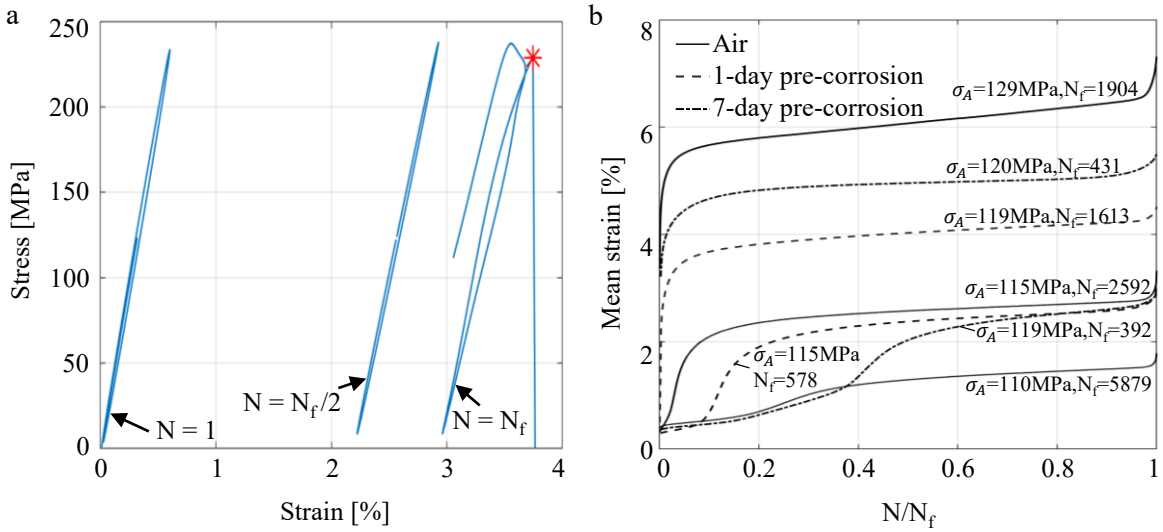

Figure 7.5.: (a) Stress-strain loops of selected cycles of stress-controlled fatigue tests in air with a stress amplitude of 115MPa, (b) mean strain versus normalised numbers of cycles-to-failure of uncorroded and pre-corroeded WE43 specimens, adapted from [121].

and strain hardening [23]. At the final fracture stage, the accumulated ratcheting strain dramatically increases again, leading to final failure. The comparison between different stress amplitudes shows that the ratcheting strain increases with higher stress amplitude and mean stress. This correlation has already been reported and linked to the increased density of twins under higher mean stress and stress amplitude [97–99]. The results within the two test groups of uncorroded and 1-day pre-corroded specimens show that the higher ratcheting strain leads to a shorter fatigue life. These results are consistent with reported results [183].

7.3.3 Fractography

Figure 7.6 shows the fatigue fracture surfaces of the WE43 specimens under different loading conditions. Except the 7-day pre-corroded specimen tested with a low stress amplitude of 91.6MPa, all fracture surfaces show three morphologically distinct zones: the crack initiation zone, the crack propagation zone and the overload zone. Additionally, shear lips are visible at the circumference. At lower stress amplitudes, the crack propagation zones are larger than at higher stress amplitudes, which corresponds to a larger number of cycles to failure.

SEM images of the three morphologically distinct zones of a WE43 specimen tested in air are presented in Figure 7.7. Crack initiation of the uncorroded specimen, which is marked in Figure 7.7a, cannot be clearly related to microstructural defects. In air, the fatigue source is related to surface or microstructural defects such as microcracks, micropores or inclusions [36, 130]. In magnesium specimens free of defects, twin or slip boundary have also been reported as potential fatigue source, as they locally increase stress concentrations [164, 166]. In the region near the crack initiation, as shown in Figure 7.7b, striation marks are visible as well as transgranular cracking. A mixed mode

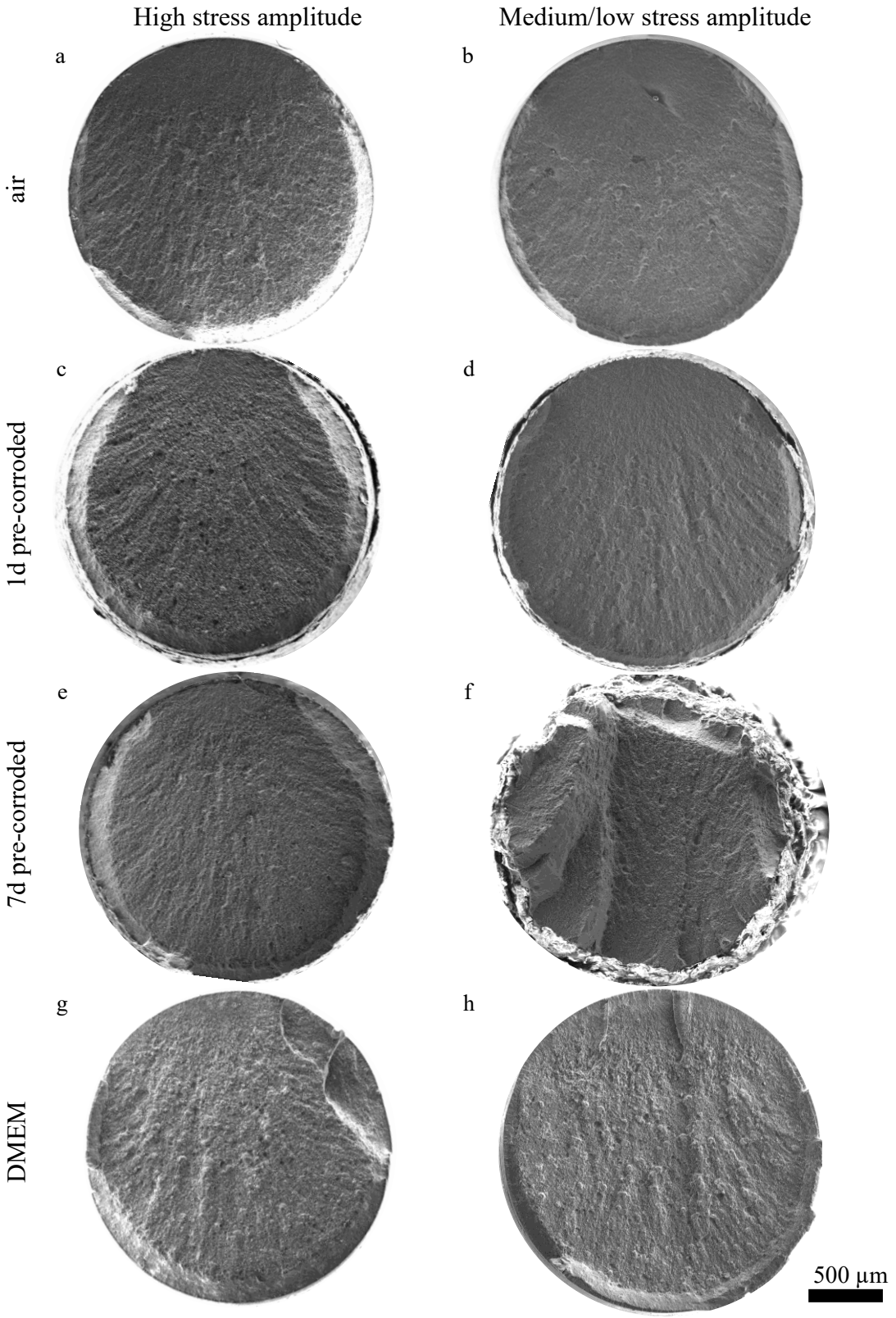

Figure 7.6.: Fracture surfaces of WE43 specimens cyclically loaded in air, in air after pre-corrosion for 1 or 7 days in DMEM or in DMEM, adapted from [121].

has already been identified for the alloy in SCC conditions and has been observed in additively manufactured WE43 [94, 122]. In the overload failure zone, a dimple-like morphology is observed, as shown in Figure 7.7c.

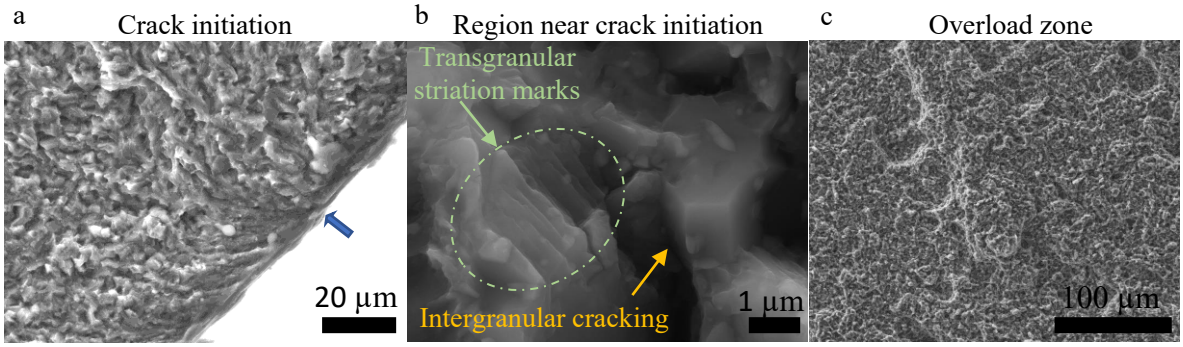

Figure 7.7.: SEM images of high magnification showing distinct fracture surface regions of specimens tested in air: (a) crack initiation site (marked with blue arrow) of an uncorroded specimen failing after 9.3×10^4 cycles in air (in Figure 7.6b), (b) crack propagation zone of 1-day pre-corroded specimen (in Figure 7.6c) with evidence of inter- and transgranular cracking, (c) overload zone of uncorroded specimen (in Figure 7.6b), adapted from [121].

The crack initiation zone of the 1-day pre-corroded specimen failing after 18,753 cycles at the stress amplitude of 105MPa (specimen shown in 7.6d) is shown at a higher magnification in Figure 7.8a. Corrosion products are clearly visible on the specimen's circumference. Localised corrosion, but no severe corrosion pits can be identified. Hence, crack initiation might not be related to an increased stress concentration at a deep pit for the 1-day pre-corroded group. The SEM image shows cracks in the corrosion products that have propagated throughout the thickness of the passive layer. At the interface of a brittle material and ductile metallic substrate, cracks can easily form inside the brittle material due to differing elastic properties. Owing to the high stress concentration at the crack tip, the crack can easily propagate into the metallic substrate and initiate fatigue failure of the alloy [59, 200]. Crack formation at the interface between the oxide layer and the alloy has already been observed in an AZ91D alloy after straining in organic solution [60]. Such cracks can serve as additional CF sources and result in lower cycles-to-failure despite the lower measured ratcheting strain in the 1-day pre-corroded group, compared to the uncorroded specimen group. Figure 7.8b and c show the side view of the pre-corroded specimen after fatigue failure. A layer of corrosion products is visible on the surface that is traversed by a dense network of aligned secondary cracks (marked by red arrows), which confirms the intensive cracking of the passive layer under cyclic loadings. The side view also shows regions with exfoliated corrosion products (marked in red), which usually appears at larger strains due to a mismatch of elastic properties between surface layer and substrate. At the circumference close to the fatigue fracture, the corrosion products have almost entirely exfoliated, revealing secondary cracks on the circumference of the specimen. These cracks are rather short but aligned perpendicularly to the loading direction and are usually associated with local material embrittlement [85]. The embrittlement is caused by the absorption of hydrogen by the magnesium matrix during the preceding exposure to the corrosion environment. The

cracks on the circumference seen in Figure 7.8c might have developed from microcracks that formed in the brittle corrosion product layer. Crack propagation into the metallic substrate leads to high stress concentrations in the crack tip and can trigger hydrogen embrittlement during the post-exposure straining [73]. The hydrogen accumulates at locations of high stresses and weakens the atomic bonds. Pre-immersion in an aggressive corrosion environment has shown to increase the hydrogen concentration [85]. Hence, the secondary cracks are attributed to a combination of crack propagation from the corrosion products and hydrogen embrittlement.

A prolonged pre-corrosion period of 7 days has a significantly detrimental effect on the fatigue life of the alloy, which can be confirmed by characteristics in the fracture surface of the specimen loaded with a stress amplitude of 92MPa, shown in Figure 7.6f. The SEM image shows multiple shear lips as crack initiation zones. As analysed in previous studies, 7-day pre-corrosion can cause localised corrosion damage, forming pits of about 230μm in DMEM and about 150μm in c-SBF [50, 118], which is sufficient to locally increase the stress concentration, facilitating crack initiation [198]. In addition, the hydrogen concentration in the magnesium substrate may increase due to the prolonged exposure time to the corrosion environment, leading to a high degree of material embrittlement [84]. Moreover, a passive layer of up to up to 220μm in thickness can form after 7 days in DMEM. As a result, larger cracks can form inside the passive layer, which can propagate into the magnesium alloy substrate, accelerating the propagation of fatigue cracks in magnesium substrate. Very few secondary cracks of up to 170μm were observed in the side view (see Figure 7.9).

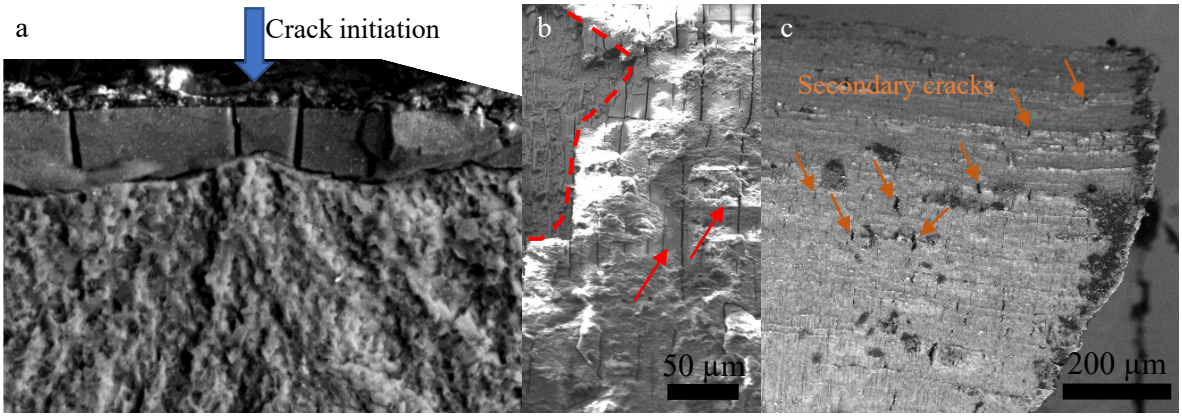

Figure 7.8.: SEM images of 1-day pre-corroded specimens: (a) crack initiation zone marked with blue arrow (in Figure 7.6d), (b) side view after fatigue failure with evidence of corrosion rpoduct cracking (hightlighted by arrwos) and evidence of product exfoliation (area highlighted with dashed line) (in Figure 7.6c), (c) side view close to fatigue fracture with evidence of secondary cracks (highlighted with arrows) (in Figure 7.6c), adapted from [121].

In the the CF experiments, several shear lips can be observed in specimens loaded in DMEM with high stress amplitudes, which are more pronounces, as observed in Figure 7.6g. The crack initiation zone of the specimen loaded with a stress amplitude of 102MPa (shown in Figure 7.6h) is presented in more detail in Figure 7.10a. Close to the fatigue source, the fracture is covered by a thin layer of corrosion products,

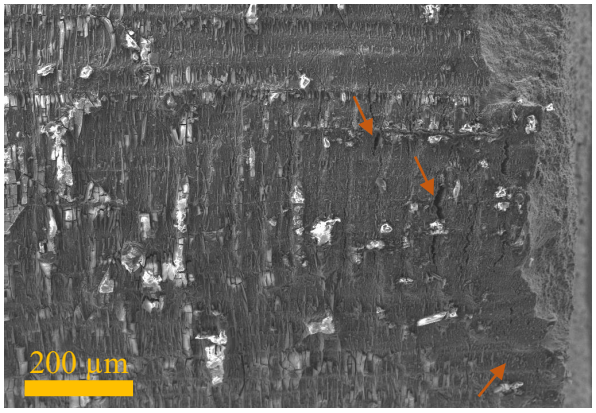

Figure 7.9.: SEM images with side view of 7-day pre-corroded specimens after fatigue failure with evidence of secondary cracks (highlighted with arrows) and exfoliated corrosion products (in Figure 7.6e), adapted from [121].

and a distinct layer is visible on the circumference distant from the crack initiation zone, as shown in Figure 7.10b. This is a clear indication of simultaneous deformation and corrosion processes. When the alloy is exposed to the corrosive environment, microgalvanic corrosion occurs, leading to localised corrosion attack and the release of atomic hydrogen. In a static corrosion environment, the dissolution of the magnesium matrix would be decelerated by the formation of a protective oxide layer. In contrast, the corrosion process is accelerated by the stress-induced passive layer breakdown under cyclic loading [113]. In addition, the stress-assisted hydrogen absorption and dissolution of the magnesium matrix can lead to increased corrosion rates [25, 51]. These deteriorative mechanisms become evident through a large number of stress corrosion cracks on the specimen's circumference, which are of several hundred micrometres in length, as shown in Figure 7.10c [85, 128, 144]. All of the above mechanisms mutually interact and take place repetitively, resulting in a significantly shorter fatigue life in the CF experiments.

With increased exposure time to the corrosion environment, the formation of fatigue source is facilitated by environmentally assisted mechanisms. The corrosion processes are more dominant at low stress amplitudes with a higher number of cycles-to-failure. At high stress amplitudes, the fatigue damage is mainly attributed to the mechanical loadings. Since the CF is an intrinsic time-dependent process, the test frequency of magnesium alloys for medical applications should be in the physiological regime. Another important factor is the physiological chloride concentration of the fluid, as high concentration of chlorides increases susceptibility to stress corrosion cracking [134].

Figure 7.11 shows SEM images of the crack propagation zone of the four different test configurations at higher magnification. All specimens show a mixed mode of intergranular cracking with striation marks and transgranular cracking, but significant differences in the predominant modes are visible. In uncorroded state, transgranular cracking is predominant. Interestingly, less striation marks, more intergranular cracking and more secondary cracks along grain boundaries are observed in the longer pre-corroded specimen and in the specimen loaded inside the fluid. The intergranular mode

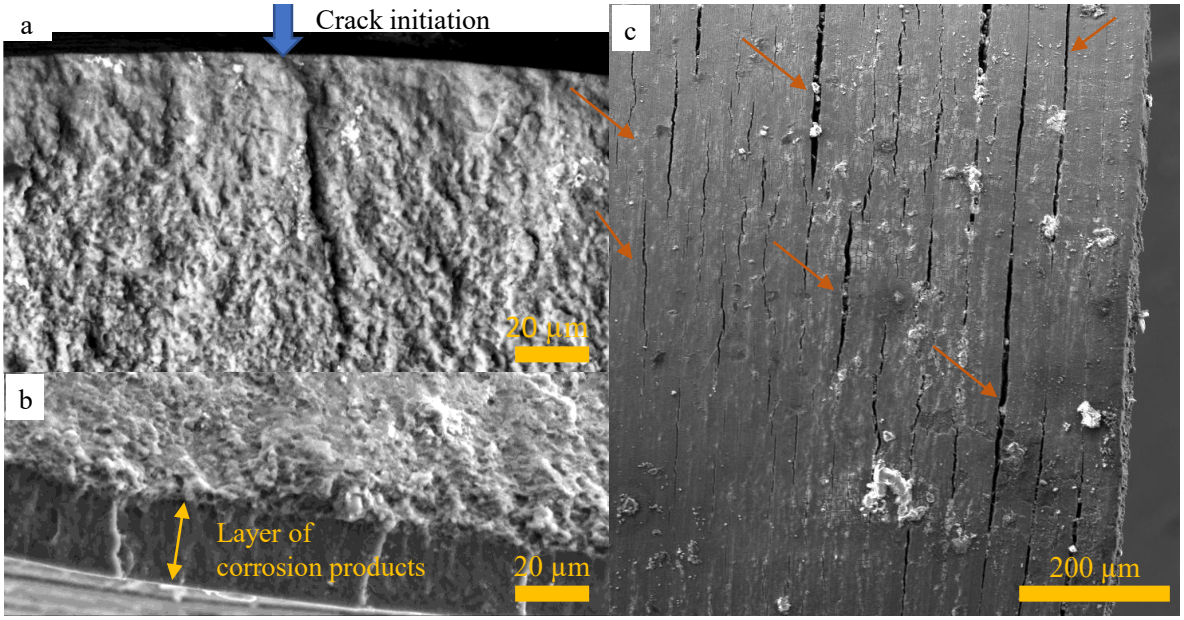

Figure 7.10.: SEM images of specimen dynamically loaded in the corrosion fluid (in Figure 7.6h): (a) crack initiation zone (marked with blue arrow), (b) BSE SEM image of fracture surface distant from crack initiation zone, (c) side view close to the fatigue fracture with evidence of secondary cracks (highlighted by arrows) and corrosion products, adapted from [121].

even prevails in CF configuration. This may be an indicator for the presence of hydrogen assisted mechanisms that weakens the bounds between grains and lead to more crack branching.

In aluminium-containing magnesium alloys, cleavage or transgranular fracture was identified as the prevalent fracture mode in CF experiments [48,49]. The same applies to these alloys in fatigue tests after pre-corrosion, with no significant changes in the failure modes reported after pre-corrosion [10, 152]. In the aluminium-free alloy ZK60, intergranular brittle fracture patterns and secondary cracks were observed in CF. The differences in the prevalent failure mode between the uncorroded, the pre-corroded and the specimens tested in fluid shows, that the failure mode of the WE43 alloy strongly depends on the experimental fatigue configuration. The failure mode changes after pre-corrosion and is dependent on the pre-corrosion period as well as on the cyclical loading in the corrosive environment.

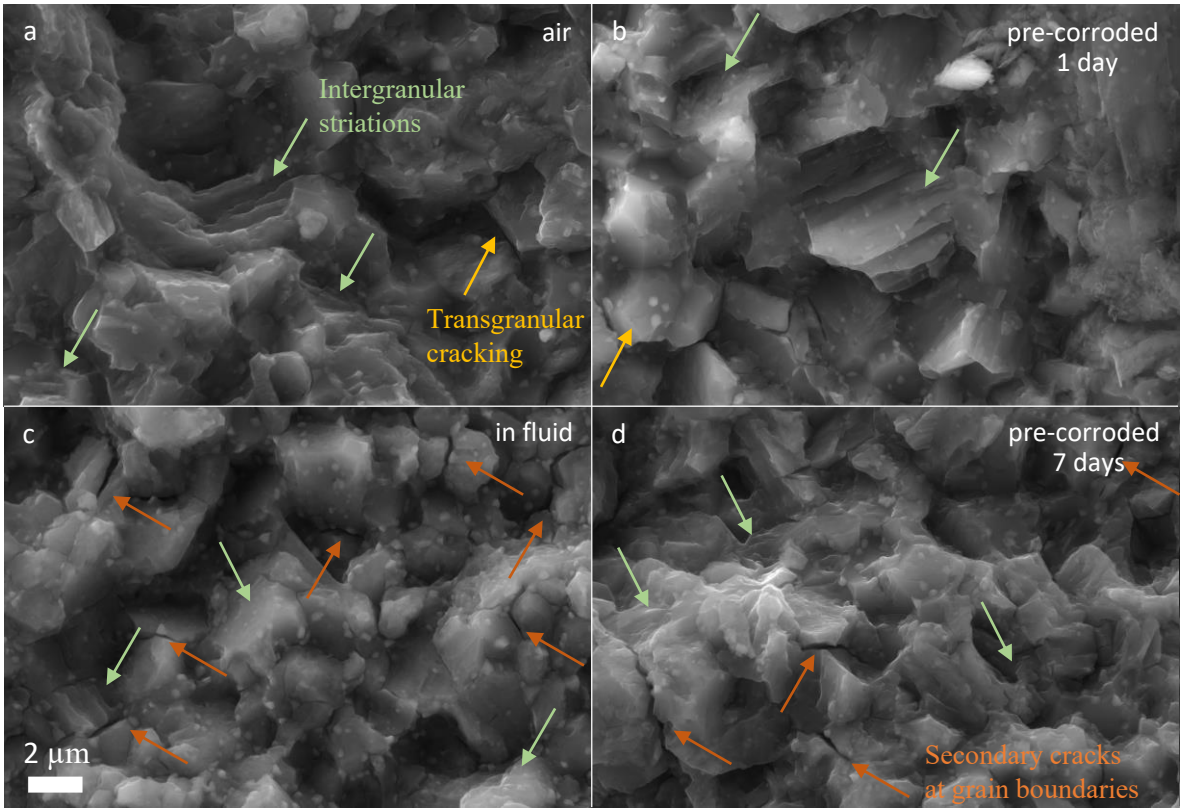

Figure 7.11.: SEM images of crack propagation zones of WE43 specimens of different test conditions: (a) uncorroded specimen, (b) 1-day pre-corroded specimen, (c) specimen tested in DMEM fluid, (d) 7-day pre-corroded specimen. Scale bar applies for all images. Intergranular cracking indicated by green arrow, transgranular cracking indicated by yellow arrow, and secondary cracks at grain boundaries indicated by orange arrow, adapted from [121].

7.4 Conclusions

Corrosion-fatigue experiments were conducted with pre-corroded specimens and in the fluid to assess the corrosion-fatigue behaviour of the medical-grade magnesium alloy WE43. The physiological test conditions were approached using a cell culture fluid DMEM containing organic compounds. To overcome the experimental limitations arising from the susceptibility of the fluid to contamination, sterile test conditions were employed. Finally, fracture surfaces were analysed using scanning electron microscopy. Based on the experimental results, the following conclusion can be drawn:

1. The WE43 alloy exhibits cyclic softening in air with a fatigue limit of 99MPa at 2×10^6 cycles. The ratcheting strain tends to be higher with increasing stress amplitudes.
2. Compared to the effect of 1-day pre-corrosion on the fatigue life, 7-days pre-corrosion significantly deteriorated the fatigue performance, independently of the stress amplitude. This can be attributed to large secondary cracks potentially induced by hydrogen embrittlement that formed perpendicularly to the loading direction during cyclic loading. These cracks developed either from corrosion pits

or from cracks that formed in the brittle corrosion product layer and propagated into the magnesium matrix.

3. In the corrosion-fatigue experiment in the organic fluid, the fatigue life was considerably reduced due to continuous exposure to the corrosive environment. This particularly applied for small stress amplitudes. The corrosion-fatigue strength was 85MPa at 8×10^3 cycles.
4. Stress corrosion mechanisms generally reduce the fatigue life of bioabsorbable magnesium alloys. The present results of WE43 fatigue life testing in DMEM confirms this behaviour. Clear signs of environmentally assisted cracking are visible on the specimen's circumference. A significant number of long and aligned secondary cracks indicate material embrittlement.
5. Fractography reveals three distinct regions: crack initiation zone, crack propagation zone and overload zone. In the case of corrosion-fatigue experiments, the initiation of cracks causing specimen failure is linked to corrosion pits, with secondary cracks forming along the circumference. In the crack propagation zone, all specimens showed mixed modes of intergranular and transgranular cracking. In uncorroded states, transgranular cracking was dominant, while a transition to an intergranular dominant cracking was observed in corrosion-fatigue tests due to hydrogen embrittlement.

8

Summary and future work

8.1 Summary

The objective of this thesis was to systematically study the degradation behaviour of a biodegradable magnesium alloy with PEO coating that was developed for use in load-bearing implants. Several in vitro studies have been conducted to identify corrosion processes of the fine-grained and rare earth-containing alloy and to develop a mechanistic understanding of the mechano-chemical interactions, which accelerate material degradation under implant service conditions. Therefore, material degradation has been examined in corrosion experiments under consideration of different mechanical constraints.

The physiological corrosion environment has been approached with a fluid containing physiological ionic concentrations and organic compounds. As the fluid is highly vulnerable to contamination, suitable test procedures have been developed for ensuring experimental sterility. A novel experimental setup has been developed for the appropriate use of the organic liquid in corrosion experiments under load. The outstanding feature of the setup is the maintenance of sterile corrosion conditions outside of sterility ensuring laboratory devices, and the ability to incorporate specimens exposed to the sterile corrosion environment into a testing machine for the application of loading protocols.

In vitro experiments revealed that the PEO coating changes the corrosion behaviour. In the organic fluid, the coating fully preserved the mechanical material integrity in the initial 14 days. This was attributed to the barrier effect of the coating. After fluid penetration, the coating converted chemically and structurally. Compared to uncoated specimens, a thicker innermost Mg-O-rich layer developed on the coated alloy, which thickened over time. This way, the coating provided corrosion protection, even after longer immersion periods. The mechanical strength decreased by 10% after 28 days. In the uncoated specimens, the corrosion progressed the fastest during the initial 7 days. With the formation of a time insensitive protective corrosion product layer, the corrosion process was slowed down. This resulted in a steady and continuous material dissolution between 7 and 28 days, which was displayed in a linear gas evolution and a nearly linear decrease in tensile strength. Tensile strength decreased by 21% after 28 days. Material dissolution was attributed to microgalvanic corrosion between the α-Mg matrix and intermetallic precipitates of Mg-Y-Nd. Due to the microstructural feature of very fine and evenly distributed intermetallic precipitates, the corrosion progressed localised

with an overall low susceptibility to pitting corrosion. This is highly favourable for a load-bearing application.

In constant load tests, a critical stress level of 80% of the material's initial tensile strength was identified for uncoated and coated specimens, resulting in a high probability of failure in the short term. Distinct regions showing the adverse effects of progressing corrosion, hydrogen-assisted mechanisms and crack propagation were observed in the fracture surfaces. In this context, it was found that the protection of the coating is limited to its undamaged state. If the coating is subjected to high local stresses, cracks will form inside the brittle coating. These cracks can provide an additional source for failure and accelerate the degradation process. This is attributed to two mechanisms. Firstly, the mechanical breakdown of the coating exposes the underlying magnesium substrate. With the substrate subjected to stresses itself, the corrosion process is accelerated. Secondly, the cracks formed inside the brittle coating can easily propagate into the metallic substrate and initiate failure. Both mechanisms contribute to a faster crack growth rate after the initiation event. This deteriorative character was more pronounced under continuous straining, which resulted in a larger decrease in mechanical strength and ductility in coated specimens. In slow strain rate testing, the material showed significant strain-rate dependent embrittlement. The relative reduction in the elongation-to-failure coincides with values reported in the literature (see chapter 6). In consideration of the absolute values, in contrast, the alloy outperformed most biodegradable magnesium alloys. Strains exceeded 10% when strained with the fastest rate and fracture occurred between 2 and 5% at slower rates. This is attributed to an excellent combination of tensile strength and ductility. The limited reduction in the tensile strength can be also attributed to the material's distinct yield strength, which is close to the tensile strength.

Corrosion-fatigue experiments revealed a considerable reduction in the fatigue performance under cyclical loading in the corrosion environment. The fatigue source develops from pits that are formed due to the adverse mechano-chemical mechanisms and are accompanied by clear signs of material embrittlement. The dominant failure mode in the crack propagation zone changes towards intergranular cracking in the fluid and signs of hydrogen embrittlement were identified. Short pre-corrosion (1 day) results in a minor decrease in the fatigue performance and a mixed fracture mode in the crack propagation zone. In comparison to other proposed biodegradable magnesium, the alloy shows a slightly larger relative loss of the fatigue strength, which might also be attributed to different applied loading conditions. In terms of absolute values of the fatigue life, the alloy outperforms results reported for biodegradable magnesium alloys. This applies for its pristine state and after short pre-corrosion. In contrast, longer pre-corrosion (7 days) is detrimental to the fatigue performance.

In summary, the alloy has shown localised corrosion with no susceptibility to pitting corrosion. This is beneficial for its intended use in load-bearing applications. In the applied experimental conditions, the PEO has shown to decelerate the corrosion process with the ability to fully preserve the mechanical integrity for an initial time period. Exposure to static loading in the corrosion environment has shown no detrimental effect to the material integrity if the critical limit is not exceeded. The brittle nature of the

coating is prone to cracking under high local stresses, which in turn can accelerate material degradation. In its undamaged state, the coating shows good corrosion protection. In corrosion experiments under loading, adverse mechano-chemical interactions cause material failure, which is accompanied by material embrittlement. Under cyclical loading in fluid, crack propagation mode has changed due to the synergetic corrosion and crack propagation. The severity of material loss due to the external loading strongly depends on the implemented loading protocol. The relative reductions in the material properties have been consistent with reported results from literature. Overall, the alloy outperformed some introduced biodegradable magnesium alloy systems in terms of absolute values. This is attributed to its microstructural features and its excellent combination of strength and ductility.

8.2 Future work

The experimental work presented in this thesis provides valuable information to the ongoing development and approval process of biodegradable implants in load-bearing applications. It has been shown that the very small and evenly dispersed secondary phases with rare-earth elements are beneficial to corrosion resistance in physiological conditions. More intense microgalvanic corrosion at Fe-rich impurities has shown that the impurities must be controlled and reduced to the largest extent possible for a predictable corrosion front. Corrosion studies under quasi-static loading conditions have shown a moderate sensitivity of the alloy to stress corrosion cracking. Yet, other research groups have shown that tailoring the alloy's microstructure in surface-near regions can improve the performance of magnesium alloys in such loading conditions. It might be interesting to combine these processing methods with PEO coating. Moreover, preliminary findings, which fall outside the intended scope, indicate that the surface finish of the alloy before the coating process can improve the corrosion protection of the material. In this context, a study on the surface finish as an influencing parameter is considered propitious.

Immersion tests have shown that the coating can fully preserve the mechanical integrity of the material for an intermediate duration and delays the degradation process. These findings should be translated into therapy in the frame of a corresponding recommendation provided to the patient. For instance, following surgery, it is advised that the patient avoids subjecting the implant to any load. In this way, the coating can decelerate implant dissolution and can significantly contribute to an optimised correlation between material degradation and bone hardening as it was shown in Figure 1.1.

The newly developed experimental setup enables the integration of the corroding specimen into a test bench. This way a broad range of loading protocols can be applied to the specimen, while the corrosion chamber ensures experimental sterility. This configuration may inspire other research groups to analyse the influence of single or multiple organic constituents on the corrosion processes under mechanical loadings. Non-sterile conditions limit such valuable investigations.

Furthermore, the results of this work will be used to design and validate a numerical

model, which describes the mechano-chemical material degradation. This model will contribute to an in-depth understanding of these complex interactions, which trigger material degradation. Moreover, the model can be used to predict an optimised implant design.

A

Test specimens

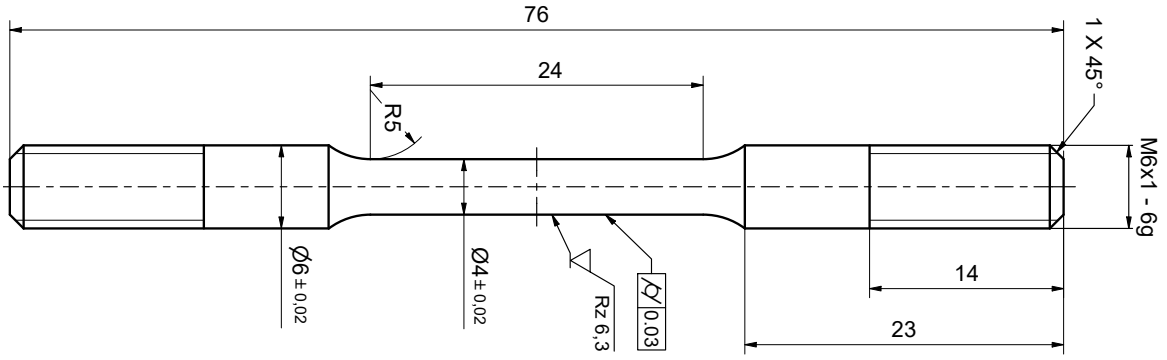

Figure A.1.: Technical drawing of tensile test specimen.

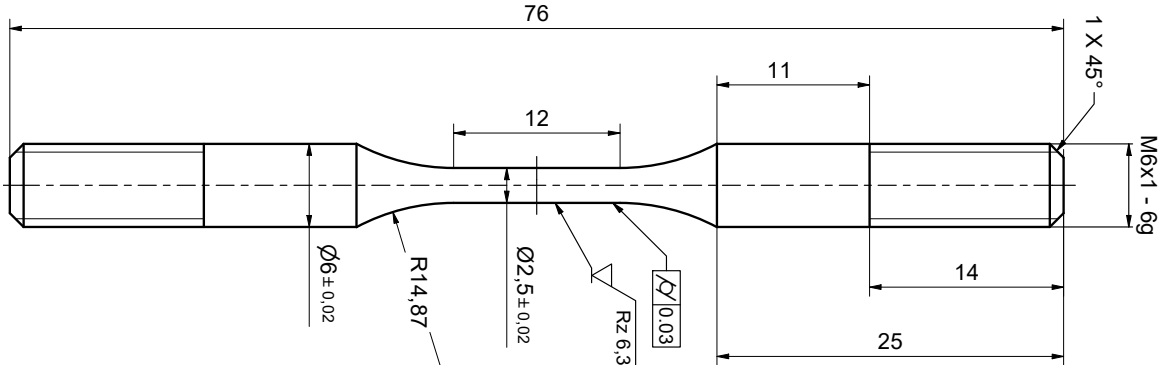

Figure A.2.: Technical drawing of fatigue test specimen.

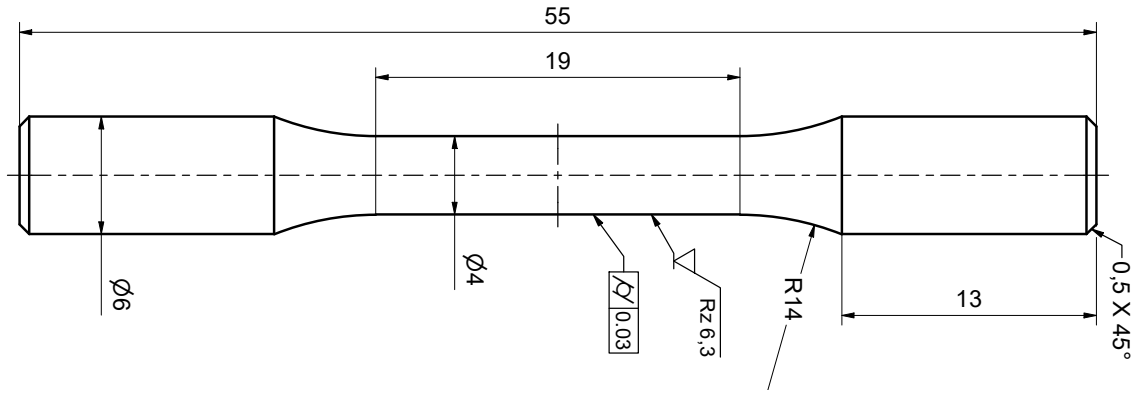

Figure A.3.: Technical drawing of fatigue test specimen for strain-controlled experiments.

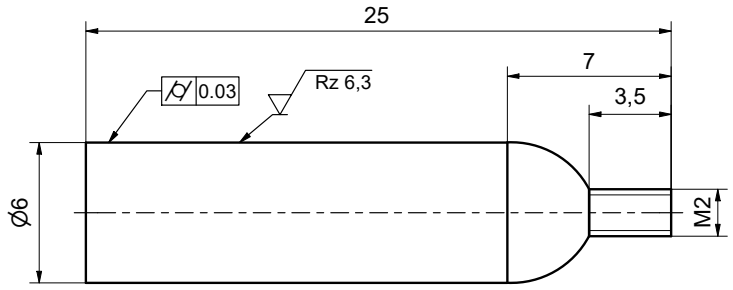

Figure A.4.: Technical drawing of pin specimen.

B

DMEM composition

Formulation	mg/l
Glycine	30
L-Arginine Monohydrochloride	84
L-Cystine Dihydrochloride	62.6
L-Histidine Monohydrochloride Monohydrate	42
L-Isoleucine	105
L-Leucine	105
L-Lysine Monohydrochloride	146
L-Methionine	30
L-Phenylalanine	66
L-Serine	42
L-Threonine	95
L-Tryptophan	16
L-Tyrosine Disodium Salt Dihydrate	103.79
L-Valine	94
Calcium Chloride Dihydrate	4265
Ferric Nitrate Nonahydrate	0.1
Magnesium Sulfate Anhydrous	97.67
Potassium chloride	400
Sodium Bicarbonate	3700
Sodium Chloride	6400
Sodium Phosphate Monobasic Anhydrous	109
Choline Chloride	4
D-Ca Pantothenate	4
Folic Acid	4
Myo-Inositol	7.2
Nicotinamide	4
Pyridoxal Hydrochloride	4
Riboflavin	0.4
Thiamine Hydrochloride	4
D-Glucose Anhydrous	4500
Phenol Red Solution Salt	15.9

Table B.1.: Composition of DMEM

C

Experimental preparation and mounting procedures

C.1 Sterilisation and cleaning process

The method for sterilising experimental parts before the experiment depends on the material. An overview is given in the following.

- Sterilisation in 90% ethanol
  - Coated and uncoated magnesium alloy specimens
- Sterilisation in 80% isopropanol
  - Cube of corrosion cell
  - All 3D printed lids
  - Funnel for static experiments
  - Connecting joint in corrosion chamber between funnel and burette
  - Tube for applying underpressure to the burette
- Sterilisation by autoclavation
  - Burette
  - Wide-neck bottle
  - Magnetic stirrer
  - All O-rings
  - Funnel for corrosion chamber
  - Tool for specimen mounting in corrosion chamber
- Single use products that are sterile packed
  - Syringe
  - Filtering caps

Between experiments, all parts for multiple-use must be cleaned appropriately before sterilisation according to the following protocol:

1. Firmly washed under running tap water and air dried
2. Rinsed in 20% mucasol
3. Washed with distilled water and air dried

C.2 Experimental preparation protocol for immersion experiments

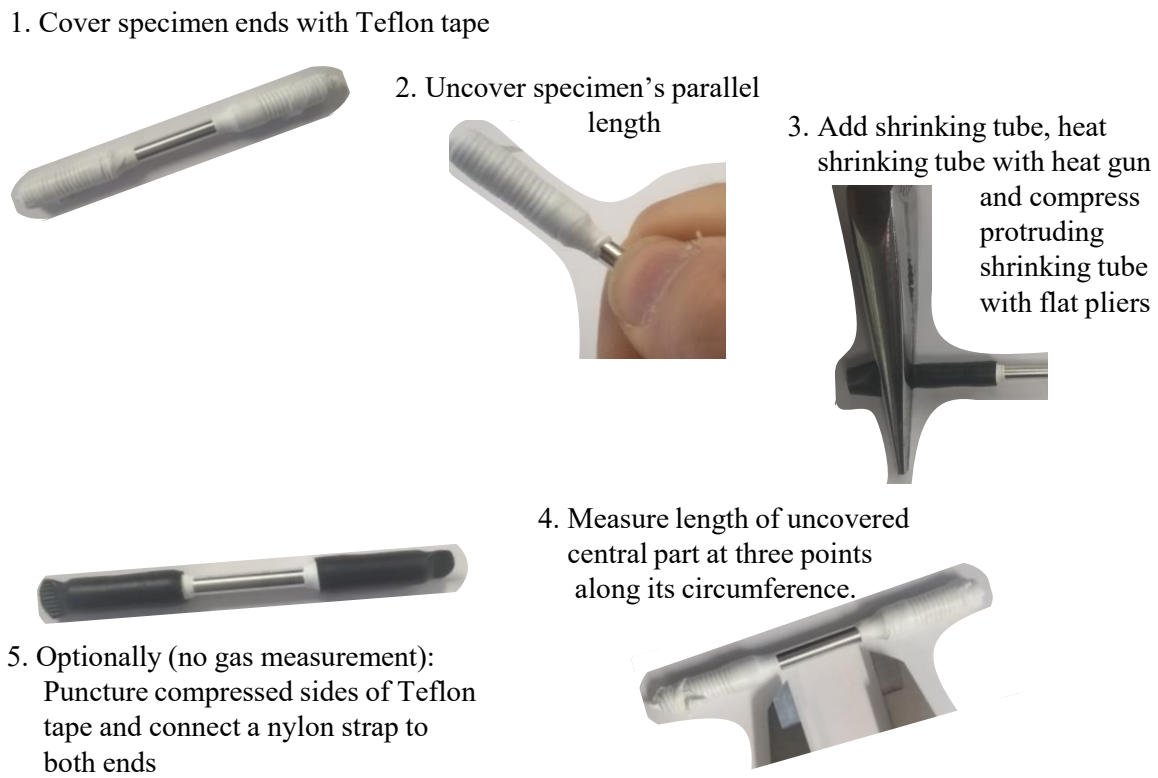

Figure C.1.: Specimen preparation procedure for immersion test.

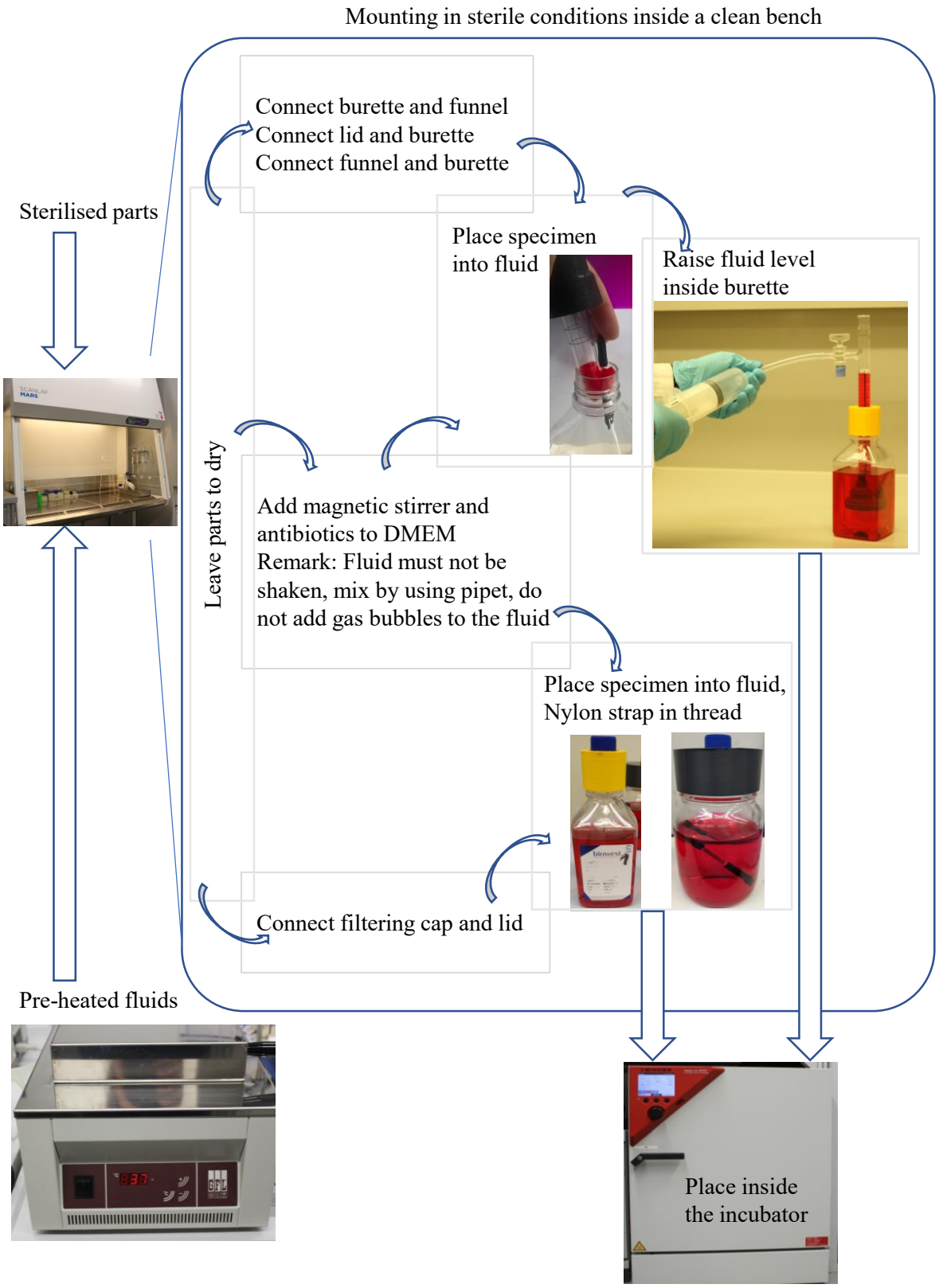

Figure C.2.: Workflow chart of the preparation procedure for immersion tests.

C.3 Experimental preparation protocol for corrosion experiments under loading

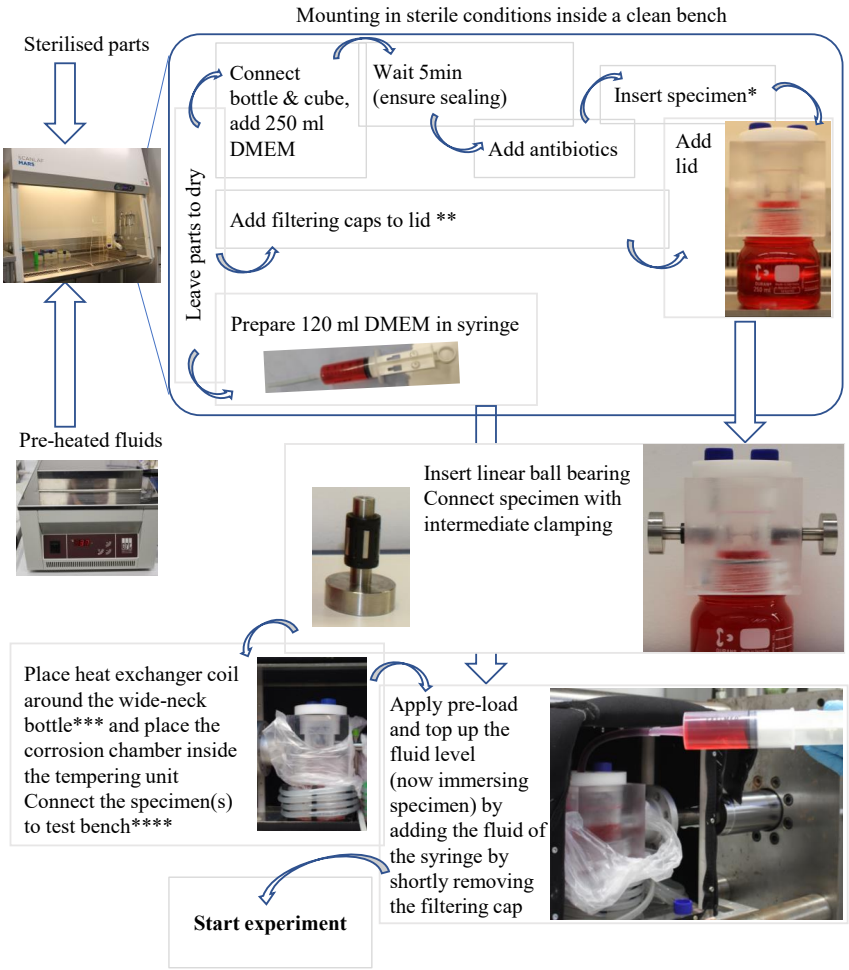

∗ For fully sterile conditions required, top up fluid level at this processing step
∗∗ For integrating gas measurement: 1. Place burette into the central guide of the lid, 2. insert custom-made funnel via the connecting plug
∗ ∗ ∗ When specimen failure expected add plastic bag
∗ ∗ ∗∗ For serial use: 1. connect both outermost specimen to the test bench, 2. establish pin connections, last connection on actuator side

Figure C.3.: Workflow chart of the experimental preparation and mounting procedure for the newly developed setup.

D
Analytics

D.1 Electron microscopy

In electron microscopy, an electron beam is shot at a sample. Depending on the measurement application, the distinct interactions between the atoms of the sample and the electron beam are measured by different detectors. In the scanning electron microscope configuration, the electron source and detectors are all located above the sample. In the transmission electroscope, the electron beam is shot through the sample and the detector is located on the opposite side of the electron source. The schematic setup of the two devices is presented in Figure D.2. In both devices, an electron gun emits electrons that are accelerated by an anode and focused by ring-shaped electromagnetic lenses. The position of the beam can be precisely controlled to scan the surface of the sample.

D.1.1 Scanning electron microscope

In the scanning electron microscope, the electron beam hits the target and scattering occurs between the primary electrons of the beam and orbiting electrons of the atoms of the sample. These interactions can be either elastic or plastic in nature and allow the measurement of secondary electrons, back-scattered electrons or energy-dispersive X-rays, as illustrated in Figure D.1 and explained in the following sections.

SEM images - Secondary electrons

If the primary electron collides with an orbiting electron in an elastic way, the orbiting electron can be knocked from its shell and turned into a secondary electron, as shown in Figure D.1a. Its energy is significantly lower than that of the primary electron. The secondary electron can be collected by a charged detector, which counts the number of electrons. If the electron beam hits a more exposed spot, a larger number of secondary electrons are detected and vice versa. When the number of secondary electrons counted is converted into a corresponding grey value, the topographical surface information can be displayed.

If non-conductive samples or surfaces are analysed, as is the case in ceramic coatings, charging artefacts can occur between the negatively charged near-surface area and the

electron beam. This can be prevented by sputtering the surface with a conductive material such as evaporated carbon or gold or by applying a low voltage to establish charge equilibrium at the specimen's surface.

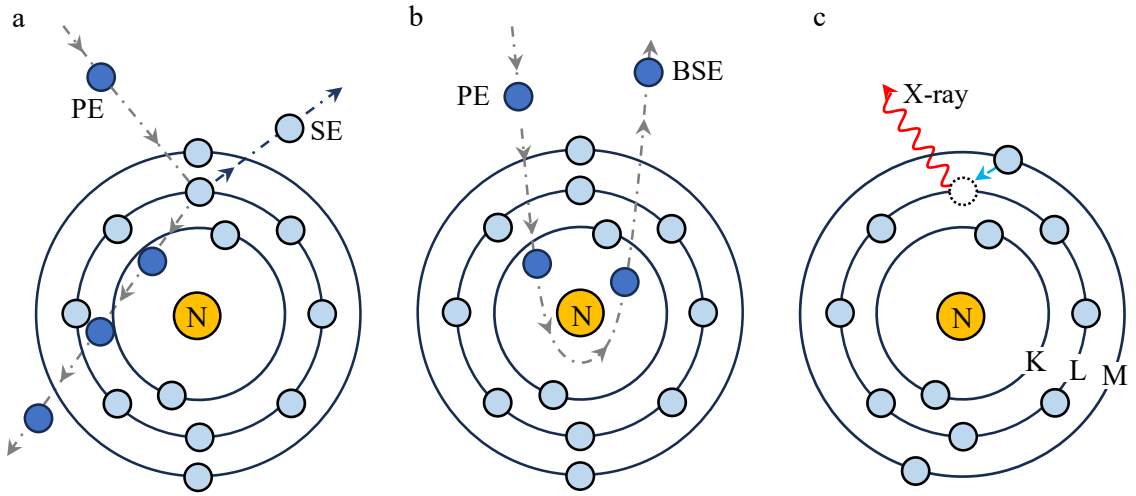

Figure D.1.: Scattering of electrons: (a) inelastic interaction with the ejection of a secondary electron, (b) elastic interaction with the scattering of the BSE, (c) characteristic X-ray emission.

SEM BSE images - Back-scattered electrons

When the primary electron is reflected by elastic scattering, the reflected primary electrons are called back-scattered electrons (BSE), as shown in Figure D.1b. The BSE detector is located underneath the ring-shaped electromagnetic lenses (see Figure D.2a). The intensity of the reflected BSE signal depends strongly on the atomic number of the material. This correlation can be used to visualise differences in phases in the surface region, with heavier elements appearing brighter as they cause a stronger back-scattering. The BSE electrons have a high energy compared to SE. By using detectors that require high electron energy levels, detection can be limited to BSE.

EDS analysis - Energy dispersive spectroscopy

If the primary electron collides with an orbiting electron from an inner shell, the electron can be ejected. As shown in Figure D.1c, the resulting electron hole will be filled by an electron dropping from an outer orbit. To maintain energy balance, the electron must release the energy difference between the outer higher-energy and inner lower-energy shell in the form of an X-ray. The energy of the emitted X-ray is equal to the energy difference between shells, which takes characteristic values for different elements. The emitted X-rays are detected by an energy-dispersive X-ray spectroscopy detector that measures the characteristic wavelength (corresponding to the X-ray energy) and counts the number of X-rays. This information is used to create an EDS spectrum that shows the instances of counts over the corresponding X-ray wavelengths. As the wavelengths

are characteristic for certain elements, the elemental composition of the area of interest is identified. The EDS analysis can be combined with the SEM image in EDS elemental mappings, displaying the geometric appearance of specific elements by using colour intensities.

D.1.2 Transmission electron microscopy

The arrangement of specimen and detector is different in the transmission electron microscope (TEM) than in the scanning electron microscope. The detector is positioned opposite the electron gun and detected electrons are shot through the sample. That is why only ultra-thin samples, which allow the electron beam to pass through, can be analysed. Hence, specimens need to be prepared accordingly. When transmitting through the sample, the primary electrons will interact with the sample. Their scattering probability depends on the material density. If the electron passes through more electron dense regions, they lose more energy. Hence, differences in material density can be visualised in the TEM image. After transmission, the beam is magnified by objective and projector lenses before it hits a fluorescence sensor. The brightness of the fluorescence screen corresponds to the energy of the impinging electrons. Finally, the brightness value is captured by a camera sensor. In this way, a 2D image is generated that assigns a brightness value to the scanned location.

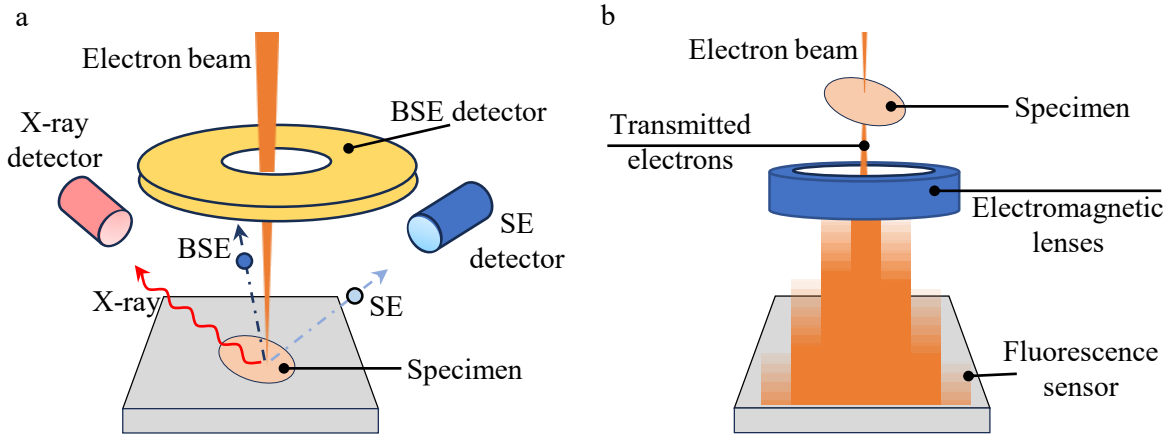

Figure D.2.: Schematic description of the arrangement of (a) SEM and (b) TEM devices.

D.2 X-ray diffraction

X-ray diffraction (XRD) is used to analyse the crystallographic structure of a material. The technique is based on diffraction patterns that result from constructive or destructive interference between electromagnetic waves, as shown in Figure D.3.

An X-ray beam is shot at the target and excites the atoms of the target material. The energy of the X-ray is absorbed by the atoms (indicated in yellow colour in Figure D.3) and needs to be immediately re-emitted in the form of X-rays of equal energy. Elastic scattering takes place at atoms of different crystalline planes of the material, and since the energy between incident and scattered X-ray needs to be the same, all electromagnetic waves have the same wavelength and their interference is measured by the detector. If the waves interfere destructively, the signal can be cancelled out. If the waves interfere constructively, the signal will be amplified. Constructive interference is present when the scattered X-rays are in alignment. This is the case when the difference in the traveling distance between X-rays from the source to the detector is equal to a whole number of wavelengths. With the inclination and deflection angle θ being equal, the distance between atomic planes a and the wavelength λ, the correlation can be described by Bragg's law:

$$n\lambda = 2asin\theta. \tag{D.1}$$

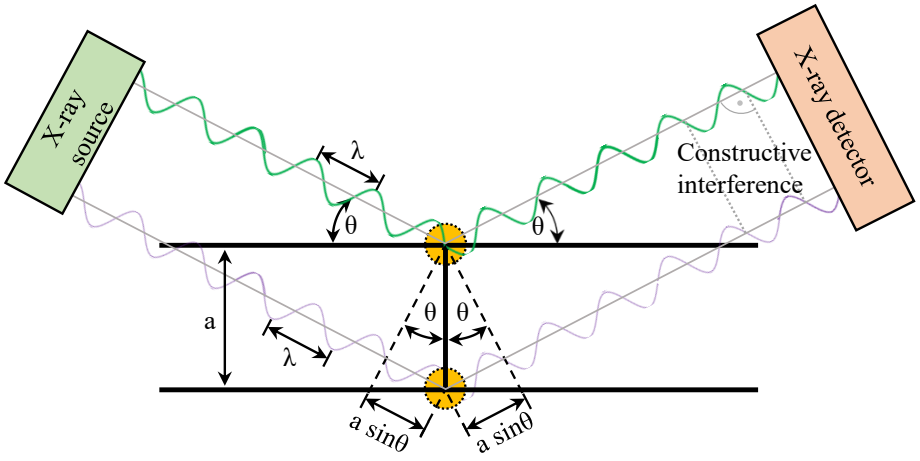

Figure D.3.: Principle of X-ray diffraction. The X-ray excites the atom (yellow) inside a specimen and energy is re-emitted immediately. Constructive interference is portrayed in the schemata.

The measuring principle only works if the wavelengths of X-rays and the distance between atomic planes are similar. Furthermore, X-ray source and detector need to be aligned symmetrically with respect to the sample. In an XRD measurement, the scattered signal is measured as a function of the incident angle θ. Therefore, X-ray source and detector perform a synchronised movement to change the angle θ in small steps. As each material possesses its own diffraction pattern, the 2θ corresponding signal peaks allow the identification of the material structure.

E

Supplementary material of the microstructural analysis

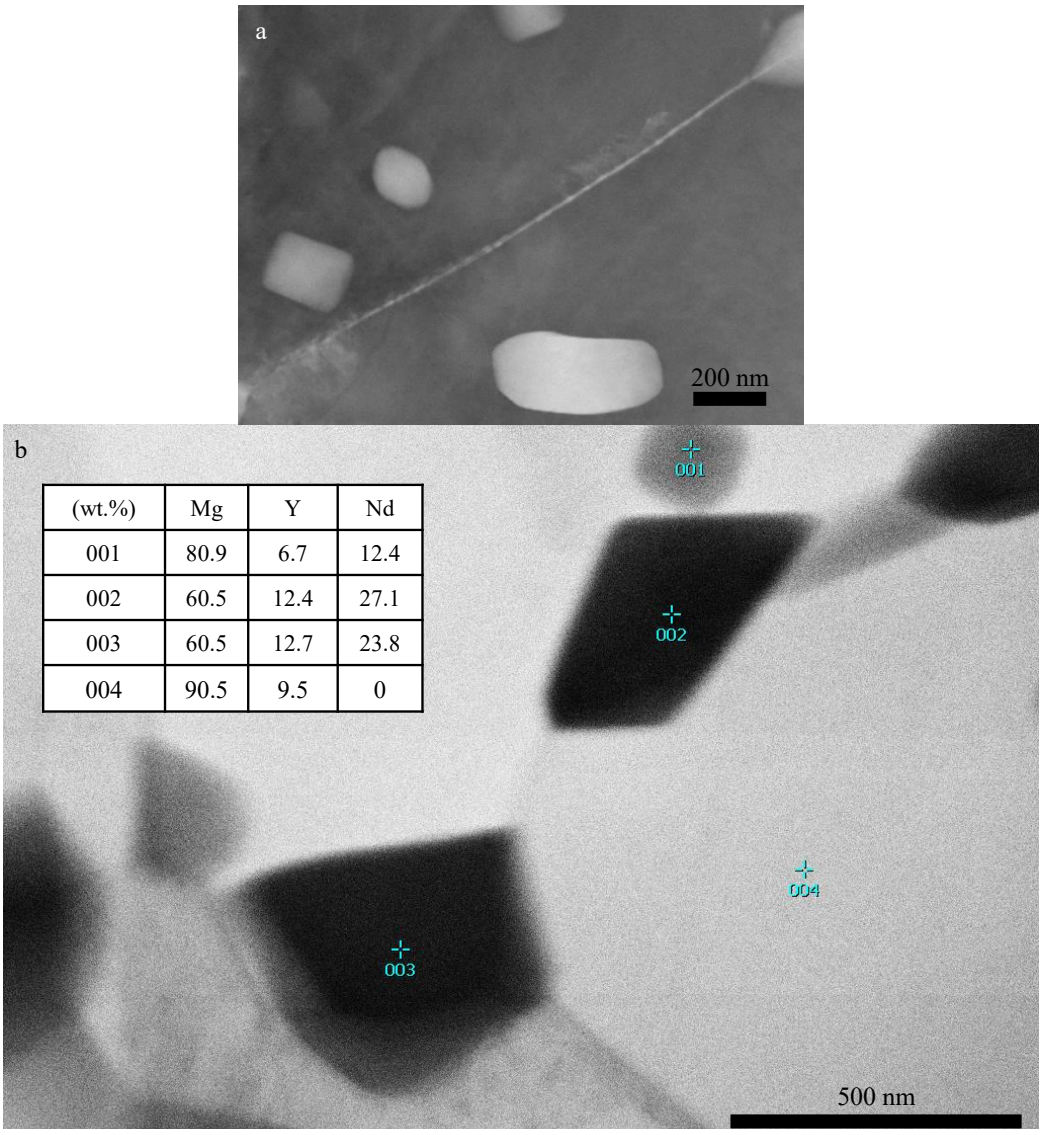

(wt.%)	Mg	Y	Nd
001	80.9	6.7	12.4
002	60.5	12.4	27.1
003	60.5	12.7	23.8
004	90.5	9.5	0

Figure E.1.: Microstructural analysis: (a) TEM image of grain boundary, (b) TEM image with elemental analysis of precipitates [122].

F

Supplementary material of long-term corrosion experiments

F.1 Corrosion surface analysis

The corrosion products on WE43 specimens were analysed using optical microscopy, laser microscopy, and optical profilometer. The analysis presented in this subsection and in Figure F.11 has been performed in valuable cooperation with Igor Schestakow from meotec GmbH (Aachen, Germany)

Figure F.1.: Morphological analysis of corrosion products on an uncoated WE43 specimen after 7 days immersion in DMEM: (a) optical microscope image, (b) topographic profile, (c) laser microscopical image.

Figure F.2 and F.3 show a white accumulation of corrosion products on the surfaces of uncoated specimens after immersion in DMEM for 7 and 14 days, respectively. The laser microscopical images reveal grooves that are arranged perpendicular to the specimen axis. It is assumed that these grooves are machine threads that result from the manufacturing process. This implies that uncorroded WE43 magnesium is present in areas surrounding the accumulation. This area appears larger in the 7-day specimen than in the 14-day specimen.

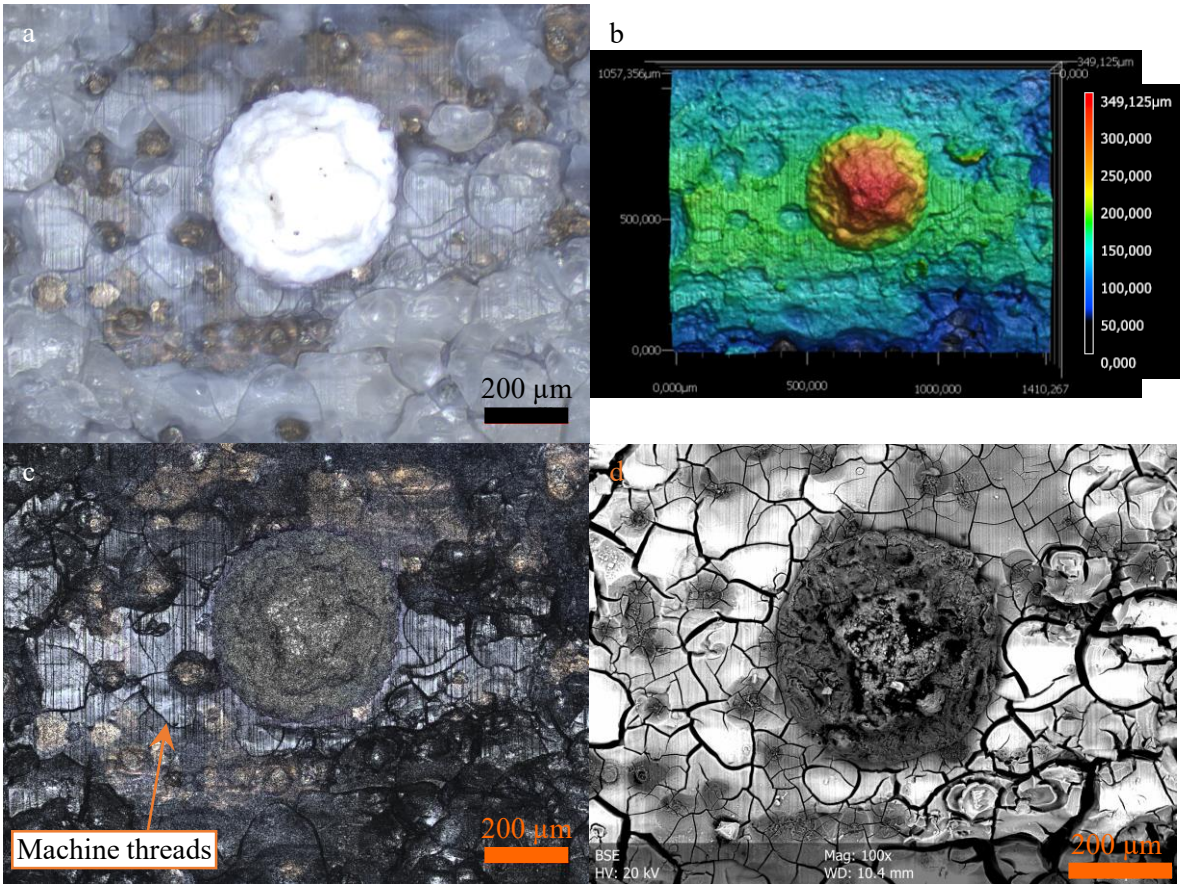

Figure F.2.: Morphological analysis of area around accumulated corrosion products on an uncoated WE43 specimen after 7 days immersion in DMEM: (a) optical microscope image, (b) topographic profile, (c) laser microscopical image, (d) SEM BSE image.

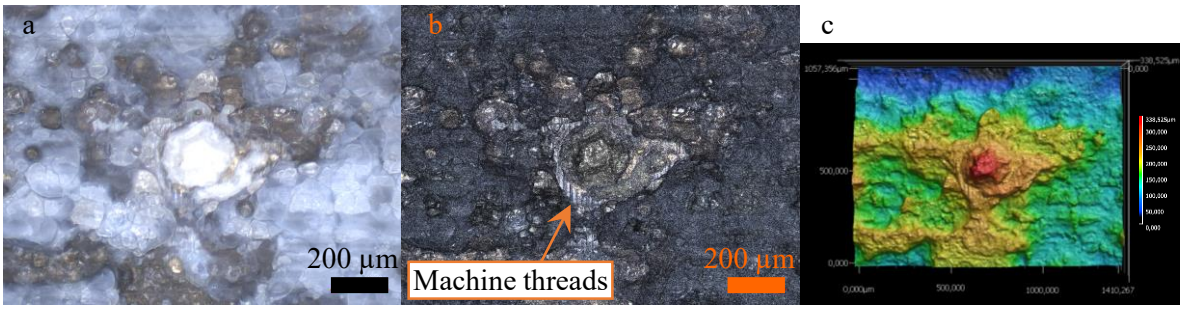

Figure F.3.: Morphological analysis of area around accumulated corrosion products on an uncoated WE43 specimen after 14 days immersion in DMEM: (a) optical microscope image, (b) topographical profile, (c) laser microscopical image.

F.2 Microgalvanic corrosion

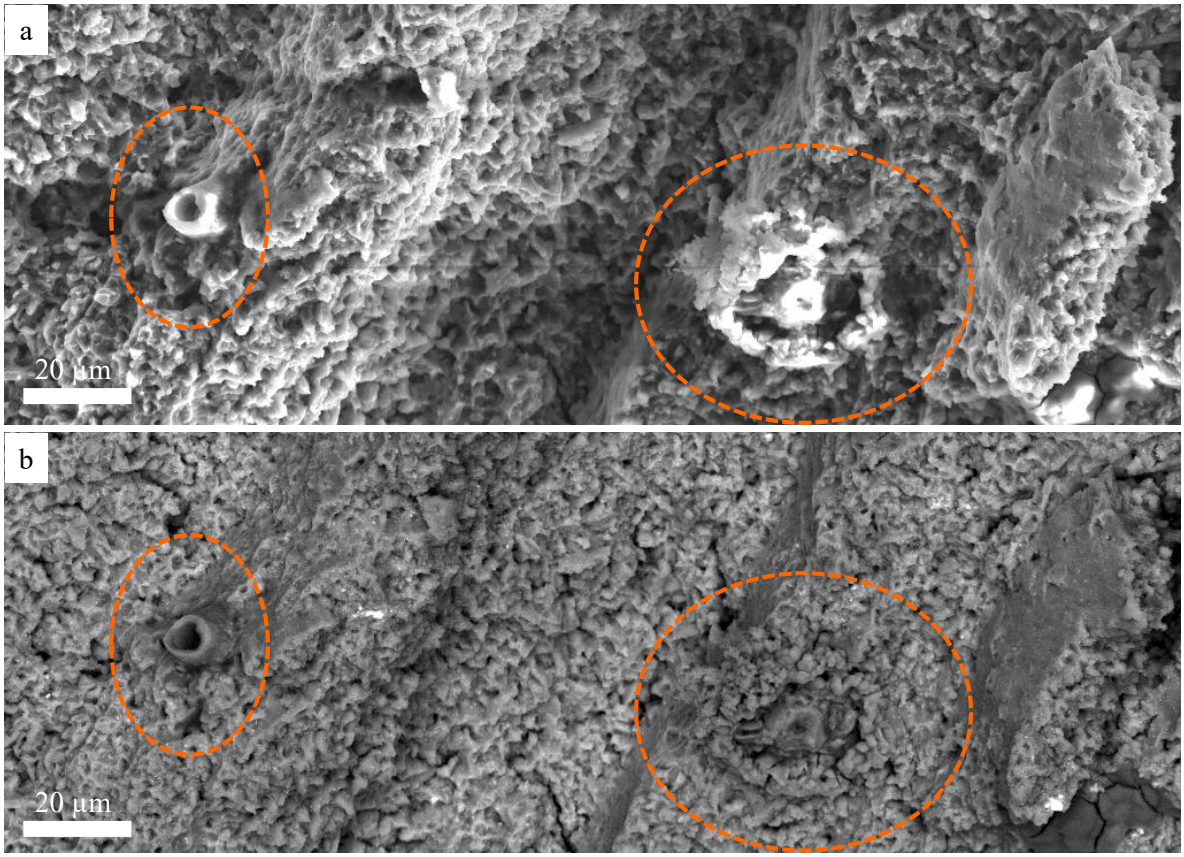

Figure F.4.: Volcano-like structures observed in the fracture surface of a SSRT tested specimen after short exposure of the fracture surface to the corrosive environment: (a) SEM image, (b) SEM BSE image.

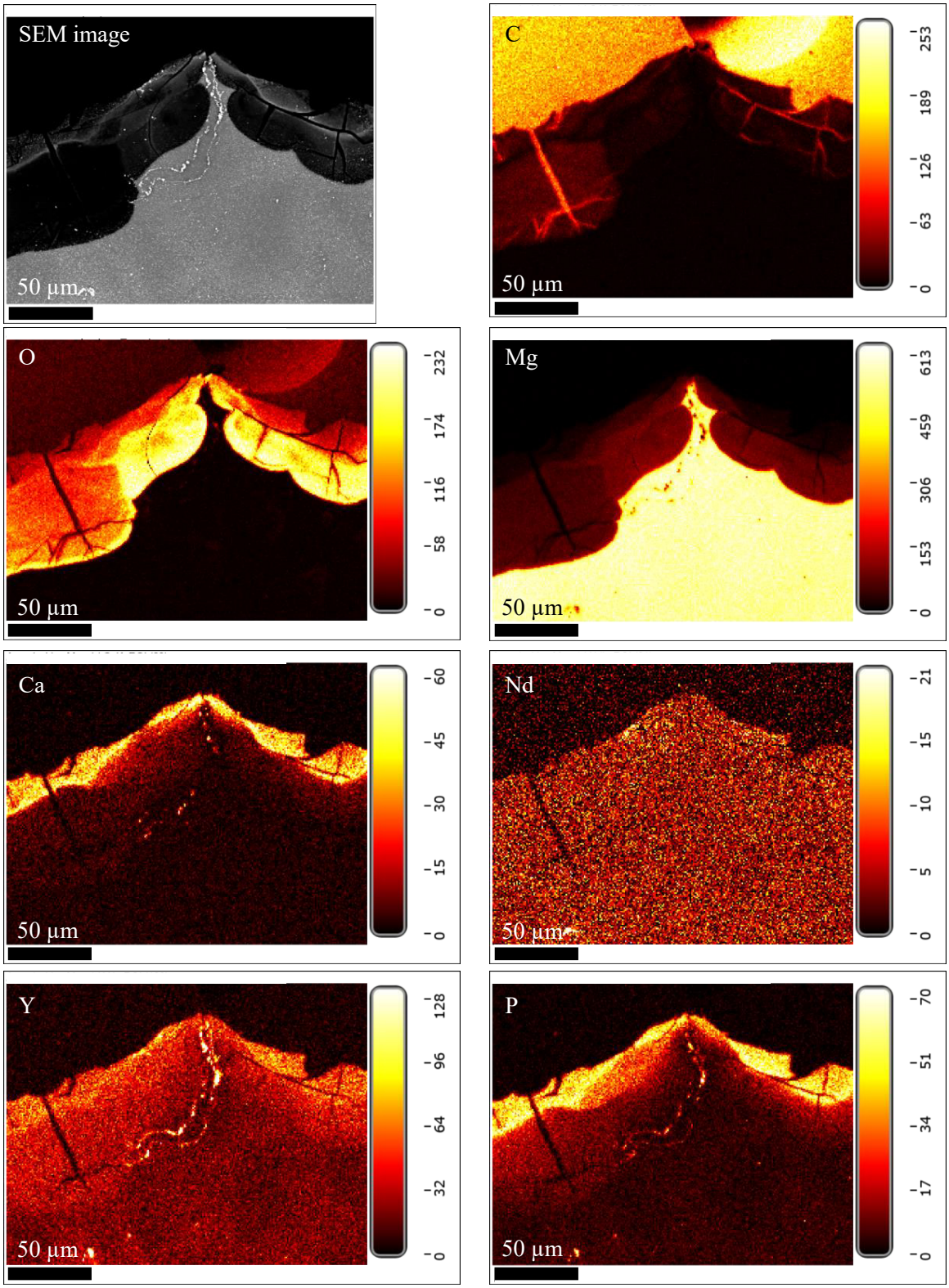

Figure F.5.: Elemental mapping of Figure 5.6b analysing the elements carbon (C), oxygen (O), magnesium (Mg), calcium (Ca), neodymium (Nd), Yttrium (Y), and phosphorous (P). The corresponding SEM BSE image is shown at the top left. High concentration levels are shown in yellow, low concentrations in red, and no detection is indicated by black colour.

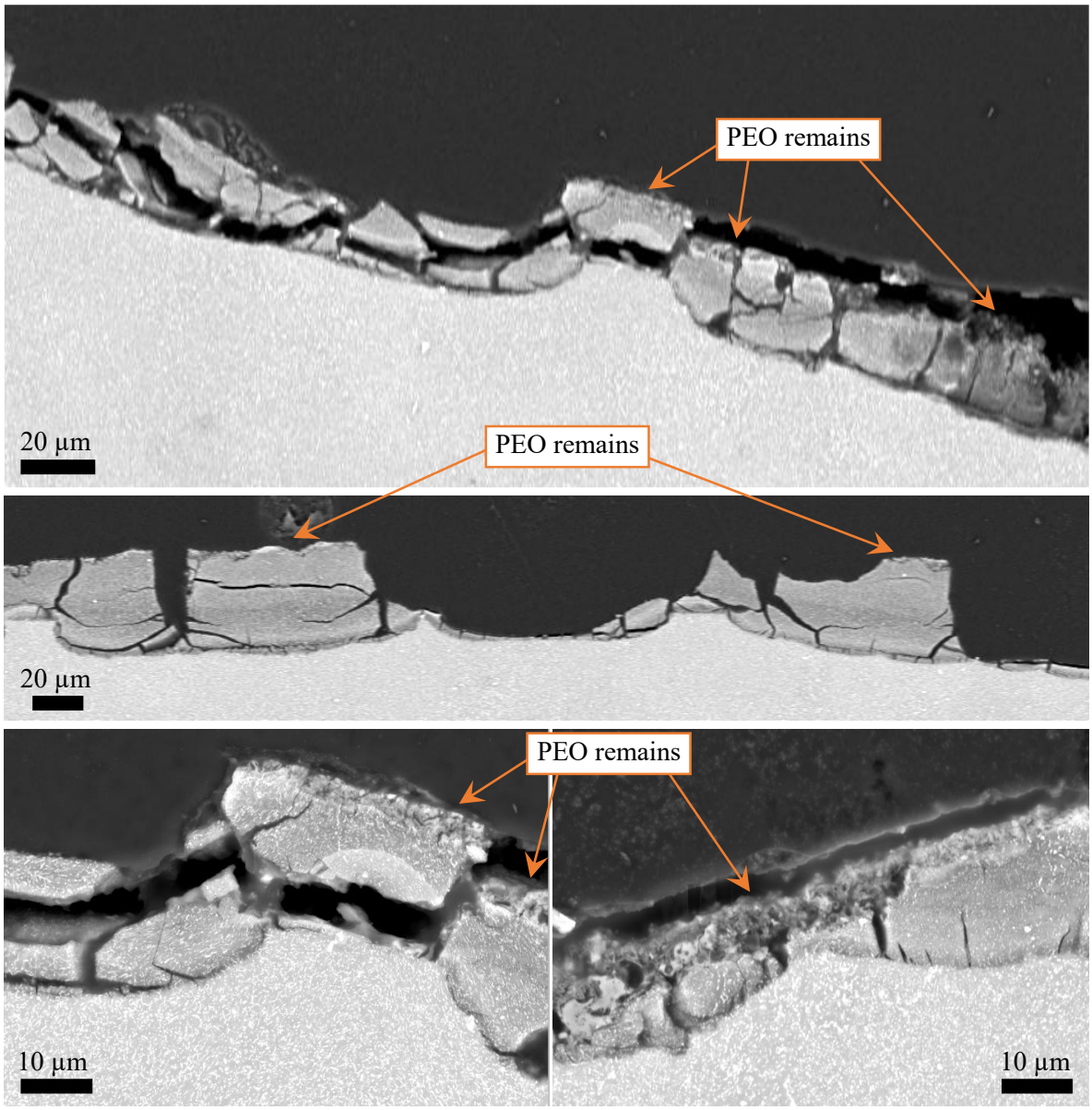

Figure F.6.: High resolution SEM BSE image of a coated specimen after 7 days corrosion.

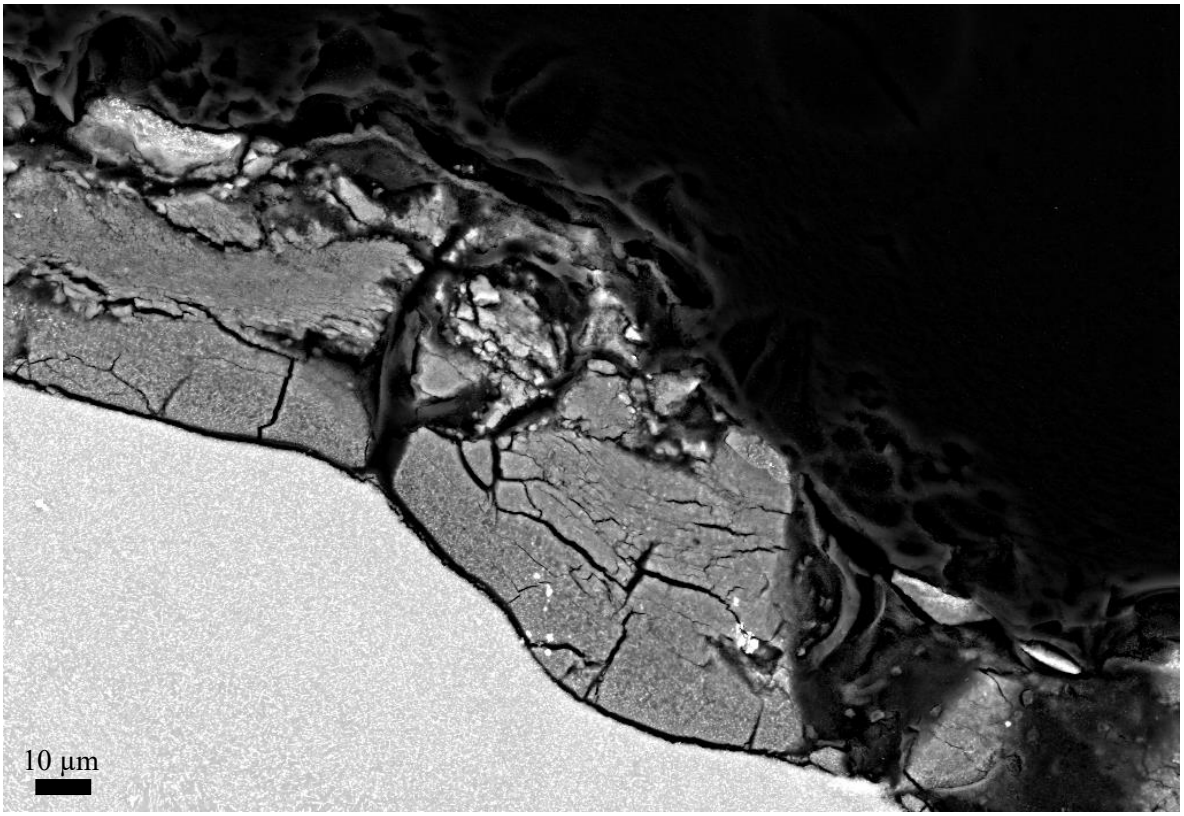

Figure F.7.: High resolution SEM BSE images of a coated specimen after 14 days corrosion.

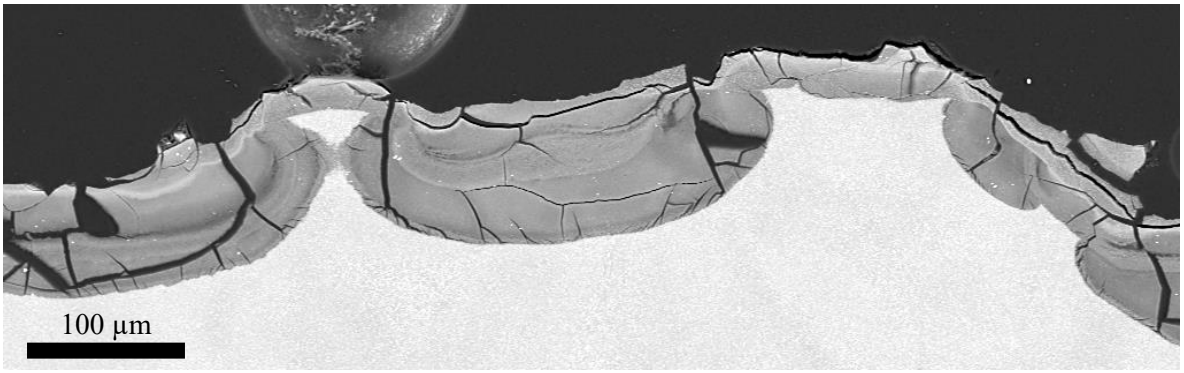

Figure F.8.: High resolution SEM BSE image of a coated specimen after 21 days corrosion.

F.3 Tensile test results

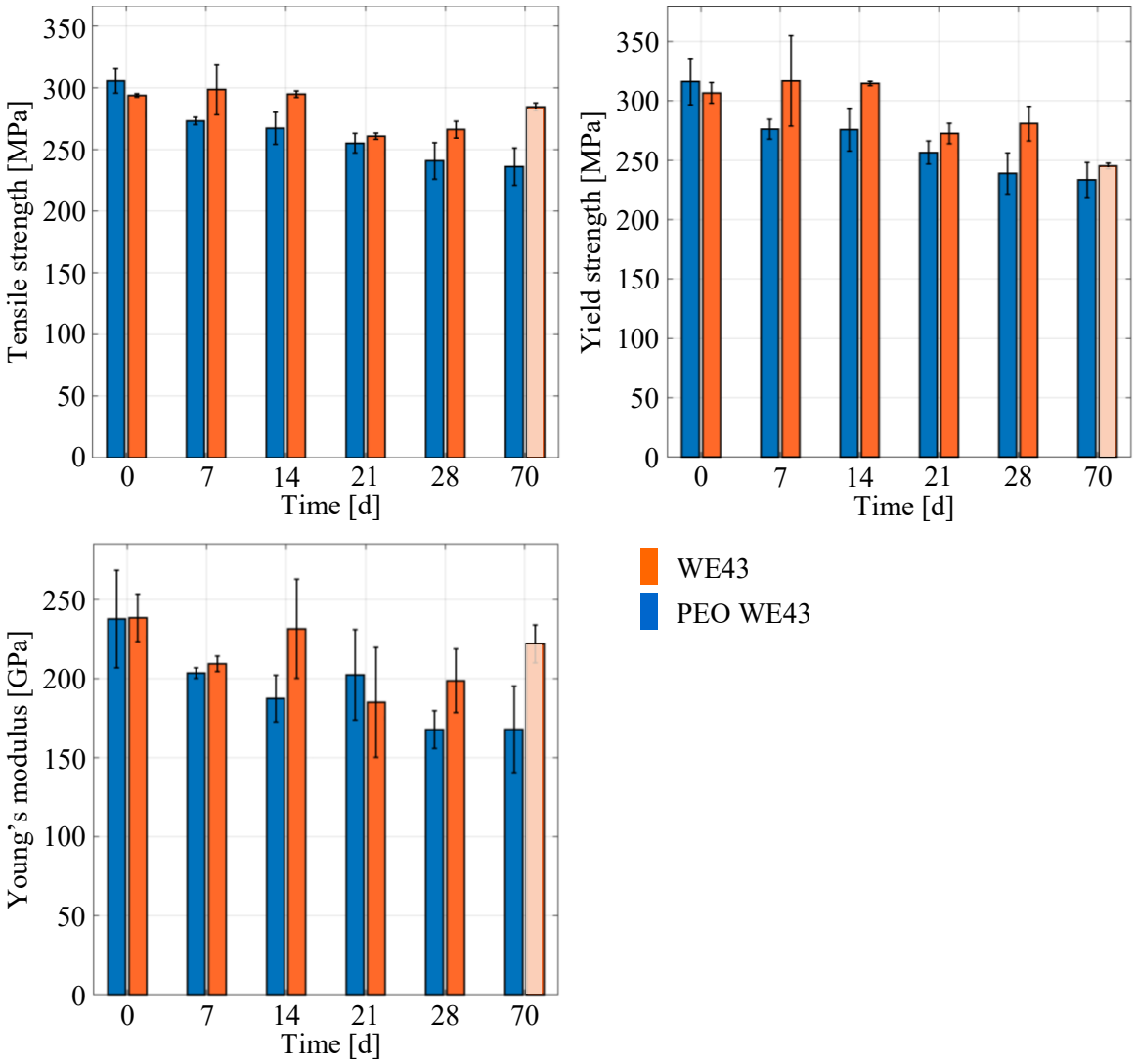

Figure F.9.: Mechanical properties determined by tensile tests of uncoated and PEO-coated specimens after varying immersion periods: tensile strength R_m, yield strength R_{eH} [119], Young's modulus E [190]. Results of non-coated specimens in blue and of coated specimens in red.

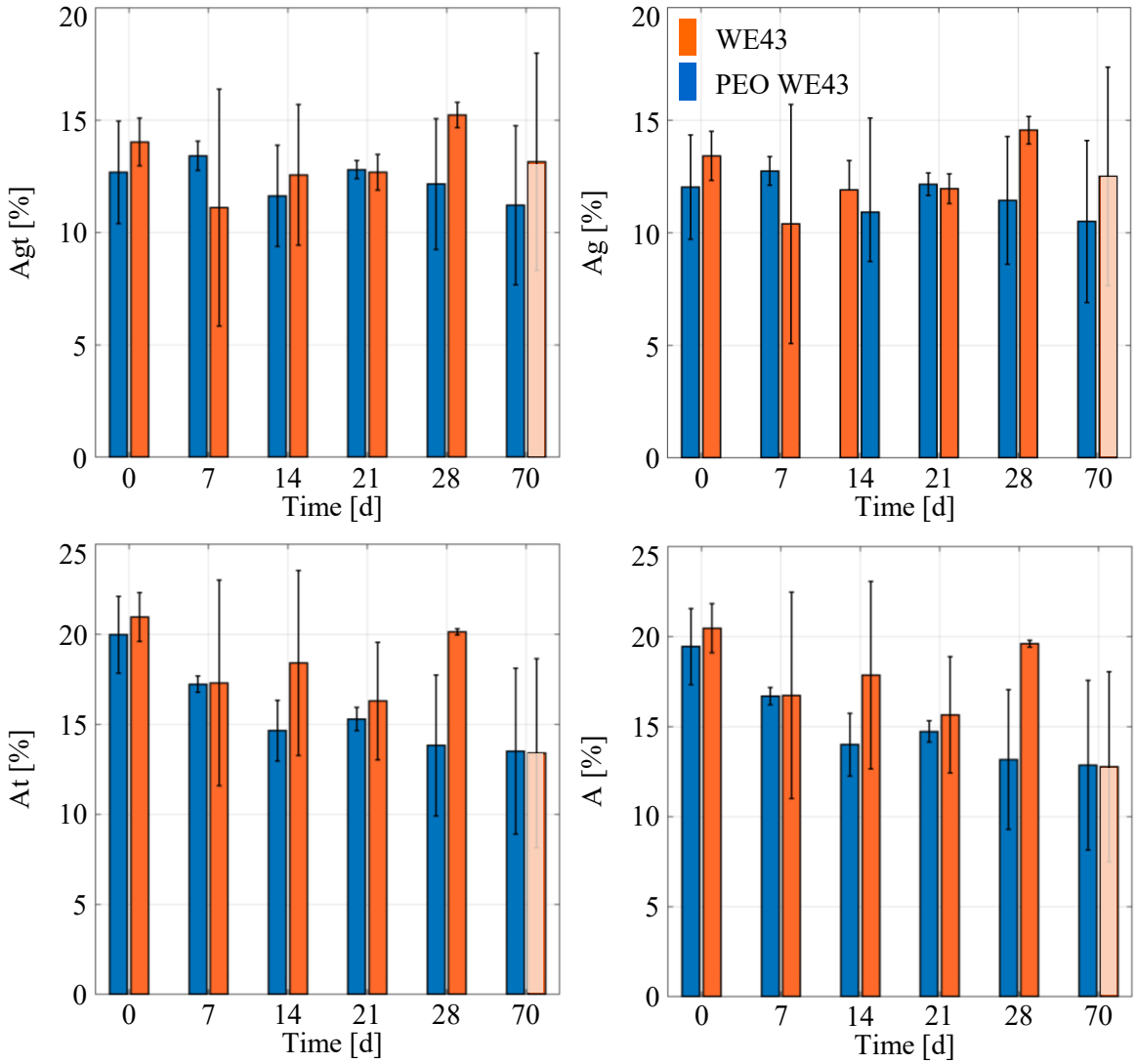

Figure F.10.: Deformation parameters determined by tensile test of uncoated and PEO-coated WE43 specimens after varying immersion periods: Total elongation at maximum force A_{gt}, non-proportional elongation at maximum force A_g, total elongation at fracture A_t, elongation after fracture A. Results of non-coated specimens in blue and of coated specimens in red.

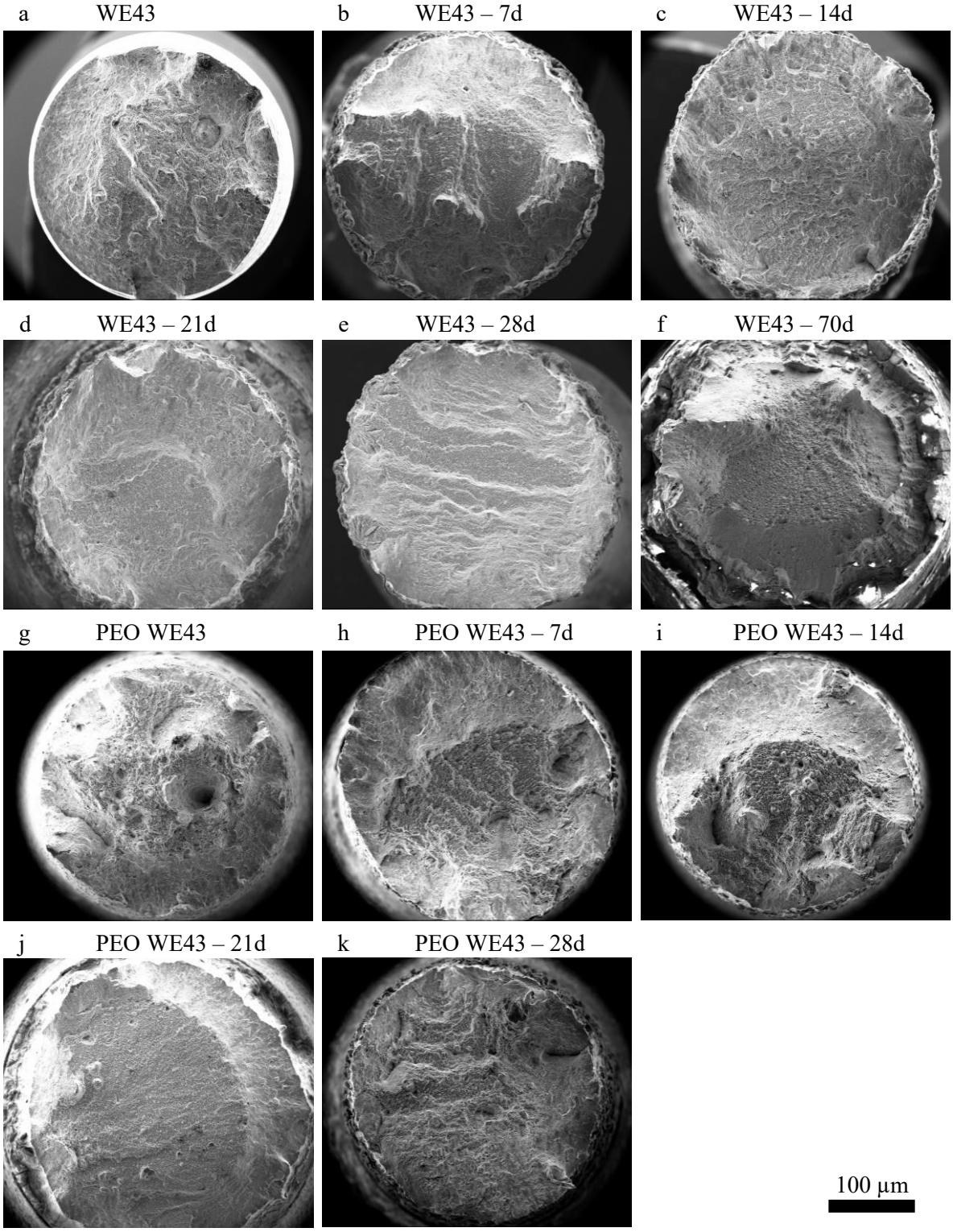

Figure F.11.: SEM images of fracture surfaces of tensile tested specimens after different corrosion periods.

G

Supplementary material of SCC experiments

G.1 SSRT

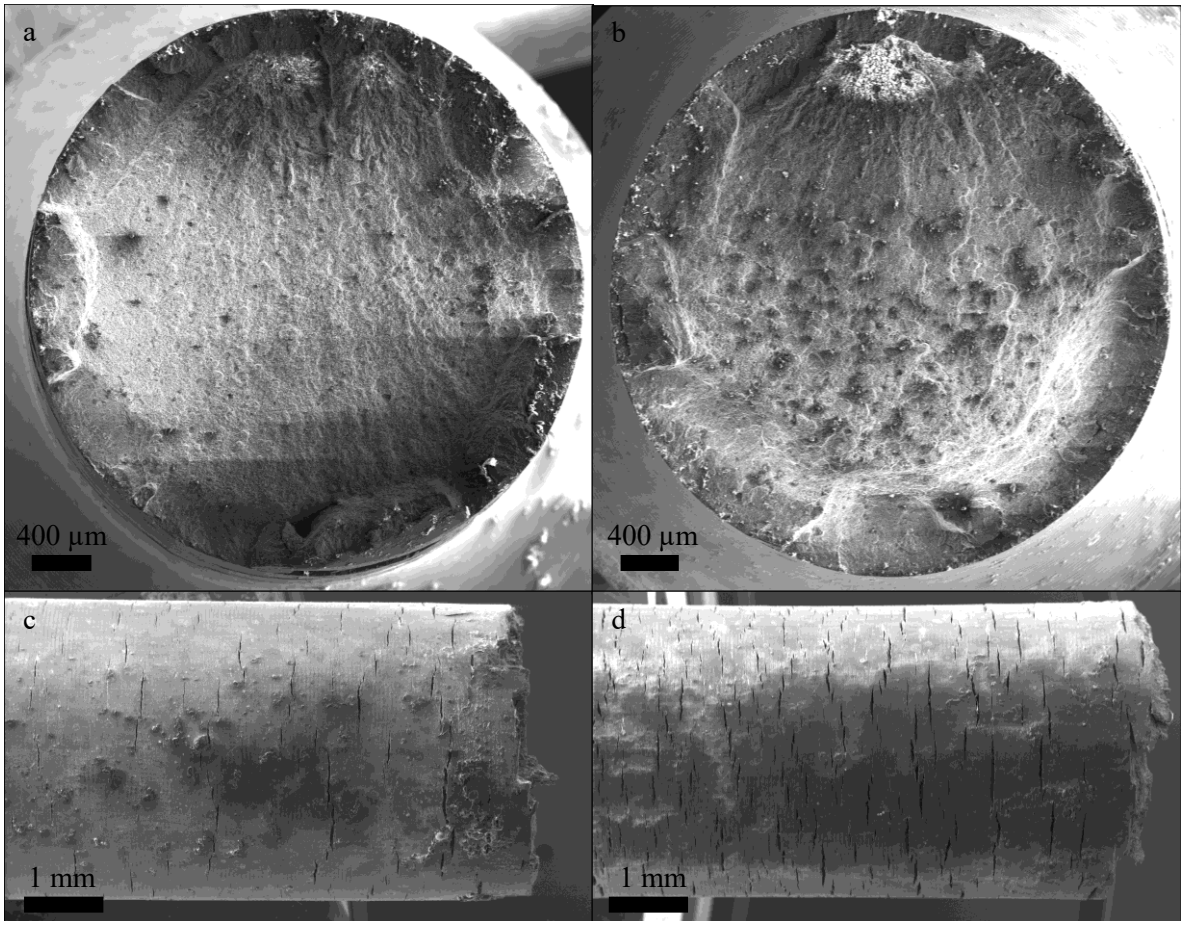

Figure G.1.: SEM images of uncoated SSRT tested specimens. Fracture surface of specimen tested at v2 (a). Fracture surface of specimen tested at v3 (b). Side view of specimen tested at v2 (c). Side view of specimen tested at v3 (d).

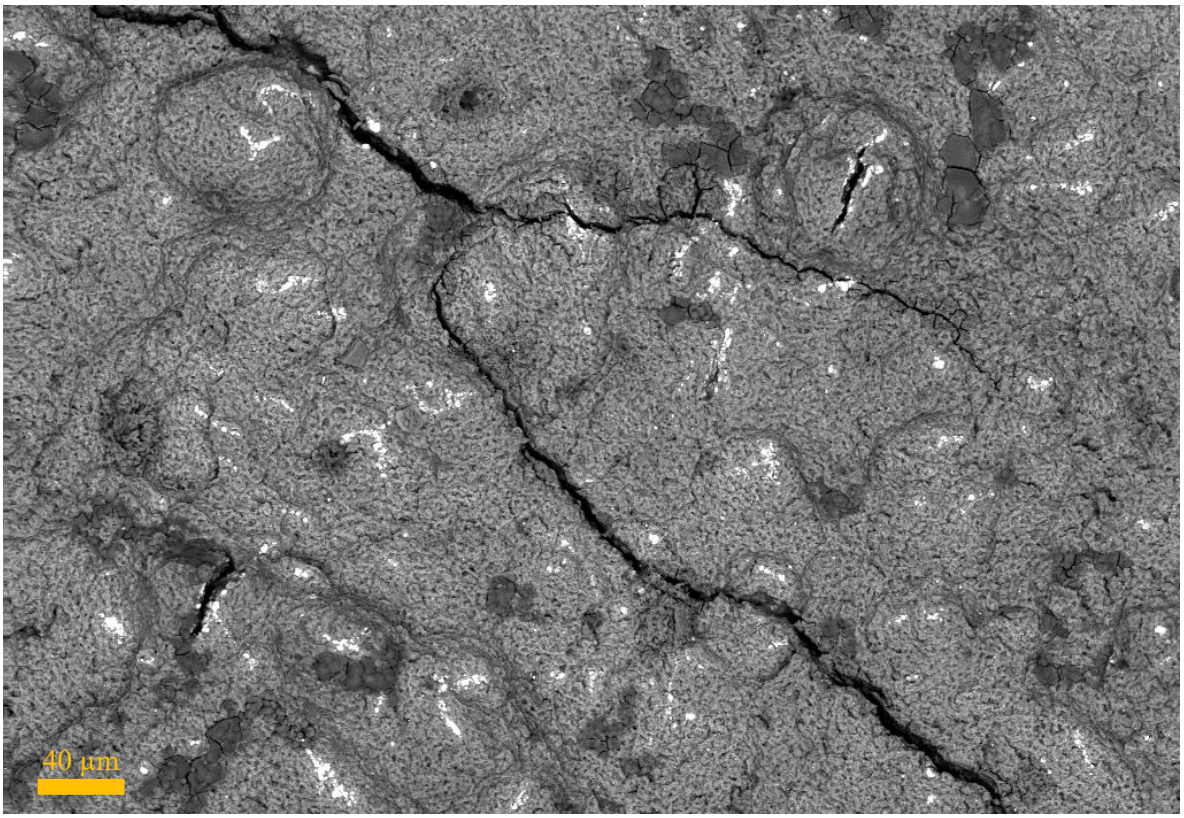

Figure G.2.: Large secondary crack in the central region of the fracture surface of an uncoated SSRT specimen tested at v3 and shown in Figure G.1b.

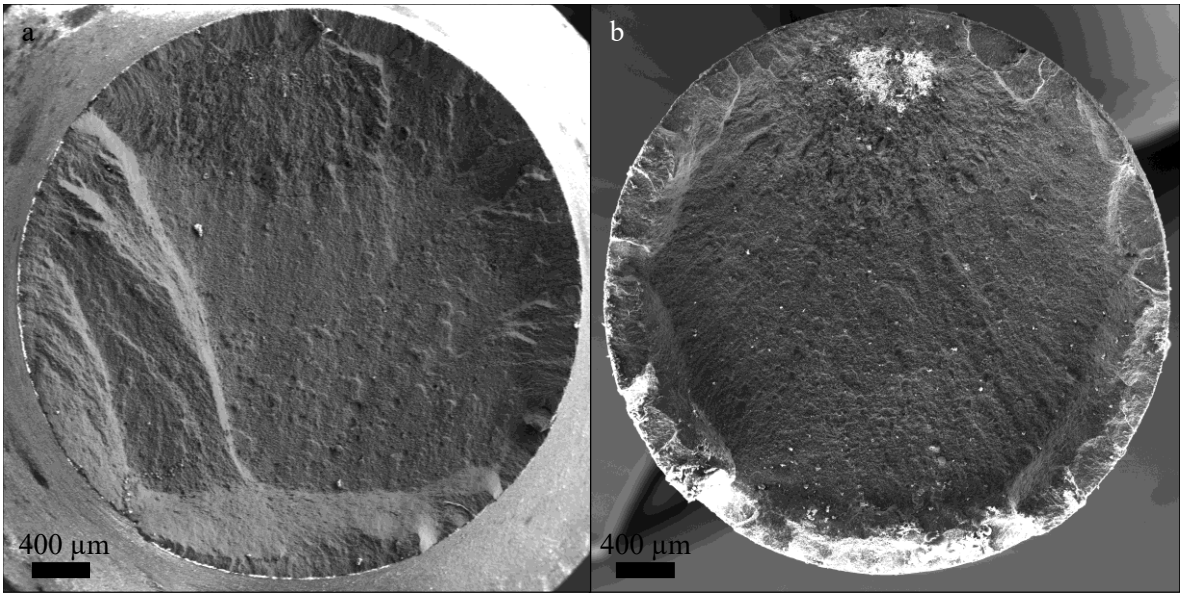

Figure G.3.: SEM images of PEO-coated SSRT specimens. Fracture surface of specimen tested at v2 (a). Fracture surface of specimen tested at v3 (b).

Bibliography

[1] Abidin, N. I. Z.; Rolfe, B.; Owen, H.; Malisano, J.; Martin, D.; Hofstetter, J.; Uggowitzer, P. J. & Atrens, A.: The in vivo and in vitro corrosion of high-purity magnesium and magnesium alloys WZ21 and AZ91. *Corrosion Science* **75** (2013), 354–366, ISSN 0010938X.

[2] Agarwal, S.; Curtin, J.; Duffy, B. & Jaiswal, S.: Biodegradable magnesium alloys for orthopaedic applications: A review on corrosion, biocompatibility and surface modifications. *Materials Science and Engineering C* **68** (2016), 948–963, ISSN 09284931.

[3] Altun, H. & Sen, S.: Studies on the influence of chloride ion concentration and pH on the corrosion and electrochemical behaviour of AZ63 magnesium alloy. *Materials and Design* **25** (2004), 637–643, ISSN 18734197.

[4] Arrabal, R.; Matykina, E.; Hashimoto, T.; Skeldon, P. & Thompson, G. E.: Characterization of AC PEO coatings on magnesium alloys. *Surface and Coatings Technology* **203** (2009), 2207–2220, ISSN 02578972.

[5] Arrabal, R.; Matykina, E.; Skeldon, P.; Thompson, G. E. & Pardo, A.: Transport of Species during Plasma Electrolytic Oxidation of WE43-T6 Magnesium Alloy. *Journal of The Electrochemical Society* **155** (2008), C101, ISSN 00134651.

[6] Arrabal, R.; Matykina, E.; Viejo, F.; Skeldon, P. & Thompson, G. E.: Corrosion resistance of WE43 and AZ91D magnesium alloys with phosphate PEO coatings. *Corrosion Science* **50** (2008), 1744–1752, ISSN 0010938X.

[7] Ascencio, M.; Pekguleryuz, M. & Omanovic, S.: An investigation of the corrosion mechanisms of WE43 Mg alloy in a modified simulated body fluid solution: The influence of immersion time. *Corrosion Science* **87** (2014), 489–503, ISSN 0010938X.

[8] Atrens, A.; Shi, Z.; Mehreen, S. U.; Johnston, S.; Song, G. L.; Chen, X. & Pan, F.: Review of Mg alloy corrosion rates. *Journal of Magnesium and Alloys* **8** (2020), 989–998, ISSN 22139567.

[9] Aung, N. N. & Zhou, W.: Effect of grain size and twins on corrosion behaviour of AZ31B magnesium alloy. *Corrosion Science* **52** (2010), 589–594, ISSN 0010938X.

[10] Bahmanabadi, H. & Shamsarjmand, M.: Modeling of fatigue behavior in pre-corroded AZ31 magnesium alloy. *Forces in Mechanics* **14** (2024), ISSN 26663597.

[11] Bahmani, A.; Lotfpour, M.; Taghizadeh, M. & Kim, W. J.: Corrosion behavior of severely plastically deformed Mg and Mg alloys. *Journal of Magnesium and Alloys* **10** (2022), 2607–2648, ISSN 22139567.

[12] Basquin, O. H.: The experimental law of endurance tests. 1969, p. 625.

[13] Beachem, C. D.: A New Model for Hydrogen-Assisted Cracking (Hydrogen "Embrittlement"). *Metallurgical and Materials Transactions B* **3** (1972), 441–455.

[14] Bhuiyan, M. S.; Mutoh, Y.; Murai, T. & Iwakami, S.: Corrosion fatigue behavior

of extruded magnesium alloy AZ61 under three different corrosive environments. *International Journal of Fatigue* **30** (2008), 1756–1765, ISSN 01421123.

[15] Bian, D.; Zhou, W.; Liu, Y.; Li, N.; Zheng, Y. & Sun, Z.: Fatigue behaviors of HP-Mg, Mg–Ca and Mg–Zn–Ca biodegradable metals in air and simulated body fluid. *Acta Biomaterialia* **41** (2016), 351–360, ISSN 18787568.

[16] Boland, E. L.; Shirazi, R. N.; Grogan, J. A. & McHugh, P. E.: Mechanical and Corrosion Testing of Magnesium WE43 Specimens for Pitting Corrosion Model Calibration. *Advanced Engineering Materials* **20** (2018), ISSN 15272648.

[17] Bondy, S. C.: Low levels of aluminum can lead to behavioral and morphological changes associated with Alzheimer's disease and age-related neurodegeneration. *NeuroToxicology* **52** (2016), 222–229, ISSN 18729711.

[18] Bordbar-Khiabani, A.; Yarmand, B. & Mozafari, M.: Enhanced corrosion resistance and in-vitro biodegradation of plasma electrolytic oxidation coatings prepared on AZ91 Mg alloy using ZnO nanoparticles-incorporated electrolyte. *Surface and Coatings Technology* **360** (2019), 153–171, ISSN 02578972.

[19] Bordbar-Khiabani, A.; Yarmand, B. & Mozafari, M.: Effect of ZnO pore-sealing layer on anti-corrosion and in-vitro bioactivity behavior of plasma electrolytic oxidized AZ91 magnesium alloy. *Materials Letters* **258** (2020), ISSN 18734979.

[20] Cao, F.; Shi, Z.; Hofstetter, J.; Uggowitzer, P. J.; Song, G.; Liu, M. & Atrens, A.: Corrosion of ultra-high-purity Mg in 3.5% NaCl solution saturated with $Mg(OH)_2$. *Corrosion Science* **75** (2013), 78–99, ISSN 0010938X.

[21] Cao, G.; Zhang, D.; Zhang, W. & Zhang, W.: In vitro corrosion study of friction stir processed WE43 magnesium alloy in a simulated body fluid. *Materials* **9** (2016), ISSN 19961944.

[22] Chaharmahali, R.; Fattah-alhosseini, A. & Babaei, K.: Surface characterization and corrosion behavior of calcium phosphate (Ca-P) base composite layer on Mg and its alloys using plasma electrolytic oxidation (PEO): A review. *Journal of Magnesium and Alloys* **9** (2021), 21–40, ISSN 22139567.

[23] Chen, G.; Lu, L. T.; Cui, Y.; Xing, R. S.; Gao, H. & Chen, X.: Ratcheting and low-cycle fatigue characterizations of extruded AZ31B Mg alloy with and without corrosive environment. *International Journal of Fatigue* **80** (2015), 364–371, ISSN 01421123.

[24] Chen, J.; Xu, Y.; Kolawole, S. K.; Wang, J.; Su, X.; Tan, L. & Yang, K.: Systems, Properties, Surface Modification and Applications of Biodegradable Magnesium-Based Alloys: A Review. *Materials* **15** (2022), ISSN 19961944.

[25] Chen, K.; Lu, Y.; Tang, H.; Gao, Y.; Zhao, F.; Gu, X. & Fan, Y.: Effect of strain on degradation behaviors of WE43, Fe and Zn wires. *Acta Biomaterialia* **113** (2020), 627–645, ISSN 18787568.

[26] Chen, L.; Carsten Blawert; Yang, J.; Hou, R.; Wang, X.; Zheludkevich, M. L. & Li, W.: The stress corrosion cracking behaviour of biomedical Mg-1Zn alloy in synthetic or natural biological media. *Corrosion Science* **175** (2020), ISSN 0010938X.

[27] Chen, L.; Sheng, Y.; Zhou, H.; Li, Z.; Wang, X. & Li, W.: Influence of a MAO + PLGA coating on biocorrosion and stress corrosion cracking behavior of a magnesium alloy in a physiological environment. *Corrosion Science* **148** (2019), 134–143, ISSN 0010938X.

[28] Chen, L.; Tseng, C. M.; Qiu, Y.; Yang, J.; Chang, C. L.; Wang, X. & Li, W.: A layer-by-layer assembled coating for improved stress corrosion cracking on biomedical magnesium alloy in cell culture medium. *Surface and Coatings Technology* **403** (2020), ISSN 02578972.

[29] Choudhary, L. & Raman, R. K. S.: Mechanical integrity of magnesium alloys in a hysiological environment: Slow strain rate testing based study. *Engineering Fracture Mechanics* **103** (2013), 94–102, ISSN 00137944.

[30] Choudhary, L.; Raman, R. K. S.; Hofstetter, J. & Uggowitzer, P. J.: In-vitro characterization of stress corrosion cracking of aluminium-free magnesium alloys for temporary bio-implant applications. *Materials Science and Engineering C* **42** (2014), 629–636, ISSN 09284931.

[31] Cui, L. Y.; Hu, Y.; Zeng, R. C.; Yang, Y. X.; Sun, D. D.; Li, S. Q.; Zhang, F. & Han, E. H.: New insights into the effect of Tris-HCl and Tris on corrosion of magnesium alloy in presence of bicarbonate, sulfate, hydrogen phosphate and dihydrogen phosphate ions. *Journal of Materials Science and Technology* **33** (2017), 971–986, ISSN 10050302.

[32] Daavari, M.; Atapour, M.; Mohedano, M.; Sánchez, H. M.; Rodríguez-Hernández, J.; Matykina, E.; Arrabal, R. & Taherizadeh, A.: Quasi-in vivo corrosion behavior of AZ31B Mg alloy with hybrid MWCNTs-PEO/PCL based coatings. *Journal of Magnesium and Alloys* **10** (2022), 3217–3233, ISSN 22139567.

[33] Darband, G. B.; Aliofkhazraei, M.; Hamghalam, P. & Valizade, N.: Plasma electrolytic oxidation of magnesium and its alloys: Mechanism, properties and applications. *Journal of Magnesium and Alloys* **5** (2017), 74–132, ISSN 22139567.

[34] Darbre, P. D.; Mannello, F. & Exley, C.: Aluminium and breast cancer: Sources of exposure, tissue measurements and mechanisms of toxicological actions on breast biology. *Journal of Inorganic Biochemistry* **128** (2013), 257–261, ISSN 01620134.

[35] Das, P.; Kumar, T. S.; Sahu, K. K. & Gollapudi, S.: Corrosion, stress corrosion cracking and corrosion fatigue behavior of magnesium alloy bioimplants. *Corrosion Reviews* **40** (2022), 289–333, ISSN 03346005.

[36] Delavar, H.; Mostahsan, A. J. & Ibrahim, H.: Corrosion and corrosion-fatigue behavior of magnesium metal matrix composites for bio-implant applications: A review. *Journal of Magnesium and Alloys* **11** (2023), 1125–1161, ISSN 22139567.

[37] Dey, M. & Singh, R. K.: Neurotoxic effects of aluminium exposure as a potential risk factor for Alzheimer's disease. *Pharmacological Reports* **74** (2022), 439–450, ISSN 17341140.

[38] Dezfuli, S. N.; Huan, Z.; Mol, J. M. C.; Leeflang, M. A.; Chang, J. & Zhou, J.: Influence of HEPES buffer on the local pH and formation of surface layer during in vitro degradation tests of magnesium in DMEM. *Progress in Natural Science: Materials International* **24** (2014), 531–538, ISSN 17455391.

[39] Dietzel, W.; Srinivasan, P. B. & Atrens, A.: *Testing and evaluation methods for stress corrosion cracking (SCC) in metals*. Woodhead Publishing 2011, ISBN 978-1-84569-673-3.

[40] Dou, J.; Wang, J.; Li, H.; Lu, Y.; Yu, H. & Chen, C.: Enhanced corrosion resistance of magnesium alloy by plasma electrolytic oxidation plus hydrothermal treatment. *Surface and Coatings Technology* **424** (2021), ISSN 02578972.

[41] Dubey, D.; Kadali, K.; Panda, S. S.; Kumar, A.; Jain, J.; Mondal, K. & Singh, S. S.: Comparative study on the stress corrosion cracking susceptibility of AZ80 and AZ31 magnesium alloys. *Materials Science and Engineering: A* **792** (2020), ISSN 09215093.

[42] Fattah-alhosseini, A.; Chaharmahali, R. & Babaei, K.: Impressive strides in amelioration of corrosion and wear behaviors of Mg alloys using applied polymer coatings on PEO porous coatings: A review. *Journal of Magnesium and Alloys* **10** (2022), 1171–1190, ISSN 22139567.

[43] Fattah-alhosseini, A.; Chaharmahali, R.; Babaei, K.; Nouri, M.; Keshavarz, M. K. & Kaseem, M.: A review of effective strides in amelioration of the biocompatibility of PEO coatings on Mg alloys. *Journal of Magnesium and Alloys* **10** (2022), 2354–2383, ISSN 22139567.

[44] Fattah-alhosseini, A.; Molaei, M.; Nouri, M. & Babaei, K.: Antibacterial activity of bioceramic coatings on Mg and its alloys created by plasma electrolytic oxidation (PEO): A review. *Journal of Magnesium and Alloys* **10** (2022), 81–96, ISSN 22139567.

[45] Feng, B.; Liu, G.; Yang, P.; Huang, S.; Qi, D.; Chen, P.; Wang, C.; Du, J.; Zhang, S. & Liu, J.: Different role of second phase in the micro-galvanic corrosion of WE43 Mg alloy in NaCl and Na_2SO_4 solution. *Journal of Magnesium and Alloys* **10** (2021), 1598–1608, ISSN 22139567.

[46] Feyerabend, F.; Fischer, J.; Holtz, J.; Witte, F.; Willumeit, R.; Drücker, H.; Carla Vogt & Hort, N.: Evaluation of short-term effects of rare earth and other elements used in magnesium alloys on primary cells and cell lines. *Acta Biomaterialia* **6** (2010), 1834–1842, ISSN 17427061.

[47] Ford, E. S. & Mokdad, A. H.: Nutritional Epidemiology-Research Communication Dietary Magnesium Intake in a National Sample. *Journal of Nutrition* **133** (2003), 2879–2882.

[48] Fu, S.; Gao, H.; Chen, G.; Gao, L. & Chen, X.: Deterioration of mechanical properties for pre-corroded AZ31 sheet in simulated physiological environment. *Materials Science and Engineering: A* **593** (2014), 153–162, ISSN 09215093.

[49] van Gaalen, K.; Quinn, C.; Benn, F.; McHugh, P. E.; Kopp, A. & Vaughan, T. J.: Linking the effect of localised pitting corrosion with mechanical integrity of a rare earth magnesium alloy for implant use. *Bioactive Materials* **21** (2023), 32–43, ISSN 2452199X.

[50] van Gaalen, K.; Quinn, C.; Weiler, M.; Gremse, F.; Benn, F.; McHugh, P. E.; Vaughan, T. J. & Kopp, A.: Predicting localised corrosion and mechanical performance of a PEO surface modified rare earth magnesium alloy for implant

use through in-silico modelling. *Bioactive Materials* **26** (2023), 437–451, ISSN 2452199X.

[51] Galvin, E.; Cummins, C.; Yoshihara, S.; Donald, B. J. M. & Caitríona Lally: Plastic strains during stent deployment have a critical influence on the rate of corrosion in absorbable magnesium stents. *Medical and Biological Engineering and Computing* **55** (2017), 1261–1275, ISSN 17410444.

[52] Gangloff, R. P. & Somerday, B. P.: *Gaseous hydrogen embrittlement of materials in energy technologies. Volume 1, The problem, its characterisation and effects on particular alloy classes*. Woodhead Publishing Ltd 2012, ISBN 9781845696771.

[53] Gao, Y.; Wang, L.; Li, L.; Gu, X.; Zhang, K.; Xia, J. & Fan, Y.: Effect of stress on corrosion of high-purity magnesium in vitro and in vivo. *Acta Biomaterialia* **83** (2019), 477–486, ISSN 18787568.

[54] Ghorbanpour, S.; McWilliams, B. A. & Knezevic, M.: Low-cycle fatigue behavior of rolled WE43-T5 magnesium alloy. *Fatigue and Fracture of Engineering Materials and Structures* **42** (2019), 1357–1372, ISSN 14602695.

[55] Gu, X.; Zheng, Y.; Cheng, Y.; Zhong, S. & Xi, T.: In vitro corrosion and biocompatibility of binary magnesium alloys. *Biomaterials* **30** (2009), 484–498, ISSN 01429612.

[56] Gu, X. N. & Zheng, Y. F.: A review on magnesium alloys as biodegradable materials. *Frontiers of Materials Science in China* **4** (2010), 111–115, ISSN 16737377.

[57] Gu, X. N.; Zhou, W. R.; Zheng, Y. F.; Cheng, Y.; Wei, S. C.; Zhong, S. P.; Xi, T. F. & Chen, L. J.: Corrosion fatigue behaviors of two biomedical Mg alloys - AZ91D and WE43 - in simulated body fluid. *Acta Biomaterialia* **6** (2010), 4605–4613, ISSN 17427061.

[58] Guo, L. F.; Yue, T. M. & Man, H. C.: Excimer laser surface treatment of magnesium alloy WE43 for corrosion resistance improvement. *Journal of Materials Science* **40** (2005), 3531–3533, ISSN 00222461.

[59] Guo, T.; Chen, Y.; Cao, R.; Pang, X.; He, J. & Qiao, L.: Cleavage cracking of ductile-metal substrates induced by brittle coating fracture. *Acta Materialia* **152** (2018), 77–85, ISSN 13596454.

[60] Harandi, S. E.; Banerjee, P. C.; Easton, C. D. & Raman, R. K. S.: Influence of bovine serum albumin in Hanks' solution on the corrosion and stress corrosion cracking of a magnesium alloy. *Materials Science and Engineering C* **80** (2017), 335–345, ISSN 09284931.

[61] Harandi, S. E. & Raman, R. K. S.: Corrosion fatigue of a magnesium alloy under appropriate human physiological conditions for bio-implant applications. *Engineering Fracture Mechanics* **186** (2017), 134–142, ISSN 00137944.

[62] He, L.; Yang, J.; Xiong, Y. & Song, R.: Effect of solution pH on stress corrosion cracking behavior of modified AZ80 magnesium alloy in simulated body fluid. *Materials Chemistry and Physics* **261** (2021), ISSN 02540584.

[63] Hirano, S. & Suzuki, K. T.: Exposure, Metabolism, and Toxicity of Rare Earths

and Related Compounds. *Environ Health Perspect* **104** (1996), 85–95.

[64] Hou, R. Q.; Scharnagl, N.; Willumeit-Römer, R. & Feyerabend, F.: Different effects of single protein vs. protein mixtures on magnesium degradation under cell culture conditions. *Acta Biomaterialia* **98** (2019), 256–268, ISSN 18787568.

[65] Hussein, R. O.; Nie, X. & Northwood, D. O.: An investigation of ceramic coating growth mechanisms in plasma electrolytic oxidation (PEO) processing. *Electrochimica Acta* **112** (2013), 111–119, ISSN 00134686.

[66] Hussein, R. O.; Northwood, D. O. & Nie, X.: The influence of pulse timing and current mode on the microstructure and corrosion behaviour of a plasma electrolytic oxidation (PEO) coated AM60B magnesium alloy. *Journal of Alloys and Compounds* **541** (2012), 41–48, ISSN 09258388.

[67] Hussein, R. O.; Northwood, D. O. & Nie, X.: Processing-Microstructure Relationships in the Plasma Electrolytic Oxidation (PEO) Coating of a Magnesium Alloy. *Materials Sciences and Applications* **05** (2014), 124–139, ISSN 2153-117X.

[68] Hussein, R. O.; Northwood, D. O.; Su, J. F. & Nie, X.: A study of the interactive effects of hybrid current modes on the tribological properties of a PEO (plasma electrolytic oxidation) coated AM60B Mg-alloy. *Surface and Coatings Technology* **215** (2013), 421–430, ISSN 02578972.

[69] Hänninen, H. E.: Initiation of Stress Corrosion Cracking of Austenitic Stainless Steels in Hot Chloride Solutions. *Proceedings on an international conference organized by The Metals Society* (1977).

[70] Höhlinger, M.; Christa, D.; Zimmermann, V.; Heise, S.; Boccaccini, A. R. & Virtanen, S.: Influence of proteins on the corrosion behavior of a chitosan-bioactive glass coated magnesium alloy. *Materials Science and Engineering C* **100** (2019), 706–714, ISSN 18730191.

[71] Imwinkelried, T.; Beck, S.; Iizuka, T. & Schaller, B.: Effect of a plasmaelectrolytic coating on the strength retention of in vivo and in vitro degraded magnesium implants. *Acta Biomaterialia* **9** (2013), 8643–8649, ISSN 17427061.

[72] Jafari, S.; Harandi, S. E. & Raman, R. K. S.: A review of stress-corrosion cracking and corrosion fatigue of magnesium alloys for biodegradable implant applications. *JOM* **67** (2015), 1143–1153, ISSN 15431851.

[73] Jafari, S.; Raman, R. K. & Davies, C. H.: Stress corrosion cracking of an extruded magnesium alloy (ZK21) in a simulated body fluid. *Engineering Fracture Mechanics* **201** (2018), 47–55, ISSN 00137944.

[74] Jafari, S.; Raman, R. K.; Davies, C. H.; Hofstetter, J.; Uggowitzer, P. J. & Löffler, J. F.: Stress corrosion cracking and corrosion fatigue characterisation of MgZn1Ca0.3 (ZX10) in a simulated physiological environment. *Journal of the Mechanical Behavior of Biomedical Materials* **65** (2017), 634–643, ISSN 18780180.

[75] Jafari, S.; Raman, R. K. S. & Davies, C. H.: Corrosion fatigue of a magnesium alloy in modified simulated body fluid. *Engineering Fracture Mechanics* **137** (2015), 2–11, ISSN 00137944.

[76] Jiang, H. S.; Zheng, M. Y.; Qiao, X. G.; Wu, K.; Peng, Q. Y.; Yang, S. H.; Yuan,

Y. H. & Luo, J. H.: Microstructure and mechanical properties of WE43 magnesium alloy fabricated by direct-chill casting. *Materials Science and Engineering: A* **684** (2017), 158–164, ISSN 09215093.

[77] Jiang, J.; Xie, Q.; Qiang, M.; Ma, A.; Taylor, E. K.; Li, Y.; Song, D. & Chen, J.: Stress corrosion cracking behaviors of RE-containing ME21 magnesium alloy processed by equal-channel angular pressing. *Journal of Rare Earths* **37** (2019), 88–94, ISSN 10020721.

[78] Jin, W.; Wu, G.; Feng, H.; Wang, W.; Zhang, X. & Chu, P. K.: Improvement of corrosion resistance and biocompatibility of rare-earth WE43 magnesium alloy by neodymium self-ion implantation. *Corrosion Science* **94** (2015), 142–155, ISSN 0010938X.

[79] Johnston, S.; Dargusch, M. & Atrens, A.: Building towards a standardised approach to biocorrosion studies: a review of factors influencing Mg corrosion in vitro pertinent to in vivo corrosion. *Science China Materials* **61** (2018), 475–500, ISSN 21994501.

[80] Jones, D. A.: *Principles and Prevention of CORROSION*. Prentice-Hall, Inc. 1996, 2nd edn.

[81] Kalb, H.; Rzany, A. & Hensel, B.: Impact of microgalvanic corrosion on the degradation morphology of WE43 and pure magnesium under exposure to simulated body fluid. *Corrosion Science* **57** (2012), 122–130, ISSN 0010938X.

[82] Kannan, M. B.; Khakbaz, H. & Yamamoto, A.: Understanding the influence of HEPES buffer concentration on the biodegradation of pure magnesium: An electrochemical study. *Materials Chemistry and Physics* **197** (2017), 47–56, ISSN 02540584.

[83] Kannan, M. B. & Raman, R. K.: In vitro degradation and mechanical integrity of calcium-containing magnesium alloys in modified-simulated body fluid. *Biomaterials* **29** (2008), 2306–2314, ISSN 01429612.

[84] Kappes, M.; Iannuzzi, M. & Carranza, R. M.: Hydrogen Embrittlement of Magnesium and Magnesium Alloys: A Review. *Journal of The Electrochemical Society* **160** (2013), C168–C178, ISSN 0013-4651.

[85] Kappes, M.; Iannuzzi, M. & Carranza, R. M.: Pre-exposure embrittlement and stress corrosion cracking of magnesium alloy AZ31B in chloride solutions. *Corrosion* **70** (2014), 667–677, ISSN 00109312.

[86] Khan, R. H.; Yerokhin, A. L.; Pilkington, T.; Leyland, A. & Matthews, A.: Residual stresses in plasma electrolytic oxidation coatings on Al alloy produced by pulsed unipolar current. *Surface and Coatings Technology* **200** (2005), 1580–1586, ISSN 02578972.

[87] Kirkland, N. T.; Birbilis, N. & Staiger, M. P.: Assessing the corrosion of biodegradable magnesium implants: A critical review of current methodologies and their limitations. *Acta Biomaterialia* **8** (2012), 925–936, ISSN 18787568.

[88] Kopp, A.; Derra, T.; Müther, M.; Jauer, L.; Schleifenbaum, J. H.; Voshage, M.; Jung, O.; Smeets, R. & Kröger, N.: Influence of design and postprocessing

parameters on the degradation behavior and mechanical properties of additively manufactured magnesium scaffolds. *Acta Biomaterialia* **98** (2019), 23–35, ISSN 18787568.

[89] Lamaka, S. V.; Gonzalez, J.; Mei, D.; Feyerabend, F.; Willumeit-Römer, R. & Zheludkevich, M. L.: Local pH and Its Evolution Near Mg Alloy Surfaces Exposed to Simulated Body Fluids. *Advanced Materials Interfaces* **5** (2018), ISSN 21967350.

[90] Lamaka, S. V.; Vaghefinazari, B.; Mei, D.; Petrauskas, R. P.; Höche, D. & Zheludkevich, M. L.: Comprehensive screening of Mg corrosion inhibitors. *Corrosion Science* **128** (2017), 224–240, ISSN 0010938X.

[91] Leleu, S.; Rives, B.; Causse, N. & Pébère, N.: Corrosion rate determination of rare-earth Mg alloys in a Na_2SO_4 solution by electrochemical measurements and inductive coupled plasma-optical emission spectroscopy. *Journal of Magnesium and Alloys* **7** (2019), 47–57, ISSN 22139567.

[92] Li, M.; Cheng, Y.; Zheng, Y. F.; Zhang, X.; Xi, T. F. & Wei, S. C.: Surface characteristics and corrosion behaviour of WE43 magnesium alloy coated by SiC film. *Applied Surface Science* **258** (2012), 3074–3081, ISSN 01694332.

[93] Li, P.; Yang, Z.; He, B.; Wang, N.; Chen, Y.; Zhao, Q.; Kang, Y.; Zhang, X. & Zhao, Y.: Effect of local 'over-growth' on fracture behaviors of coated titanium fiber fabricated by plasma electrolytic oxidation. *Surfaces and Interfaces* **36** (2023), ISSN 24680230.

[94] Li, Y.; Jahr, H.; Zhang, X. Y.; Leeflang, M. A.; Li, W.; Pouran, B.; Tichelaar, F. D.; Weinans, H.; Zhou, J. & Zadpoor, A. A.: Biodegradation-affected fatigue behavior of additively manufactured porous magnesium. *Additive Manufacturing* **28** (2019), 299–311, ISSN 22148604.

[95] Li, Y.; Lu, F.; Li, H.; Zhu, W.; Pan, H.; Tan, G.; Lao, Y.; Ning, C. & Ni, G.: Corrosion mechanism of micro-arc oxidation treated biocompatible AZ31 magnesium alloy in simulated body fluid. *Progress in Natural Science: Materials International* **24** (2014), 516–522, ISSN 17455391.

[96] Lin, X.; Tan, L.; Zhang, Q.; Yang, K.; Hu, Z.; Qiu, J. & Cai, Y.: The in vitro degradation process and biocompatibility of a ZK60 magnesium alloy with a forsterite-containing micro-arc oxidation coating. *Acta Biomaterialia* **9** (2013), 8631–8642, ISSN 18787568.

[97] Lin, Y. C.; Chen, X. M.; Liu, Z. H. & Chen, J.: Investigation of uniaxial low-cycle fatigue failure behavior of hot-rolled AZ91 magnesium alloy. *International Journal of Fatigue* **48** (2013), 122–132, ISSN 01421123.

[98] Lin, Y. C.; Liu, Z. H.; Chen, X. M. & Chen, J.: Stress-based fatigue life prediction models for AZ31B magnesium alloy under single-step and multi-step asymmetric stress-controlled cyclic loadings. *Computational Materials Science* **73** (2013), 128–138, ISSN 09270256.

[99] Lin, Y. C.; Liu, Z. H.; Chen, X. M. & Chen, J.: Uniaxial ratcheting and fatigue failure behaviors of hot-rolled AZ31B magnesium alloy under asymmetrical cyclic stress-controlled loadings. *Materials Science and Engineering: A* **573** (2013), 234–244, ISSN 09215093.

[100] Linderov, M.; Brilevsky, A.; Merson, D.; Danyuk, A. & Vinogradov, A.: On the Corrosion Fatigue of Magnesium Alloys Aimed at Biomedical Applications: New Insights from the Influence of Testing Frequency and Surface Modification of the Alloy ZK60. *Materials* **15** (2022), ISSN 19961944.

[101] Linderov, M.; Vasilev, E.; Merson, D.; Markushev, M. & Vinogradov, A.: Corrosion fatigue of fine grain Mg-Zn-Zr and Mg-Y-Zn alloys. *Metals* **8** (2018), ISSN 20754701.

[102] Liu, J.; Liu, B.; Min, S.; Yin, B.; Peng, B.; Yu, Z.; Caimei Wang; Ma, X.; Wen, P.; Tian, Y. & Zheng, Y.: Biodegradable magnesium alloy WE43 porous scaffolds fabricated by laser powder bed fusion for orthopedic applications: Process optimization, in vitro and in vivo investigation. *Bioactive Materials* **16** (2022), 301–319, ISSN 2452199X.

[103] Liu, L.; Gebresellasie, K.; Collins, B.; Zhang, H.; Xu, Z.; Sankar, J.; Lee, Y. C. & Yun, Y.: Degradation rates of pure zinc, magnesium, and magnesium alloys measured by volume loss, mass loss, and hydrogen evolution. *Applied Sciences* **8** (2018), ISSN 20763417.

[104] Liu, M.; Wang, J.; Zhu, S.; Zhang, Y.; Sun, Y.; Wang, L. & Guan, S.: Corrosion fatigue of the extruded Mg–Zn–Y–Nd alloy in simulated body fluid. *Journal of Magnesium and Alloys* **8** (2020), 231–240, ISSN 22139567.

[105] Logan, H. L.: Film-Rupture Mechanism of Stress Corrosion. *Journal of Research of the National Bureau of Standards* **48** (1952).

[106] Ma, S.; Markert, B. & Yuan, H.: Multiaxial fatigue life assessment of sintered porous iron under proportional and non-proportional loadings. *International Journal of Fatigue* **97** (2017), 214–226, ISSN 01421123.

[107] Ma, W.; Liu, Y.; Wang, W. & Zhang, Y.: Effects of electrolyte component in simulated body fluid on the corrosion behavior and mechanical integrity of magnesium. *Corrosion Science* **98** (2015), 201–210, ISSN 0010938X.

[108] Mario, C. D.; Griffiths, H.; Goktekin, O.; Peeters, N.; Verbist, J.; Bosiers, M.; Deloose, K.; Heublein, B.; Rohde, R.; Kasese, V.; Ilsley, C. & Erbel, R.: Drug-eluting bioabsorbable magnesium stent. *Journal of Interventional Cardiology* **17** (2004), 391–395, ISSN 08964327.

[109] Mei, D.; Lamaka, S. V.; Feiler, C. & Zheludkevich, M. L.: The effect of small-molecule bio-relevant organic components at low concentration on the corrosion of commercially pure Mg and Mg-0.8Ca alloy: An overall perspective. *Corrosion Science* **153** (2019), 258–271, ISSN 0010938X.

[110] Mei, D.; Lamaka, S. V.; Gonzalez, J.; Feyerabend, F.; Willumeit-Römer, R. & Zheludkevich, M. L.: The role of individual components of simulated body fluid on the corrosion behavior of commercially pure Mg. *Corrosion Science* **147** (2019), 81–93, ISSN 0010938X.

[111] Mei, D.; Lamaka, S. V.; Lu, X. & Zheludkevich, M. L.: Selecting medium for corrosion testing of bioabsorbable magnesium and other metals – A critical review. *Corrosion Science* **171** (2020), ISSN 0010938X.

[112] Mei, T.; Wang, Q.; Liu, M.; Jiang, Y.; Zou, T. & Cai, Y.: The Low-Cycle Fatigue Behavior, Microstructure Evolution, and Life Prediction of SS304: Influence of Temperature. *Materials* **16** (2023), ISSN 19961944.

[113] Meng, Y.; Gao, H.; Hu, J. & Gao, L.: Effect of pH value on the corrosion and corrosion fatigue behavior of AM60 magnesium alloy. *Journal of Materials Research* **34** (2019), 1054–1063, ISSN 20445326.

[114] Milkereit, B.; Burgschat, L.; Kemsies, R. H.; Springer, A.; Schick, C. & Kessler, O.: In situ differential scanning calorimetry analysis of dissolution and precipitation kinetics in Mg–Y–RE alloy WE43. *Journal of Magnesium and Alloys* **7** (2019), 1–14, ISSN 22139567.

[115] Mirza, F. & Chen, D.: Fatigue of rare-earth containing magnesium alloys: a review. *Fatigue & Fracture of Engineering Materials & Structures* **37** (2014), 831–853, ISSN 8756-758X.

[116] Mo, N.; Tan, Q.; Bermingham, M.; Huang, Y.; Dieringa, H.; Hort, N. & Zhang, M. X.: Current development of creep-resistant magnesium cast alloys: A review. *Materials and Design* **155** (2018), 422–442, ISSN 18734197.

[117] Molaei, M.; Babaei, K. & Fattah-alhosseini, A.: Improving the wear resistance of plasma electrolytic oxidation (PEO) coatings applied on Mg and its alloys under the addition of nano- and micro-sized additives into the electrolytes: A review. *Journal of Magnesium and Alloys* **9** (2021), 1164–1186, ISSN 22139567.

[118] Nachtsheim, J.; Burja, J.; Ma, S. & Markert, B.: Long-Term in Vitro Corrosion of Biodegradable WE43 Magnesium Alloy in DMEM. *Metals* **12** (2022), ISSN 20754701.

[119] Nachtsheim, J.; Burja, J.; Ma, S. & Markert, B.: In vitro degradation behaviour of biodegradable magnesium alloys. *PAMM* **22** (2023), ISSN 1617-7061.

[120] Nachtsheim, J.; Ma, S.; Burja, J.; Šetina Batič, B. & Markert, B.: Tuning the long-term corrosion behaviour of biodegradable WE43 magnesium alloy by PEO coating. *Surface and Coatings Technology* **474** (2023), 130115, ISSN 02578972.

[121] Nachtsheim, J.; Ma, S.; Burja, J.; Kopp, A.; Seitz, J.-M. & Markert, B.: In vitro corrosion-fatigue behaviour of rare-earth containing magnesium WE43 in sterile complex cell culture medium. *International Journal of Fatigue* **188** (2024), 108531, ISSN 0142-1123.

[122] Nachtsheim, J.; Ma, S.; Burja, J. & Markert, B.: In vitro evaluation of stress corrosion cracking susceptibility of PEO-coated rare-earth magnesium alloy WE43. *Surface and Coatings Technology* **477** (2024), ISSN 02578972.

[123] Nominé, A.; Troughton, S. C.; Nominé, A. V.; Henrion, G. & Clyne, T. W.: High speed video evidence for localised discharge cascades during plasma electrolytic oxidation. *Surface and Coatings Technology* **269** (2015), 125–130, ISSN 02578972.

[124] Němcová, A.; Skeldon, P.; Thompson, G. E.; Morse, S.; Čížek, J. & Pacal, B.: Influence of plasma electrolytic oxidation on fatigue performance of AZ61 magnesium alloy. *Corrosion Science* **82** (2014), 58–66, ISSN 0010938X.

[125] Olugbade, T. O.; Omiyale, B. O. & Ojo, O. T.: Corrosion, Corrosion Fatigue, and

Protection of Magnesium Alloys: Mechanisms, Measurements, and Mitigation. *Journal of Materials Engineering and Performance* **31** (2022), 1707–1727, ISSN 15441024.

[126] Oshibe, N.; Marukawa, E.; Yoda, T. & Harada, H.: Degradation and interaction with bone of magnesium alloy WE43 implants: A long-term follow-up in vivo rat tibia study. *Journal of Biomaterials Applications* **33** (2019), 1157–1167, ISSN 15308022.

[127] Pagano, G.; Guida, M.; Tommasi, F. & Oral, R.: Health effects and toxicity mechanisms of rare earth elements-Knowledge gaps and research prospects. *Ecotoxicology and Environmental Safety* **115** (2015), 40–48, ISSN 10902414.

[128] Panindre, A. M.; Raja, V. S. & Krishnan, M. A.: Explanation for anomalous environmentally assisted cracking behaviour of a wrought Mg–Mn alloy in chloride medium. *Corrosion Science* **115** (2017), 8–17, ISSN 0010938X.

[129] Pereira, G. S.; Koga, G. Y.; Avila, J. A.; Bittencourt, I. M.; Fernandez, F.; Miyazaki, M. H.; Botta, W. J. & Filho, W. W. B.: Corrosion resistance of WE43 Mg alloy in sodium chloride solution. *Materials Chemistry and Physics* **272** (2021), ISSN 02540584.

[130] Peron, M.; Bertolini, R.; Ghiotti, A.; Torgersen, J.; Bruschi, S. & Berto, F.: Enhancement of stress corrosion cracking of AZ31 magnesium alloy in simulated body fluid thanks to cryogenic machining. *Journal of the Mechanical Behavior of Biomedical Materials* **101** (2020), ISSN 18780180.

[131] Peron, M.; Skaret, P. C.; Fabrizi, A.; Varone, A.; Montanari, R.; Roven, H. J.; Ferro, P.; Berto, F. & Torgersen, J.: The effect of Equal Channel Angular Pressing on the stress corrosion cracking susceptibility of AZ31 alloy in simulated body fluid. *Journal of the Mechanical Behavior of Biomedical Materials* **106** (2020), ISSN 18780180.

[132] Pompa, L.; Rahman, Z. U.; Munoz, E. & Haider, W.: Surface characterization and cytotoxicity response of biodegradable magnesium alloys. *Materials Science and Engineering C* **49** (2015), 761–768, ISSN 09284931.

[133] Pourbaix, M.: *Atlas of Electrochemical Equilibria in Aqueous Solutions*. 1974, 2nd edn.

[134] Raja, V. S. & Padekar, B. S.: Role of chlorides on pitting and hydrogen embrittlement of Mg-Mn wrought alloy. *Corrosion Science* **75** (2013), 176–183, ISSN 0010938X.

[135] Raman, R. K. S.; Jafari, S. & Harandi, S. E.: Corrosion fatigue fracture of magnesium alloys in bioimplant applications: A review. *Engineering Fracture Mechanics* **137** (2015), 97–108, ISSN 00137944.

[136] Rendenbach, C.; Fischer, H.; Kopp, A.; Schmidt-Bleek, K.; Kreiker, H.; Stumpp, S.; Thiele, M.; Duda, G.; Hanken, H.; Beck-Broichsitter, B.; Jung, O.; Kröger, N.; Smeets, R. & Heiland, M.: Improved in vivo osseointegration and degradation behavior of PEO surface-modified WE43 magnesium plates and screws after 6 and 12 months. *Materials Science and Engineering C* **129** (2021), ISSN 18730191.

[137] Rokhlin, L. L.: *Magnesium alloys containing rare earth metals: structure and properties*. Crc Press 2003, 1st edn.

[138] Saha, S.; Lestari, W.; Caroline Dini; Sarian, M. N.; Hermawan, H.; Barão, V. A.; Sukotjo, C. & Takoudis, C.: Corrosion in Mg-alloy biomedical implants-the strategies to reduce the impact of the corrosion inflammatory reaction and microbial activity. *Journal of Magnesium and Alloys* **10** (2022), 3306–3326, ISSN 22139567.

[139] Sanchez, A. H. M.; Luthringer, B. J.; Feyerabend, F. & Willumeit, R.: Mg and Mg alloys: How comparable are in vitro and in vivo corrosion rates? A review. *Acta Biomaterialia* **13** (2015), 16–31, ISSN 18787568.

[140] Schindelin, J.; Arganda-Carreras, I.; Frise, E.; Kaynig, V.; Longair, M.; Pietzsch, T.; Preibisch, S.; Rueden, C.; Saalfeld, S.; Schmid, B.; Tinevez, J. Y.; White, D. J.; Hartenstein, V.; Eliceiri, K.; Tomancak, P. & Cardona, A.: Fiji: An open-source platform for biological-image analysis. *Nature Methods* **9** (2012), 676–682, ISSN 15487091.

[141] Schwarz, M. L.; Kowarsch, M.; Rose, S.; Becker, K.; Lenz, T. & Jani, L.: Effect of surface roughness, porosity, and a resorbable calcium phosphate coating on osseointegration of titanium in a minipig model. *Journal of Biomedical Materials Research - Part A* **89** (2009), 667–678, ISSN 15493296.

[142] Sekar, P.; S, N. & Desai, V.: Recent progress in in vivo studies and clinical applications of magnesium based biodegradable implants – A review. *Journal of Magnesium and Alloys* **9** (2021), 1147–1163, ISSN 22139567.

[143] Shi, Z. & Atrens, A.: An innovative specimen configuration for the study of Mg corrosion. *Corrosion Science* **53** (2011), 226–246, ISSN 0010938X.

[144] Shi, Z.; Hofstetter, J.; Cao, F.; Uggowitzer, P. J.; Dargusch, M. S. & Atrens, A.: Corrosion and stress corrosion cracking of ultra-high-purity Mg5Zn. *Corrosion Science* **93** (2015), 330–335, ISSN 0010938X.

[145] Shih, C. H.; Huang, C. Y.; Hsiao, T. H. & Lin, C. S.: The effect of the secondary phases on the corrosion of AZ31B and WE43-T5 Mg alloys. *Corrosion Science* **211** (2023), ISSN 0010938X.

[146] Sikdar, S.; Menezes, P. V.; Maccione, R.; Jacob, T. & Menezes, P. L.: Plasma electrolytic oxidation (PEO) process—processing, properties, and applications. *Nanomaterials* **11** (2021), ISSN 20794991.

[147] Song, G.: Control of biodegradation of biocompatable magnesium alloys. *Corrosion Science* **49** (2007), 1696–1701, ISSN 0010938X.

[148] Srinivasan, P. B.; Blawert, C.; Dietzel, W. & Kainer, K. U.: Stress corrosion cracking behaviour of a surface-modified magnesium alloy. *Scripta Materialia* **59** (2008), 43–46, ISSN 13596462.

[149] Srinivasan, P. B.; Riekehr, S.; Blawert, C.; Dietzel, W. & Koçak, M.: Slow strain rate stress corrosion cracking behaviour of as-welded and plasma electrolytic oxidation treated AZ31HP magnesium alloy autogenous laser beam weldment. *Materials Science and Engineering A* **517** (2009), 197–203, ISSN 09215093.

[150] Staiger, M. P.; Pietak, A. M.; Huadmai, J. & Dias, G.: Magnesium and its alloys as orthopedic biomaterials: A review. *Biomaterials* **27** (2006), 1728–1734, ISSN 01429612.

[151] Sun, Y.; Helmholz, H. & Willumeit-Römer, R.: Preclinical in vivo research of magnesium-based implants for fracture treatment: A systematic review of animal model selection and study design. *Journal of Magnesium and Alloys* **9** (2021), 351–361, ISSN 22139567.

[152] Talesh, S. A. A. & Azadi, M.: High-cycle fatigue testing on AM60 magnesium alloy samples for as-received and pre-corroded conditions in simulated body fluid. *Journal of Materials Research and Technology* **27** (2023), 1922–1934, ISSN 22387854.

[153] Tang, G.; Liu, C.; Xin, Y.; Chu, P. K.; Zhang, X. & Tian, X.: Corrosion behavior of biomedical AZ91 magnesium alloy in simulated body fluids. *Journal of Materials Research* **22** (2007), 2004–2011, ISSN 0884-2914.

[154] Tekin, K. C.; Malayoğlu, U. & Shrestha, S.: Electrochemical behavior of plasma electrolytic oxide coatings on rare earth element containing Mg alloys. *Surface and Coatings Technology* **236** (2013), 540–549, ISSN 02578972.

[155] Tie, D.; Feyerabend, F.; Hort, N.; Willumeit, R. & Hoeche, D.: XPS studies of magnesium surfaces after exposure to Dulbecco's modified eagle medium, Hank's buffered salt solution, and simulated body fluid. *Advanced Engineering Materials* **12** (2010), ISSN 14381656.

[156] Trivedi, P.; Nune, K. C. & Misra, R. D.: Degradation behaviour of magnesium-rare earth biomedical alloys. *Materials Technology* **31** (2016), 726–731, ISSN 17535557.

[157] Tsakiris, V.; Tardei, C. & Clicinschi, F. M.: Biodegradable Mg alloys for orthopedic implants – A review. *Journal of Magnesium and Alloys* **9** (2021), 1884–1905, ISSN 22139567.

[158] Törne, K.; Örnberg, A. & Weissenrieder, J.: The influence of buffer system and biological fluids on the degradation of magnesium. *Journal of Biomedical Materials Research - Part B Applied Biomaterials* **105** (2017), 1490–1502, ISSN 15524981.

[159] Vagge, S. T. & Bakshi, S.: Effect of precipitation hardening on stress corrosion cracking susceptibility index of AZ31B magnesium alloy in simulated body fluid. *Materials Today: Proceedings* **38** (2020), 2191–2199, ISSN 22147853.

[160] Wagener, V. & Virtanen, S.: Influence of electrolyte composition (simulated body fluid vs. Dulbecco's modified Eagle's medium), temperature, and solution flow on the biocorrosion behavior of commercially pure Mg. *Corrosion* **73** (2017), 1413–1422, ISSN 00109312.

[161] Wang, B.; Gao, W.; Pan, C.; Liu, D. & Sun, X.: Effect of the Combination of Torsional and Tensile Stress on Corrosion Behaviors of Biodegradable WE43 Alloy in Simulated Body Fluid. *Journal of Functional Biomaterials* **14** (2023), ISSN 20794983.

[162] Wang, B. J.; Xu, D. K.; Sun, J. & Han, E. H.: Effect of grain structure on the stress corrosion cracking (SCC) behavior of an as-extruded Mg-Zn-Zr alloy.

Corrosion Science **157** (2019), 347–356, ISSN 0010938X.

[163] Wang, B. J.; Xu, D. K.; Wang, S. D.; Sheng, L. Y.; Zeng, R. C. & hou Han, E.: Influence of solution treatment on the corrosion fatigue behavior of an as-forged Mg-Zn-Y-Zr alloy. *International Journal of Fatigue* **120** (2019), 46–55, ISSN 01421123.

[164] Wang, J.; Wang, J.; Fu, Q.; Sheng, K.; Liu, M.; Sun, Y.; Mei, D.; Kou, Y.; Zhu, S. & Guan, S.: Microstructure, mechanical properties and corrosion fatigue behaviour of biodegradable Mg–Zn–Y–Nd alloy prepared by double extrusion. *Corrosion Engineering Science and Technology* **56** (2021), 584–593, ISSN 17432782.

[165] Wang, Q.; Liu, Y.; Zhu, X.; Li, S.; Yu, S.; Zhang, L. & Song, Y.: Study on the effect of corrosion on the tensile properties of the 1.0 wt.% Yttrium modified AZ91 magnesium alloy. *Materials Science and Engineering: A* **517** (2009), 239–245, ISSN 09215093.

[166] Wang, Z.; Wu, S.; Lei, Y.; Kan, Q. & Kang, G.: Damage evolution of extruded magnesium alloy from deformation twinning and dislocation slipping in uniaxial stress-controlled low cycle fatigue. *International Journal of Fatigue* **164** (2022), ISSN 01421123.

[167] Wegner, N.; Kotzem, D.; Wessarges, Y.; Emminghaus, N.; Hoff, C.; Tenkamp, J.; Hermsdorf, J.; Overmeyer, L. & Walther, F.: Corrosion and corrosion fatigue properties of additively manufactured magnesium alloy WE43 in comparison to titanium alloy Ti-6Al-4V in pysiological environment. *Materials* **12** (2019), ISSN 19961944.

[168] Weng, W.; Biesiekierski, A.; Li, Y.; Dargusch, M. & Wen, C.: A review of the physiological impact of rare earth elements and their uses in biomedical Mg alloys. *Acta Biomaterialia* **130** (2021), 80–97, ISSN 18787568.

[169] Winzer, N.; Atrens, A.; Song, G.; Ghali, E.; Dietzel, W.; Kainer, K. U.; Hort, N. & Carsten Blawert: A critical review of the Stress Corrosion Cracking (SCC) of magnesium alloys. *Advanced Engineering Materials* **7** (2005), 659–693, ISSN 14381656.

[170] Witte, F.; Fischer, J.; Nellesen, J.; Crostack, H. A.; Kaese, V.; Pisch, A.; Beckmann, F. & Windhagen, H.: In vitro and in vivo corrosion measurements of magnesium alloys. *Biomaterials* **27** (2006), 1013–1018, ISSN 01429612.

[171] Witte, F.; Hort, N.; Carla Vogt; Cohen, S.; Kainer, K. U.; Willumeit, R. & Feyerabend, F.: Degradable biomaterials based on magnesium corrosion. *Current Opinion in Solid State and Materials Science* **12** (2008), 63–72, ISSN 13590286.

[172] Witte, F.; Kaese, V.; Haferkamp, H.; Switzer, E.; Meyer-Lindenberg, A.; Wirth, C. J. & Windhagen, H.: In vivo corrosion of four magnesium alloys and the associated bone response. *Biomaterials* **26** (2005), 3557–3563, ISSN 01429612.

[173] Witte, F.; Ulrich, H.; Rudert, M. & Willbold, E.: Biodegradable magnesium scaffolds: Part I: Appropriate inflammatory response. *Journal of Biomedical Materials Research - Part A* **81** (2007), 748–756, ISSN 15493296.

[174] Wu, B.; Song, L.; Duan, G.; Du, X.; Wang, Y.; Esling, C. & Philippe, M. J.:

Effect of cyclic frequency on uniaxial ratcheting behavior of a textured AZ31B magnesium alloy under stress control. *Materials Science and Engineering: A* **795** (2020), ISSN 09215093.

[175] Wu, Y.; Wang, Y. M.; Zhao, D. W.; Zhang, N.; Li, H.; Li, J.; Wang, Y.; Zhao, Y.; Yan, J. & Zhou, Y.: In vivo study of microarc oxidation coated Mg alloy as a substitute for bone defect repairing: Degradation behavior, mechanical properties, and bone response. *Colloids and Surfaces B: Biointerfaces* **181** (2019), 349–359, ISSN 18734367.

[176] Wu, Y. F.; Wang, Y. M.; Jing, Y. B.; Zhuang, J. P.; Yan, J. L.; Shao, Z. K.; Jin, M. S.; Wu, C. J. & Zhou, Y.: In vivo study of microarc oxidation coated biodegradable magnesium plate to heal bone fracture defect of 3 mm width. *Colloids and Surfaces B: Biointerfaces* **158** (2017), 147–156, ISSN 18734367.

[177] Xin, Y. & Chu, P. K.: Influence of Tris in simulated body fluid on degradation behavior of pure magnesium. *Materials Chemistry and Physics* **124** (2010), 33–35, ISSN 02540584.

[178] Xin, Y.; Hu, T. & Chu, P. K.: Influence of Test Solutions on In Vitro Studies of Biomedical Magnesium Alloys. *Journal of The Electrochemical Society* **157** (2010), C238, ISSN 00134651.

[179] Xin, Y.; Hu, T. & Chu, P. K.: In vitro studies of biomedical magnesium alloys in a simulated physiological environment: A review. *Acta Biomaterialia* **7** (2011), 1452–1459, ISSN 17427061.

[180] Xin, Y.; Huo, K.; Hu, T.; Tang, G. & Chu, P. K.: Corrosion products on biomedical magnesium alloy soaked in simulated body fluids. *Journal of Materials Research* **24** (2009), 2711–2719, ISSN 08842914.

[181] Xin, Y.; Huo, K.; Tao, H.; Tang, G. & Chu, P. K.: Influence of aggressive ions on the degradation behavior of biomedical magnesium alloy in physiological environment. *Acta Biomaterialia* **4** (2008), 2008–2015, ISSN 17427061.

[182] Xin, Y.; Liu, C.; Zhang, X.; Tang, G.; Tian, X. & Chu, P. K.: Corrosion behavior of biomedical AZ91 magnesium alloy in simulated body fluids. *Journal of Materials Research* **22** (2007), 2004–2011, ISSN 08842914.

[183] Xiong, Y. & He, L.: Ratcheting behavior of surface-modified AZ80 magnesium alloy after pre-corrosion in simulated body fluids with various pH values. *Fatigue and Fracture of Engineering Materials and Structures* **46** (2023), 4729–4742, ISSN 14602695.

[184] Xiong, Y.; Shen, Y.; He, L.; Yang, Z. & Song, R.: Stress corrosion cracking behavior of LSP/MAO treated magnesium alloy during SSRT in a simulated body fluid. *Journal of Alloys and Compounds* **822** (2020), ISSN 09258388.

[185] Xiong, Y.; Yu, Y. & Hu, X.: Fatigue behavior of modified ZK60 magnesium alloy after pre-corrosion under stress-controlled loading. *Engineering Fracture Mechanics* **260** (2022), ISSN 00137944.

[186] Xu, L.; Liu, X.; Sun, K.; Fu, R. & Wang, G.: Corrosion Behavior in Magnesium-Based Alloys for Biomedical Applications. *Materials* **15** (2022), ISSN 19961944.

[187] Yamamoto, A. & Hiromoto, S.: Effect of inorganic salts, amino acids and proteins on the degradation of pure magnesium in vitro. *Materials Science Engineering C* **29** (2009), 1559–1568, ISSN 0928-4931.

[188] Ye, C. H.; Zheng, Y. F.; Wang, S. Q.; Xi, T. F. & Li, Y. D.: In vitro corrosion and biocompatibility study of phytic acid modified WE43 magnesium alloy. *Applied Surface Science* **258** (2012), 3420–3427, ISSN 01694332.

[189] Zeng, R. C.; Hu, Y.; Guan, S. K.; Cui, H. Z. & Han, E. H.: Corrosion of magnesium alloy AZ31: The influence of bicarbonate, sulphate, hydroge phosphate and dihydrogen phosphate ions in saline solution. *Corrosion Science* **86** (2014), 171–182, ISSN 0010938X.

[190] Zhang, D.; Ma, S.; Nachtsheim, J.; Zhang, S. & Markert, B.: A variational phase-field framework for multiphysics modelling of degradation and stress corrosion cracking in biodegradable magnesium alloys. *Journal of the Mechanics and Physics of Solids* (2024), 105694, ISSN 0022-5096.

[191] Zhang, F.; Ma, A.; Jiang, J.; Xu, H.; Song, D.; Lu, F. & Nishida, Y.: Enhanced biodegradation behavior of ultrafine-grained ZE41A magnesium alloy in Hank's solution. *Progress in Natural Science: Materials International* **23** (2013), 420–424, ISSN 17455391.

[192] Zhang, G.; Jiang, E.; Wu, L.; Ma, W.; Yang, H.; Tang, A. & Pan, F.: Corrosion protection properties of different inhibitors containing PEO/LDHs composite coating on magnesium alloy AZ31. *Scientific Reports* **11** (2021), ISSN 20452322.

[193] Zhang, S.; Zhang, X.; Zhao, C.; Li, J.; Song, Y.; Xie, C.; Tao, H.; Zhang, Y.; He, Y.; Jiang, Y. & Bian, Y.: Research on an Mg-Zn alloy as a degradable biomaterial. *Acta Biomaterialia* **6** (2010), 626–640, ISSN 17427061.

[194] Zhang, T.; Meng, G.; Shao, Y.; Cui, Z. & Wang, F.: Corrosion of hot extrusion AZ91 magnesium alloy. Part II: Effect of rare earth element neodymium (Nd) on the corrosion behavior of extruded alloy. *Corrosion Science* **53** (2011), 2934–2942, ISSN 0010938X.

[195] Zhao, J.; Gao, L. L.; Gao, H.; Yuan, X. & Chen, X.: Biodegradable behaviour and fatigue life of ZEK100 magnesium alloy in simulated pysiological environment. *Fatigue and Fracture of Engineering Materials and Structures* **38** (2015), 904–913, ISSN 14602695.

[196] Zhao, M. C.; Liu, M.; Song, G. L. & Atrens, A.: Influence of pH and chloride ion concentration on the corrosion of Mg alloy ZE41. *Corrosion Science* **50** (2008), 3168–3178, ISSN 0010938X.

[197] Zhao, Y.; Wu, G.; Lu, Q.; Wu, J.; Xu, R.; Yeung, K. W. & Chu, P. K.: Improved surface corrosion resistance of WE43 magnesium alloy by dual titanium and oxygen ion implantation. *Thin Solid Films* **529** (2013), 407–411, ISSN 00406090.

[198] Zhou, L. F.; Liu, Z. Y.; Wu, W.; Li, X. G.; Du, C. W. & Jiang, B.: Stress corrosion cracking behavior of ZK60 magnesium alloy under different conditions. *International Journal of Hydrogen Energy* **42** (2017), 26162–26174, ISSN 03603199.

[199] Zhu, L.; Petrova, R. S.; Gashinski, J. P. & Yang, Z.: The effect of surface roughness

on PEO-treated Ti-6Al-4V alloy and corrosion resistance. *Surface and Coatings Technology* **325** (2017), 22–29, ISSN 02578972.

[200] Zou, Y.; Wang, Y.; Wei, D.; Du, Q.; Ouyang, J.; Jia, D. & Zhou, Y.: In-situ SEM analysis of brittle plasma electrolytic oxidation coating bonded to plastic aluminum substrate: Microstructure and fracture behaviors. *Materials Characterization* **156** (2019), ISSN 10445803.

[201] Öcal, E. B.; Esen, Z.; Aydınol, K. & Dericioğlu, A. F.: Comparison of the short and long-term degradation behaviors of as-cast pure Mg, AZ91 and WE43 alloys. *Materials Chemistry and Physics* **241** (2020), ISSN 02540584.

Nomenclature

Experimental & material parameters

Symbol	Unit	Description
Δt	(h)	Immersion time
$\Delta \mathrm{m}_{A,Mg}$	(mg/cm^2)	Mass loss of magnesium per surface area
Δm_{Mg}	(mg)	Mass loss of magnesium
ε	(–)	Strain
ε_a	(–)	Strain amplitude
ε_a^e	(–)	Elastic strain $\varepsilon_f^{'}$
ε_a^p	(–)	Plastic strain $\varepsilon_f^{'}$
$\varepsilon_f^{'}$	(–)	Fatigue strength coefficient
ε_{f-air}	(–)	Elongation to failure in air
$\varepsilon_{f-fluid}$	(–)	Elongation to failure in fluid
θ	(degree)	Incline angle of XRD measurement
λ	(nm)	Wave length of X-ray
ρ_{Mg}	g/cm^3	Density of magnesium
σ	(N/mm^2)	Stress
σ_a	(N/mm^2)	Stress amplitude
σ_{air}	(N/mm^2)	Stress amplitude in air
$\sigma_f^{'}$	(N/mm^2)	Fatigue strength coefficient
σ_{fluid}	(N/mm^2)	Stress amplitude in fluid
a	(nm)	Distance between atoms
A	(cm^2)	Surface area
A	(%)	Elongation after fracture
A	(–)	Basquin coefficient
A_g	(%)	Non-proportional elongation at maximum force
$\mathrm{A}_g t$	(%)	Total elongation at maximum force
A_t	(%)	Total elongation at fracture
b	(–)	Fatigue strength exponent
b	(–)	Basquin exponential factor
CR	(mm/year)	Corrosion rate
c	(–)	Fatigue ductility exponent

E	(GPa)	Elasticity constant (Young's modulus / E-Modulus)
I_{ε}	(%)	Susceptibility index for the elongation-to-failure
I_{UTS}	(%)	Susceptibility index for the ultimate tensile strength
$K^{'}$	(–)	Cyclic strengthening coefficient
M_{Mg}	(g/mol)	Molar mass of magnesium
n	(–)	Number of tests
N	(–)	Number of loading cycles
N_f	(–)	Number of cycles to failure
$n^{'}$	(–)	Cyclic hardening coefficient
p	(N/m^2)	Gas pressure
R	(J/(Kmol))	Molar gas constant
Ra	(nm)	Average surface roughness
RRSE	(%)	Reduction ratio of fatigue strength
R_{eH}	(MPa)	Yield strength
R_m	(MPa)	Tensile strength
R_{avg}	(μm)	Average radius
R_{min}	(μm)	Minimal radius at most corroded spot
R_{max}	(μm)	Maximal remaining radius at least corroded spot
Rz	(μm)	Mean peak-to-valley roughness
T	(K)	Temperature
UTS_{air}	(MPa)	Ultimate tensile strength measured in air
UTS_{fluid}	(MPa)	Ultimate tensile strength measured in fluid
V_H	(ml)	Gas volume
v1	(s^{-1})	Fastest strain rate
v2	(s^{-1})	Intermediate strain rate
v3	(s^{-1})	Slowest strain rate

Acronyms

Selected Acronym	Definition
A	Ampere
Ag	Silver
Al	Aluminium
AM50	Magnesium alloy
AZ31	Magnesium alloy
AZ31B	Magnesium alloy

AZ60	Magnesium alloy
AZ61	Magnesium alloy
AZ80	Magnesium alloy
AZ91	Magnesium alloy
AZ91D	Magnesium alloy
Be	Beryllium
BSA	Bovine serum albumin
BSE	Back-scattered electron
C	Carbon
Ca	Calcium
CC	Cryogenic cooling
CF	Corrosion fatigue
Cl	Chloride
CLT	Constant load test
cm^2	Square centimetre
Cu	Copper
d	days
DMEM	Dulbecco's Modified Eagle Medium
e	electron
EDS	Energy dispersive spectroscopy
EIS	Electrochemical impedance spectroscopy
Fe	Iron
FBS	Fetal bovine serum
GPa	Giga Pascal
H	Hydrogen
h	hours
HE	Hydrogen embrittlement
HEDE	Hydrogen-enhanced decohesion
HELP	Hydrogen-enhanced localised-plasticity
HEPA	High-efficiency particulate air
HEPES	2-[4-(2-Hydroxyethyl)piperazin-1-yl]ethane-1-sulfonic acid (buffer system)
IGSCC	Intergranular stress corrosion cracking
K	Potassium
l	Litre
LSP	Laser shock peening

MAO	Micro-arc oxidation, equal to PEO
ME21	Magnesium alloy
Mg	Magnesium
Mg-Y-Zn	Magnesium alloy
Mg-Zn-Zr	Magnesium alloy
Mg-Zn-Y-Nd	Magnesium alloy
Mg-1Ca	Magnesium alloy
Mg-1Zn	Magnesium alloy
Mg-2Zn-0.2Ca	Magnesium alloy
Mg3Zn1Ca	Magnesium alloy
micro-CT	X-ray microtomography
min	Minute
ml	Millilitre
mm	Millimetre
mmol	Millimole
m-SBF	modified Simulated Body Fluid
Mn	Manganese
mol	Mole
MPa	Mega Pascal
N	Newton
Na	Sodium
Nd	Neodymium
Ni	Nickel
No.	Number
O	Oxygen
OCP	Open circuit potential
P	Phosphorus
PBS	Phosphate buffered saline
PC	Phosphate conversion
PE	Primary electron
PEO	Plasma electrolytic oxidation
rpm	Rounds per minute
s	seconds
SBF	Simulated body fluid
SCC	Stress corrosion cracking
SE	Secondary electron

SEM	Scanning electron microscopy
S	Sulphur
Si	Silicon
SSRT	Small strain rate test
S-N	Relationship between stress amplitude and number of cycles to failure
TEM	Transmission electron microscopy
TGSCC	Transgranular stress corrosion cracking
TPU	Thermoplastic polyurethane
Tris	tris(hydroxymethyl)aminomethane (buffer system)
WE43	Magnesium alloy
wt.%	percentage by weight
WZ21	Magnesium alloy
XRD	X-ray diffraction spectroscopy
Y	Yttrium
ZEK100	Magnesium alloy
ZK40-0.4Sr	Magnesium alloy
Zr	Zirconium
ZX10	Magnesium alloy
ZX50	Magnesium alloy
α-matrix	Solid solution phase of metal alloys
α-Mg	Solid solution phase of magnesium alloys
β	Solid solution phase of metal alloys
$\beta 1$	Solid solution phase of metal alloys
ϵ-N	Relationship between strain amplitude and number of cycles to failure
μm	Micrometre
μg	Microgram
$^\circ$	Degree
$^\circ$C	Degree Celsius
2D	Two-dimensional
3D	Three-dimensional

List of Figures

List of Tables